Tuning of ground state and phase transition in complex oxide nanomaterials

A Thesis
Submitted for the Degree of
Doctor of Philosophy
In Jadavpur University

by

Tapati Sarkar

DST Unit for NanoSciences
Department of Material Science
S. N. Bose National Centre for Basic Sciences
Block – JD, Sector – III
Salt Lake
Kolkata – 700098
India.

May 2009

CERTIFICATE FROM SUPERVISOR

This is to certify that the thesis entitled "**Tuning of ground state and phase transition in complex oxide nanomaterials"** submitted by Smt. Tapati Sarkar, who got her name registered on 09th. November 2006 for the award of Ph.D. (Science) degree of Jadavpur University, is absolutely based upon her own work under the supervision of Prof. A. K. Raychaudhuri, and that neither this thesis nor any part of it has been submitted for any degree/diploma or any other academic award anywhere before.

(SIGNATURE OF SUPERVISOR)

To Ma & Baba…….

……for being the best parents ever

Acknowledgements

This dissertation would not have been possible without the involvement of a number of people. First and foremost among them is my research supervisor, Prof. A. K. Raychaudhuri. He was the one to whom I could turn to for guidance when I was taking baby steps into the world of research in late 2004. Over the last four and a half years that I have known him, he has been most instrumental in honing my skills, pushing me a little more so that I could overcome my inhibitions and do those things which I would otherwise have left undone, and making me self-reliant enough so that now I can move out into the world with confidence and self belief. Thank you Sir, not only for your constant encouragement and support, but also for the times you chided me when I made some mistake, because though it seemed unfair at the time, it always yielded positive results at the end.

When I first joined NanoLab in September 2004, along with my research career, this laboratory was also in its infancy. Prof. Raychaudhuri had just moved to S. N. B. N. C. B. S., Kolkata from IISc., Bangalore, and we hardly had any of the experimental facilities available. Without the help of some people my work would not have progressed at all in those initial months. I am particularly grateful to Dr. Uday K. Singh who went out of his way to allow me access to various facilities in his laboratory, often inconveniencing himself in the process. Dr. Dipten Bhattacharya of C. G. C. R. I., Kolkata was also extremely helpful, not only in those starting months, but also at later stages of my Ph.D. His extremely helpful nature made me take his help almost for granted, but today I would like to take this opportunity to express my heartfelt thanks for all his support.

A large part of this thesis work would not have been possible without the active involvement of Prof. Tapan Chatterji of ILL, Grenoble, France. My collaboration with him started in a most fortuitous manner. I sent him four samples for some neutron diffraction measurements. It was his initiative that turned our ideas into a concrete experimental proposal, we got some beamtime at E.S.R.F., Grenoble and I found myself in the world of high resolution diffraction studies. The structural studies which followed turned out to be the most crucial part of this thesis work, and I am most grateful to Prof. Chatterji without whose help these studies would never have been possible. Here I would also like to mention Dr. Pranab Chowdhury, Dr. S. M. Yusuf, Anup K. Bera and Dr. Emil Bozin who, at various times, have helped me learn various aspects of the techniques of structural refinements.

A part of my thesis work involved measurements which were taken at C. S. R., Indore. I would like to specifically mention Dr. V. Ganesan, Dr. Alok Banerjee, L.S. Sharath Chandra, Ashim K. Pramanik and Kranti Kumar for all their help during the one month that I stayed there.

Of course, the four and a half years of my Ph.D. life would never have been so enjoyable had it not been for the wonderful people with whom I shared this lab. Thanks to all of them for making these years so pleasant and memorable – Barnali di (who introduced me to the world of sol gel synthesis), Anindya di (whom I always turned to whenever I needed some advice related to chemistry), Sudeshna di (this laboratory would never have been such a lively place without

you), Subrata, Saptarshi, Ritwik, Rajesh, Kuntal da, Kaustuv da, Sharathi da, Rajib, Shahnewaz and Manotosh.

A special mention has to be made of a special person, Venkat. Though I first met him just after joining S. N. B. N. C. B. S. in August 2002, our friendship began only after I joined my Ph.D. With time our friendship has grown and matured, and this was the best thing that happened to me during my Ph.D. years. Venkat has helped me face all the difficulties that came my way during these years. Apart from the emotional support, he has also helped me academically many many times. At the risk of sounding mushy, he really has been the wind beneath my wings. Thank you Venkat. I am glad I found you.

Lastly, two people who have really been my pillars of strength – my parents. I feel lucky to have them as my parents. They are two of the most understanding and undemanding people on earth. They never let me feel the need to think about anything else other than my work. They gave me the freedom to do exactly what I wanted, never imposing anything on me ever. I owe, not only this thesis, but everything that I have ever done in my life to them. Since my childhood I have always taken them for granted, knowing that no words of gratitude could ever be enough. But today I would like to spell it out. Thank you Ma, thank you Baba just for being my parents. I love you.

PUBLICATIONS

1. **Tapati Sarkar**, Barnali Ghosh, A. K. Raychaudhuri and Tapan Chatterji, Crystal structure and physical properties of half-doped manganite nanocrystals of less than 100-nm size, *Physical Review B*, Vol. 77, 235112 (2008)

2. **Tapati Sarkar**, A. K. Raychaudhuri and Tapan Chatterji, Size induced arrest of the room temperature crystallographic structure in nanoparticles of $La_{0.5}Ca_{0.5}MnO_3$, *Applied Physics Letters*, Vol. 92, 123104 (2008)

3. **Tapati Sarkar**, M. Venkata Kamalakar and A. K. Raychaudhuri, Transport properties of nanoparticles of complex oxides: Likely presence of Coulomb blockade at low temperature, accepted in *Journal of Nanoscience and Nanotechnology* (2008)

4. **Tapati Sarkar**, P. K. Mukhopadhyay, A. K. Raychaudhuri and Sangam Banerjee, Structural, magnetic and transport properties of nanoparticles of the manganite $Pr_{0.5}Ca_{0.5}MnO_3$, *Journal of Applied Physics*, Vol.101, 124307 (2007)

5. **Tapati Sarkar**, Barnali Ghosh and A. K. Raychaudhuri, Effect of size reduction on charge ordering in $L_{a0.5}C_{a0.5}Mn_{O3}$, *Journal of Nanoscience and Nanotechnology,* Vol. 7, 2020 – 2024 (2007)

CONTENTS

List of Figures

List of Tables

CHAPTER 1. INTRODUCTION

This dissertation deals with a basic question – Can size reduction in crystals lead to the evolution of new crystal structures and physical properties? To probe this question, we have chosen hole – doped rare – earth manganites and cobaltates for case studies. These systems show a variety of phases with interesting physical properties. These physical properties are closely related to the structure. It is thus expected that size reduction, if they have an effect on the structure of these systems, can modify the physical properties qualitatively. Thus, the size reduction can lead to "tuning" of the ground state. As we will see below, this is the recurring theme of this thesis.

As stated above, this thesis deals with the nature of the ground state of nanoparticles of complex oxides. Most of the investigations were done on manganites (manganese compounds of composition $A_{1-x}B_xMnO_3$, A being a trivalent rare earth ion like La, Pr etc. and B being a divalent alkaline earth ion like Ca, Sr etc.). The cobaltates ($La_{0.5}Sr_{0.5}CoO_3$) have also been investigated.

Both these oxides crystallize in the cubic structure of the perovskite mineral $CaTiO_3$ (because of which they are referred to as perovskite oxides), but the actual crystal structure is often a distorted perovskite (eg. $La_{0.5}Ca_{0.5}MnO_3$ has a crystal symmetry which is orthorhombic at high temperatures and monoclinic at low temperatures[1], and $La_{0.5}Sr_{0.5}CoO_3$ has a crystal symmetry which is a rhombohedral[2]). The most fundamental property of these materials, which has made them quite unique and exciting to study is a strong correlation between structure, transport and magnetic properties. The electronic transport properties of these oxides strongly interact with the magnetic properties and with the crystal lattice. These compounds are thus part of the 'strongly correlated electron systems'. Due to this strong coupling between the electron orbitals, the spin and the lattice, a small change in the chemical composition (by changing the ratio between the trivalent and divalent ions at the A and B sites respectively, or by changing the ion on the B site and thereby changing the average ionic radius), can induce large changes in the physical properties. This gives rise to a rich phase diagram for these class of oxides (e.g. $La_{1-x}Ca_xMnO_3$ progressively changes from an antiferromagnetic insulator to a ferromagnetic insulator to a ferromagnetic metal, and back to an antiferromagnetic insulator as x is increased from 0 to 1[3]). A similar change can occur due to external effects, such as a magnetic field[4], a hydrostatic pressure[5], or the temperature. The ground state of these perovskite oxides is thus sensitive to a variety of perturbations. One such perturbation, which has been comparatively less studied, is the effect of reducing the particle size. Can size reduction also tune the interactions, thereby changing the nature of the ground state, and if so, how exactly do the modifications occur? These are the questions which this thesis tries to address. The representative oxides which have been studied in the nano regime are $La_{1-x}Ca_xMnO_3$ (with x = 0.33, the optimal doping concentration and x = 0.5, the charge – ordered regime), $Pr_{0.5}Ca_{0.5}MnO_3$ (which is a charge – ordered antiferromagnet in the bulk state), and $La_{0.5}Sr_{0.5}CoO_3$, a ferromagnetic metal. But before we can expand on the new and main work on nanoparticles of these oxides in the subsequent chapters, it is necessary to highlight some of the properties which are important to understand these results.

1.1 Crystal Structure and its Relevance

The parent compound crystallizes in $AMnO_3$ type perovskite structure which consists of a network of corner – shared MnO_6 octahedra with the A – site cation situated at the centre of the cube (Fig1.1). Although the ideal perovskite structure is cubic (e.g. as seen in $SrTiO_3$), partial substitution of the trivalent A ion by divalent B ion ($A_{1-x}B_xMnO_3$) almost always leads to a distortion of the structure from its ideal cubic one. This distortion occurs due to a change in the average ionic size. This substitution also leads to the formation of a mixed valence state of Mn i.e. Mn^{3+} and Mn^{4+} in order to maintain charge neutrality of the system (e.g. $La_{1-x}^{3+}Ca_x^{2+}Mn_{1-x}^{3+}Mn_x^{4+}O_3^{2-}$).

The degree of distortion in the unit cell is conveniently quantified by the "Goldsmith tolerance factor (f)" which when defined in terms of the distance between the atoms in the lattice can be written as $f = \dfrac{r_{A-O}}{\sqrt{2}r_{Mn-O}}$. Thus, for an ideal cubic unit cell, $f = 1$ (see Fig.1.1 for clarification). An alternative (but equivalent) and more commonly used definition of f is that in terms of the ionic radii[9]: $f = \dfrac{r_A + r_O}{\sqrt{2}(r_{Mn} + r_O)}$. In both cases, f has a simple geometric meaning and describes the degree of deviation of the lattice from the ideal cubic perovskite structure (for which $f = 1$, and the Mn – O – Mn angle is 180^0). Rotations and deformations of the octahedra cause a lowering of the space group and $f < 1$. Thus, for $1 > f > 0.96$, the structure is rhombohedral, and for $f < 0.96$, the structure becomes orthorhombic. For a doped manganite, since there are two possible ions at the A site, the tolerance factor is defined as a density – weighted average of the individual tolerance factors.
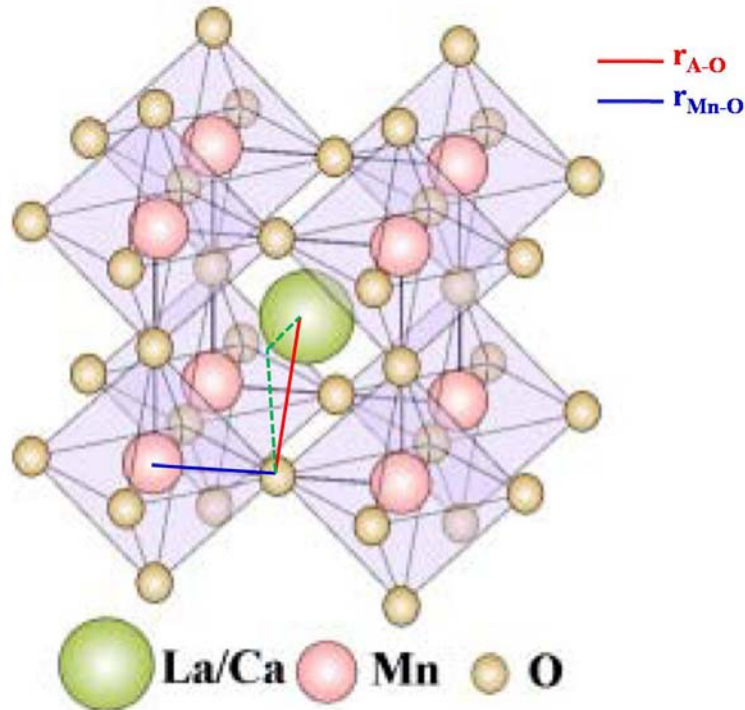
Fig1.1. Schematic crystal structure of a perovskite manganite ($AMnO_3$).

In perovskite manganites, the properties of the system are inherently linked with the degree of deviation from the ideal perovskite cubic structure. Thus, as the A radius is reduced, the MnO_6 octahedra rotate and tilt resulting in a decrease of the Mn-O-Mn bond angle (θ) from 180°. The hopping amplitude for carriers to move from one Mn site to the next also decreases as θ is reduced from 180° (for a 90° bond, the hopping involving a p – orbital at the oxygen is zero). As a consequence, as the tolerance factor decreases, the tendencies to charge localization increase due to a reduction in the carrier mobility. The relevance of the crystal structure arises from the fact that in the manganites the three degrees of freedom – charge, spin and lattice – are coupled to each other. Thus, a change in the structure (lattice) is reflected in a change in the magnetic state (spin degree of freedom) or electronic state (charge degree of freedom) of the system. The most convenient way of illustrating this importance of the crystal structure is through phase diagrams where the tolerance factor (f) is one of the axes. (This is because, as stated earlier, the tolerance factor is a very convenient way of quantifying the degree of distortion of the lattice from the ideal cubic perovskite structure). Such examples of phase diagrams are shown in Fig.1.2. The phase diagram shown in Fig.1.2(a) is representative of the system $La_{0.67}Ca_{0.33}MnO_3$ which we study in details in Chapter 3. Fig.1.2(b) shows the phase diagram of $(La_yPr_{1-y})_{0.5}Ca_{0.5}MnO_3$. The end members of this series ($La_{0.5}Ca_{0.5}MnO_3$ and $Pr_{0.5}Ca_{0.5}MnO_3$) are the two systems which we study in details in Chapter 4.
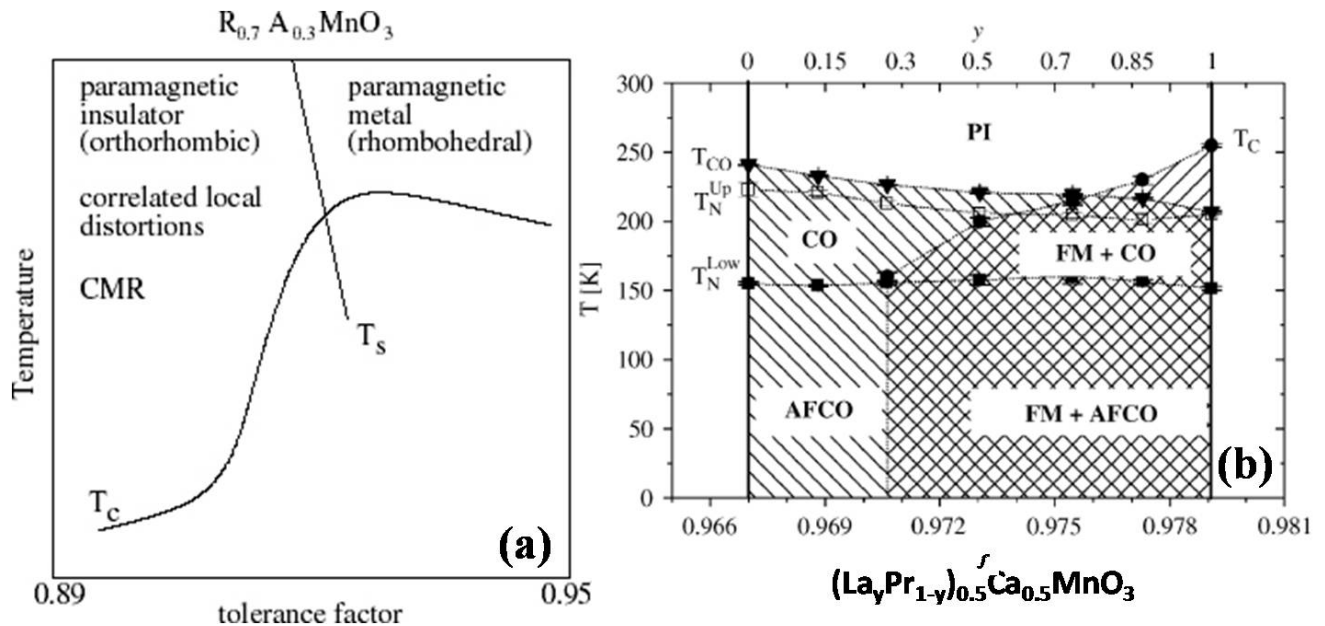
Fig1.2. (a) General temperature versus tolerance factor phase diagram of (a) hole-doped manganites with $x \sim 0.3$: T_C, Curie temperature; T_S, the orthorhombic – to – rhombohedral transition temperature (reproduced from [10]) and (b) the $(La_yPr_{1-y})_{0.5}Ca_{0.5}MnO_3$ series. T_C is the ferromagnetic Curie temperature, T_N is the antiferromagnetic Neel temperature, PI stands for paramagnetic insulator, FM for ferromagnetic, CO for charge order and AFCO for antiferromagnetic with charge order (reproduced from [11]).

3

Thus, the crystal structure (quantified by the tolerance factor, f) decides whether the system should be a paramagnetic insulator, a paramagnetic metal or a CMR metal. A natural question in the context of this thesis is whether f can be tuned by size reduction. In other words, whether the structure, and hence the properties can be controlled by controlling the particle size. An investigation of the structure of these oxides in the nanocrystalline form might well answer this question (and it does, as we will see in later chapters).

1.2 Phase Diagram

The phase diagrams of doped perovskite manganites are exceptionally rich with different resistive, magnetic as well as structural phases[12,13,14]. These phase diagrams have been constructed from detailed measurements of macroscopic physical quantities like resistivity, susceptibility and magnetization on single crystal and bulk ceramic samples. Even though the phase diagram of each composition is different due to the difference in radii of the atoms involved, but they have some common features. Since the majority of samples studied in this dissertation consist of variously doped $La_{1-x}Ca_xMnO_3$ (LCMO), we discuss the phase diagram of LCMO (Fig. 1.3) in some details.

LCMO is an intermediate bandwidth compound and is among the most studied compounds of the manganite family. Schiffer et. al. gave the first phase diagram of LCMO in 1995[3] but the complete phase diagram was established in 2000 by Cheong and Hwang[15]. At low temperatures LCMO undergoes the following transitions: the end compositions ($x = 0$ and $x = 1$) are insulators at all temperatures, and canted antiferromagnetic (CAF) insulators at low temperatures. On increasing the Ca concentration, a ferromagnetic insulating (FI) phase occurs till $x = 0.22$. Between $x = 0.22$ and $x = 0.5$, we get a ferromagnetic metal (FM) exhibiting the colossal magnetoresistance (CMR) effect. $x = 0.33$ is the optimal doping concentration yielding the highest ferromagnetic Curie temperature (T_C) = 270 K. At $x = 0.5$ where the Mn^{3+}:Mn^{4+} ratio is 1:1, a charge – ordered (CO) antiferromagnetic insulating phase starts to evolve at low temperatures. This phase continues till $x = 0.87$, beyond which we again get a canted antiferromagnetic regime. At high temperatures, we get a paramagnetic insulating phase.
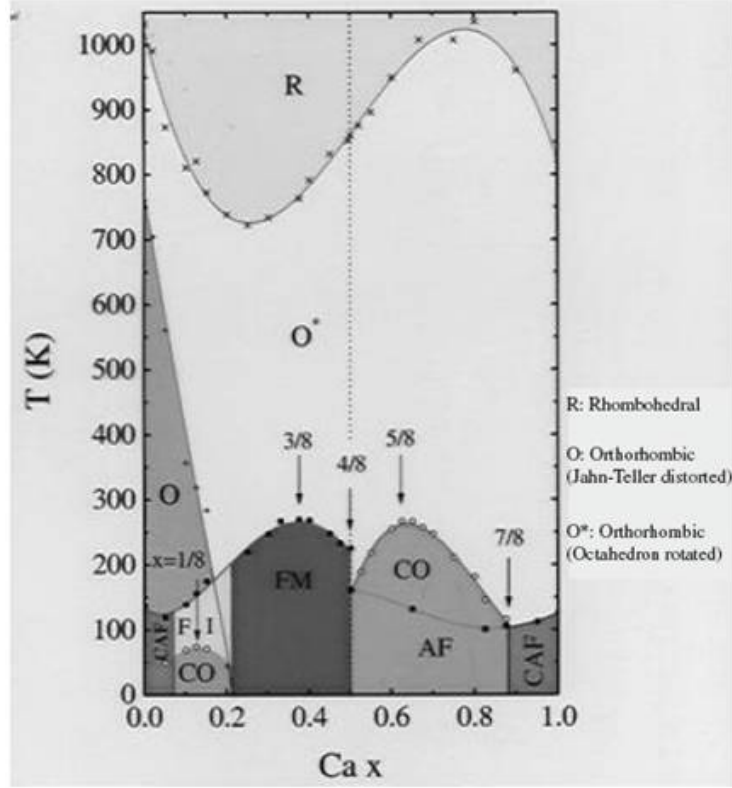
Fig1.3. Phase diagram of La$_{1-x}$Ca$_x$MnO$_3$ in the doping concentration (x) – temperature (T) plane (reproduced from [16]).

Kim et. al.[17] identified a tricritical point in the La$_{1-x}$Ca$_x$MnO$_3$ phase diagram for x = 0.4, thereby marking a boundary between the first order (x < 0.4) and second order (x > 0.4) phase transitions within the ferromagnetic range (0.22 < x < 0.5). Recently, the point (x$_t$ = 0.25, T$_t$ = 205 K) on the (x, T) phase diagram of La$_{1-x}$Ca$_x$MnO$_3$ has also been identified[18] as a tricritical point, so that if T$_C$ < T$_t$, the ferromagnetic – to – paramagnetic transition is second order, while at T$_C$ > T$_t$, the transition is first order.

The phase diagram of LCMO thus consists of all possible phases (canted antiferromagnetic, ferromagnetic metallic, charge ordered and paramagnetic insulating). There are a variety of interactions and mechanisms that decide such a rich phase diagram. In the following sections, we will briefly touch upon the various known mechanisms and their role in deciding the phase diagram of the manganite system.

1.3 Crystal Field Splitting and Jahn Teller effect – Manganese ion

The physical properties of the doped manganite system strongly depends on the spin structure of the Mn ion. Considered in isolation, the Mn ion has an active d – shell with five degenerate levels. The situation drastically changes once the ions become part of the perovskite crystal structure. In a cubic environment, since the three axes (x,y,z) are equivalent, the d_{xy}, d_{yz} and d_{zx} orbitals are affected similarly and form a triplet (t_{2g}). The other two orbitals ($3z^2 – r^2$ and $x^2 – y^2$) form a doublet (e_g). In addition, the doublet has a higher energy than the triplet since the

5

orbitals of the doublet point along the directions where the negative oxygen ions are located, thereby increasing the energy due to Coulombic repulsion. This crystal field splitting between the t_{2g} and e_g states is about $1 - 2$ eV. If the crystal was tetragonal (instead of cubic), there would be additional splittings because now the lattice spacings in one direction would be different from the other two (say, $a = b \neq c$). In such a case, the orbitals d_{zx} and d_{yz} would remain degenerate by symmetry (if c is along the z – axis), but d_{xy} will have a different energy. Similarly, d_{x2-y2} and d_{3z2-r2} will have different energies. The situation described above is shown schematically in Fig1.4.
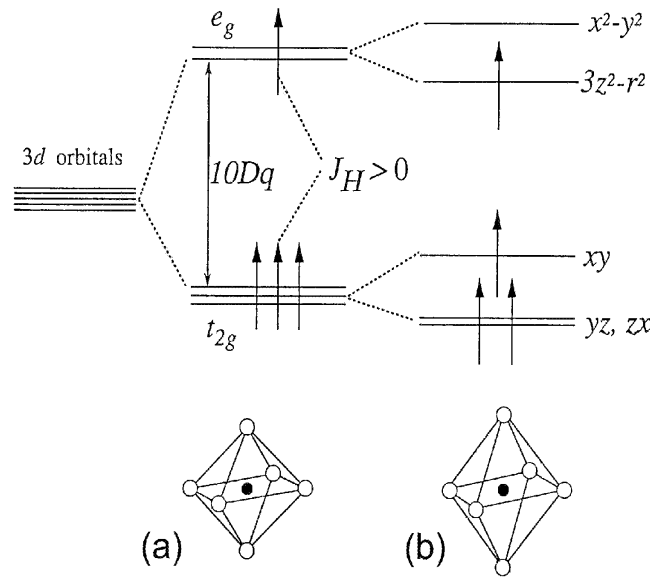
Fig.1.4. Schematic representation of the crystal field splitting of the d – levels of Mn ion. (a) corresponds to a cubic, while (b) corresponds to a tetragonal environment with lattice spacing c larger than a and b (reproduced from [19]).

The case of interest here (Mn^{3+}) has four electrons ($3d^4$). Due to strong intra – atomic Hund's coupling all electrons are aligned parallel in the ground state, leading to a total spin of S = 2. As seen in Fig1.4, only one orbital of the e_g doublet will not have an electron. For Mn^{4+} which has three electrons ($3d^3$), both e_g orbitals are empty, and S = 3/2. The t_{2g} orbitals overlap relatively less with the p – orbitals of the nearby oxygen atoms. Thus the t_{2g} electrons form a localized core spin. The e_g orbitals, on the other hand, have a greater overlap with the p – orbitals of the oxygen atoms. The e_g electron is more mobile. They can be either itinerant as in the metallic compositions of the manganites or localized as in $LaMnO_3$.

Thus, crystal field splitting removes the degeneracy of the 3d orbitals. The remaining degeneracy can be broken by lattice motion. The oxygen ions of the MnO_6 octahedra can slightly readjust their locations, creating an asymmetry between the different directions and thereby removing the degeneracy. This lifting of the degeneracy due to the orbital – lattice interaction is known as the Jahn – Teller cooperative effect. This lattice distortion is energetically favorable and tends to occur spontaneously. The Jahn – Teller lattice distortion can be "static", or "dynamic" (i.e. a given ion is not frozen in one distorted configuration but evolves among several configurations as a function of time).

A classic example of the Jahn – Teller effect is seen in undoped $LaMnO_3$ which shows a temperature dependent structure[20]. The magnetic order also follows the changes in the structure. At room temperature, $LaMnO_3$ is an A – type antiferromagnetic insulator (details of the A – type as well as other magnetic structures are given in the next section) in which a cooperative Jahn – Teller (JT) effect in the MnO_6 octahedra induces an orbital ordering. The cooperative JT distortion of MnO_6 octahedra is characterized by the parameter (δ_{JT}), where,

$\delta_{JT} = \sqrt{\frac{1}{3}\sum_i \left[(d_{Mn-O})_i - \langle d_{Mn-O}\rangle\right]^2}$. The summation is over i = 1,2,3 corresponding to the three

nonequivalent pairs of Mn-O bonds. In $LaMnO_3$, the structure becomes quasi-cubic in which the MnO_6 octahedra become quasi-regular above $T_{JT} \approx 750$ K[20]. Chatterji et.al.[21] have systematically investigated the doping dependence of the JT transition in $La_{1-x}Sr_xMnO_3$ (0 < x ≤0.1). They found that the JT transition temperature is drastically reduced on doping with Sr. Thus, doping with divalent cation "dilutes" the cooperative JT, and eventually for x = 0.33, we get only local distortions and no cooperative JT ordering.

1.4 Exchange interactions and Magnetic structures

Knowing the electronic and spin states of the Mn ion, the next natural question to address is how the spins order so as to achieve the lowest energy state. This leads us to the age – old problem of exchange interaction. In the simplest situation of two identical spins $\mathbf{S_m}$ and $\mathbf{S_{m+n}}$ ($\mathbf{m}$ and $\mathbf{m+n}$ are nearest – neighbor sites), the Hamiltonian has the Heisenberg form:

$H_{ex} = \frac{1}{2}\sum_{m,n}J_{m,m+n}S_m \bullet S_{m+n}$. Here, $J_{m,m+n}$ is the exchange constant which is determined by the

superexchange interaction via the p_σ and p_Π states of the O^{2-} ion and has an antiferromagnetic character. Superexchange is the coupling between two next – to – nearest neighbor cations (in this case Mn) through a non – magnetic anion (in this case O). Thus, the spins of the Mn ions are able to couple even though they are too far apart to have a direct exchange interaction. Superexchange usually produces antiferromagnetic interactions between nearest – neighbor sites (in this case Mn – O). This is clear from Fig.1.5.
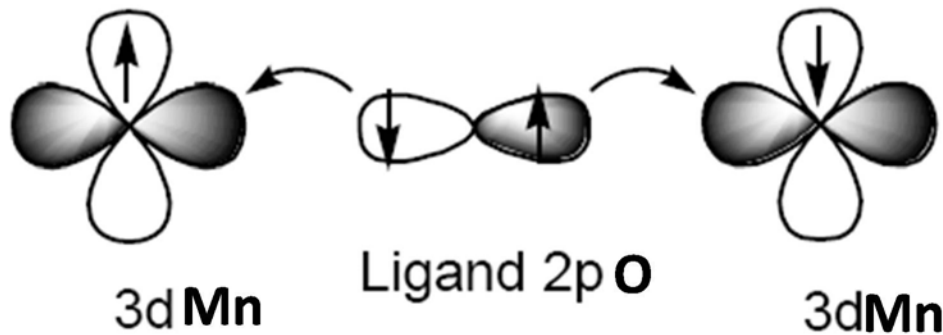
Fig.1.5. Schematic diagram showing superexchange interaction resulting in antiferromagnetic coupling between Mn spins.

However, the deformation and rotation of the octahedral in the lattice can lead to an appreciable change in the interatomic distances, which in turn can affect the superexchange interaction between the Mn – Mn pairs. This can destroy the simple formation of exchange interactions of the antiferromagnetic type between the Mn ions. As a result, the corresponding exchange constant for certain neighbours can acquire a ferromagnetic character while still being of a superexchange origin i.e. occurring via the ligand (O^{2-}) states. These are elaborated in the famous Anderson – Goodenough – Kanamori rules for superexchange interactions [22-24], which state that certain cooperative arrangements of the Jahn – Teller distortions will lead to ferromagnetism, while other arrangements may result in antiferromagnetism. Thus, following Goodenough, $J_{m,m+n}^{22}$ and $J_{m,m+n}^{3/2\,3/2}$ have antiferromagnetic signs, while $J_{m,m+n}^{2\,3/2}$ has a ferromagnetic sign (the superscripts indicate the spins S = 2 and 3/2 of the Mn^{3+} and Mn^{4+} ions respectively). Lattice distortions can further modify these rules.

In Fig1.6, we show schematic representations of the different possible magnetic structures. The circles are the Mn ions and the signs represent the orientation of the z – axis spin projection. Thus, A – type has planes which are ferromagnetic with antiferromagnetic coupling between them. The B – type structure is the standard ferromagnetic arrangement, while G – type corresponds to an antiferromagnet in all three directions. The C – type has antiferromagnetism in two directions and ferromagnetism along the third. The antiferromagnetic and ferromagnetic directions are marked in Fig.1.6 by the two blue and one red lines respectively.
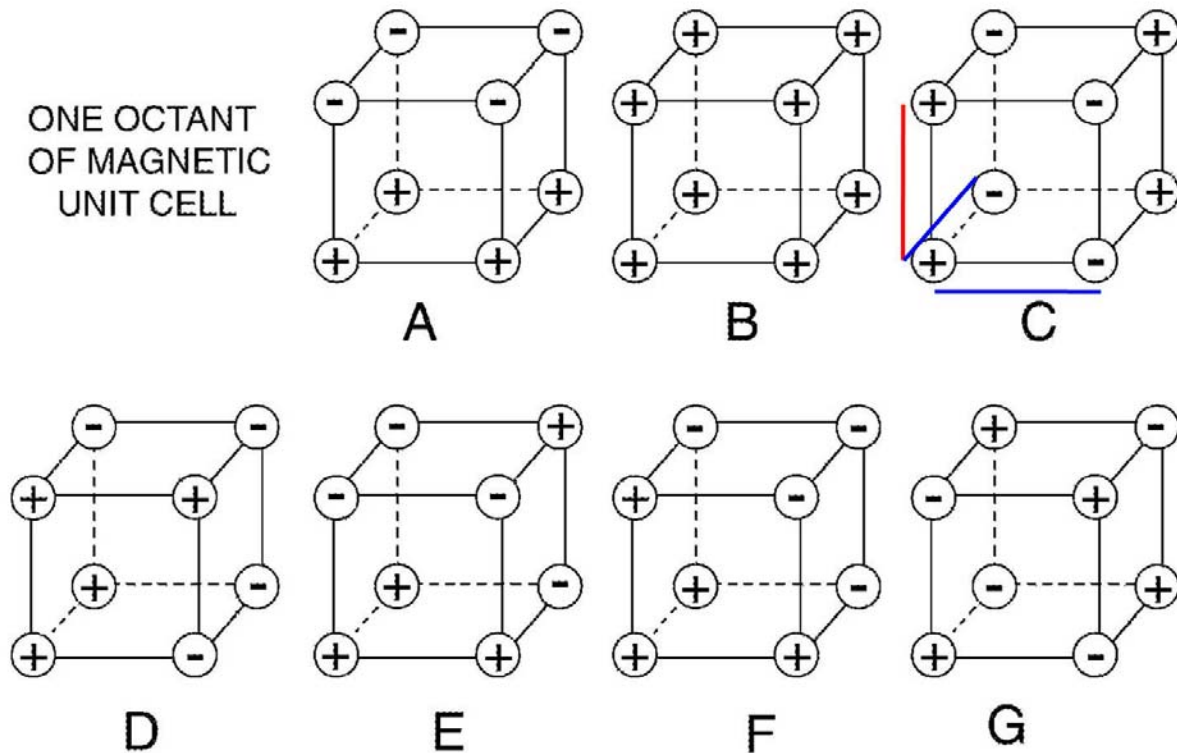
Fig.1.6. Schematic diagram showing the different possible magnetic structures and their labels (reproduced from [25]).

As stated earlier, the undoped LaMnO$_3$ exists in the A – type antiferromagnetic structure. We show this in Fig.1.7(a). Here, all the manganese ions are Mn^{3+}. The other end member of the La$_{1-x}$Ca$_x$MnO$_3$ series (CaMnO$_3$ with x = 1) exists in the G – type antiferromagnetic structure (Fig.1.7(b)). Here, all the manganese ions are Mn^{4+} and each Mn^{4+} ion is antiferromagnetically coupled to its six nearest neighbor Mn^{4+} ions. In the lower panel (Fig.1.7(c) and (d)), we show the schematic electron spin configurations that have been used to depict the ferromagnetic and antiferromagnetic directions in the A – type and G – type structures in Fig.1.7(a) and (b).
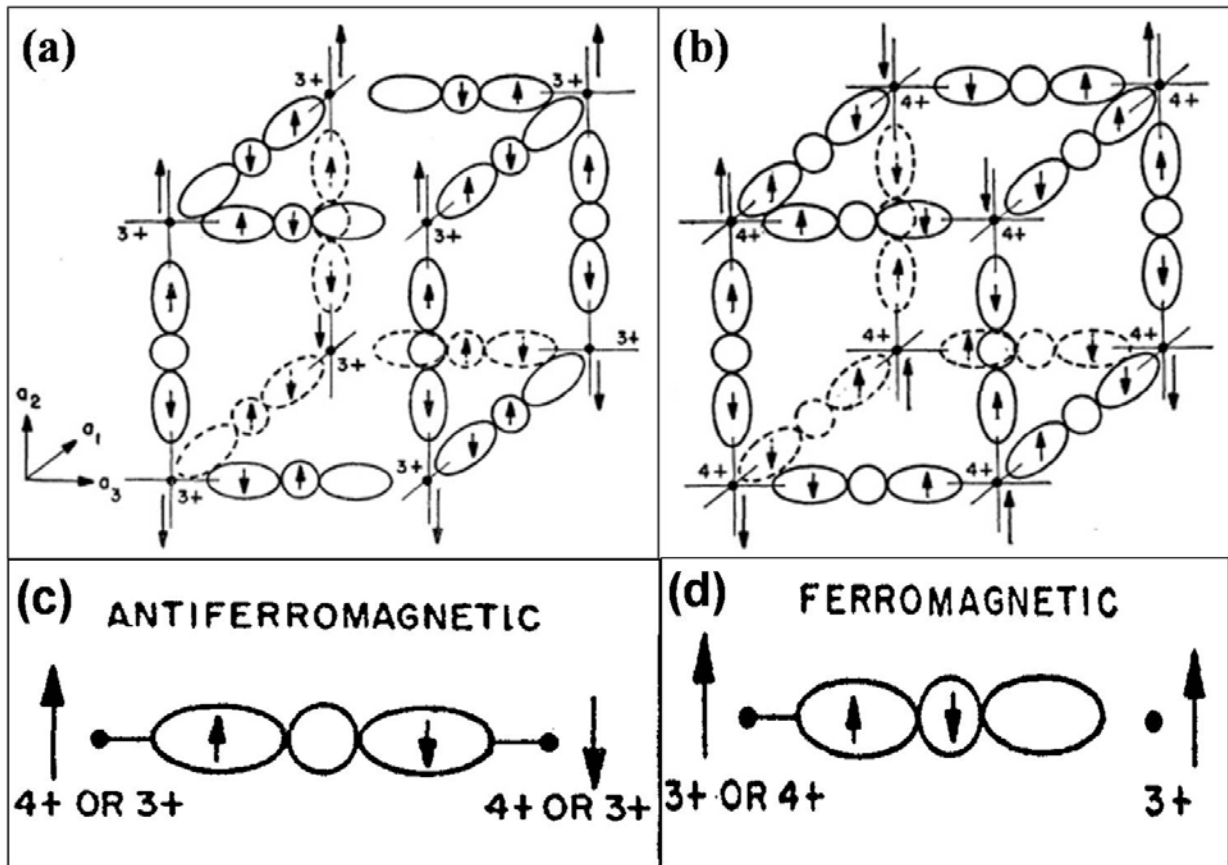
Fig.1.7. Magnetic lattice for (a) LaMnO$_3$ (Type – A) and (b) CaMnO$_3$ (Type – G), Schematic electron spin configurations for (c) antiferromagnetic and (d) ferromagnetic configurations (reproduced from [23]).

1.5 Ferromagnetism in manganites: Zener's Double Exchange mechanism?

Up till now we were working on the tacit assumption that the electrons (or holes created) at one of the sites (of the *3d* ions) remains in place. This is not always true. Owing to strong overlap of the *3d* functions with the *p* orbitals of the oxygen ion, the electron at one Mn site can pass to one of the oxygen sites of the surrounding octahedron, from which it can move to another Mn site. This is the basic idea behind the Double Exchange mechanism which we elaborate in this section. In fact, this also constitutes the main difference between the superexchange and double exchange mechanisms. While the double exchange mechanism involves an actual transfer

9

of electrons from one Mn site to the next, the superexchange interaction is only mediated through the oxygen ion, but does not involve an actual charge transfer.

The Double Exchange (DE) mechanism was first proposed by Zener in 1951[26 – 28], and is widely regarded as providing an explanation of manganite ferromagnetism. The DE mechanism tries to interpret the ferromagnetism as arising from an indirect coupling between incomplete d – shells (of the Mn ions) via conducting electrons. In the context of manganites, the incomplete d – shells are the t_{2g} localized spins and the conduction electrons are the e_g electrons. The mechanism is shown schematically in Fig1.8. It simply amounts to the simultaneous transfer of an electron from the O ion to the right Mn ion and from the left Mn ion to the O ion, so that the net transfer is of an electron from the left Mn ion to the right Mn ion. Thus, the process is a real charge transfer process. Because of strong Hund's rule coupling, the effective nearest – neighbor hopping amplitude for e_g electrons depends on the angle between the corresponding t_{2g} spins since the e_g spin direction is enslaved to the t_{2g} spin on the same site and the e_g electron conserves its spin direction on intersite hopping. The hopping amplitude and therefore, the kinetic energy gain due to e_g electron motion is maximum when the t_{2g} spins point parallel to each other i.e. are ferromagnetically aligned. Thus, this mechanism leads to a simultaneous occurrence of metallic conductivity and ferromagnetism. As the temperature increases and t_{2g} spins disorder thermally, the average kinetic energy of the e_g electrons decrease and their incoherence increases. One thus explains strong correlation between metallicity and the ferromagnetic to paramagnetic transition, which is observed. However, DE mechanism fails to explain the ferromagnetic insulating states. Thus, although this mechanism captures the essence of the tendency to ferromagnetism, it can, at best, be considered to provide only the zeroth – order explanation of manganite ferromagnetism.
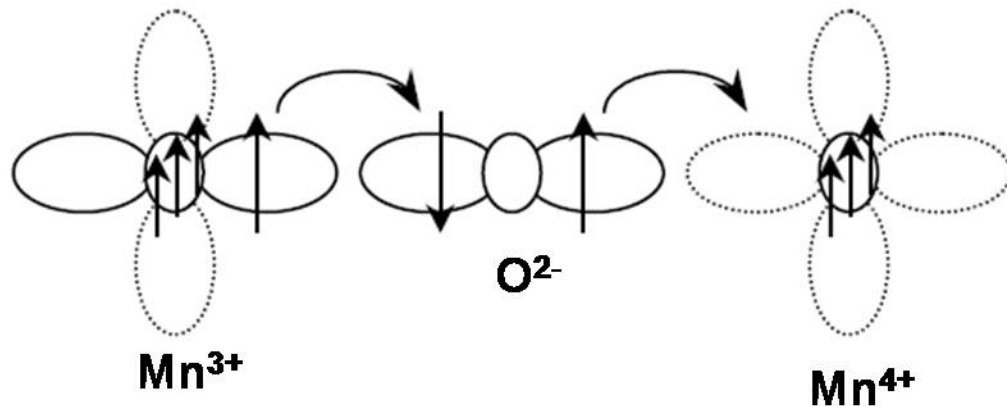
Fig.1.8. Schematic representation of the DE process. The Mn ions are represented by a small circle for the t_{2g} orbitals and lobes for the e_g orbitals. The 3d electrons are represented by their spins. Empty e_g orbitals are indicated by dotted lines.

The theory of the DE mechanism was further enriched by Anderson and Hasegawa[29]. They proposed that a better way to move electrons from one Mn site to the next was by transferring them one by one, still using the oxygen ions as a bridge between the Mn ions, rather than simultaneously, as believed by Zener. They also showed that the effective hopping (t_{eff}) of an electron jumping between two nearest – neighbor Mn sites is directly proportional to $cos(\theta/2)$,

where, θ is the angle between t_{2g} spins located at the two sites (Mn^{3+} and Mn^{4+}) involved in the electron transfer.

More recently, T.V.Ramakrishnan and co-workers have modeled the behaviour of CMR manganites by a new microscopic two – fluid model of nearly localized (l) polarons and band (b) electrons (lb model)[16]. This model includes the effect of the strong coupling of the two – fold degenerate e_g orbitals to the octahedral symmetry – breaking Jahn – Teller lattice modes. This electron lattice coupling was absent in the DE formalism. In the lb model, the large electron – lattice coupling leads to two distinct effective fermionic species or fluids, l and b. The former is a Jahn – Teller polaron, essentially site – localized, and the latter is a band electron, hopping from site to site in a random medium which has zero site energy on hole sites and large repulsive energy on l polaron sites. Thus metallic conduction can coexist with the presence of polarons and will occur when there is a sizeable density of b electrons in the system. In the insulating phase (at high temperatures, for instance) when the density of b electrons is low, diffusion (or variable range hopping) of l polarons can contribute significantly to electrical transport. The density and nature of the l polaron is expected to change with temperature, doping and chemical composition of the manganite. In this model, nanoscopic inhomogeneities (of the l and b regions) are also inevitable.

In Fig.1.9, we show the calculated density of states of the b band and l polaron level for various doping concentration x and temperature T. The effective b bandwidth goes as $\sim \sqrt{x}$ for small x so that the b band is relatively narrow for small x. The band bottom for small x can therefore lie above $-E_{JT}$ so there are no occupied or low energy b (extended) states, only localized or easily localized polaronic states are occupied and the ground state is a ferromagnetic insulating dense polaron liquid in this picture. In reality, the system is most likely a ferromagnetic polaron glass because of the pinning of l polarons by even weak random potentials (e.g. Coulomb interactions). This situation is shown in Fig.1.9(a). The insulating ferromagnetic ground state (which cannot be explained using the DE mechanism) is quite easily explained in the two-fluid model.

As doping increases, the effective bandwidth of the b electrons increases and there is b density of states below $-E_{JT}$ so extended states are occupied and the system is a ferromagnetic metal. This situation is shown in Fig.1.9(b). In the metallic state, electron transport is by the mobile b electrons which we find to be small in density ($<< x$). As the temperature increases at a given doping, the effective mobile electron b bandwidth decreases because of the t_{2g} spin disorder. Consequently, the number of occupied b states decreases dramatically, and one can have an insulator. This situation is shown in Fig.1.9(c).
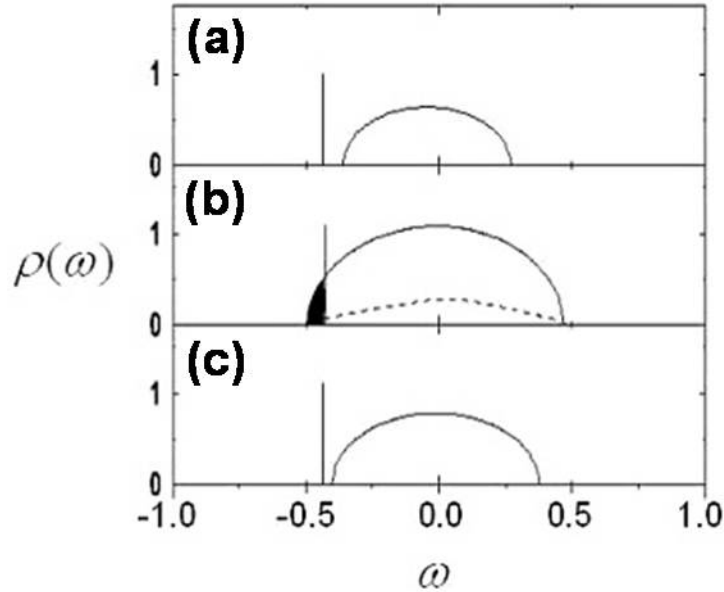
Fig.1.9. Density of states of the *b* band for various doping x and temperature T. The effective *l* polaron level is marked as a vertical line (reproduced from [16]).

1.6 Charge and Orbital Ordering

Charge ordered phases of manganites are novel manifestations arising from interactions between the charge carriers and phonons, giving rise to the localization of carriers at specific sites in the lattice below a certain temperature. This renders the material insulating. Accompanying this phenomenon, the e_g orbitals of the Mn^{3+} ions and the associated lattice distortions also exhibit long range ordering which is known as orbital ordering. When the Mn^{3+} and Mn^{4+} ions are randomly distributed in the lattice the material is considered to be in the charge disordered phase. Although charge ordering is expected to be favoured when x = 0.5 (due to the presence of equal proportions of Mn^{3+} and Mn^{4+} states), it is also found in various compositions in the range 0.3 < x < 0.75 depending on the A and B site ions. This kind of real space ordering of the charge carriers occurs when the Coulomb repulsion is predominant over the kinetic energy of the electrons. Due to the associated orbital ordering, the magnetic exchange interactions between the Mn ions become anisotropic giving rise to complex magnetic ordering in these structures. Thus, at low temperatures, the rare earth manganites are antiferromagnetically ordered with CE or A – type ordering. The CE – type spin ordering is characterized by the ordering of Mn^{3+} and Mn^{4+} ions alternately. The spin ordering in the *ab* plane is somewhat complex and it stacks antiferromagnetically along the *c* axis. In the A – type spin ordering, the spins order ferromagnetically in the *ab* plane and these planes stack antiferromagnetically along the *c* axis. The features of the CE and A – type antiferromagnetic ordering are shown in Fig1.10. Charge ordering is observed only in CE – type spin ordering.
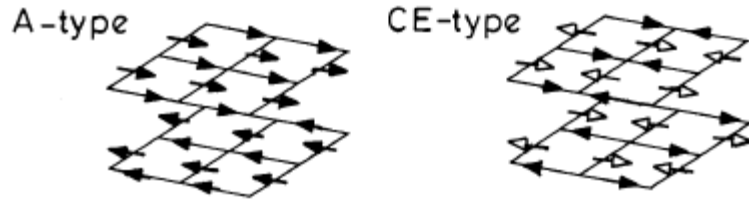
Fig1.10. A – type and CE – type antiferromagnetic ordering in charge – ordered rare earth manganites.

One of the charge – ordered manganites which we study extensively in this thesis is $La_{0.5}Ca_{0.5}MnO_3$. It shows ferromagnetic and antiferromagnetic (charge – ordering) transitions at 225 K and 170 K respectively[1]. Between T_C and T_N, Jahn – Teller distortions develop with the d_z^2 orbitals oriented perpendicular to the orthorhombic b – axis. Magnetic domain boundaries break the coherence of spin ordering of the Mn^{3+} sites while preserving the coherence of spin ordering on the Mn^{4+} sublattice. Static charge stripes are thus seen in the antiferromagnetic insulating ground state of $La_{0.5}Ca_{0.5}MnO_3$, somewhat similar to the stripe phases found in high T_C cuprates [30]. For the x = 2/3 composition ($La_{0.33}Ca_{0.67}MnO_3$), extremely stable pairs of $Mn^{3+}O_6$ stripes associated with large lattice contractions (due to the Jahn – Teller effect) separated by undistorted $Mn^{4+}O_6$ octahedra are found [31]. These Jahn- Teller stripes seem to be building blocks of the charge – ordered state in these manganese oxides.

An important question which we probe in this thesis is the stability of the charge ordered phase. Experimental investigations in the past have revealed that the charge ordered phase is extremely sensitive to the average size of the A – site cations. The charge ordered phase is stable over a wider range of x for low bandwidth perovskites like $Pr_{1-x}Ca_xMnO_3$. This is because low bandwidth (which occurs when the A – site cation has a small ionic radius) implies weaker ferromagnetic interaction. Any distortion that weakens the ferromagnetic interaction would stabilize the competing interaction i.e. charge ordering. The magnitude of the charge ordering gap Δ_{CO} (a gap in the density of states at the Fermi level) is higher for low bandwidth manganites making the charge ordering more robust.

The small radius of the A – site cation is thus an internal factor which stabilizes the charge ordered state. But there are a number of external perturbations like pressure[5,32], magnetic[4] and electric fields[33,34], biaxial strains, irradiation of x-ray[35], electron irradiation[36], and infrared – visible – ultraviolet light irradiation[37,38], high voltage[33], as well as isotopic and chemical substitutions which can destabilize it. This sensitivity to external perturbations arises from the fact that the charge – ordered insulating state and the ferromagnetic metallic state are energetically almost degenerate.

In this thesis we show that keeping all other factors (internal as well as external) constant, the charge – ordered phase in half – doped manganites can be destabilized only by reducing the particle size to the nanometer regime. The investigation has been done using two compounds, $La_{0.5}Ca_{0.5}MnO_3$ (LCMO) and $Pr_{0.5}Ca_{0.5}MnO_3$ (PCMO), one of which (LCMO) is an intermediate bandwidth manganite and the other (PCMO) is a low bandwidth manganite. Details regarding the charge ordered phase in these two compounds, and how they respond to size reduction will be discussed in Chapter 4.

13

1.7 Ferromagnetic insulating phase at low doping

For most manganites there exists a ferromagnetic insulating region at low doping (for the LCMO system this region lies between x = 0.17 to x = 0.22). As already mentioned earlier, this ferromagnetic insulating region cannot be explained by the DE mechanism. Rather its presence points towards some kind of orbital ordering. For example, Mizokawa et.al.[39] have argued that in lightly hole – doped perovskite – type manganites, the holes (Mn^{4+} sites) are surrounded by nearest neighbours Mn^{3+} sites in which the occupied 3d orbitals have their lobes directed towards the central hole (Mn^{4+}) with spins coupled ferromagnetically to the central spin. Such a situation (referred to as an orbital polaron) is shown schematically in Fig1.11. Such an orbital orientation can occur for two reasons. One is simply steric: Oxygen ions sitting in between the Mn ions move towards the Mn^{4+} site and consequently, the MnO_6 octahedra of the neighbouring Mn^{3+} sites are elongated along the axis pointing to the Mn^{4+} site. Another factor is that the e_g electrons directed towards the Mn^{4+} site allow for maximal Mn – O – Mn hopping. An important consequence of such an orbital ordering is that the exchange interaction between the Mn^{3+} and Mn^{4+} in this cluster is ferromagnetic. Theoretical calculations have shown that for certain doping levels these orbital polarons may crystallize into a charge and orbitally ordered ferromagnetic insulating state. The ferromagnetic insulating phase is also explained by the two-fluid model as described earlier. Certain other explanations like phase separation (relative volume fraction of ferromagnetic metallic and ferromagnetic insulating clusters) have also been put forward by some authors for the existence of the ferromagnetic insulating state in manganites. More details regarding phase separation in manganites have been given in the next section.
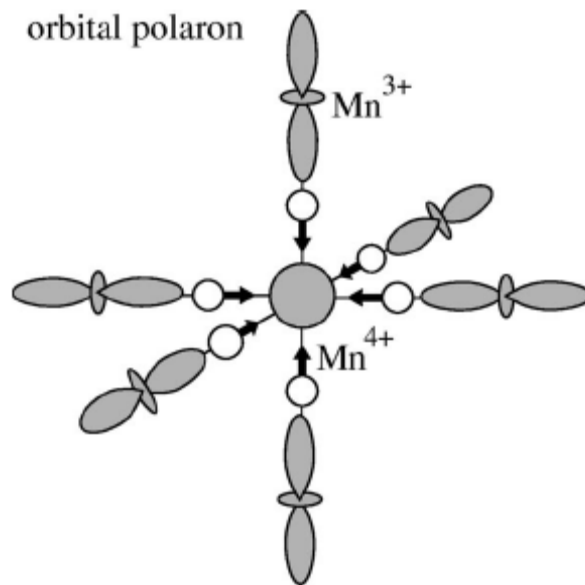
Fig.1.11. Schematic representation of an orbital polaron around Mn^{4+} ion. The shaded orbitals and circles represent Mn^{3+} and Mn^{4+} ions respectively. The open circles represent the O ions. The arrows indicate the shift of the O ions.

1.8 Phase separation in manganites

The phase diagrams of manganites as discussed in Section 1.2 and the different phases described in the subsequent sections should not lead one into the misconception that by varying the doping concentration we can prepare samples which are homogeneously ferromagnetic (or antiferromagnetic) even at the microscopic level. In fact, the ground situation is that whatever be the macroscopic physical properties of a sample, at the microscopic level manganites are almost invariably phase separated into hole – rich ferromagnetic and hole – poor antiferromagnetic regions. This inhomogeneity is intrinsic and arises from phase competition between ferromagnetic metallic and charge – ordered insulating phases. Direct evidence of phase separation has been obtained using scanning tunneling spectroscopy techniques[40]. The fact that metallic and insulating regions coexist as interpenetrating clusters give rise to novel electronic and magnetic properties with colossal magnetoresistance in doped perovskite manganites.

Phase separation in manganites can have two different origins: (i) Electronic phase separation, where competing states have different hole densities and $1/r$ Coulomb effects lead to nanocluster coexistence, (ii) Disorder – driven phase separation near first order transitions[41] leading to large coexisting clusters. Fig1.12 shows a generic phase diagram of two competing phases in (a) the absence of quenched disorder (or when this disorder is very weak). Thick (thin) lines denote first (second) – order transitions. g is some parameter needed to change from one phase to the other, (b) With increase in disorder, the temperature range of first – order transitions separating the ordered state is decreased, (c) With further increase in disorder, a window opens between the ordered phases. The state in between is composed of coexisting clusters of both phases. The size of the coexisting islands can be regulated by the disorder. One instance when disorder is unavoidable is during chemical doping because the doped ions have different charge and hence can produce trapping centres for the e_g electrons moving in this environment or due to size mismatch of the A – site cations (in case the doped ion has the same charge but a different ionic radius).
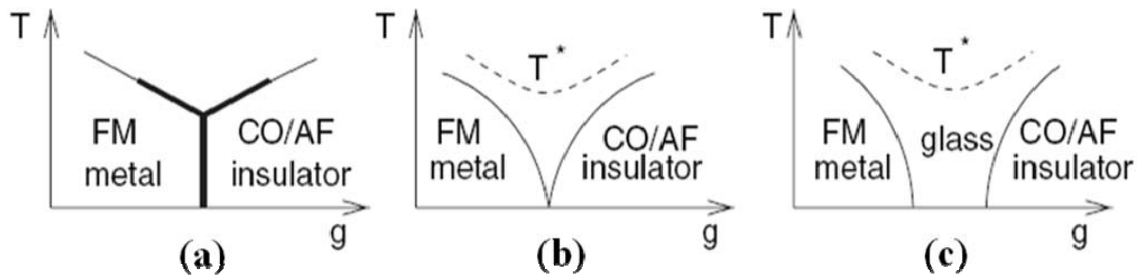
Fig.1.12. Generic phase diagram of two competing phases.

Experimentally such phase separation in manganites in the submicron level can be probed using various microscopic tools. For example, in Fig.1.13(a) we show the submicron domain structure of $La_{1-x-y}Pr_yCa_xMnO_3$ (x = 3/8)[42]. The dark regions correspond to antiferromagnetic insulating domains while the light regions correspond to ferromagnetic metallic domains. The arrows indicate the directions of magnetization in the ferromagnetic domains. Such measurements yield electronic phase diagrams like those shown in Fig. 1.13(b) and (c). These

phase diagrams clearly show a phase separated (PS) regime appearing between the ferromagnetic (FM) and charge ordered (CO) phases.
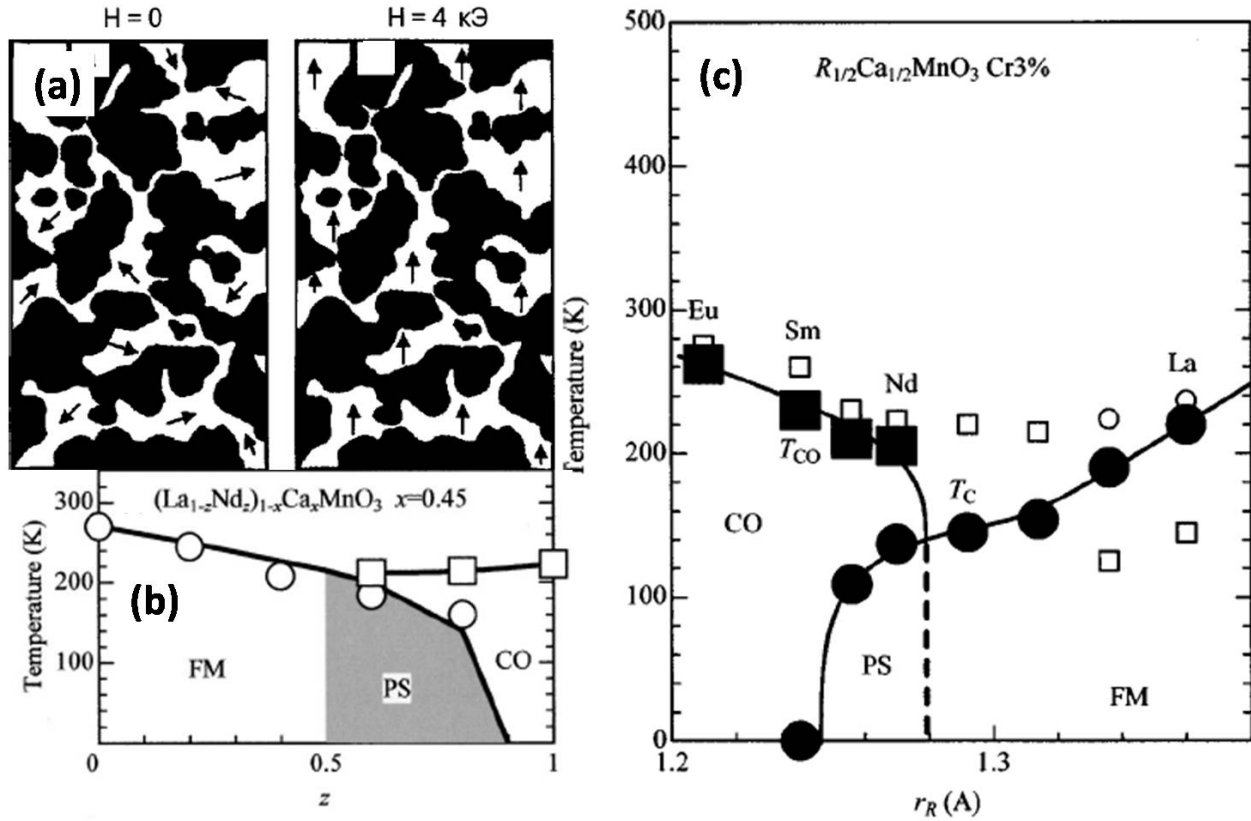
Fig.1.13.(a) submicron domain structure of $La_{1-x-y}Pr_yCa_xMnO_3$ (x = 3/8)[reproduced from 42], (b) Phase diagram of $(La_{1-z}Nd_z)_{1-x}Ca_xMnO_3$, x = 0.45 (reproduced from [43]), (c) Phase diagram of $R_{1/2}Ca_{1/2}(Mn_{0.97}Cr_{0.03})O_3$ (reproduced from [44]).

Nanoscale phase separation is, thus, at the heart of various magnetotransport phenomena in manganites. Whether it still exists, and is of any consequence in nanomanganites is one of the questions that we will attempt to answer in this thesis.

1.9 Cobaltates

Jonker and Van Santen[45] first showed that the system $La_{1-x}Sr_xCoO_3$ becomes ferromagnetic for x > 0.15 and associated the ferromagnetism with the concentration of tetravalent cobalt which increases with Sr^{2+} concentration. Even though hole doping (by substitution of Sr^{2+} for La^{3+}) in antiferromagnetic insulating $LaMnO_3$ as well as in $LaCoO_3$ renders ferromagnetism and metallicity, there are certain differences in the spin structure of these two systems.

Sr (or Ca) substitution in $LaMnO_3$ leads to the conversion of Mn^{3+} ($t_{2g}^3 e_g^1$, S = 2) into Mn^{4+} (t_{2g}^3, S = 3/2). Magnetic studies have shown that there is a core spin arising from ½ - filled t_{2g}^3 levels. Since the exchange energy is larger than the crystal field energy, the high – spin state is stable in Mn – based systems. No thermal variation of the spin state of the Mn ion is known. A

strong Hund's rule coupling of the core spin with the more mobile carriers (hole or electron) in the e_g orbitals determines most of the observable behaviour of the Mn – based systems. However, in LaCoO$_3$, the Co ion is predominantly in low – spin – state Co^{III} (t_{2g}^6, S = 0) at low temperature. As the temperature is increased, a progressive conversion of low – spin Co^{III} into high – spin Co^{3+} ($t_{2g}^4 e_g^2$, S = 2) takes place[45 – 48]. This happens because at low temperatures a large crystal field stabilizes the low – spin state. However, the energy difference between the two spin states being low, thermal excitation can provide a transition to a high – spin configuration. This transition from low – spin to high – spin state occurs at ~ 200 K[49] and gets reflected in the transport properties (ρ vs T curve) (Fig.1.14).
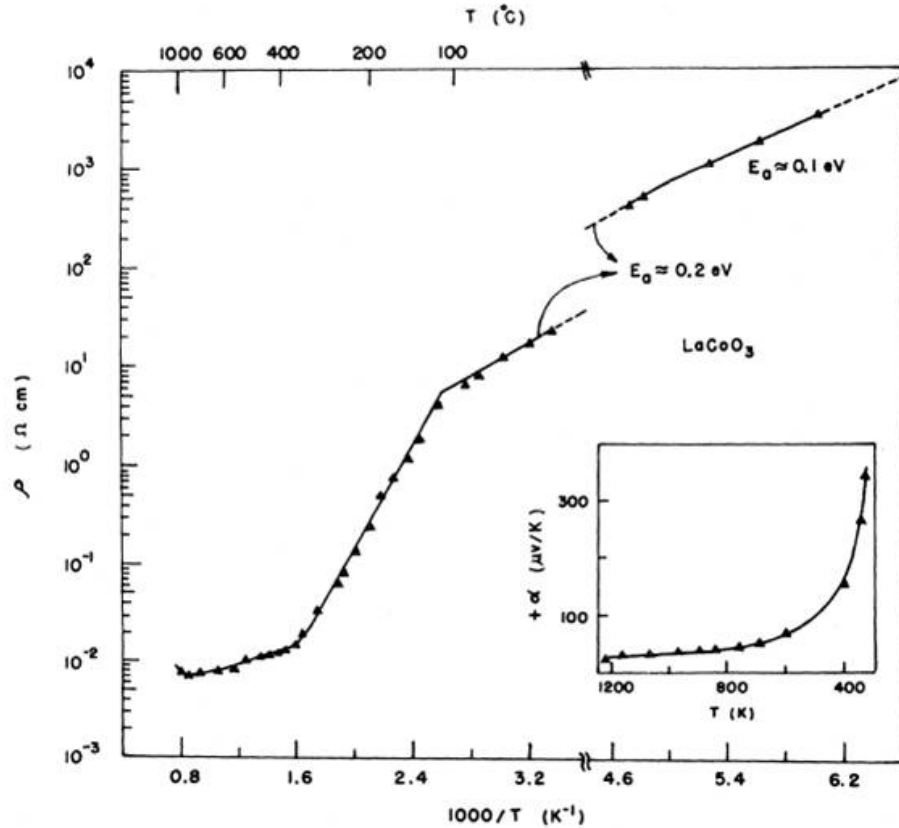
Fig.1.14. Electrical resistivity versus temperature curve for LaCoO$_3$ (reproduced from [49]).

On Sr substitution, tetravalent Co ions are created. They can be low – spin Co^{IV} (t_{2g}^5, S = ½) or high – spin Co^{4+} (t_{2g}^3, e_g^2, S = 5/2). La$_{1-x}$Sr$_x$CoO$_3$ thus contains a mixture of low – spin Co^{III}, low – spin Co^{IV}, and some high – spin Co^{3+} and high – spin Co^{4+} depending on the temperature as well as the value of x. With an increase in the doping concentration x, more and more Co^{3+} is converted to Co^{4+} (which is a high spin state). This is what makes the system metallic and gives it the magnetic moment, eventually making it ferromagnetic. These different spin structures of Mn and Co ions are shown schematically in Fig.1.15.

The absence of a half – filled t_{2g} orbital in the low – spin Co ion gives rise to less strong Hund's coupling of the carrier to the core spin. This creates a big difference between the Co – based oxides and the Mn – based oxides. The superexchange interaction Co^{IV} – O – Co^{3+} or Co^{4+}

$– O – Co^{3+}$ is known to be ferromagnetic and the exchange interactions between the ions with the same valency state are antiferromagnetic[45 – 48]. However, whether the ferromagnetism in cobaltates is mediated by a double – exchange mechanism or not is contentious. The absence of the half – filled t_{2g} level providing the core spin and a strong Hund's rule coupling makes this mechanism less likely.
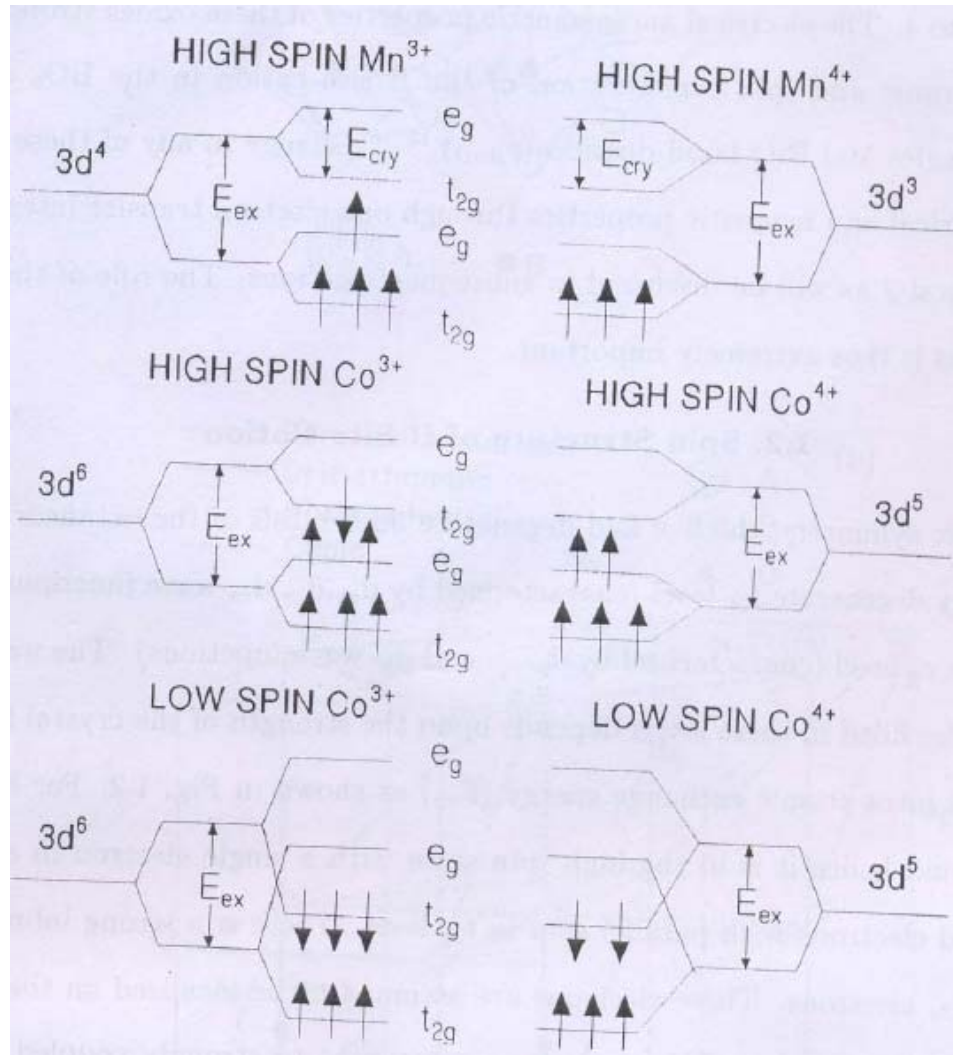
Fig.1.15. Spin structures of Mn and Co ions (reproduced from [50]).

In Fig.1.16 we show the magnetic phase diagram of $La_{1-x}Sr_xCoO_3$. There are two distinct regions in the phase diagram. For $x > 0.2 – 0.25$, there is an onset of a ferromagnetic transition (denoted by T_C), but the resulting ferromagnetic state does not have a long – range order. Rather it becomes like a cluster of ferromagnetic regions embedded in a nonferromagnetic matrix. For $x < 0.1$, there is a spin – glass – like state at lower temperature and there seems to exist a spin – state – transition temperature marked by T_S in this region. In the transition region $(0.2 > x > 0.1)$, the behaviour is more complicated.
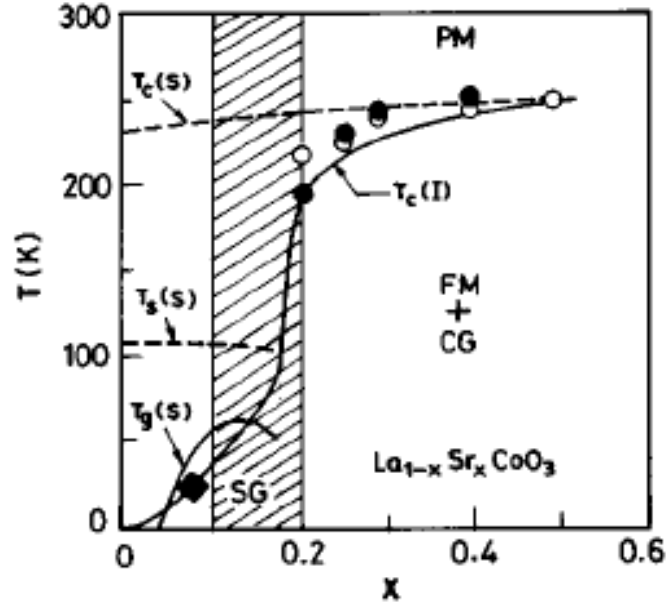
Fig.1.16. Schematic phase diagram of La$_{1-x}$Sr$_x$CoO$_3$ (reproduced from [51]).

1.10   Stability of the ground state of the complex oxides

The uniqueness of the oxides discussed so far lies in the fact that their ground state can be readily tuned between different electronic phases by small external perturbations, be it magnetic field, electric field, strain or pressure. The different interactions (which we have detailed above) prevalent in these oxides are often of comparable strength. As a result, the ground state of the oxides depends on which of the interactions win over. This sensitivity of the stability of their ground state makes these oxides both fascinating case studies as well as extremely tunable as per the "customer's" requirements. In the following sections, we briefly describe how pressure (both external as well as internal) has an effect on the ground state of these oxides. The reason for singling out pressure out of the many possible external perturbations will become clear in the later chapters. The pressure effect has a special significance in the study of nanoparticles and we will elaborate on this later in this chapter as well as in Chapters 3 and 4. For now we confine ourselves to a brief review of some representative studies of the pressure effect on manganites and cobaltates.

Bulk samples of manganese oxides (by "bulk" we mean samples having an average particle size greater than 1 μm) can be subjected to pressure in the following ways:

1.10.1 External hydrostatic pressure

External hydrostatic pressure increases the bandwidth (W) of manganites. This is because the bandwidth is inversely proportional to the Mn – O bond distance (d_{Mn-O}): $W \propto \dfrac{1}{d_{Mn-O}^{3.5}}$ [52]. As the pressure is increased, the ions come closer and the bandwidth and hopping amplitude increase. This decreases the resistivity (Fig.1.17). As the bandwidth increases, it favours the

double exchange mechanism, and ferromagnetism is expected to be strengthened. This is reflected as an increase in the ferromagnetic T_C (inset of Fig.1.17).
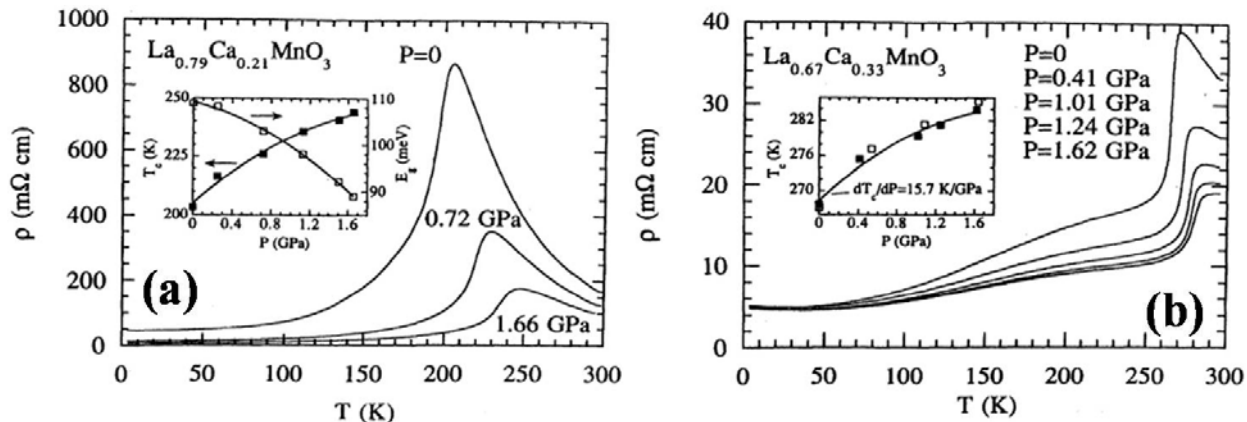
Fig1.17. Electrical resistivity versus temperature curves for (a) $La_{0.79}Ca_{0.21}MnO_3$ and (b) $La_{0.67}Ca_{0.33}MnO_3$ taken at different hydrostatic pressures (reproduced from [53]).

As a corollary of favouring the ferromagnetic state, external hydrostatic pressure destabilizes the charge ordered state. Thus, it melts the insulating state (which accompanies the charge – ordered state) and makes the samples metallic (Fig.1.18).
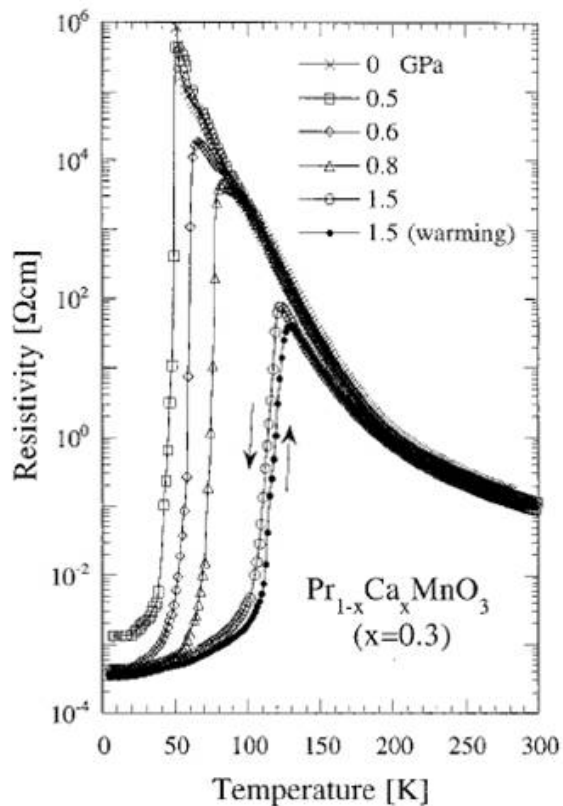
Fig1.18. Electrical resistivity versus temperature curves for $Pr_{0.7}Ca_{0.3}MnO_3$ taken at different hydrostatic pressures (reproduced from [54]).

The effect of hydrostatic pressure on the electrical and magnetic properties of a system can ultimately be traced to its effect on the structure of the system. Thus, external hydrostatic pressure not only changes the unit cell dimensions but application of a suitable high pressure can even change the symmetry of the system. For example, application of a pressure greater than 15 GPa changes the symmetry of $La_{0.5}Ca_{0.5}MnO_3$ from orthorhombic (*Pnma* symmetry) to monoclinic (*P2$_1$/m* symmetry) (Fig.1.19).
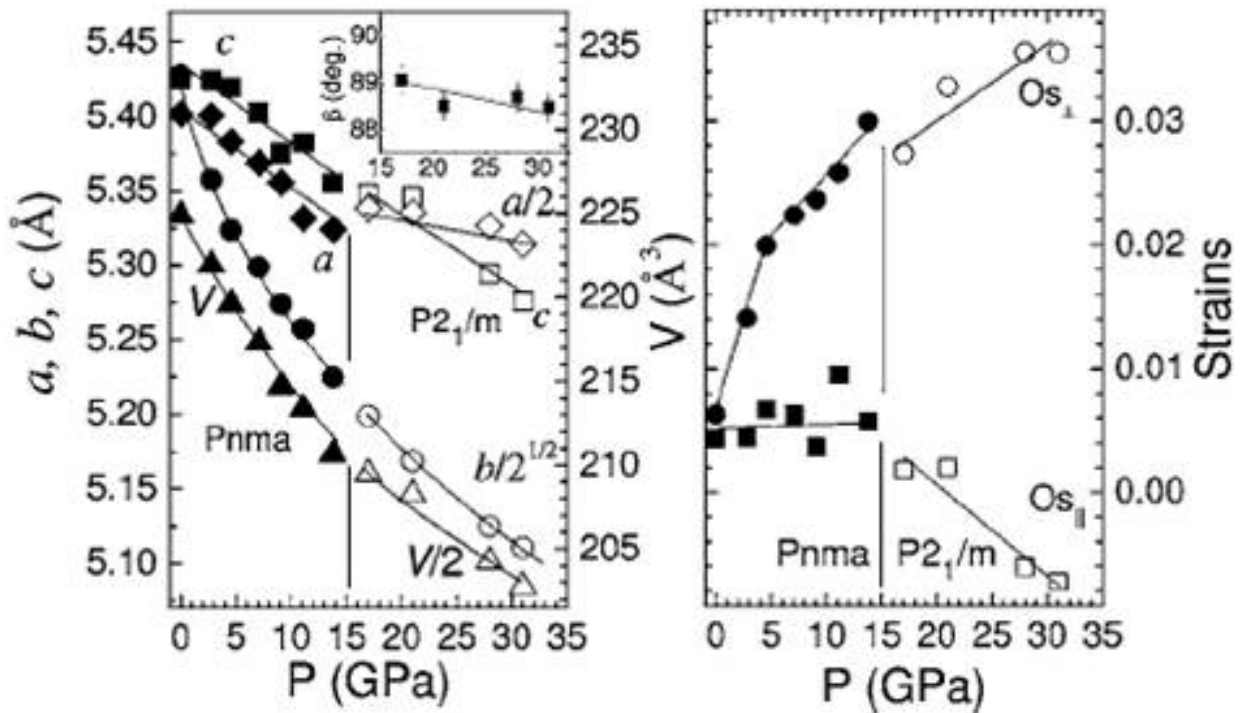
Fig.1.19. Lattice parameters, unit cell volume and orthorhombic strains in $La_{0.5}Ca_{0.5}MnO_3$ (reproduced from [55]).

1.10.2 Internal pressure

Internal pressure can be varied by varying the average size of the A cation $<r_A>$. Substitution with different cations alters the lattice constant, and hence, the bandwidth. In fact, varying $<r_A>$ directly changes the tolerance factor (which we have defined and discussed in details before). Hwang et.al.[56] have systematically studied the evolution of T_C in the compounds $A_{0.7}A'_{0.3}MnO_3$ and found that an increase in $<r_A>$ (i.e. an increase in the internal pressure) corresponds to an increase in T_C (Fig.1.20(a)). An increase in the internal pressure also leads to a decrease in the resistivity (Fig.1.20(b)).
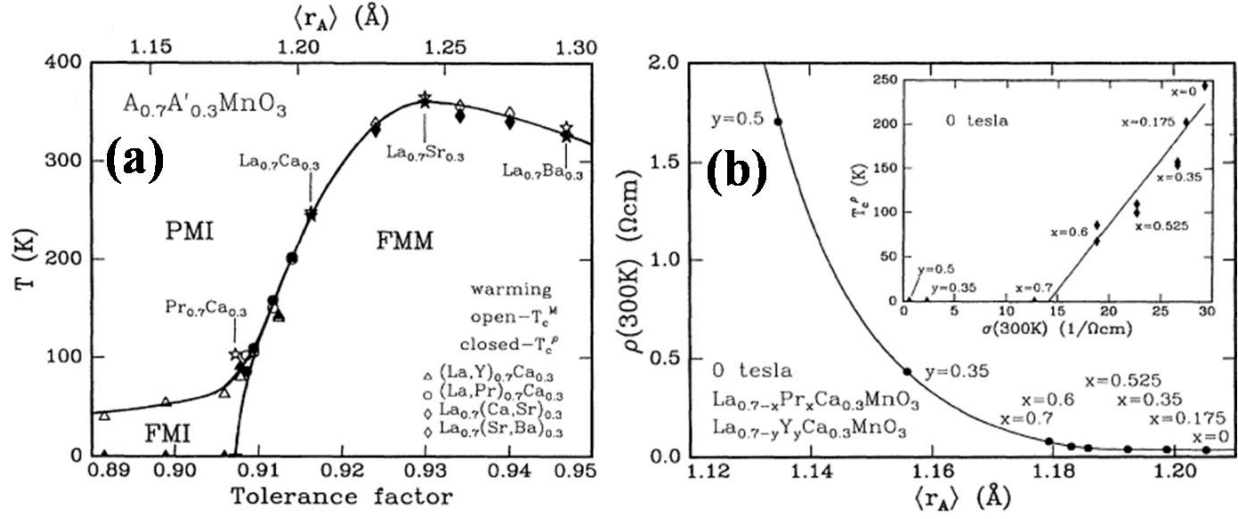
Fig1.20. (a) Phase diagram of temperature vs <r_A>, (b) Variation of room temperature resistivity with <r_A> for $A_{0.7}A'_{0.3}MnO_3$ (reproduced from [56]).

Smaller A – site cations tend to stabilize charge – ordered insulating states over ferromagnetic metallic states. It is also more difficult to destabilize the charge ordered phase for systems with smaller <r_A> values. In Table 1.1, we summarize the effect of <r_A> on the ground state of some half – doped manganites.

Table 1.1 Stable room temperature phases, <r_A> values and charge – ordering temperatures (T_{CO}) for $Ln_{0.5}A_{0.5}MnO_3$ (adapted from [57]).

Ln	A = Ca			A = Sr		
	<r_A> (Å)	Stable phase	T_{CO} (K)	<r_A> (Å)	Stable phase	T_{CO} (K)
Y	1.127	CO[a]	260			
Dy	1.132	CO[a]	260			
Gd	1.143	CO[a]	260	1.208	Spin glass	
Nd	1.172	CO[b]	240	1.236	FMM	150
Pr	1.179	CO[b]	240	1.244	FMM	140 (T_N; no T_{CO})
La	1.198	PMI	170	1.263	FMM	0

[a] = Magnetic field (6 T) has no effect; [b] = Magnetic field (6 T) melts the CO state to a FMM state.

The dependence of the ground state on the internal pressure can again be traced back to the latter's effect on the structure of the system. Thus, an increase in the internal pressure increases the Mn – O – Mn bond angle mking it closer to 180^0 (Fig.1.21(a)), thereby increasing the bandwidth (Fig.1.21(b)) and stabilizing the ferromagnetic metallic phase.
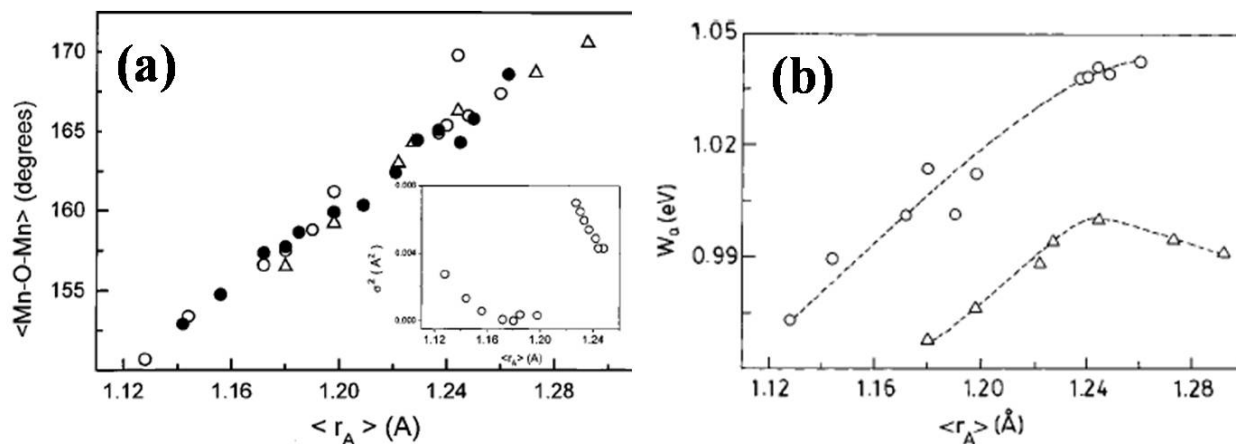
Fig.1.21. Variation of (a) Mn – O – Mn bond angle and (b) bandwidth with $<r_A>$ (reproduced from [57]).

Increasing the internal pressure by increasing $<r_A>$ works in a way which is equivalent to increasing the external hydrostatic pressure. As an example, in Fig.1.22, we show the phase diagram of $A_{0.7}A'_{0.3}MnO_3$ which has been varied by both the internal as well as the external pressure. Closed circles represent variations due to internal pressure (variations of the average A – site ionic radius $<r_A>$) and open circles indicate variations due to externally applied hydrostatic pressure. It can be seen that the top and bottom axes are closely related.
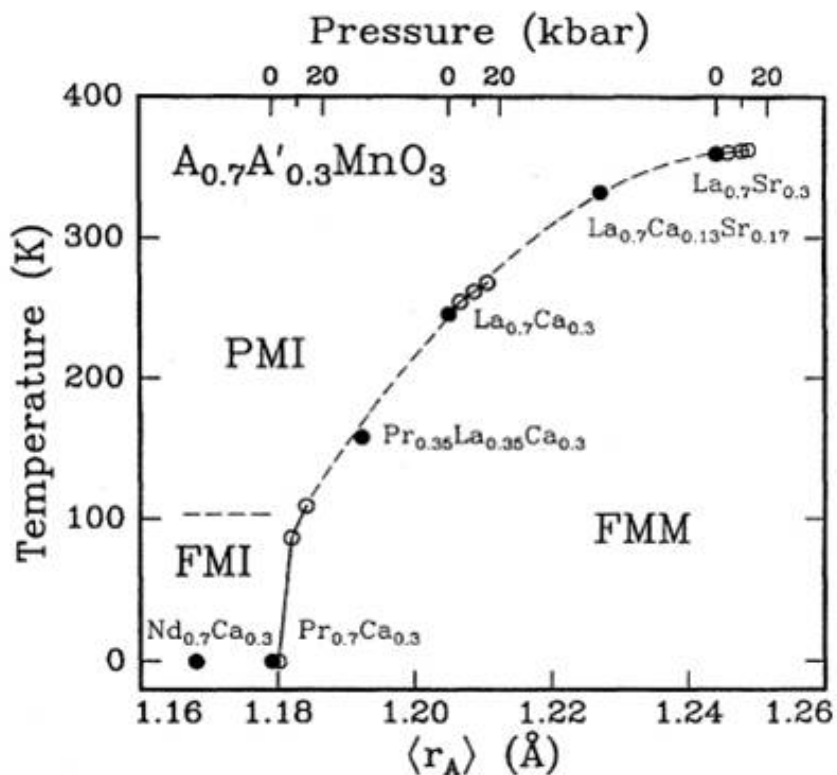
Fig.1.22. Phase diagram of $A_{0.7}A'_{0.3}MnO_3$ as a function of both internal as well as external pressure (reproduced from [58]).

Apart from the average size of the A-site cation ($<r_A>$) of these perovskite oxides (which determines the internal pressure in these systems), the size mismatch at the A-site also determines the ground state of these oxides. This size mismatch at the A-site is quantified by the variance σ^2 of the A-cation radius distribution which was first introduced by Rodriguez-Martinez and Attfield[59]. For two or more A-site species with fractional occupancies y_i ($\left(\sum y_i = 1\right)$), they defined the variance of the ionic radii r_i about the mean $<r_A>$ as $\sigma^2 = \sum y_i r_i^2 - \left\langle r_A \right\rangle^2$. As σ^2 increases, local distortions are induced that reduce T_C significantly even if $<r_A>$ remains constant[59,60,61] (Fig.1.23). The activation energy in the high temperature paramagnetic regime also depends on the extent of this disorder[62]. Size mismatch, since it introduces local distortion and consequently a great variation of the Mn-O-Mn angles favours the appearance of a spin glass insulating state[63] (Fig.1.24). Thus, spin glass insulating states are obtained for larger $<r_A>$ values even if they tend to favour the ferromagnetic metallic state, provided large σ^2 values are involved.
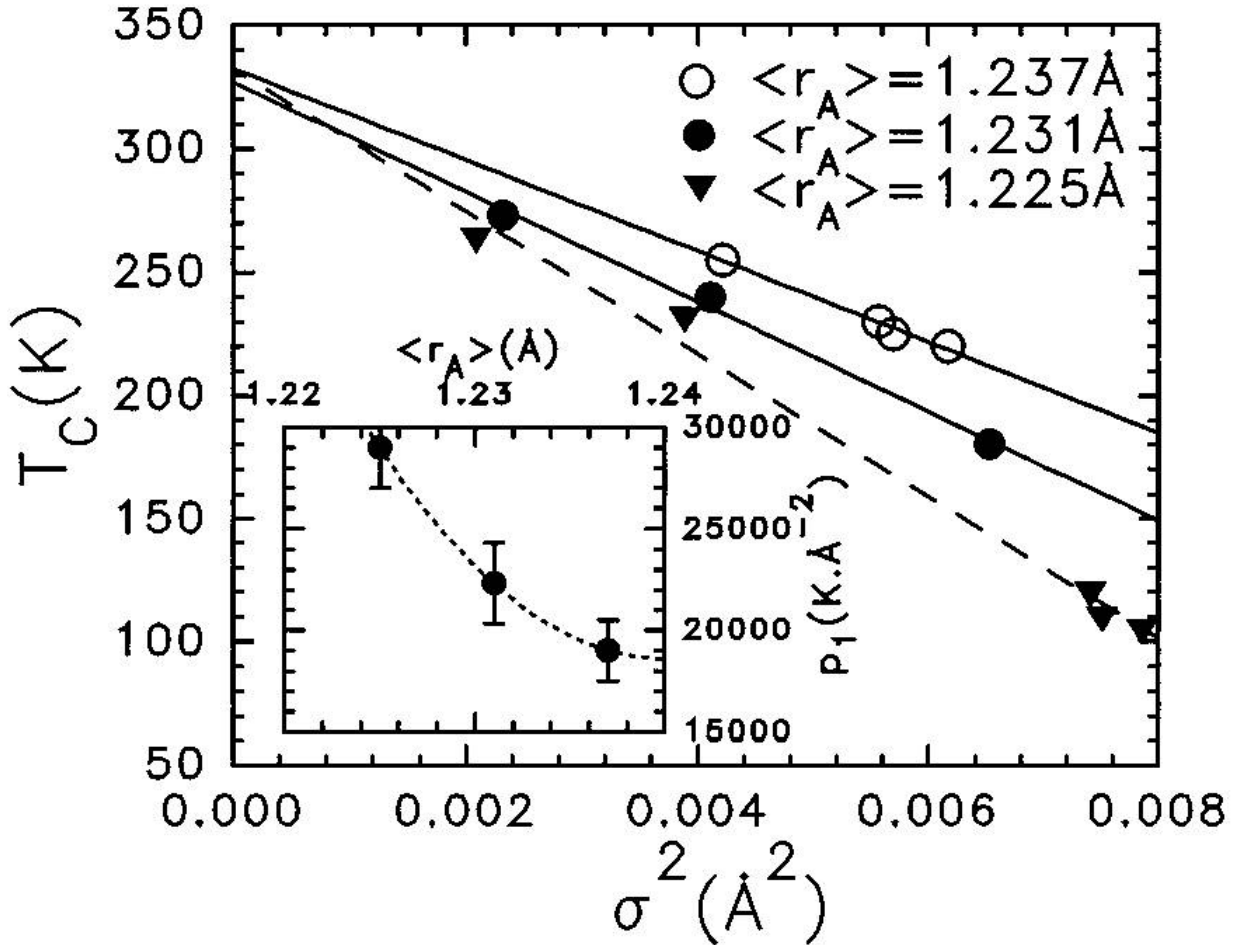
Fig.1.23. T_C vs σ^2 at constant $<r_A>$ for three series of compounds (reproduced from [60]).
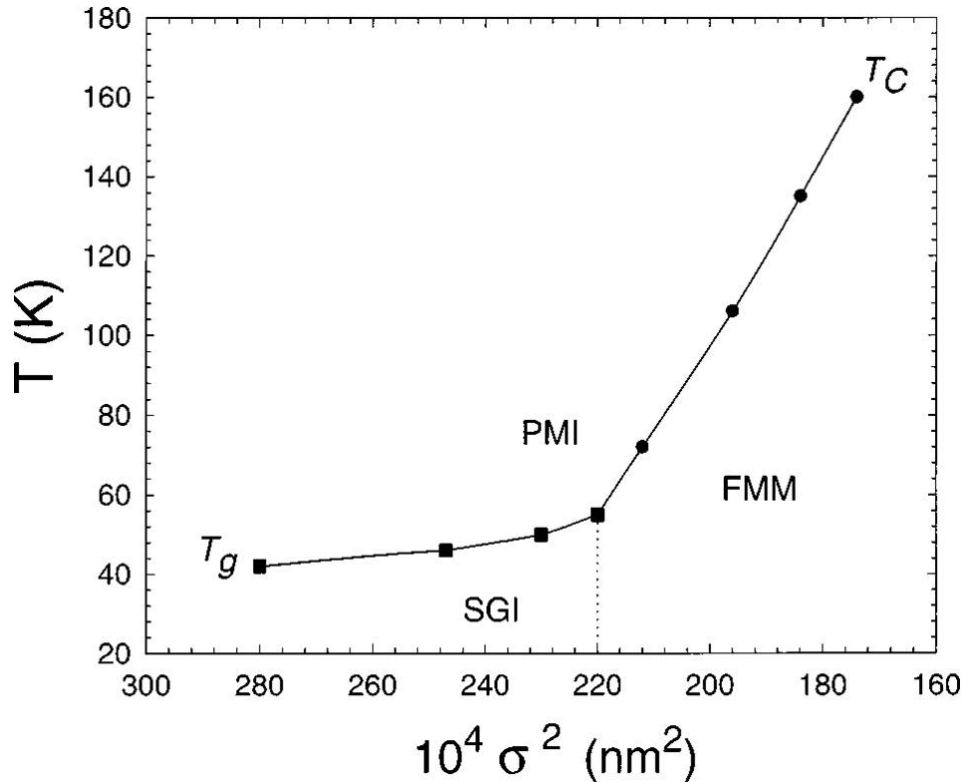
Fig1.24. Electronic and magnetic phase diagram for $Th_{0.65}A_{0.35}MnO_3$ (reproduced from [63]).

1.11 Complex Oxides in the nanocrystalline form – is this one more way of applying pressure?

Reducing the particle size to the nanometer regime and looking for new properties opens up a totally new field of scientific investigation. During the last decade nanocrystalline forms of various materials have drawn considerable attention because they typically exhibit physical and chemical properties that are distinct from their bulk counterparts. But the point of interest in the context of the present discussion is whether reducing the particle size has any parallelism with pressure effects. A recent work by our group[64] on nanocrystalline $La_{0.67}Ca_{0.33}MnO_3$ pointed out that size reduction, in fact, does work in a way which is equivalent to increasing the externally applied hydrostatic pressure. This single result acted as a major motivation for the work presented in this thesis. Although the results published in reference 64 do point towards a role of size reduction in modifying the ground state of the manganites, a proper understanding of the mechanism by which the ground state changes was lacking. It showed changes in the unit cell structure but detailed structural studies were yet to be done. Most importantly, the results were presented on only one system ($La_{0.67}Ca_{0.33}MnO_3$), and whether the sensitivity to size reduction was a more general phenomenon was still an open question. All the above questions have been answered in this thesis. But before we start addressing these questions and answering them in the subsequent chapters, it would be worthwhile to end the present chapter with a brief review of nanoparticles, focusing on those issues which we will come across in the latter chapters of this thesis.

Reduction in size often does more than simply making things smaller, and therein lies its appeal. There are many properties of materials that undergo qualitative, often sudden changes below a certain size scale. Effects due to enhanced grain boundaries and increased surface-to-volume ratio are at the core of these changes in the properties of the materials. The increased surface effects arise from the fact that nanoparticles have dimensions close to atomic dimensions and so a much higher fraction of the total atoms are present on their surfaces. The surface is more populated than the bulk (interior) of the material. This leads to broken bonds and unfilled valencies, which in turn can change the physical properties of the system.

Magnetic properties of nanocrystals: Magnetic properties at the nanoscale strongly depend on the interplay involving the surface atoms and the energetics of spin reversal. In order to understand size – dependent magnetic properties, it is instructive to follow the changes in a magnetic substance as the particle size is decreased from a few microns to a few nanometers. In a ferromagnetic substance, the T_C generally decreases with a decrease in size. In the region close to the ordering temperature, the correlation length $\xi(t)$ of the fluctuation in the order parameter M diverges logarithmically with the reduced temperature $\left(t = \dfrac{T - T_{order}}{T_{order}} \right)$, where, the ordering temperature T_{order} is T_C for a ferromagnetic material and T_N for an antiferromagnetic material. With the geometric confinement effect on $\xi(t)$, the magnetic transition temperature (T_C or T_N) is reduced from the bulk value. This decrease in T_C is given by the finite size scaling formula[65]:

$$\frac{T_C(\infty) - T_C(d)}{T_C(\infty)} = \pm \left(\frac{d}{\xi_0} \right)^{-\lambda}$$, where, $T_C(\infty)$ corresponds to the bulk Curie temperature and ξ_0 gives

the spin-spin correlation length and should be of the order of a characteristic microscopic dimension. λ is the critical shift exponent which is the reciprocal of the correlation length exponent v according to the standard finite size scaling theory[66]. The finite particle size limits the divergence of the spin-spin correlation length ξ_0 at T_C which results in a decrease of T_C with respect to the bulk value where $d < \xi_0$. The shift exponent λ reflects the appropriate universality class which is primarily characterized by the dimensionality of the system. The λ values for the three dimensional Ising, XY and Heisenberg models are 1.59, 1.49 and 1.41 respectively[67]. In the 2D limit, a power law is obtained only for the Ising model where the theory predicts the value $\lambda = 1$. Thus, this theory predicts that the shift in the transition temperature from that of the bulk should depend on a dimension of the system. Experimentally, this finite size effect has been reported mainly in two dimensional magnetic films[68,69,70]. In comparison, there are much less reports concerning the finite size effect on lower dimensional magnetic samples such as nanowires[71] or nanoparticles[72,73]. The finite size effect is true for some other transition temperatures associated with long range order also. For example, ferroelectric transition temperatures also decrease with a decrease in the particle size. The decrease in the ferroelectric transition temperature has been linked to changes in structural parameters (e.g. in $BaTiO_3$[74] and $PbZrO_3$[75]). However, as we have mentioned earlier, size reduction can often strengthen ferromagnetism also (as in reference 64). In such cases, other factors (also related to size reduction) come into play. Exploring the dynamics of size reduction in such systems forms a major aim of this thesis work. We deal with these systems in details in Chapter 3.

In ferromagnetic nanoparticles, the finite size effect is complicated by single domain effects and superparamagnetism. Whether a particle has entered the single domain regime or not can easily be determined by a study of the coercivity as a function of the particle size. With a decrease in the diameter, the coercivity (H_C) increases initially till a critical particle diameter (d_S) and thereafter it decreases (Fig.1.25). d_S is the critical size below which the particle changes from being a multi-domain particle to a single-domain particle. The value of d_S is usually in the regime of few tens of nanometers. Below d_S, H_C tends to decrease due to thermal effects. Below another critical particle size (d_P), the coercivity becomes zero as the thermal energy becomes sufficient to randomize the magnetic moments in the particle. This is the superparamagnetic regime. Superparamagnetic particles do not possess long – range magnetic order, but show characteristic magnetic properties at low temperatures (below the blocking temperature T_B where the thermal energy is not high enough to randomize the magnetic moments and they become blocked or frozen along the easy axis). Thus, below T_B the nanocrystals acquire a finite coercivity.
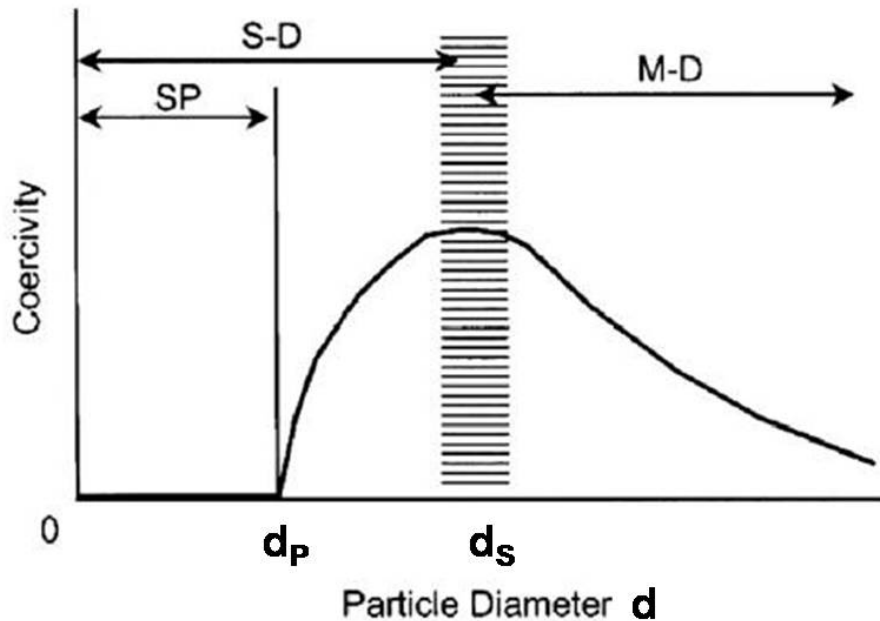
Fig.1.25. Schematic illustration of the change of coercivity of a ferromagnetic particle with diameter. SP indicates the superparamagnetic regime, S-D the single domain regime and M-D the multi-domain regime.

A particle becomes single domain if the particle size becomes less than the ferromagnetic exchange length $\left(L_{ex} = \sqrt{\dfrac{2J}{\mu_0 M_S}} \right)$, where, J is the exchange constant (related to the overlap of the charge distribution of the adjacent atoms) and M_S is the saturation magnetization. Thus, L_{ex} measures the critical particle size below which the magnetostatic energy associated with a uniform magnetization is smaller than the energy required to demagnetize the particle. The material is expected to consist of single domain particles when the particle size is smaller than L_{ex}. On the other hand, when the particle size is larger than L_{ex}, the material becomes a multi domain system.

27

A related length scale is the exchange correlation length or the wall thickness $\left(L = \sqrt{\dfrac{J}{K}}\right)$, where, K is the anisotropy constant (K is actually the anisotropy energy per unit volume). L gives the typical thickness of the domain walls. Thus, particles with size smaller than L, even though they are larger than L_{ex} cannot become multi domain. The width of the domain wall depends on the balance between J (which prefers a wide wall) and K (which prefers a narrow wall). A single domain particle has high magnetostatic energy but no domain wall energy, whereas a multi domain particle has lower magnetostatic energy but higher domain wall energy.

Magnetic properties such as the saturation magnetization also exhibit size dependent changes at the nanoscale. The saturation magnetization of nanocrystals is less than that of the corresponding bulk system because of the dead layer on the surface. The surface layer contains uncompensated spins which are disordered and lack the long range order present in the core of the nanoparticles. The net effect is to reduce the overall saturation magnetization[76].

1.12 Plan of the thesis

We end this chapter with a layout of the thesis. Excluding the present chapter, this dissertation has five more chapters as follows:

- ✓ Chapter 2 contains the experimental details of the sample preparation and their characterization. This chapter also deals with a description of the main physical techniques used and the nature of information these techniques can give us.
- ✓ Chapter 3 deals with the magnetic state of $La_{1-x}Ca_xMnO_3$ and $La_{1-x}Sr_xCoO_3$ in the optimum doping concentration regime. Thus, we have selected $La_{0.67}Ca_{0.33}MnO_3$ and $La_{0.5}Sr_{0.5}CoO_3$ as the materials to be studied. In the bulk state, both are ferromagnetic metals with a Curie temperature of 270 K and 250 K respectively. We look at the differences arising in the two systems on size reduction solely from the point of view of magnetism and the nature of magnetic transition.
- ✓ Chapter 4 deals with the ground state of nanoparticles half – doped manganites $La_{0.5}Ca_{0.5}MnO_3$ and $Pr_{0.5}Ca_{0.5}MnO_3$. Both these materials exhibit charge ordering in the bulk state. This chapter describes, in details, the structural (long range as well as short range) and physical (magnetic as well as electrical transport) properties of these nanomanganites, draws conclusions from the results and tries to explain the cause of the drastic change in the ground state that we see.
- ✓ Chapter 5 deals with the magnetotransport properties of nanoparticles of three classes of oxides – $La_{0.67}Ca_{0.33}MnO_3$, $La_{0.5}Sr_{0.5}CoO_3$ and $LaNiO_3$. This chapter puts a special emphasis on the transport properties at low temperature (below 10K and down to 0.3K) and explores the novel behavior shown by these functional oxides in this low temperature range.
- ✓ In Chapter 6 we sum up all the important observations made in this thesis. The new insight gained from the present work in understanding the behavior of nanoparticles of complex oxides is discussed.

REFERENCES

[1] P.G.Radaelli, D.E.Cox, M.Marezio and S-W.Cheong, Phys. Rev. B, **55**, 3015 (1997)

[2] Ryan P Haggerty and Ram Seshadri, J. Phys. Condens. Matter, **16**, 6477 (2004)

[3] P.Schiffer, A.P.Ramirez, W.Bao and S.W.Cheong, Phys. Rev. Lett., **75**, 3336 (1995)

[4] H.Kuwahara, Y.Tomioka, A.Asamitsu, Y.Moritomo and Y.Tokura, Science, **270**, 961 (1995)

[5] D.P.Kozlenko, Z.Jirak, I.N.Goncharenko and B.N.Savenko, J. Phys. Condens. Matter, **16**, 5883 (2004)

[6] J.Mira, J.Rivas, F.Rivadulla, C.Vazquez – Vazquez and M.A.Lopez – Quintela, Phys. Rev. B, **60**, 2998 (1999)

[7] S.Mori, T.Katsufuji, N.Yamamoto, C.H.Chen and S-W.Cheong, Phys. Rev. B, **59**, 13573 (1999)

[8] N.Menyuk, P.M.Raccah and K.Dwight, Phys. Rev., **166**, 510 (1968)

[9] G.H.Jonker and J.H.Van Santen, Physica, **16**, 337 (1950)

[10] V.Kiryukhin, New Journal of Physics, **6**, 155 (2004)

[11] J.Curiale, C.A.Ramos, P.Levy, R.D.Sanchez, G.Aurelio and F.Rivadulla, Physica B, **384**, 65 (2006)

[12] Joonghoe Dho, W.S.Kim and N.H.Hur, Phys. Rev. Lett., **87**, 187201 (2001)

[13] H.Kawano, R.Kajimoto, M.Kubota and H.Yoshizawa, Phys. Rev. B, **53**, R14709 (1996)

[14] H.Kawano, R.Kajimoto, M.Kubota and H.Yoshizawa, Phys. Rev. B, **53**, 2202 (1996)

[15] S-W.Cheong and H.Y.Hwang, *Ferromagnetism vs Charge/Orbital Ordering in Mixed – Valent Manganites*

[16] T.V.Ramakrishnan, J. Phys. Condens. Matter, **19**, 125211 (2007)

[17] D. Kim, B. Revaz, B.L. Zink, F. Hellman, J.J.Rhyne and J.F.Mitchell, Phys. Rev. Lett., **89**, 227202 (2002)

[18] R.I. Zainullina, N.G. Bebenin, V.V. Ustinov, Ya.M. Mukovskii and D.A. Shulyatev, Phys. Rev. B, **76**, 014408 (2007)

[19] Y.Tokura, *Fundamental Features of Colossal Magnetoresistive Manganese Oxides, in Colossal Magnetoresistance Oxides*, edited by Y.Tokura (Gordon and Breach, Monographs in Condensed Matter Science, London, 1999)

[20] Q.Huang, A.Santoro, J.W.Lynn, R.W.Erwin, J.A.Borchers, J.L.Peng and R.L.Greene, Phys. Rev. B, **55**, 14987 (1997); J.Rodríguez-Carvajal, M.Hennion, F.Moussa and A.H.Moudden, Phys. Rev. B, **57**, R3189 (1998)

[21] Tapan Chatterji, Bachir Ouladdiaf, P.Mandal, B.Bandyopadhyay and B.Ghosh, Phys. Rev. B, **66**, 054403 (2002)

[22] P.W.Anderson, Phys. Rev., **79**, 350 (1950)

[23] J.B.Goodenough, Phys. Rev., **100**, 564 (1955)

[24] J.Kanamori, J.Phys.Chem.Solids, **10**, 87 (1959)

[25] E.O.Wollan and W.C.Koehler, Phys. Rev. **100**, 545 (1955)

[26] C.Zener, Phys. Rev., **81**, 440 (1951)

[27] Clarence Zener, Phys. Rev., **83**, 299 (1951)

[28] Clarence Zener, Phys. Rev., **82**, 403 (1951)

[29] P.W.Anderson and H.Hasegawa, Phys. Rev., **100**, 675 (1955)

[30] C.H.Chen, S.W.Cheong and H.Y.Hwang, J. Appl. Phys., **81**, 4326 (1997)

[31] S.Mori, C.H.Chen and S.W.Cheong, Nature, **392**, 473 (1998)

[32] Y.Moritomo, H.Kuwahara, Y.Tomioka and Y.Tokura, Phys. Rev. B, **55**, 7549 (1997)

[33] A.Asamitsu, Y.Tomioka, H.Kuwahara and Y.Tokura, Nature (London), **388**, 50 (1997)

[34] Ayan Guha, Arindam Ghosh, A.K.Raychaudhuri, S.Parashar, A.R.Raju and C.N.R.Rao, Appl.Phys. Lett., **75**, 3381 (1999)

[35] V.Kiryukhin, D.Casa, J.P.Hill, B.Keimer, A.Vigilante, Y.Tomioka and Y.Tokura, Nature, **386**, 813 (1997)

[36] M.Hervieu, A.Barnabe, C.Martin, A.Maignan and B.Raveau, Phys. Rev. B, **60**, R726 (1999)

[37] M.Fiebig, K.Miyano, Y.Tomioka and Y.Tokura, Science, **280**, 1925 (1998)

[38] K.Miyano, T.Tanaka, Y.Tomioka and Y.Tokura, Phys. Rev. Lett., **78**, 4257 (1997)

[39] T.Mizokawa, D.I.Khomskii and G.A.Sawatzky, Phys. Rev. B, **63**, 024403 (2000)

[40] M.Fäth, S.Freisem, A.A.Menovsky, Y.Tomioka, J.Aarts and J.A.Mydosh, Science, **285**, 1540 (1999)

[41] Adriana Moreo, Matthias Mayr, Adrian Feiguin, Seiji Yunoki and Elbio Dagotto, Phys. Rev. Lett., **84**, 5568 (2000)

[42] M.Uehara, S.Mori, C,H,Chen and S.W.Cheong, Nature (London), **399**, 560 (1999)

[43] Y.Moritomo, Phys. Rev. B, **60**, 10374 (1999)

[44] Y.Moritomo, A.Machida, S.Mori, N.Yamamoto and A.Nakamura, Phys. Rev. B, **60**, 9220 (1999)

[45] G.H. Jonker and J.H. Van Santen, Physica, **19**, 120 (1953)

[46] V.G. Bhide, D.S. Rajoria, C.N.R. Rao, G. Rama Rao and V.G. Jadhao, Phys. Rev. B, **12**, 2832 (1975)

[47] P. Ganguly and C.N.R. Rao in *Metallic and Non – metallic State of Matter*, edited by P.P.Edwards and C.N.R. Rao (Taylor & Francis, London, 1985)

[48] M.A. Senaris – Rodriguez and J.B.Goodenough, J. Solid State Chem. **118**, 323 (1995)

[49] V.G.Bhide, D.S.Rajoria, G.Rama Rao and C.N.R.Rao, Phys. Rev. B, **6**, 1021 (1972)

[50] From Ph.D. thesis, R. Mahendiran, Department of Physics, Indian Institute of Science, Bangalore, India.

[51] R. Mahendiran and A.K.Raychaudhuri, Phys. Rev. B, **54**, 16044 (1996)

[52] M.Medarde, J.Mesot, P.Lacorre, S.Rosenkranz, P.Fischer and K.Gobrecht, Phys. Rev. B, **52**, 9248 (1995)

[53] J.J.Neumeier, M.F.Hundley, J.D.Thompson and R.H.Heffner, Phys. Rev. B, **52**, R7006 (1995)

[54] Y.Moritomo, H.Kuwahara, Y.Tomioka and Y.Tokura, Phys. Rev. B, **55**, 7549 (1997)

[55] D.P.Kozlenko, L.S.Dubrovinsky, I.N.Goncharenko, B.N.Savenko, V.I.Voronin, E.A.Kiselev and N.V.Proskurnina, Phys. Rev. B, **75**, 104408 (2007)

[56] H.Y.Hwang, S-W.Cheong, P.G.Radaelli, M.Marezio and B.Batlogg, Phys. Rev. Lett., **75**, 914 (1995)

[57] C.N.R.Rao, Anthony Arulraj, P.N.Santosh and A.K.Cheetham, Chem. Mater., **10**, 2714 (1998)

[58] H.Y.Hwang, T.T.M.Palstra, S-W.Cheong and B.Batlogg, Phys. Rev. B, **52**, 15046 (1995)

[59] Lide M. Rodriguez-Martinez and J. Paul Attfield, Phys. Rev. B, **54**, R15622 (1996)

[60] F.Damay, C.Martin, A.Maignan and B. Raveau, J. Appl. Phys., **82**, 6181 (1997)

[61] Lide M. Rodriguez-Martinez and J. Paul Attfield, Chem. Mater., **11**, 1504 (1999)

[62] Himanshu Jain, A.K.Raychaudhuri, Ya M.Mukovskii and D.Shulyatev, Solid State Comm., **138**, 318 (2006)

[63] A.Maignan, C.Martin, G.Van Tendeloo, M.Hervieu and B.Raveau, Phys. Rev. B, **60**, 15214 (1999)

[64] K.Shantha Shankar, Sohini Kar, G.N.Subbanna and A.K.Raychaudhuri, Solid State Communications, **129**, 479 (2004)

[65] M.N.Barber in *Phase Transitions and Critical Phenomena*, edited by C.Domb and J.L.Lebowitz (Academic, New York, 1983)

[66] Michael E. Fisher and Michael N. Barber, Phys. Rev. Lett., **28**, 1516 (1972)

[67] J. Zinn Justin, in *Quantum Field Theory and Critical Phenomena*, Oxford University Press, 1993

[68] Dirk Fuchs, Thorsten Schwarz, Oswaldo Moran, Peter Schweiss and Rudolf Schneider, Phys. Rev. B, **71**, 092406 (2005)

[69] M.Ziese, H.C.Semmelhack, K.H.Han, S.P.Sena and H.J.Blythe, J. Appl. Phys., **91**, 9930 (2002)

[70] D.Fuchs, O.Moran, P.Adelmann and R.Schneider, Physica B, **349**, 337 (2004)

[71] L.Sun, P.C.Searson and C.L.Chien, Phys. Rev. B, **61**, R6463 (2000)

[72] Z.X.Tang, C.M.Sorensen, K.J.Klabunde and G.C.Hadjipanayis, Phys. Rev. Lett., **67**, 3602 (1991)

[73] M.L.Moreira, J.M.Soares, W.M.de Azevedo, A.R.Rodriguez, F.L.A.Machado and J.H.de Araujo, Physica B, **384**, 51 (2006)

[74] S. Tsunekawa, S. Ito, T. Mori, K. Ishikawa, Z.-Q. Li and Y. Kawazoe, Phys. Rev. B, **62**, 3065 (2000)

[75] Soma Chattopadhyay, Pushan Ayyub, V.R. Palken, A.V. Gurjar, R.M. Wankar and Manu Multani, J. Phys.: Condens. Matter, **9**, 8135 (1997)

[76] P.Kameli, H.Salamati and A.Aezami, J. Appl. Phys., **100**, 053914 (2006)

CHAPTER 2. EXPERIMENTAL DETAILS – SAMPLE PREPARATION AND EXPERIMENTAL TECHNIQUES USED

This chapter has been divided into two parts. The first part gives the details of the sample preparation technique and their characterization. The second part introduces the various experimental techniques that have been used during the course of this thesis work.

2.1 Synthesis routes

All the different oxide nanoparticles were prepared using a chemical synthesis route. Before we go into the details of the sample preparation technique that has been used during the course of this dissertation, we briefly describe the different chemical routes of sample preparation that are commonly used for synthesizing complex oxide nanoparticles.

2.1.1 Solid State synthesis followed by ball milling

The solid state (or ceramic) route is, perhaps, one of the oldest and most conventional methods of preparing polycrystalline oxides. It involves mixing the solid components and reacting the mixture at elevated temperatures. By its very nature, the method requires large diffusion distances (up to 10^5 Å) of the reacting species and is, therefore, of disadvantage. The steps to be followed in this synthesis route are the following:

1. Select appropriate starting materials (which can be high purity oxides or carbonates of the metal cations present in the final product).
2. Weigh the starting materials to ensure proper stoichiometry.
3. Mix the starting materials together (either in an agate mortar pestle using an organic solvent or in a planetary ball mill).
4. Calcine at a temperature high enough for the solid state reaction to occur and the desired products to form.
5. Regrind the product and repeat steps 3 to 5 till pure product is obtained.

Mixing the starting materials as well as regrinding the products is essential so as to maximize the area of contact between the reacting solids. Smaller particles will present a larger surface area for the reaction to occur. Hence, it helps to pulverize the starting materials individually before mixing them. The reaction occurs by solid state diffusion, and the rate of diffusion can be increased by increasing the temperature. The final product (which often has a particle size in excess of 1 μm) is then subjected to milling (using planetary ball mills) which mechanically crushes the material and reduces the particle size to the nanometer regime. The optimal rotation speed of the bowls depends on their diameter. For cylindrical bowls, the optimal rotation speed was estimated by Sundrica et.al.[1], who gave the formula: $R = \dfrac{32}{\sqrt{d}}$, where, d is the outer diameter of the bowl in meters and R is the optimal speed in rpm. The ceramic route + ball milling technique of producing nanocrystals has its own advantages and disadvantages

which have been summarized in Table 2.1. More details regarding the synthesis of complex metal oxides can be found in review articles written by Rao et.al.[2] and references listed therein.

2.1.2 The sol gel method

The sol gel technique[3] is an improvement over the solid state synthesis route because in the former the reactions occur in a solution medium instead of in the solid state. This decreases the diffusion distances through intimate mixing of the cations. As a result, reactions can occur at lower temperatures and the products formed are more homogeneous.

The sol gel process can be defined as the "formation of an oxide network through polycondensation reactions of a molecular precursor in a liquid". A sol is a stable dispersion of colloidal particles (amorphous or crystalline) or polymers in a solvent. A gel, on the other hand, consists of a three dimensional continuous network which encloses a liquid phase. The sol gel process is based on the transition of a system from a liquid solution (sol) into a gelatinous network (gel) phase. This process is generally irreversible.

Fig.2.1 gives an overview of the sol gel process. Typically the sol is first formed by mechanically mixing a liquid alkoxide precursor (such as tetramethoxysilane (TMOS) or tetraethoxysilane (TEOS)) with water and a cosolvent together with an acid or base catalyst at room temperature. During this step, alkoxide groups are removed by acid- or base-catalyzed hydrolysis reactions and networks of O-M-O linkages are formed in subsequent condensation reactions. Depending upon the water:alkoxide molar ratio, pH, temperature and solvent, further condensation leads to different polymeric structures such as linear, entangled chains, clusters and colloidal particles. The sol is then heated. During the heating the particles get linked to form chains and the networks extend throughout the liquid medium, ultimately thickening into a gel. The gel is then aged (to allow its network to strengthen) and dried (to remove the liquid). If the gel is dried by evaporation, then the capillary forces will result in shrinkage and the gel network will collapse. In such an event, the product is termed a xerogel. If the drying is performed under supercritical conditions, the network structure may be retained and a gel with large pores are formed. This is termed an aerogel.
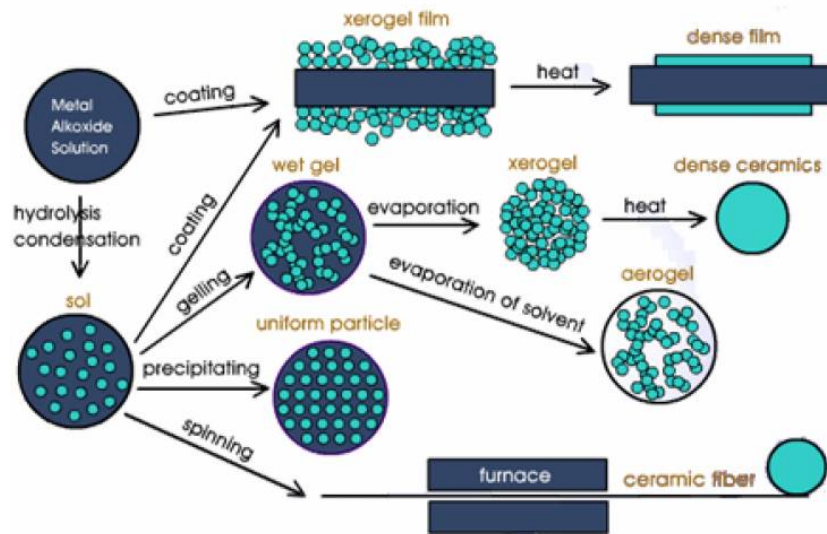
Fig.2.1. Overview of the sol gel process (reproduced from [4]).

The salient features of the sol gel technique are, thus, the following:

1. The idea behind this synthesis process is to dissolve the precursors in a liquid in order to bring it back as a solid in a controlled manner.
2. Multi component compounds may be prepared with a controlled stoichiometry by mixing the precursors in proper stoichiometry.
3. The sol gel process prevents problems of inhomgeneity by a gelation reaction.
4. It enables mixing at an atomic level.
5. It results in small particles, which can be sintered easily.

2.1.3 The reverse micelle route

Another versatile (albeit less used) method for preparing complex oxide nanocrystals is the reverse micellar route[5]. Micelles are thermodynamically stable aggregates of soluble amphiphilic compounds or surfactants (organic compounds which contain both a polar portion (a hydrophilic head) as well as a non-polar portion (a hydrophobic tail)) that form spontaneously above a critical micellar concentration and a critical micellar temperature. Thus, in aqueous solutions, they form regular micelles with the hydrophilic heads facing outward (Fig.2.2(a)), and in organic solvents, they form reverse micelles with the hydrophilic tails facing outward (Fig.2.2(b)). Reverse micelles can form both in the presence as well as in the absence of water. However, if the medium is completely free of water, the reverse micelles formed are very small and polydisperse. The presence of water is necessary to form larger reverse micelles as well as to control their size. Thus, the size of core of the reverse micelles is characterized by the water – surfactant molar ratio $\left(w = \dfrac{[H_2O]}{[S]} \right)$. The reverse micelles where $w < 15$ are usually used for nanomaterial synthesis[6].
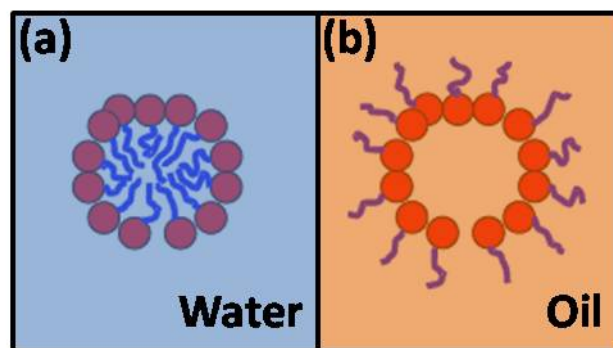
Fig.2.2. Schematic illustration of (a) micelles and (b) reverse micelles.

The strategy to prepare nanocrystals using this technique is to dissolve the precursor salts in water and use these aqueous solutions (instead of pure water) to form the microemulsions. This ensures that the cations get trapped inside the reverse micelles. The microemulsions are then mixed and stirred. This leads to collisions between the reverse micelles and exchange of the water content. The precursor salts then react inside the reverse micelle. By controlling the size of

the reverse micelle cores (by controlling *w*), the size of the products can also be controlled to the nanometer regime. The reaction mechanism is shown schematically in Fig.2.3. To prepare complex oxides, the product is then centrifuged out, washed and subjected to heat treatment for proper phase formation.
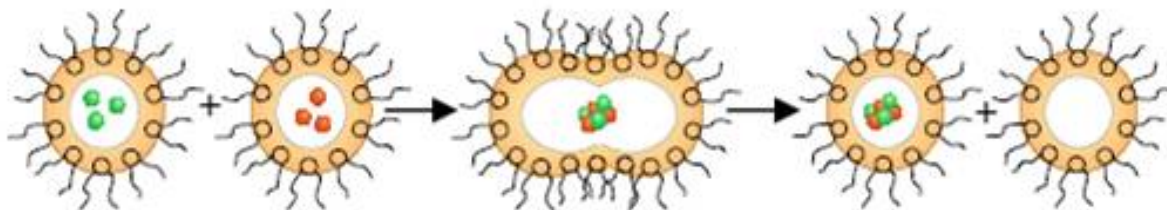
Collisions between micelles → Exchange of the water content

Fig.2.3. Schematic illustration of nanoparticle synthesis using the reverse micellar route.

2.1.4 Sonochemical route

Sonochemistry is the research area in which molecules undergo chemical reaction due to the application of powerful ultrasound radiation (20 kHz – 10 MHz). The physical phenomenon responsible for the sonochemical process is acoustic cavitation – the formation, growth and implosive collapse of bubbles in liquids irradiated with high intensity ultrasound. Bubble collapse during cavitation serves as an effective means of concentrating the diffuse energy of sound: compression of a gas generates heat. When the compression of bubbles occurs during cavitation, heating is more rapid than thermal transport, creating a short – lived, localized hot spot.

The extreme conditions of cavitation can be used to produce a variety of nanostructured materials. The strategy is to subject a mix of reagents dissolved in a solvent to ultrasound radiation. The creation of bubbles is due to the suspended particulate matter and impurities in the solvent. The growth of a bubble by expansion leads to the creation of a vacuum that induces the diffusion of volatile reagents into the bubble. The volatile organometallic compounds decompose inside a collapsing bubble, and the resulting metal atoms agglomerate to form nanostructured materials. The sonochemical route of synthesis of nanomaterials is also extremely versatile. Various forms of nanophase materials can be generated simply by changing the reaction medium. For example, when precursors are sonicated in low volatility alkanes, nanostructured metal powders are formed. If sonication occurs in the presence of a bulky or polymeric surface ligand, stable nanophase metal colloids are created. Sonication of the precursor in the presence of an inorganic support (such as silica or alumina) provides an alternative means of trapping nanometer size clusters.

Theories of the hot spot mechanism claim that very high temperatures (5000 K – 25000 K) are obtained from the collapse of the bubble. Since the collapse occurs in less than a nanosecond, very high cooling rates, in excess of 10^{11} K/sec, are obtained. This high cooling rate hinders the organization and crystallization of the products. As such, in most cases, amorphous nanoparticles are obtained. The reason that the products are nanostructured is that the fast

35

kinetics do not permit the growth of the nuclei. A review of the sonochemical method for preapartion of nanomaterials has been given by Rao et.al.[7].

2.1.5 Chemical Solution Deposition (The Acetate/Nitrate Route)

This is a modified sol gel technique designed specially for the preparation of complex oxide nanoparticles. All the different oxide nanoparticles during this thesis work were prepared using this method. In the next section, we describe this synthesis method in details. But before that we give a table comparing the relative advantages and disadvantages of the ceramic route and sol gel method.

Table 2.1 A comparison of the relative advantages and disadvantages of the ceramic and sol gel methods of sample preparation

	Ceramic route	**Sol gel (including CSD route)**
Scaling	The quantity of product formed can be easily scaled up by increasing the quantity of the starting materials	The quantity of product formed can be scaled up but not as much as that in the ceramic route
Compositional and chemical homogeneity control	Controlling the stoichiometry and chemical homogeneity is relatively more difficult	Precise control of the stoichiometry can be achieved. The final product is more homogeneous chemically
Temperature of synthesis	Requires higher temperatures because reaction occurs in the solid state	Low temperature synthesis since reaction occurs in the solution phase
Toxicity	No solvent required	The solvents used are often toxic
Size dispersion	Greater size dispersion	More monodisperse
Grain size of final product	Bulk samples (particle size > 1μm) are formed	Samples with particle size as low as 10 – 15 nm can be produced

2.2 Oxide nano powder preparation – The CSD Route

This is essentially a modified polymeric precursor synthesis route. The essential steps of the process are shown schematically in Fig.2.4. In a typical synthesis process, high purity (> 99%) metal acetates (procured from Sigma Aldrich[8]) were dissolved in the desired stoichiometric proportions in acetic acid and water. To this solution, an appropriate amount of ethylene glycol (molecular weight = 62.07 gm/mol) was added and heated until the sol was formed. The gel was dried overnight at 150^0C. Pyrolysis was done at 350^0C and 450^0C followed by a sintering at higher temperature to obtain the desired chemical phase. For the manganites, phase pure samples could be obtained at temperatures as low as 650^0C, while for the cobaltates

the final annealing had to be done at 800^0C. The particle size of the final product could be controlled both by the heat treatment temperatures as well as the water – ethylene glycol ratio. We could prepare samples with particle size as low as ~ 15 nm by optimizing these process parameters.
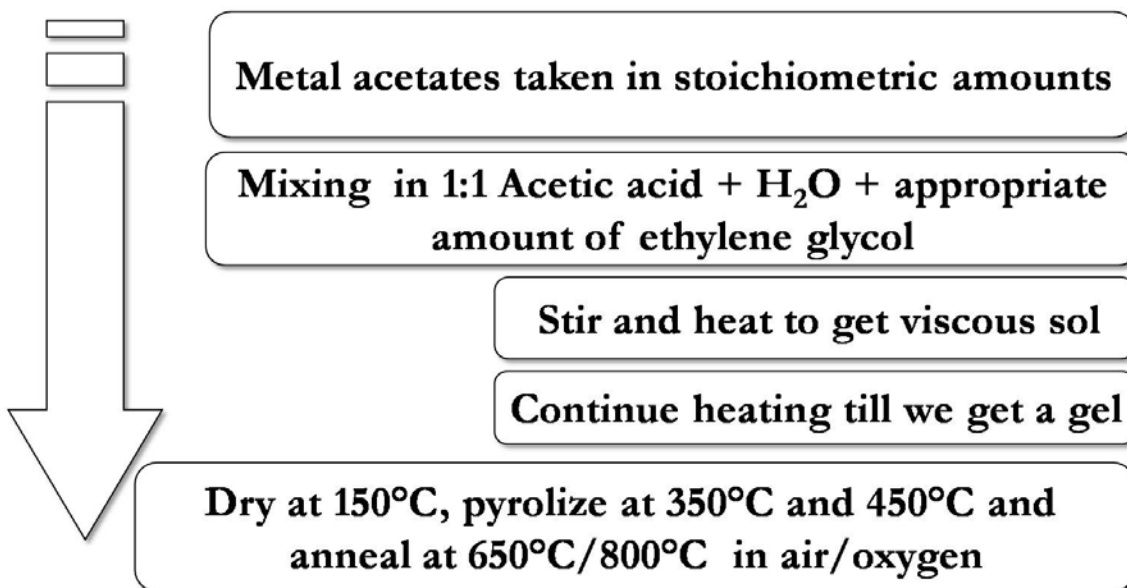
Fig.2.4. Schematic illustration of the essential steps of the CSD technique.

A major challenge encountered in the synthesis of nanocrystalline multicomponent oxides is the poor control of stoichiometry and homogeneity at the nano level. The CSD technique overcomes this problem successfully. This is related to the use of ethylene glycol which has an extremely important role in the reaction mechanism. It helps in forming a close network of cations from the precursor solution thereby assisting the reaction and also phase formation at low temperatures. This reaction mechanism was first given by Shankar et. al.[9]. On heating the acetates in water and ethylene glycol ($C_2H_4(OH)_2$) mixture to moderate temperatures, $C_2H_4(OH)_2$ polymerizes to polyethylene glycol (PEG) with the concurrent formation of water. Polyethylene glycol distributes the metal cations atomically throughout the polymeric structure by forming coordination bonds between the oxygen and metal ions. With the formation of this complex, the hydrogen bonding between PEG oligomers decreases as the cations bind to the oxygen by replacing the hydrogen ion. On heating to higher temperatures, a solid resin forms with the removal of excess water. As the gel sets to form the solid polymeric resin, the high viscosity of the resin prevents the different cations from segregating and this ensures a high level of homogeneity. This resin consists of metal atoms bonded to organic radicals through oxygen comprising a cross – linked network, thereby interconnecting the reaction species. Heating of the resin causes breakdown of the polymer and finally oxidation of the cations. This reaction mechanism is schematically illustrated in Fig.2.5.

$$x\,A-acetate+y\,B-acetate+z\,(Mn/Co/Ni)-acetate+nH_2O+m(CH_2OH)_2$$
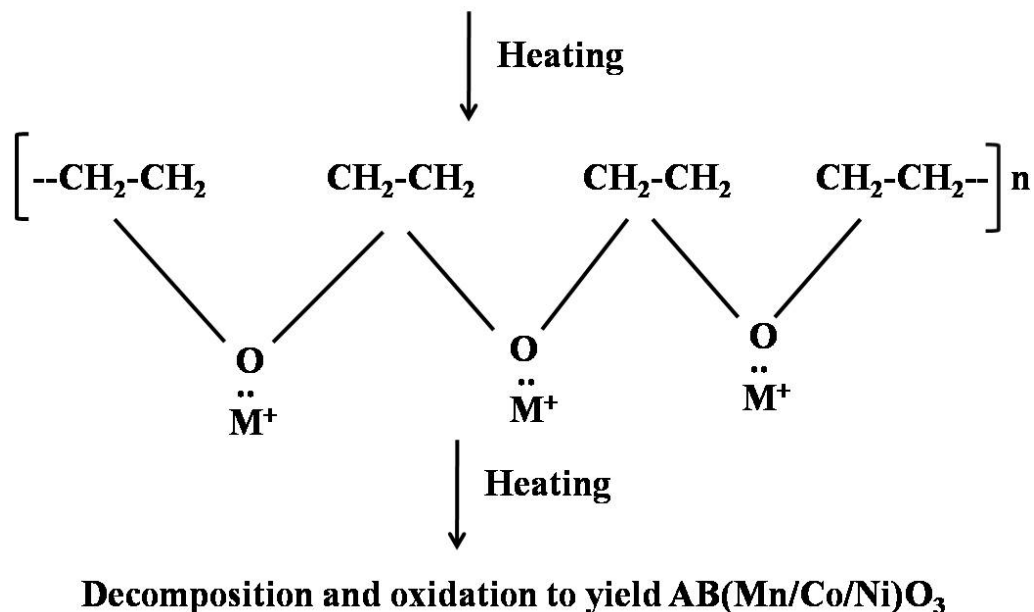
Fig.2.5. Phase evolution of oxide nanoparticles.

2.3 Experimental monitoring of the mechanism of oxide nanoparticle phase formation

The mechanism of the oxide nanoparticle phase formation, as detailed above, could be monitored by Fourier Transform Infrared spectra (FTIR) measurements, in combination with X-Ray diffraction (XRD) at various stages of calcination. The FTIR spectroscopy was performed on the samples after they were mixed with dry KBr to form pellets. We used JASCO FT/IR – 6300 Spectrometer[10] for these measurements. The X-Ray diffraction measurements were done with X'Pert PRO Diffractometer[11] using CuKα radiation. The pyrolysis of the sol was also monitored using simultaneous thermogravimetry and differential thermal analysis with Al_2O_3 as the reference material. We used the Diamond Thermogravimetric/Differential Thermal Analyzer from PerkinElmer, Inc[12]. Below we elaborate on these studies for the three systems $La_{0.67}Ca_{0.33}MnO_3$ (LCMO), $La_{0.5}Sr_{0.5}CoO_3$ (LSCO) and $LaNiO_3$ (LNO).

2.3.1. $La_{0.67}Ca_{0.33}MnO_3$

In Fig.2.6, we show the FTIR spectra of $La_{0.67}Ca_{0.33}MnO_3$ precursor powders calcined at various temperatures. The final calcination temperatures are written alongside the corresponding curves. On the right hand side panel, we show the blown up region between wavenumber 363 cm^{-1} to 348 cm^{-1} to emphasize the presence of the Mn – O bond in all the samples. Each spectrum has been taken with a fresh sample, and not the same sample annealed successively at different temperatures.
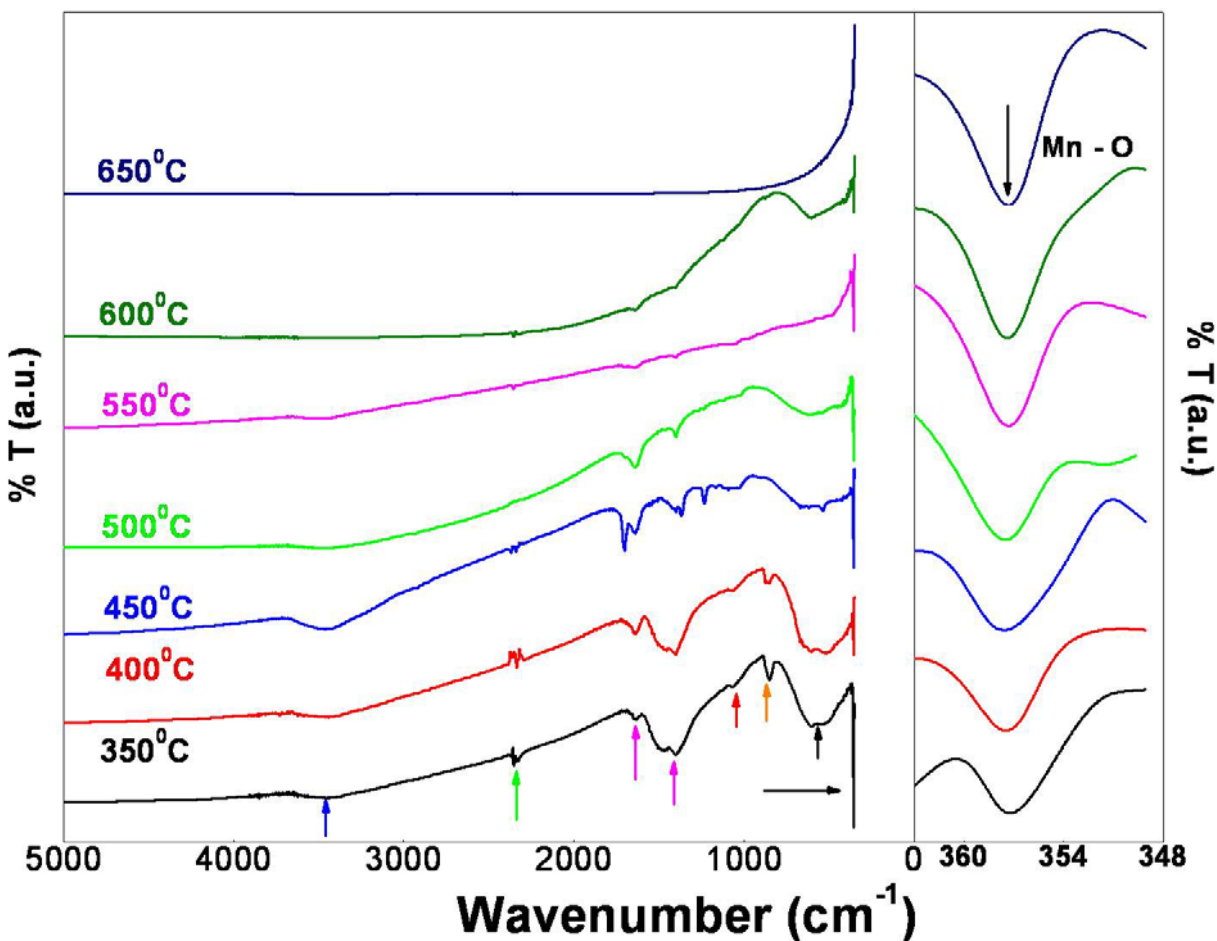
Fig.2.6. FTIR spectra recorded on $La_{0.67}Ca_{0.33}MnO_3$ powder samples heated to different temperatures.

For the lower sintering temperatures, the organic impurities are still present and can be seen from their corresponding absorption peaks in the FTIR spectra. These are shown as arrows for the spectrum of the sample annealed at 350^0C. The two black arrows at 357 and 560 cm^{-1} arise from the bending and stretching of Mn – O bond, and are thus, the indicators of perovskite phase formation. It is amazing that these bands appear at temperatures as low as 350^0C. However, we are yet to get phase pure samples. The impurities, in the form of organic compounds, are indicated in the FTIR spectrum by the following peaks.

At 3465 cm^{-1}, we get a broad peak (indicated by a blue arrow) which is due to the O – H stretching. The band located at 2350 cm^{-1} corresponds to atmospheric CO_2 (green arrow). CH_2 – CO bending results in bands at 1400 and 1640 cm^{-1} (pink arrows). The C – O – C asymmetric stretching shows a small peak around 1050 cm^1 (red arrow). The band at 855 cm^{-1} (orange arrow) corresponds to CH_2 – CHO bond.

As the sintering temperature is increased, we first see a splitting and an initial increase in the intensity of the peaks. However, above 500^0C the intensity of the peaks start decreasing, until they finally disappear at 650^0C. In the sample annealed at 650^0C, only peaks corresponding to the Mn – O bond remain, indicating that oxidation and phase formation is complete by this temperature. This is in agreement with the XRD and thermal analysis results also (shown later).

Thus, the FTIR data show that for the manganite samples, phase formation starts at a very low temperature (350^0C) and gets completed by 650^0C.

This fact is borne out by the X-Ray Diffraction spectra also. In Fig.2.7, we show the X-Ray Diffraction spectra of the $La_{0.67}Ca_{0.33}MnO_3$ precursor powders calcined at various temperatures. At the lower most temperature of 200^0C, the sample is totally amorphous with no XRD peaks. At higher temperatures (350^0C to 450^0C) we get a broad peak at around 29.4^0 (shown by an asterisk). This peak probably corresponds to the impurity phase $CaCO_3$. From 500^0C, peaks corresponding to the perovskite phase start appearing. The impurity peak of $CaCO_3$ is still present, though much diminished in intensity. At a higher temperature (650^0C), the peaks corresponding to the impurity phases disappear completely, and we get phase pure $La_{0.67}Ca_{0.33}MnO_3$.
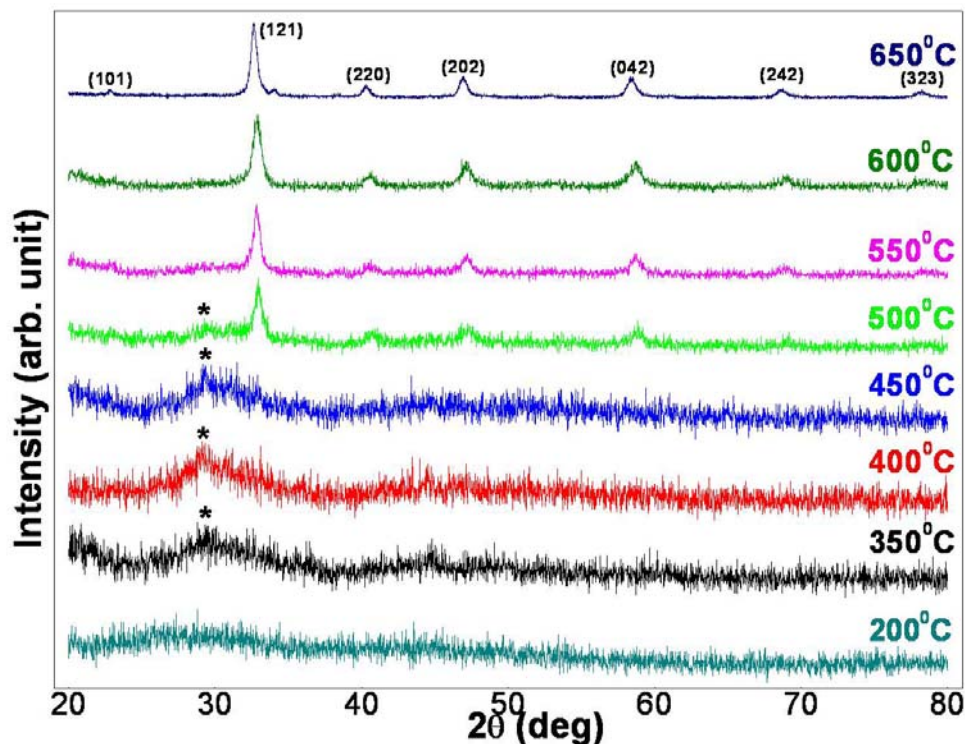
Fig.2.7. XRD data of $La_{0.67}Ca_{0.33}MnO_3$ powder samples heated to different temperatures.

We show the results of the thermal analysis (both thermogravimetric as well as differential thermal analysis) in Fig.2.8. These measurements were done in air atmosphere with a heating rate of 10^0C/min. The TG curve shows a large fall just above 100^0C accompanied by an endothermic peak in the DTA (marked by a blue arrow). This is followed by a smaller weight loss till about 650^0C to 700^0C. The major weight loss above 100^0C is due to the elimination of trapped water. The DTA plot shows an exotherm at around 290^0C (marked by a pink arrow) and a broad exotherm starting at around 330^0C with a peak at 556^0 (marked by a green arrow). The exotherm at 290^0C is due to the decomposition of the resin with the elimination of gases. The

broad exotherm indicates the slow oxidation of the complex with the peak at 556^0C indicating the completion of the reaction. Thus, the thermal analysis also corroborates our earlier conclusion that the manganite phase formation starts at around 350^0C and is completed at 600^0C – 650^0C. Note the small peak (marked by an orange arrow) in the DTA curve at ~ 800^0C. This peak probably corresponds to the orthorhombic to rhombohedral structural transition in LCMO. However, in absence of high temperature structural data, it was not possible to confirm this.
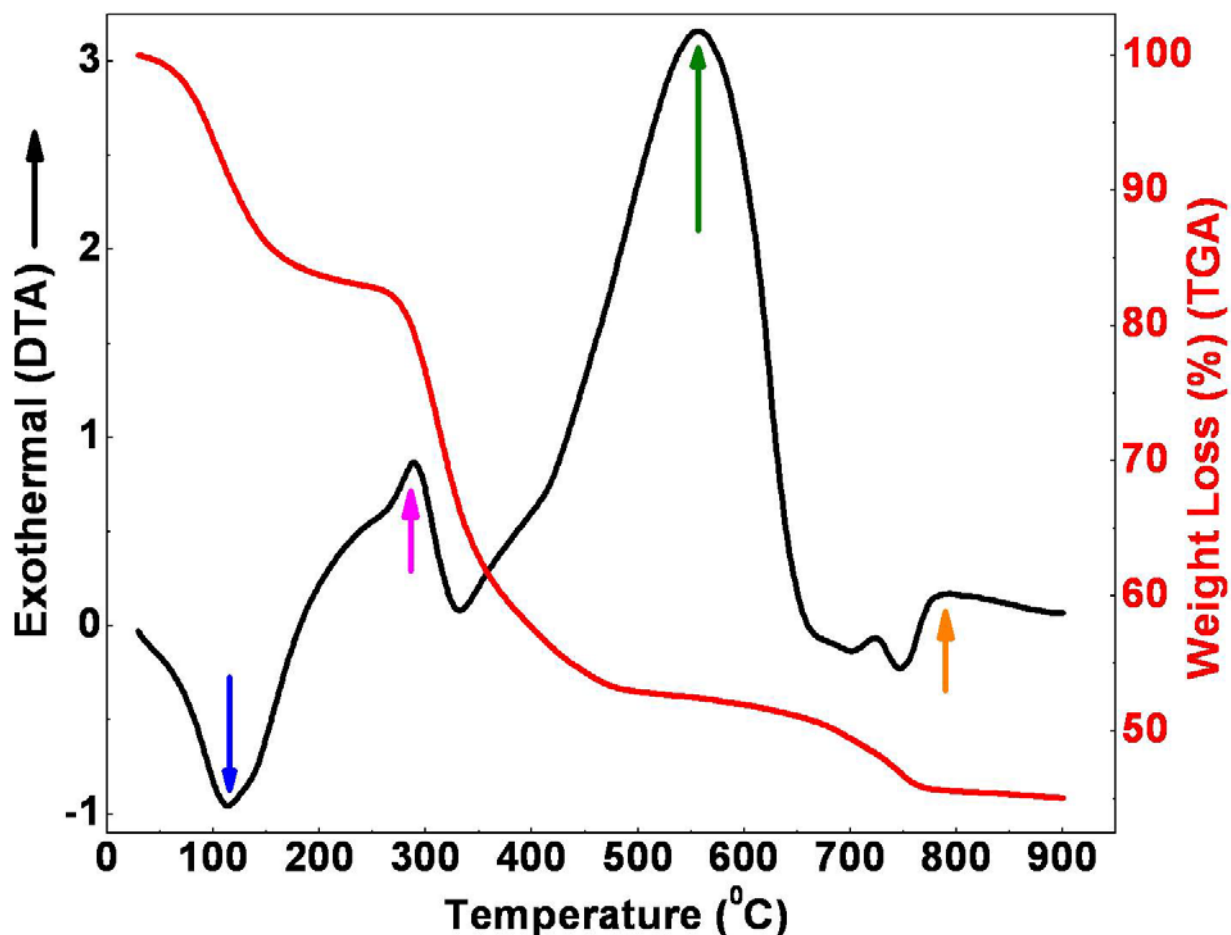
Fig.2.8. TGA/DTA curves of LCMO sol.

Note: It was later observed that in the case of $La_{0.5}Ca_{0.5}MnO_3$ samples, very small amounts of Mn_3O_4 phase remains even after annealing the sample at 650^0C. The decomposition temperature of Mn_3O_4 is 1590^0C and annealing at any temperature lower than 1590^0C is insufficient to get rid of this impurity phase. For most experiments (magnetic and electrical transport measurements etc.), the presence of this impurity phase turns out to be inconsequential because it is present in extremely small quantities and its presence mostly goes undetected. For high resolution x – ray diffraction measurements, the Mn_3O_4 gave rise to some small impurity peaks which could not be indexed using the space group *Pnma* during the refinement process (details of the Rietveld refinement technique given later in the chapter). Nevertheless, the problem could be overcome by a two – phase refinement where the second phase corresponded

41

to Mn_3O_4. The problem arose while doing neutron diffraction experiments. Mn_3O_4 is known to be ferromagnetic with a Curie temperature ~ 42 K[13]. This extra magnetic phase made magnetic refinements at low temperature virtually impossible. This problem was overcome by annealing the samples at 1600^0C and subsequently subjecting them to ball milling so as to prepare the nanopowders. This can be seen in Fig.2.9 where we show the XRD data of two $La_{0.5}Ca_{0.5}MnO_3$ samples, one annealed at 1300^0C (Fig.2.9(a)), and the other at 1600^0C (Fig.2.9(b)). LCMO-1300 (upper panel) shows the presence of Mn_3O_4 phase. (The 100% peak of Mn_3O_4 has been marked by a red asterisk, and also shown in the inset in the upper panel). Fig.2.9 (b) and the inset in the lower panel shows that Mn_3O_4 is not present in the sample annealed at 1600^0C. The bulk samples (samples annealed at 1600^0C) when ball milled for 60 hrs brought down the particle size to ~ 15 nm. The milling was carried out in agate bowls of diameter 6 inches with agate balls of diameter 10 mm. The ball to sample mass ratio was maintained at 8:1 and the optimum milling speed was chosen to be 80 rpm. The milled powder was then used to prepare batches of samples of larger particle size via the process described later in Section 2.4.
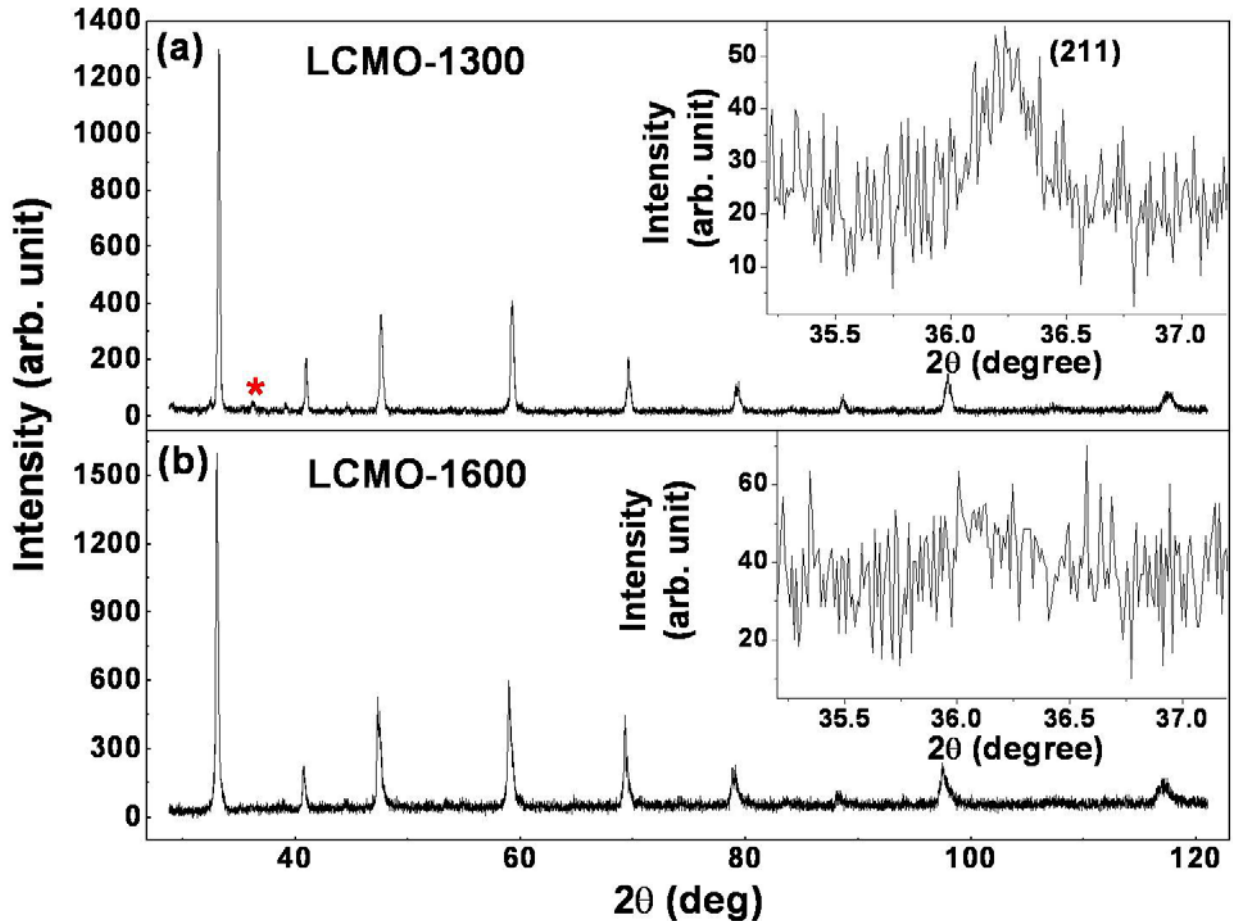
Fig.2.9. XRD data of $La_{0.5}Ca_{0.5}MnO_3$ annealed at (a) 1300^0C and (b) 1600^0C. The insets show the expanded region between $2\theta = 32.5^0$ to 37.5^0.

2.3.2. La$_{0.5}$Sr$_{0.5}$CoO$_3$

In Fig. 2.10 and 2.11, we show the FTIR spectra and XRD data of La$_{0.5}$Sr$_{0.5}$CoO$_3$ precursor powders calcined at various temperatures with an interval of 50^{0}C, and in Fig. 2.12, we show the TGA/DTA curves of LSCO sol. The LSCO sol was prepared using Lanthanum Acetate, Strontium Acetate and Cobalt Acetate as precursors. In the lower most panel of Fig. 2.10 (FTIR spectrum of the sample annealed at 350^{0}C), we show the various organic impurities present by colored arrows (color code is same as that used for the manganite case). As in the manganite case, the cobaltate sample also shows the presence of Co – O bond (shown by black arrows at 580 and 670 cm^{-1}) in the sample annealed at as low a temperature as 350^{0}C. However, there is a strong presence of the organic impurities, and these persist till ~ 500^{0}C. Above 500^{0}C, the intensity of the absorption peaks due to the organic elements present decrease, but they disappear completely only for the sample which is annealed at a temperature of 800^{0}C. In the latter sample, only the Co – O bonds are present (indicated by black arrows).
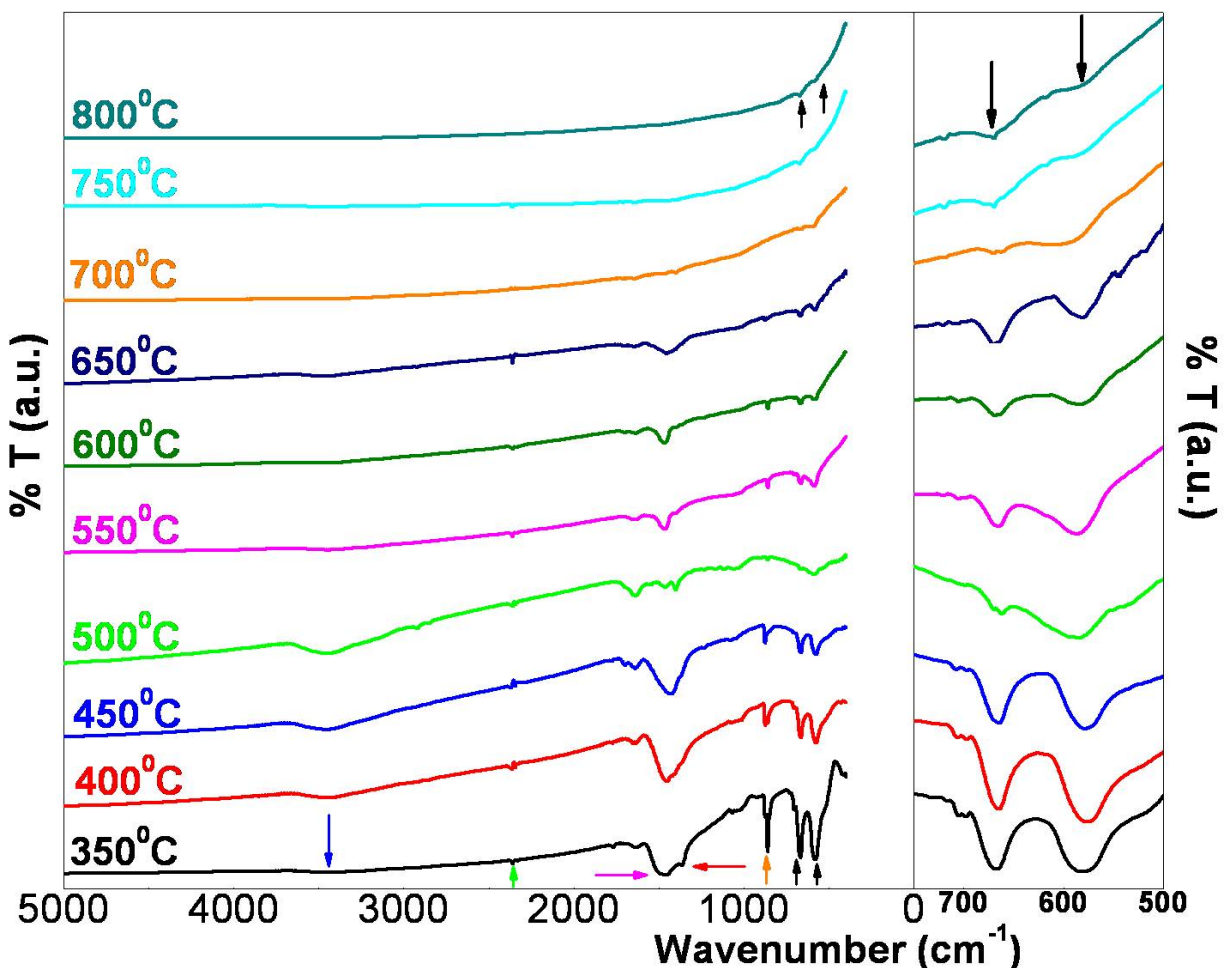
Fig.2.10. FTIR spectra recorded on La$_{0.5}$Sr$_{0.5}$CoO$_3$ powder samples heated to different temperatures.

The XRD data (Fig. 2.11) again confirms the conclusions we draw from the FTIR spectra. The sample annealed at 200^0C is totally amorphous. Between 350^0C and 550^0C, we see some peaks which correspond mostly to the organic impurity phases present. From 600^0C, the perovskite phase of $La_{0.5}Sr_{0.5}CoO_3$ starts appearing, but the phase formation is complete only at 800^0C.
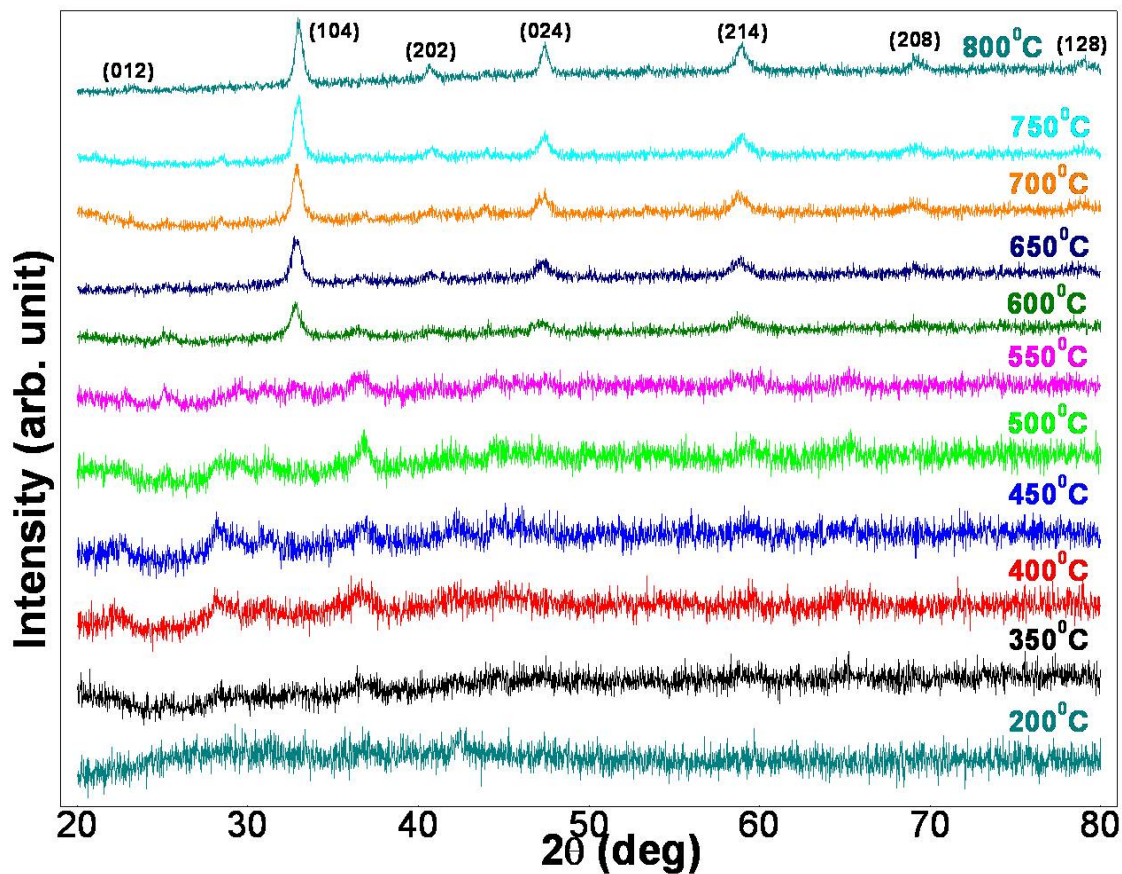
Fig.2.11. XRD data of $La_{0.5}Sr_{0.5}CoO_3$ powder samples heated to different temperatures.

In Fig. 2.12, we show the results of the thermal analysis of the LSCO sol. The thermogravimetric analysis (TGA) curve shows a weight loss, in multiple steps, upto around 800^0C. The differential thermal analysis (DTA) curve shows three major exothermic peaks. The first peak at around 285^0C (shown by a pink arrow) indicates the temperature at which the resin decomposes with the elimination of gases. The second peak at 465^0C (shown by a green arrow) is an indication of the oxidation process leading to the formation of the cobaltate. However, the presence of a third exothermic peak (shown by a blue arrow) indicates that the reaction is not complete at the second peak. The third peak at 720^0C indicates the completion of the reaction and formation of pure $La_{0.5}Sr_{0.5}CoO_3$.
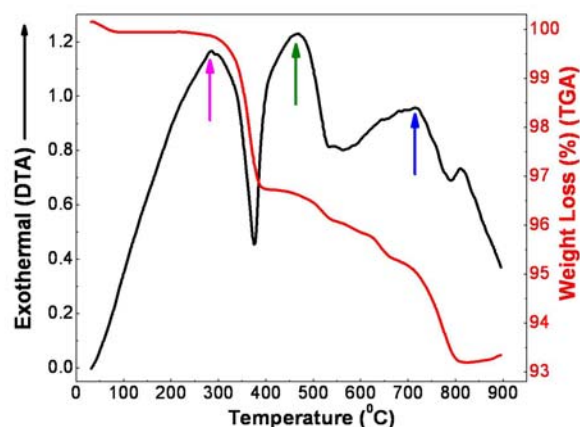
Fig.2.12. TGA/DTA curves of LSCO sol.

2.3.3. LaNiO₃

In Fig. 2.13 and 2.14, we show the FTIR spectra and XRD data of $LaNiO_3$ precursor powders calcined at various temperatures with an interval of 50^0C, and in Fig. 2.15, we show the TGA/DTA curves of LNO sol. The LNO sol was prepared using the Lanthanum Nitrate and Nickel Acetate as precursors. The various absorption peaks in the FTIR spectra due to the organic elements present as well as the Ni – O bond are shown in Fig.2.13 itself. As is clear from the FTIR spectra, phase pure $LaNiO_3$ forms at a temperature as low as 500^0C. The FTIR spectrum of the sample annealed at 500^0C (green curve) does not show any absorption peak other than those due to Ni – O bond and atmospheric CO_2.
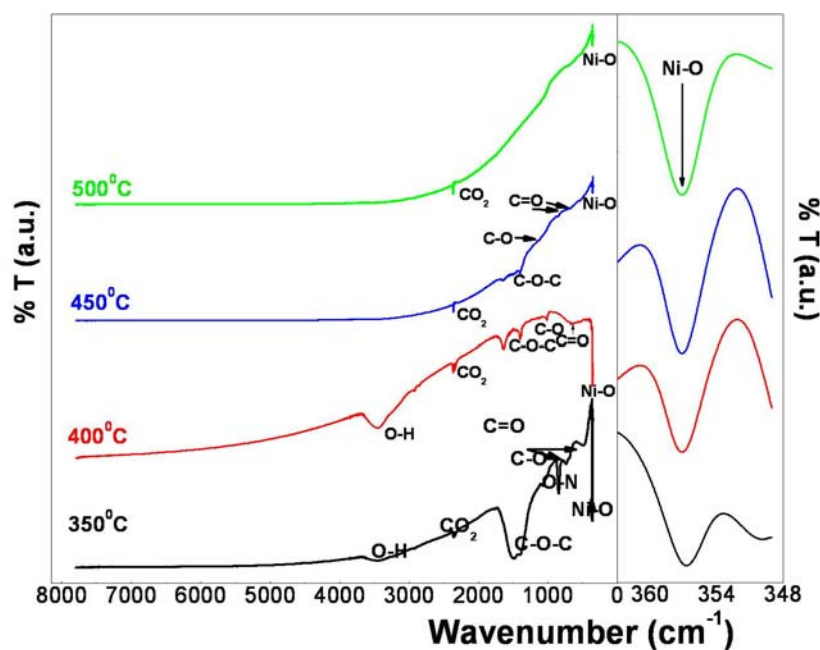
Fig.2.13. FTIR spectra recorded on $LaNiO_3$ powder samples heated to different temperatures.

45

This fact is borne out by the XRD data also (Fig.2.14). The sample annealed at 200^0C is totally amorphous. Perovskite phase formation starts at 450^0C and is complete within 500^0C. The XRD data of the sample annealed at 500^0C does not show the presence of any impurity phase.
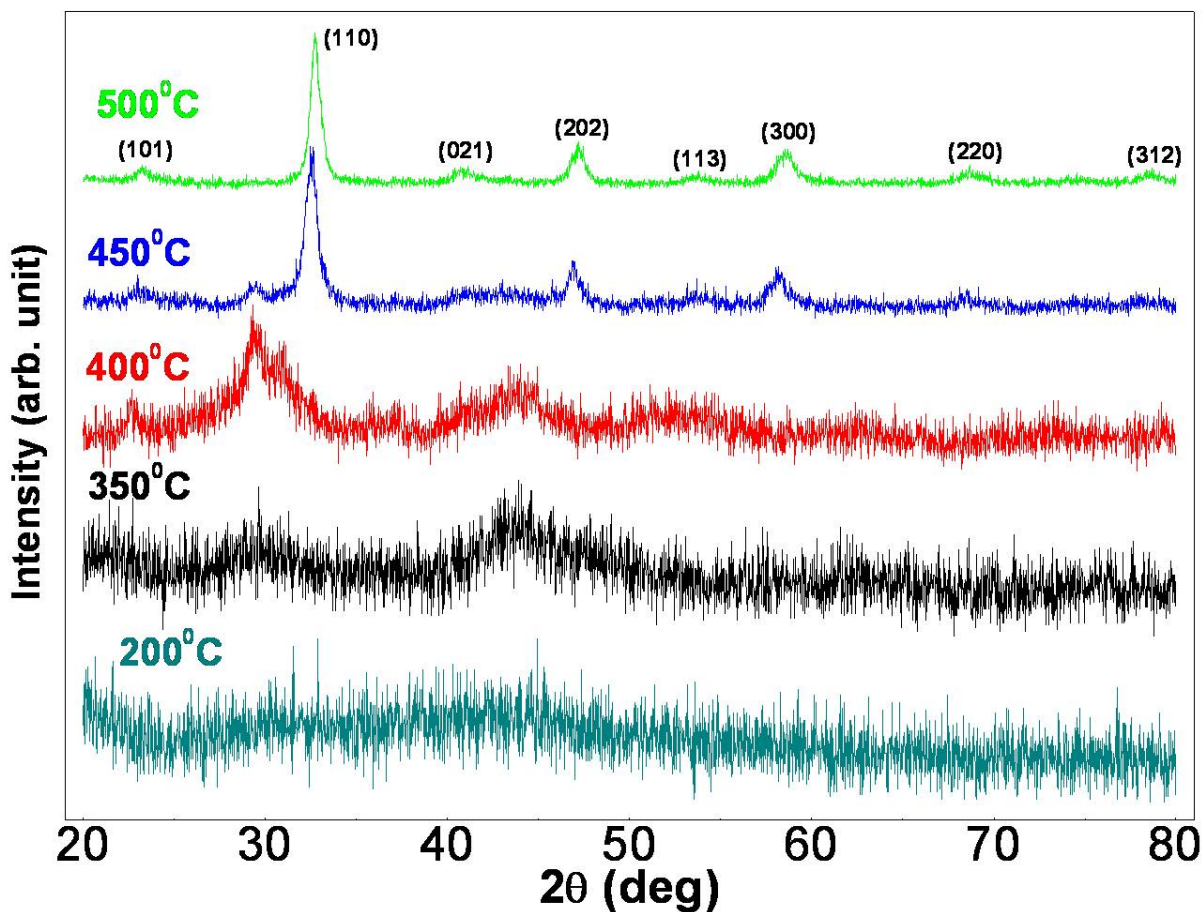
Fig.2.14. XRD data of LaNiO$_3$ powder samples heated to different temperatures.

The results of the thermal analysis on the LNO sol (Fig.2.15) are very similar to that on the LCMO sol (Fig.2.8) with the difference that in the former the major exothermic peak (shown by a green arrow) occurs at ~ 500^0C whereas in the case of LCMO it occurred at a higher temperature. Thus, the reaction for the LaNiO$_3$ phase formation gets completed at a lower temperature, and one gets pure LaNiO$_3$ at 500^0C. We may note here that this is, perhaps, the lowest reported temperature for the phase formation of any perovskite oxide.
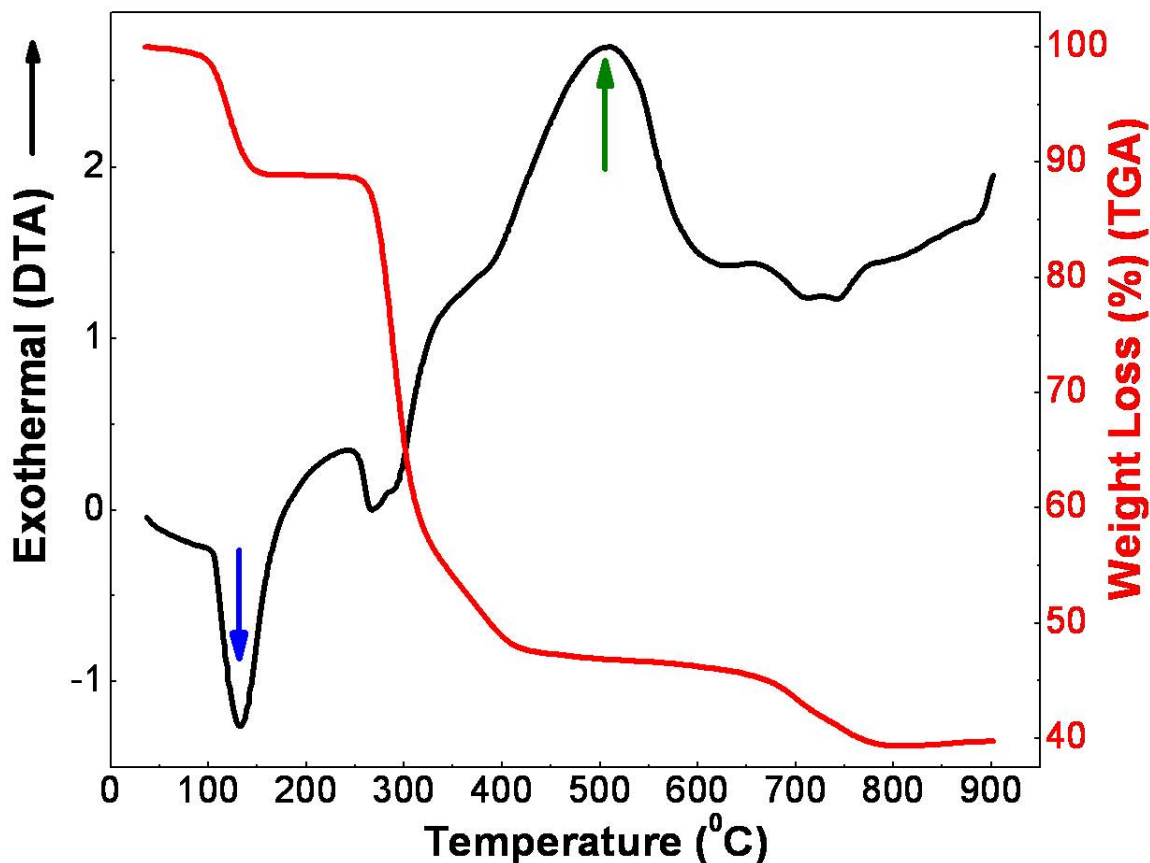
Fig.2.15. TGA/DTA curves of LNO sol.

2.4 Preparation of samples with larger particle size – process of grain growth

For most of our studies (detailed in later chapters), our main motivation was to study the tuning of properties of the oxides by tuning the size of the particles. For this we needed to prepare whole batches of samples having the same stoichiometry, but different particle sizes. The nanocrystals prepared in the technique described in earlier sections were used for making samples of larger particle size by heat treatment. The as prepared powder was pelletized and the pellets were sintered at different temperatures and for varying time periods. The sintering at different temperatures leads to particle growths to different sizes making it possible to grow grain sizes as large as 3 μm or more. (For carrying out subsequent experiments which required the samples in powder form, the pellets were crushed in a mortar pestle and the pulverized powder was annealed at 600^0C for 8 hrs to get rid of any strain effects incorporated during the grinding process).

The process of sintering involves heating the compressed powder (the green powder) to a suitable temperature below its melting point but high enough to allow bonding or fusion of the

individual paricles. The sintering process mainly occurs through atomic diffusion in the solid state. It can be described as a three stage process:

1. *Initial stage*: This stage involves the rearrangement of particles to increase points of contact and neck formation (bonding at points with highest surface energy). At this stage, the pores are interconnected and the pore shapes are irregular.
2. *Intermediate stage*: This stage is characterized by rapid neck growth and volume shrinkage, grain growth and lengthening of the grain boundaries. The pore channels first become cylindrical in nature, and eventually they become spherical and rounded. This stage ends when the pore system inside the material becomes discontinuous.
3. *Final stage*: This stage is characterized by further grain growth, the pores are isolated and grain boundary pores are eliminated.

The three stages are shown schematically in Fig.2.16.
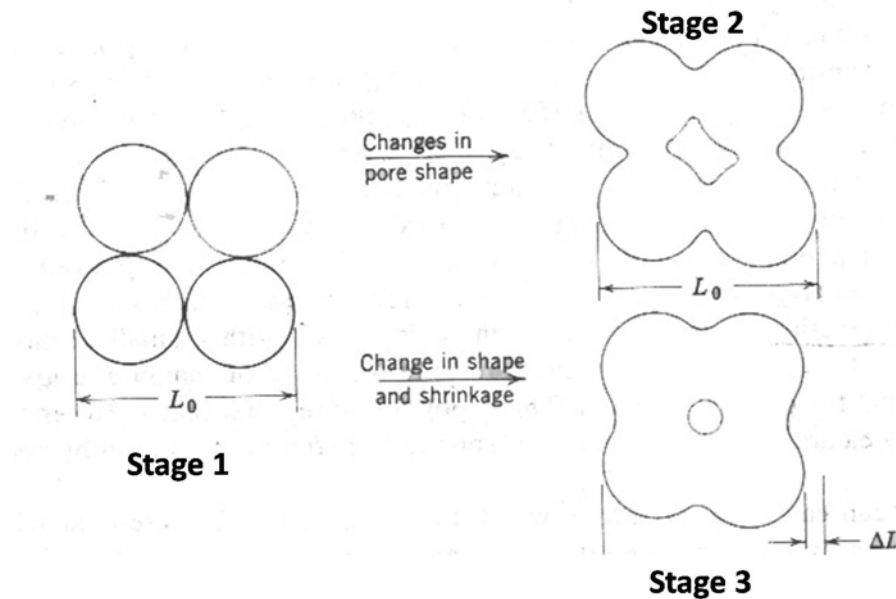
Fig.2.16. Schematic representation of the stages during the process of grain growth (reproduced from [14]).

The driving force for solid state sintering is the difference in surface energy between the free surfaces of particles and the points of contact between adjacent particles. The surface energy can be reduced by transporting material from different areas so as to eliminate the pores. It occurs at high temperatures where material transport due to diffusion is appreciable. (Surface diffusion is not sufficient, bulk diffusion is required). The rate of grain growth is inversely proportional to the particle diameter ($dr/dt = 1/r^n$, $n \approx 1$). Hence, smaller particles grow faster. This is because nanomaterials have a higher surface – to – volume ratio, and since surface energy is proportional to the surface area, nanomaterials have a correspondingly higher total surface energy. Thus, the driving force (which tends to minimize the surface energy) is greater for nanoparticles.

Additionally, the sintering process depends on factors such as particle shape, particle size distribution and packing. Poor packing makes porosity difficult to eliminate and irregular shaped particles can result in large irregular pores which are again difficult to eliminate. A mix of

particle sizes can improve compacting as particles of different sizes can be pressed together leaving fewer voids. A distribution in the particle size, thus, improves the packing efficiency. Excessively rapid grain growth must be avoided because it often leads to entrapment of pores, which is undesirable.

The variation of the particle size with the annealing temperature for three different oxides is shown in Fig.2.17. The time of annealing was varied from 5 hrs (at the lower most temperatures in a bid to control the particle size) to 30 hrs at 1100^0C. However, it was observed that at higher temperatures the growth process was dependent more on the temperature of annealing and less on the time of annealing. Hence, at the higher most temperature of 1300^0C, an annealing time of 2 hrs was sufficient to grow the particles to around 3 μm. (Increasing the annealing time did not result in further growth of the particles).

Since all the samples are made from the same starting nanocrystals, it is ensured that they have the same chemical stoichiometry. The control of proper stoichiometry among the samples with different sizes was extremely important for us to ensure that any change in physical property arose only because of a reduction in the size.
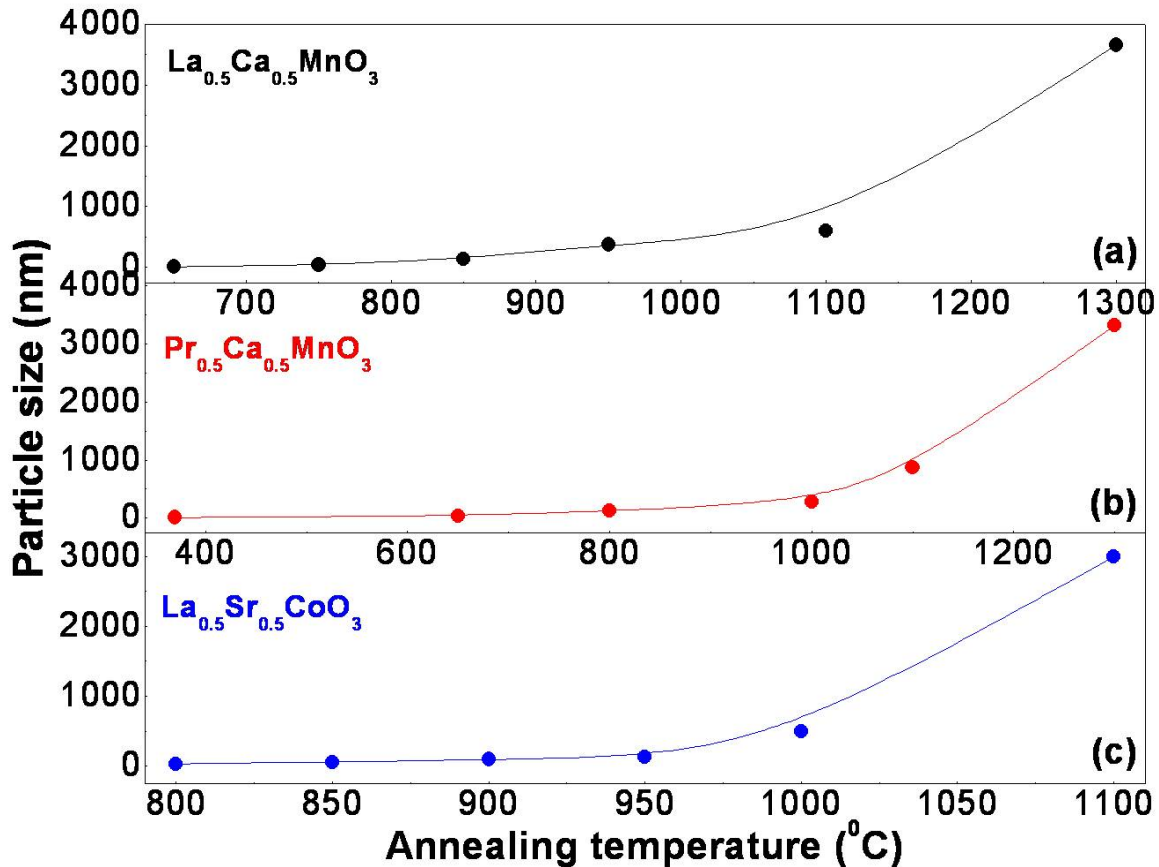
Fig.2.17. Variation of the average particle size with the annealing temperature for
(a) $La_{0.5}Ca_{0/5}MnO_3$, (b) $Pr_{0.5}Ca_{0.5}MnO_3$, (c) $La_{0.5}Sr_{0.5}CoO_3$

2.5 Characterization – Grain size and morphology

The synthesized samples were characterized using powder X-Ray Diffraction and imaging techniques like Transmission Electron Microscopy (TEM) and Scanning Electron Microscopy (SEM). The stoichiometry was also checked using Inductively Coupled Plasma Atomic Emission Spectroscopy (ICPAES) and the oxygen stoichiometry was checked using iodometric titration.

2.5.1. X-Ray Diffraction

All synthesized samples were characterized using powder X-Ray Diffraction (Fig.2.18, Fig.2.19 and Fig.2.20) using CuKα radiation (λ = 1.54 Å) at room temperature to establish the purity of the chemical phases and also to estimate the average particle size of the nanoparticle samples (for the samples having average particle size < 500 nm) using the Williamson Hall plot[15]. The Williamson Hall plot makes use of the broadening (due to finite size as well as strain) in the XRD peaks to estimate the particle size and the strain. Since the peak broadening due to finite size ($\beta_{size} = \lambda/d\cos\theta$, d being the particle size) can be decoupled from the peak broadening due to strain ($\beta_{strain} = 2\varepsilon\tan\theta$, ε being the strain), so the Williamson Hall plot was used to estimate both the particle size as well as the strain in the samples. However, this could be done only for the samples with an average particle size < 500 nm where the peak broadening due to size and strain effects was substantially larger than the peak broadening due to instrumental effects ($\beta_{instrumenal}$). For samples with larger particle size the peaks become narrower, and the broadening due to size and strain effects becomes comparable to $\beta_{instrumenal}$. In those cases, X-Ray Diffraction is not able to give the particle size correctly, and in such cases, we had to resort to imaging tools (like SEM) to get an idea of the average particle size.
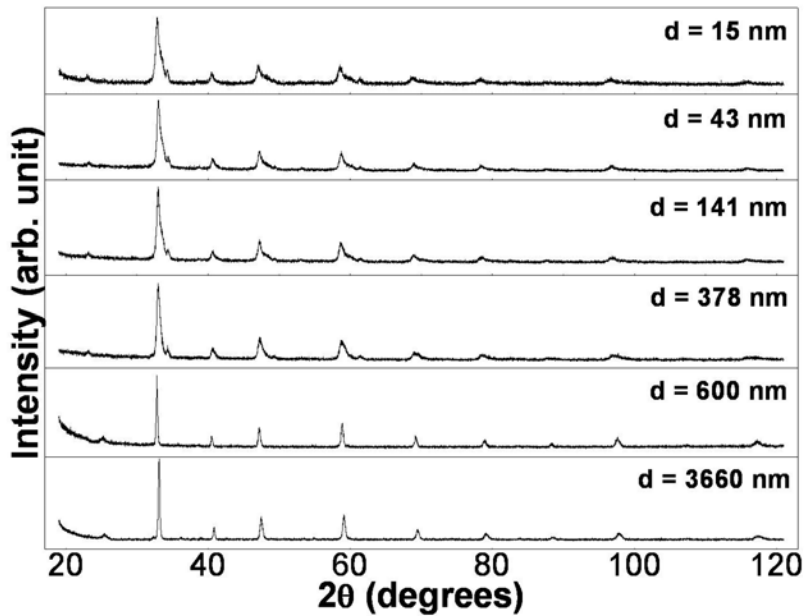
Fig.2.18. XRD patterns for La$_{0.5}$Ca$_{0.5}$MnO$_3$ samples of different particle sizes.
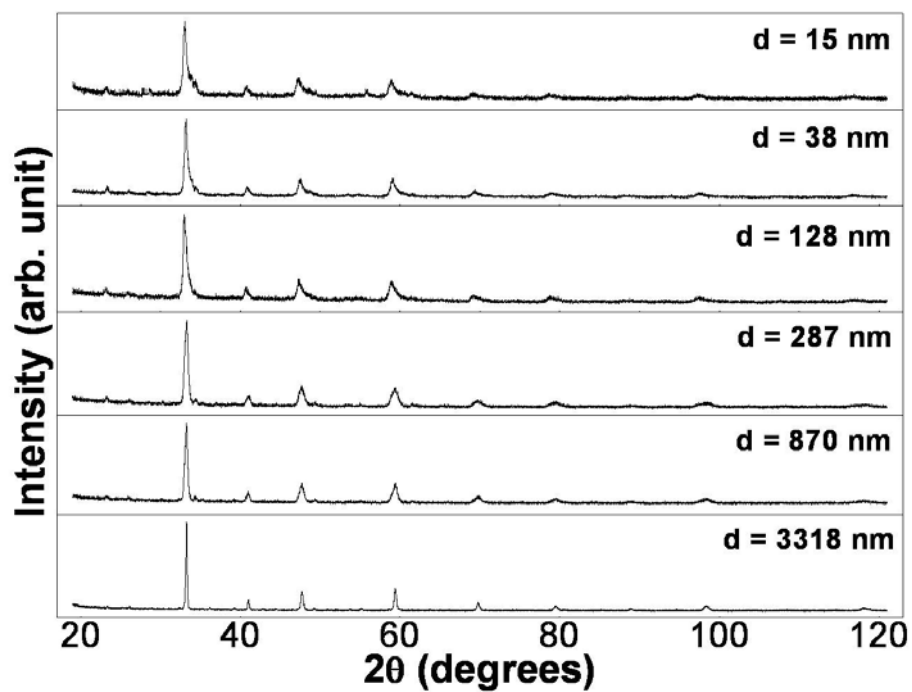
Fig.2.19. XRD patterns for $Pr_{0.5}Ca_{0.5}MnO_3$ samples of different particle sizes.
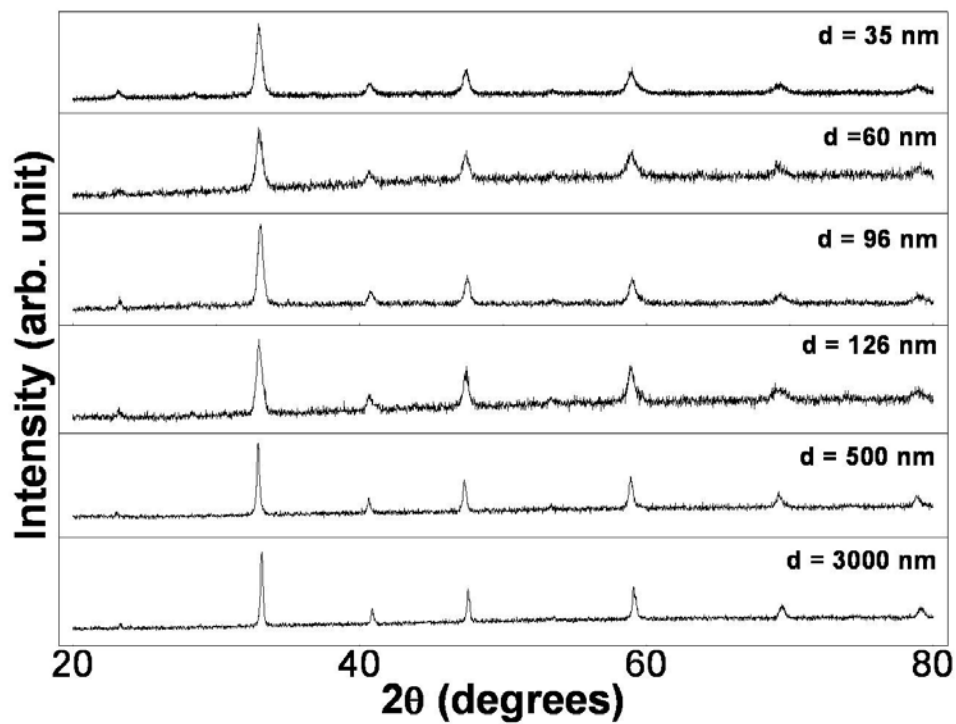
Fig.2.20. XRD patterns for $La_{0.5}Sr_{0.5}CoO_3$ samples of different particle sizes.

51

2.5.2. Transmission Electron Microscopy and Scanning Electron Microscopy

The average particle size of the samples could be extracted from the X – Ray Diffraction patterns (as described above). However, it is also important to have an idea of the distribution in size in these samples. This information could be extracted from imaging techniques (Transmission Electron Microscopy for the smaller size as – prepared nano powders and Scanning Electron Microscopy for the larger bulk samples). The TEM images were taken using JEOL 200 kV[16] and the SEM images were taken using FEI Quanta 200[17].

In Fig.2.21, Fig.2.22 and Fig.2.23, we show the (a) TEM images, (c) High Resolution TEM images and (d) Selected Area Electron Diffraction patterns of $La_{0.5}Ca_{0.5}MnO_3$, $Pr_{0.5}Ca_{0.5}MnO_3$ and $La_{0.5}Sr_{0.5}CoO_3$ nanoparticles respectively. The histograms giving the particle size distribution are also shown in the respective figures. Typically, the distributions show a standard deviation of 25% to 35%. Here, we would like to mention that the distribution of particle size in our samples does not present a very crucial problem as far as our investigation of the physical properties are concerned even though the physical properties are all size dependent. This is because the samples that we have chosen for investigation are far apart in size (much more than the distribution in particle size in the individual samples). For example, the smallest size sample in the case of $La_{0.5}Ca_{0.5}MnO_3$ has an average particle size of 17 nm and a distribution of size from 8 nm to 28 nm. The next sample in the series has an average particle size of 43 nm and a distribution in size from 34 nm to 54 nm. Thus, the particle sizes are well separated. In fact, this separation increases as we move to larger particle sizes thereby eliminating the possibility of the size distribution of one sample overlapping with the next.

The HRTEM images as well as the electron diffraction patterns bring out the single crystalline nature of the particles. Our nanoparticle samples constitute of millions of small particles (of size in the nanometer regime), and each nanometer size particle is a perfect single crystal. The process of indexing the electron diffraction pattern is explained in Section 2.7.3 where we have described the working of the Transmission Electron Microscope.
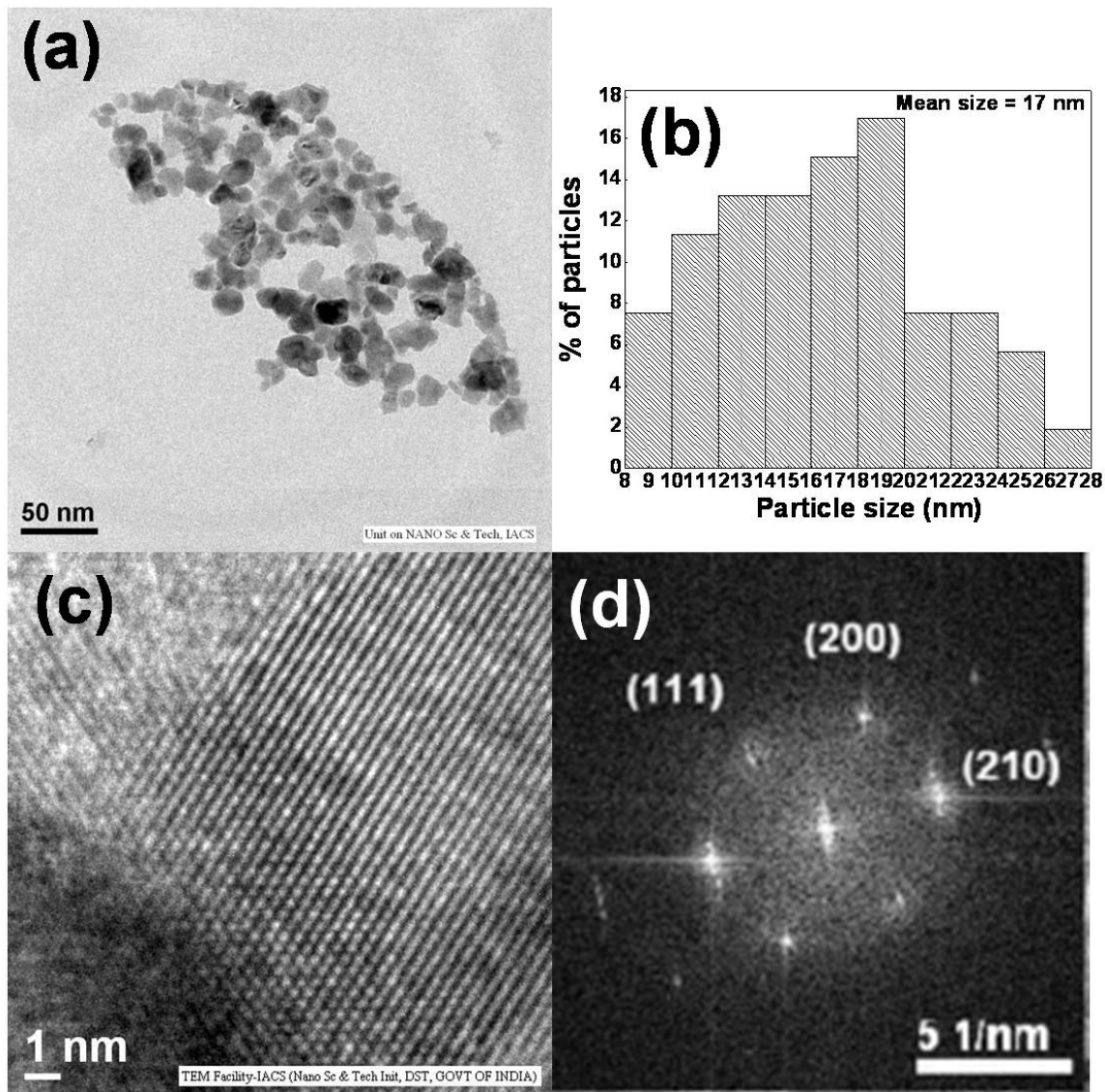
Fig.2.21. (a) TEM image, (b) histogram showing size distribution, (c) HRTEM image (the fringes are along the (111) direction and the lattice spacing is ~ 0.345 nm) and (d) Eletcron diffraction pattern of $La_{0.5}Ca_{0.5}MnO_3$ nanoparticles
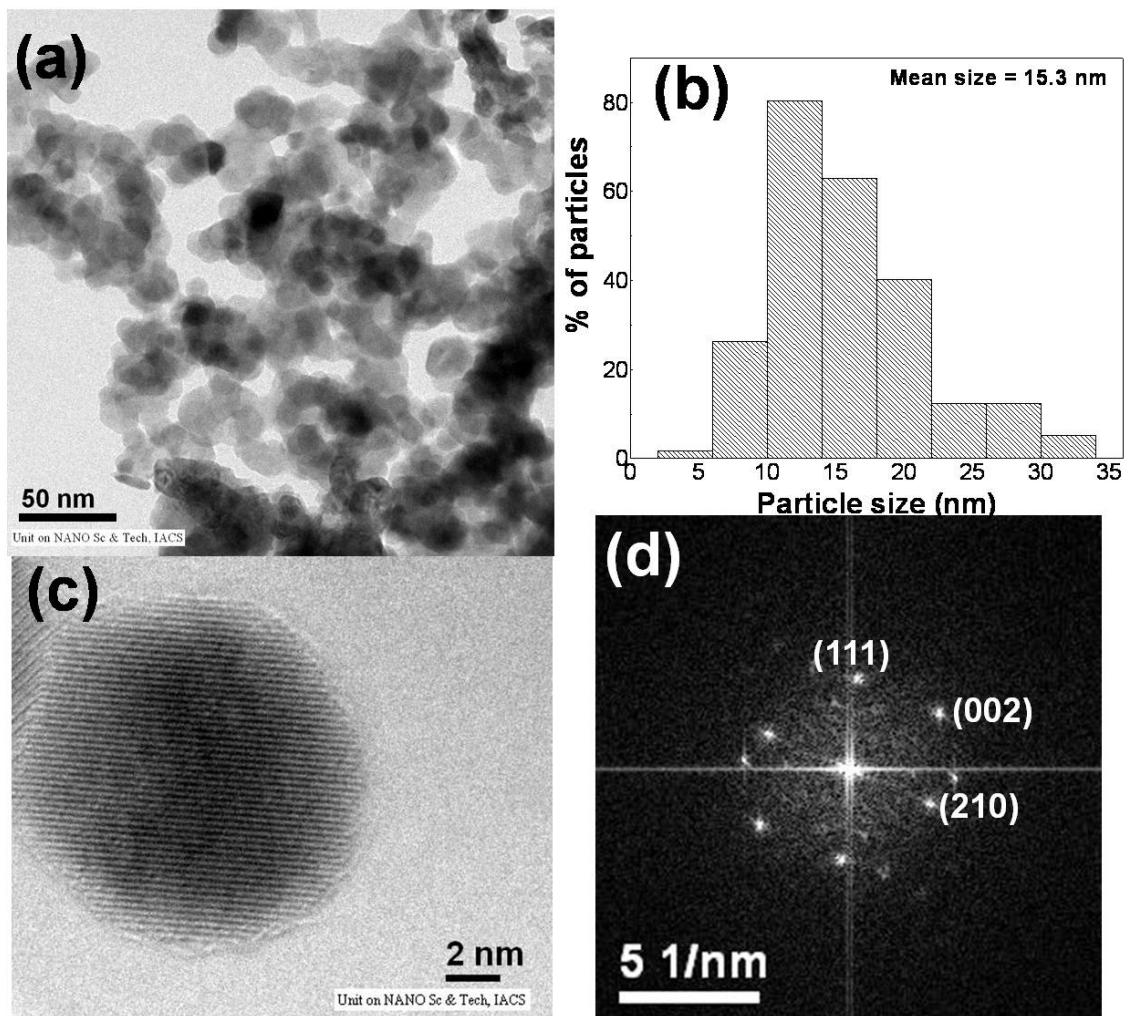
Fig.2.22. (a) TEM image, (b) histogram showing size distribution, (c) HRTEM image (the fringes are along the (210) direction and the lattice spacing is ~ 0.254 nm) and (d) Eletcron diffraction pattern of $Pr_{0.5}Ca_{0.5}MnO_3$ nanoparticles
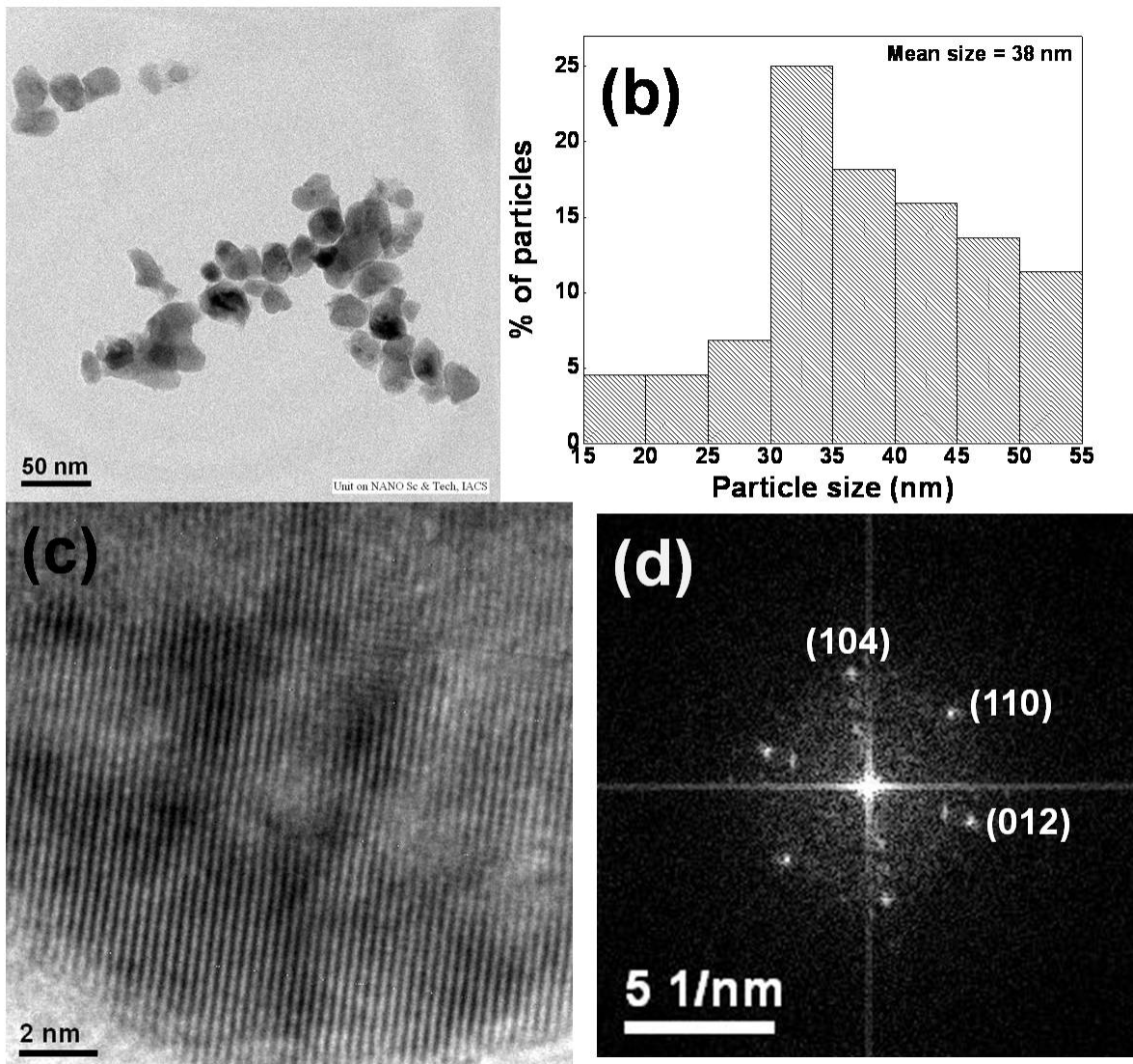
Fig.2.23. (a) TEM image, (b) histogram showing size distribution, (c) HRTEM image (the fringes are along the (104) direction and the lattice spacing is ~ 0.267 nm) and (d) Eletcron diffraction pattern of $La_{0.5}Sr_{0.5}CoO_3$ nanoparticles

For the larger particle size samples, the size distribution was extracted from FEG-SEM images. Representative images for the $La_{0.5}Ca_{0.5}MnO_3$, $Pr_{0.5}Ca_{0.5}MnO_3$ and $La_{0.5}Sr_{0.5}CoO_3$ bulk samples are shown in Fig.2.24 (a), (b) and (c) respectively, alongwith the histograms showing the size distribution (Fig.2.25 (d), (e) and (f)). The distributions are broader in the bulk samples as compared to the nanoparticle samples, with the typical standard deviation in the former varying between 35% to 45%.
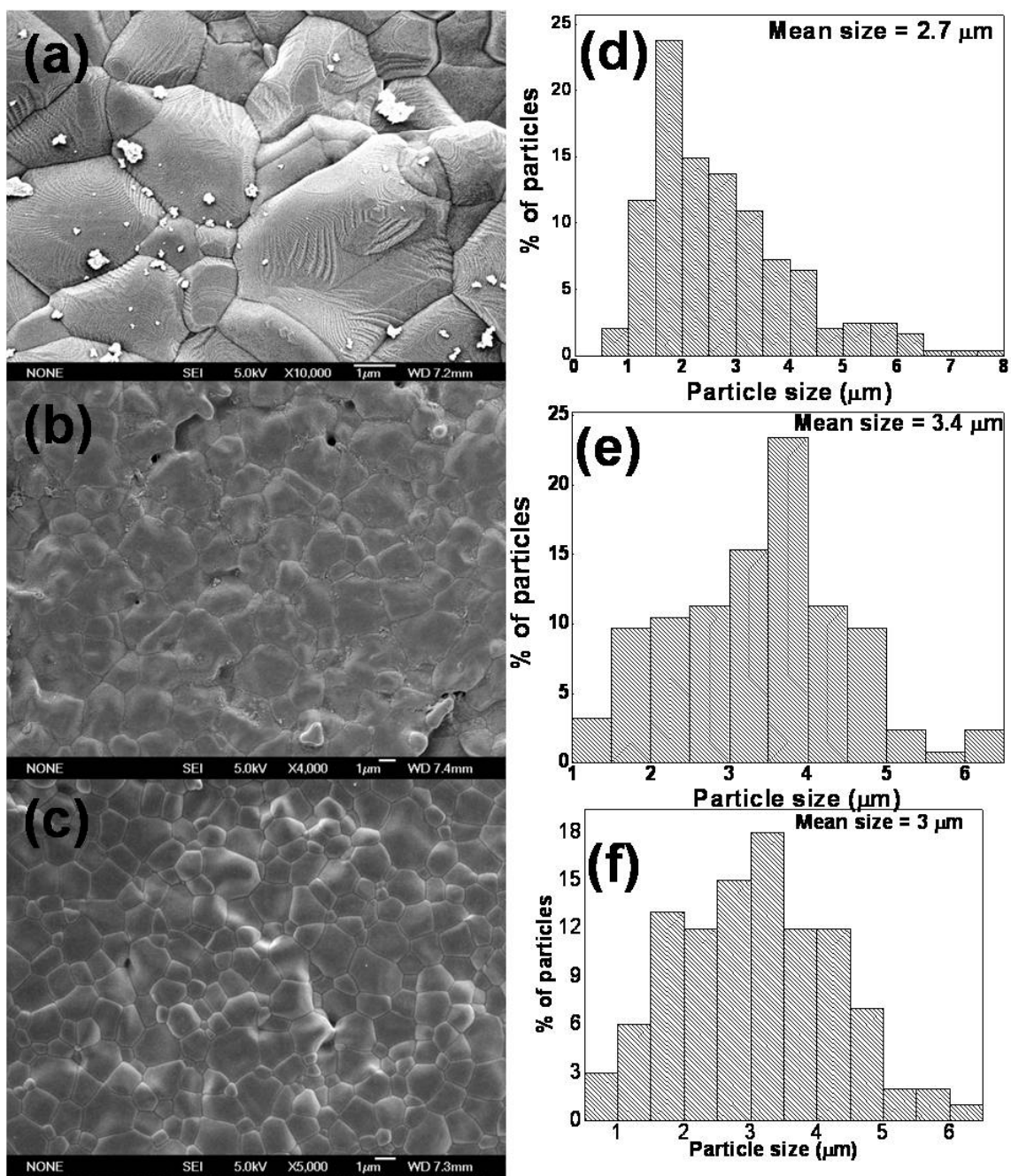
Fig.2.24. FEG-SEM images of (a) $La_{0.5}Ca_{0.5}MnO_3$, (b) $Pr_{0.5}Ca_{0.5}MnO_3$ and (c) $La_{0.5}Sr_{0.5}CoO_3$ bulk samples, and the histograms showing the size distribution in the (d) $La_{0.5}Ca_{0.5}MnO_3$, (e) $Pr_{0.5}Ca_{0.5}MnO_3$ and (f) $La_{0.5}Sr_{0.5}CoO_3$ bulk samples

2.6 Stoichiometry checks

The control of proper stoichiometry (both the cation composition as well as the oxygen stoichiometry) in these complex oxide ($A_{1-x}B_x Mn/CoO_3$) samples was of utmost importance for the kind of studies they were subjected to. The need for such a rigid control of the stoichiometry becomes apparent from a look at the phase diagrams of these oxides (detailed in Section 1.2 of Chapter 1). Some of the phenomena that we study in this thesis (for example, the charge ordering phenomena in $La_{1-x}Ca_x MnO_3$) occur only at specific carrier concentration (in this case, at x = 0.5). In such cases, we have taken special care to ensure that the samples used have proper stoichiometry and hence the proper carrier concentration. The cation concentration was checked using Inductively Coupled Plasma Atomic Emission Spectroscopy (ICPAES) technique. We have checked that our synthesis method maintains a reproducible and good stoichiometry from batch to batch. In addition, we have also checked the stoichiometry on the microstructural level from EDAX measurement done on each sample (in pellet form), at different points using the FEG-SEM.

Oxygen stoichiometry is also an important parameter in the oxides. Variation in the oxygen stoichiometry can have strong effects on the physical properties of these oxides[18 – 20]. We checked the oxygen stoichiometry of the pellets by iodometric titration. All the pellets had some oxygen deficiency ($A_{1-x}B_x Mn/CoO_{3-\varepsilon}$, with ε positive and less than 0.03 for all samples). ε was greater for the bulk samples than the corresponding nanoparticle samples. Thus, the particles with smaller size had better oxygen stoichiometry. The annealing conditions (oxygen flow etc.) were optimized to prepare samples with proper oxygen stoichiometry. For example, the cobaltate and nickelate samples required a higher rate of oxygen flow during annealing than the manganite samples.

Thus, the cation composition and the oxygen stoichiometry of the bulk and the nanosized crystal were determined to be almost the same within the experimental accuracy. The nanometer sized crystals are characterized by better chemical and crystalline homogeneity which arises mainly from reduced crystallite size.

2.7 Experimental techniques

In the following sections, we briefly introduce some of the major experimental techniques that have been utilized during the course of this thesis work.

2.7.1 X – Ray Diffraction

2.7.1.1 Principle

Interaction between matter and x – rays with suitable wavelengths results in inelastic and elastic scattering of the radiation. It is the elastic scattering from the electrons inside the matter which leads to the observed diffraction of the incident x – ray beam by the sample. By recording and analyzing the diffraction pattern, information on the crystal structure of the material is obtained. Although the scattering takes place from individual atoms, the observed patterns can also be explained by assuming that planes of atoms are sources for the scattered radiation wave. This picture leads to Bragg's law, which states that large diffracted intensity takes place only

when the phases of the scattered waves differ by an integral multiple number of wavelengths ($n\lambda$). When this is the case, the waves sum up leading to constructive interference and a peak is seen in the diffraction pattern. Otherwise, the waves cancel each other causing destructive interference and a lower intensity is observed. Bragg's law is illustrated in Fig.2.25, where n = 1,2,3,.....; λ = wavelength, d_{hkl} = distance between adjacent planes of atom indexed as hkl. The condition $n\lambda = 2d_{hkl}\sin\theta$, derived from simple geometry (as can be seen from the figure), has to be valid for the waves 1 and 2 to interfere constructively.
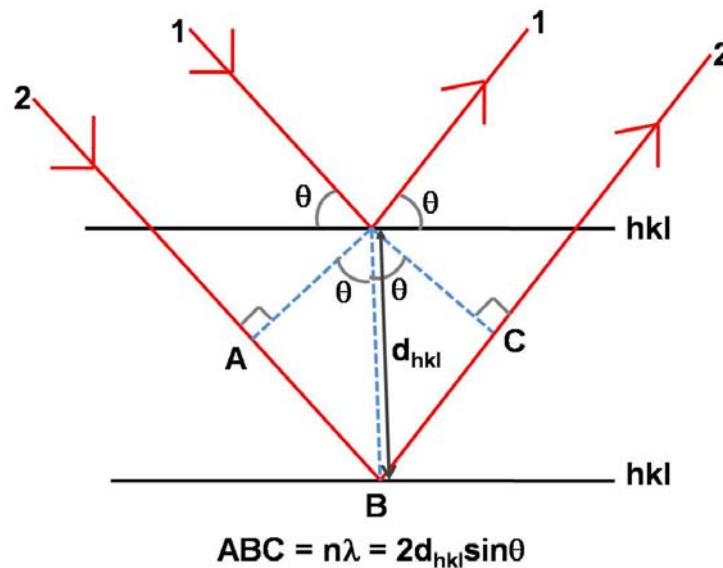
Fig.2.25. Bragg's law.

2.7.1.2 Laboratory based x – ray sources

Powder diffraction using laboratory based x – ray source was used majorly for phase identification and purity checks. The X-Ray diffraction measurements were done with X'Pert PRO Diffractometer[11]. This diffractometer works in the Bragg – Brentano geometry with a $\theta{:}\theta$ arrangement i.e. the sample remains fixed while the tube rotates at a rate of $-\theta^0$/min and the detector rotates at a rate of $+\theta^0$/min. A schematic representation is shown in Fig.2.26.
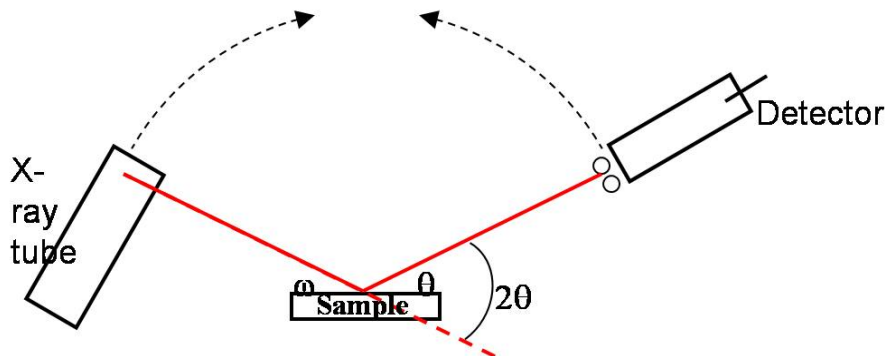
Fig.2.26. Schematic representation of the Bragg – Brentano geometry.

The x – ray tube (PW3373/10 Cu LFF DK 184115) used is a ceramic tube with a maximum tube power of 1.8 kW. The x – ray radiation is generated in the tube which consists of a source of electrons and a metallic anode (made of Cu) kept under high vacuum. The source of electrons is a filament of tungsten heated by an electric current, which expels electrons by the thermionic effect. A high voltage of 45 kV is applied between the source of electrons (cathode) and the metallic anode which accelerates the electrons. The radiation produced has a discrete number of wavelengths and a broad background. For conventional purposes, we have used Cu Kα radiation (λ = 1.5418 Å). LFF stands for Long Fine Focus and has a focusing dimension of 12 mm X 0.4 mm. This focusing dimension gives optimum resolution combined with high intensity and is useful for phase analysis.

The detector used is a gas proportional detector (PW3011/20). It has a typical energy resolution (for Cu Kα radiation) of 20%. (The energy resolution of a detector is a measure of its ability to resolve two X – ray photons of different energy). The resolution of this instrument in terms of scanning angle is 0.001^0. The incident and diffracted beam optics are tabulated in Table 2.2.

Table 2.2 Incident and diffracted beam optics used during laboratory XRD measurements

Beam optics components	Incident beam path	Diffracted beam path
Divergence slit	Fixed (1^0)	None
Receiving slit	None	Fixed (Height = 0.50 mm)
Soller slit	0.04 rad	0.04 rad
Anti – scatter slit	None	Programmable
Filter	None	Nickel (thickness = 15 μm)
Monochromator	None	None
Mask	Fixed (10 mm)	None

Before ending this section dealing with the laboratory based x – ray sources, we briefly describe the functions of the various beam optics components below:

Divergence slit: They control the divergence of the incident beam emitted from the line focus of the x – ray tube. The divergence slit defines the length of the sample that is irradiated by the incident x – ray beam.
Receiving slit: They are fitted at the focal point of the diffracted beam path to control the 2θ resolution. A narrow slit improves the resolution at the expense of the measured x – ray beam intensity.
Soller slit: They limit the axial divergence of the x – ray beam. The use of Soller slits improves the peak shape and the resolution of the analysis.
Anti – scatter slit: They can be fitted either in the incident or diffracted beam path to reduce the air scatter, and thus, the background radiation. When placed in the diffracted beam path, it also helps to form a beam tunnel in combination with the receiving slit.
Filter: The beam from an x – ray tube contains not only the complete K and L spectrum, but also a continuous spectrum over a wide band of wavelengths. However, most experiments require monochromatic x – ray radiation. Using a filter that exhibits an absorption edge between the K_α and K_β lines of an anode material reduces the intensity of both lines drastically. By inserting a β

– filter with an appropriate thickness into the x – ray beam, the K_β line (and all other undesired parts of the x – ray spectrum) almost disappears, leaving only the K_α line. β – filters can be placed in either the incident or diffracted beam path. However, placing them in the diffracted beam path has certain advantages. For example, if the atoms in a sample are excited by the incident radiation, and in turn give fluorescence radiation from the sample, the background radiation will increase considerably. Placing a β – filter between the sample and the detector serves to reduce this background considerably. The Nickel filter that has been used for this work reduced the K_β intensity by 98% and the K_α intensity by 48%.

Mask: They are used to limit the width of the x – ray beam.

2.7.1.3 Synchrotron sources for x – ray diffraction

The generation of x – rays in a synchrotron radiation source uses the principle that charged particles moving under the influence of an accelerating field emit electromagnetic radiation. These charged particles are ultrarelativistic i.e. they move with a speed close to the speed of light. This is realized in a synchrotron radiation facility where the charged particles (electrons) are accelerated by a synchrotron, and then injected into a storage ring (an ultrahigh vacuum ring on a closed loop), in which they circulate a vast number of times producing synchrotron radiation, but without gaining further energy. The radiation is projected at a tangent to the electron storage ring and captured by beamlines. The beamlines may originate at *bending magnets*, which mark the corners of the storage ring and introduce single bends in the particle trajectory to pull them out of the trajectory, or *insertion devices*, which are located in the straight sections of the storage ring and consist of an array of magnets. These periodic magnetic structures (composed of many magnets that have a repeating row of N and S poles) force the electrons into a sinusoidal or helical path. Thus, instead of a single bend (as in the case of a bending magnet), many tens or hundreds of wiggles at precisely calculated positions add up the total intensity that is seen at the end of the straight section. An insertion device thus effectively consists of a series of bending magnets. At the end of the beamline is the experimental end station, where samples are placed in the line of the radiation, and detectors are positioned to measure the resulting diffracted radiation.

In a synchrotron, the electrons are accelerated to high speeds in several stages to achieve a final energy that is typically in the GeV range. For example, the European Synchrotron Radiation Facility (E.S.R.F.) situated at Grenoble, France (which we have used for the structural studies of some of our samples) works at a power of 6 GeV and its storage ring has a diameter of 844 m. All the synchrotron measurements reported in this thesis were done using the BM-01B beamline at E.S.R.F. (BM stands for Bending Magnet). The BM-01B is a specialized high resolution powder diffraction beamline with an available wavelength range of 0.37 Å to 1.2 Å. The diffractometer is equipped with 6 counting chains so that 6 complete patterns are collected simultaneously with an offset in 2θ. Low temperature measurements down to 5 K can be performed with the sample in He atmosphere.

Synchrotron sources have a number of advantages over conventional laboratory based x – ray sources:

1. Synchrotron radiation is characterized by high brightness and high intensity, many orders of magnitude more than that of the x – rays produced in conventional x – ray tubes. As an

example of this, in Fig.2.27 we show the x – ray patterns of the same sample taken using (a) laboratory based x – ray source and (b) synchrotron x – ray source. The signal to noise ratio increases by a factor of 5 in the latter case as compared to the former. Here, we note that the time for which the scans were taken is also different in the two cases. Hence, a real comparison between the two sources can be made in terms of photon flux which we define below.

2. High collimation i.e. small angular divergence of the beam
3. Possibility to tune the wavelength (or energy) to the value required for a particular experiment.
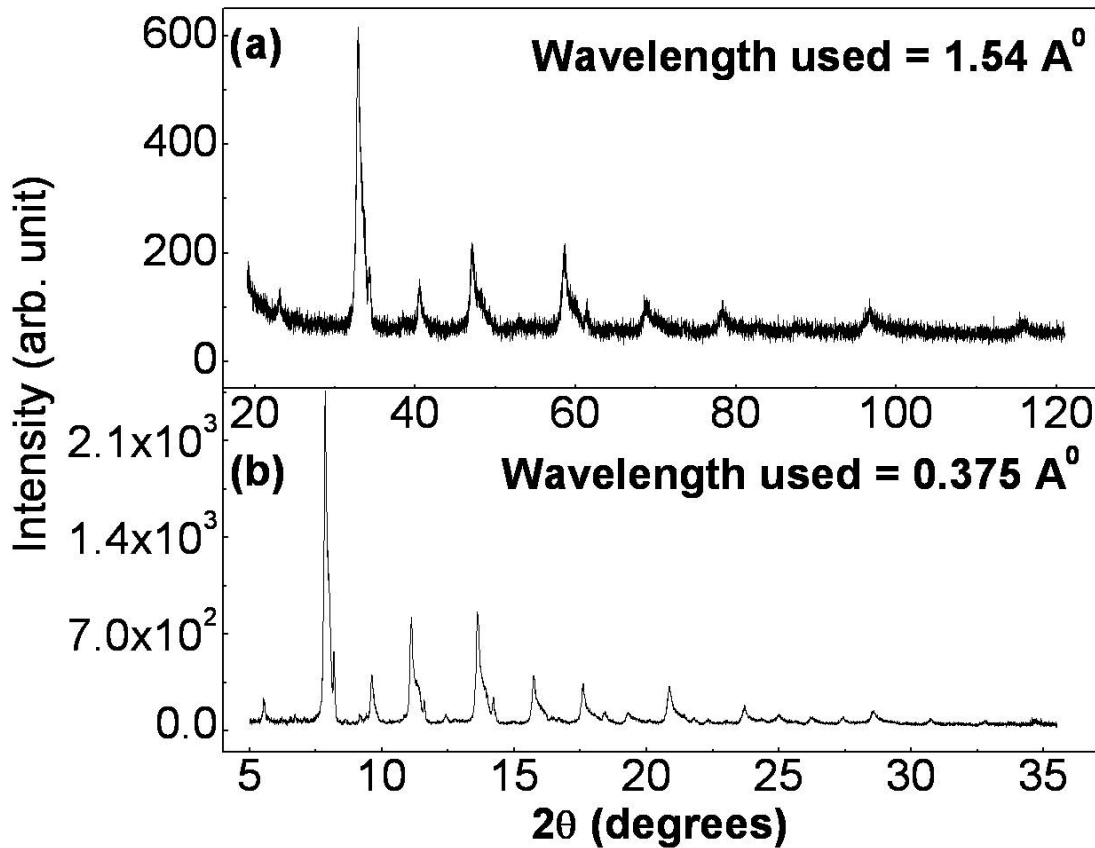
Fig.2.27. X – ray patterns of the same sample taken using (a) laboratory based x – ray source and (b) synchrotron radiation source.

The intensity of the X – ray sources can be defined in terms of the photon flux on the target or the "brilliance". The brilliance is defined as the number of photons/sec/source size/ angular divergence/0.1% energy width of the spectrum. Thus, the unit of brilliance (*B*) is as follows: $B = \dfrac{photons}{\sec .mrad^2 .mm^2 .0.1\%}$. Fig.2.28 shows the brilliance of several beamlines at the E.S.R.F. In Fig.2.29, we show the brilliance of several other synchrotron sources as a function of

the photon energy. The CuK lines and MoK lines which are used for laboratory based x – ray sources are also shown for comparison, which shows that the photon flux of the laboratory – based x – ray sources are atleast two orders of magnitude less than the synchrotron sources.
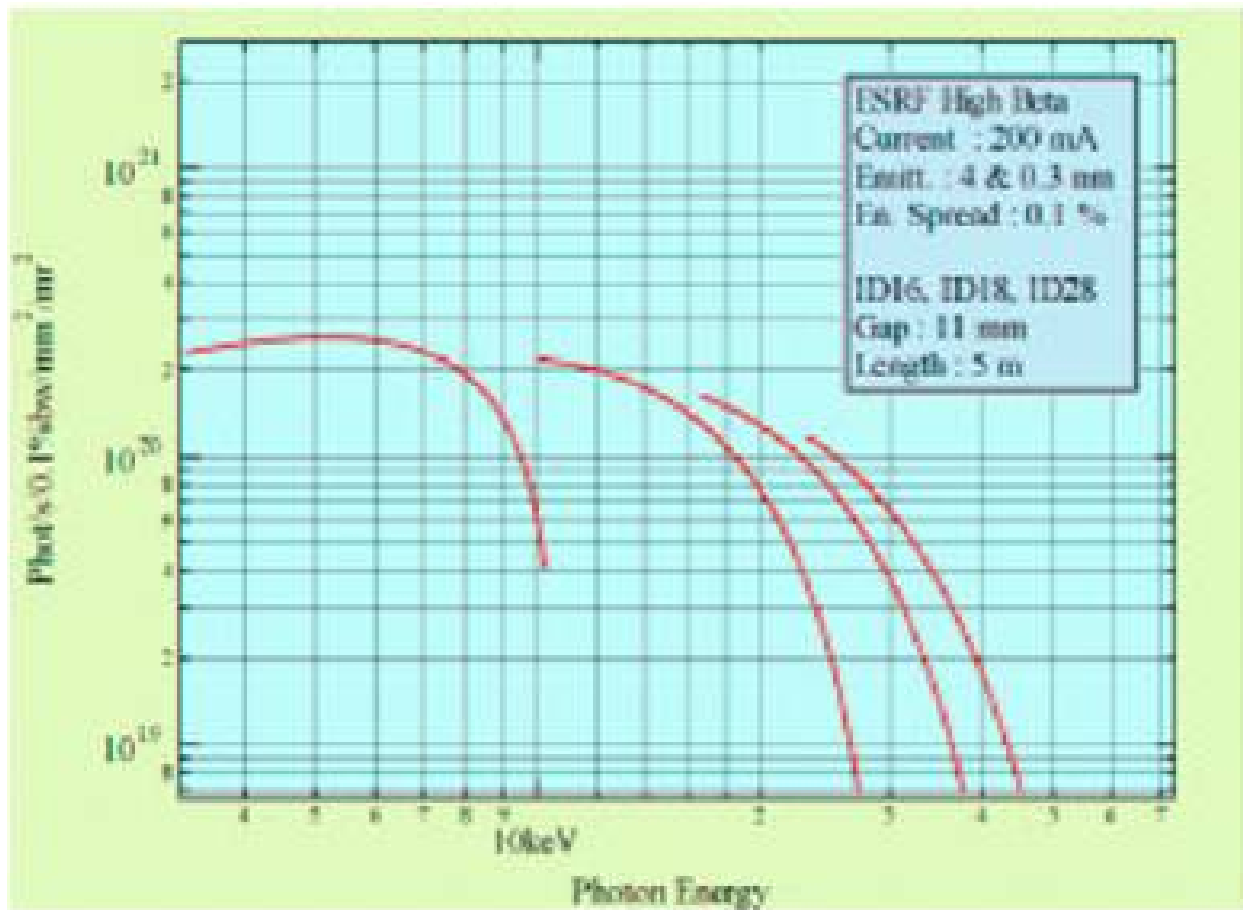
Fig.2.28. Brilliance versus photon energy for several beamlines at the E.S.R.F.
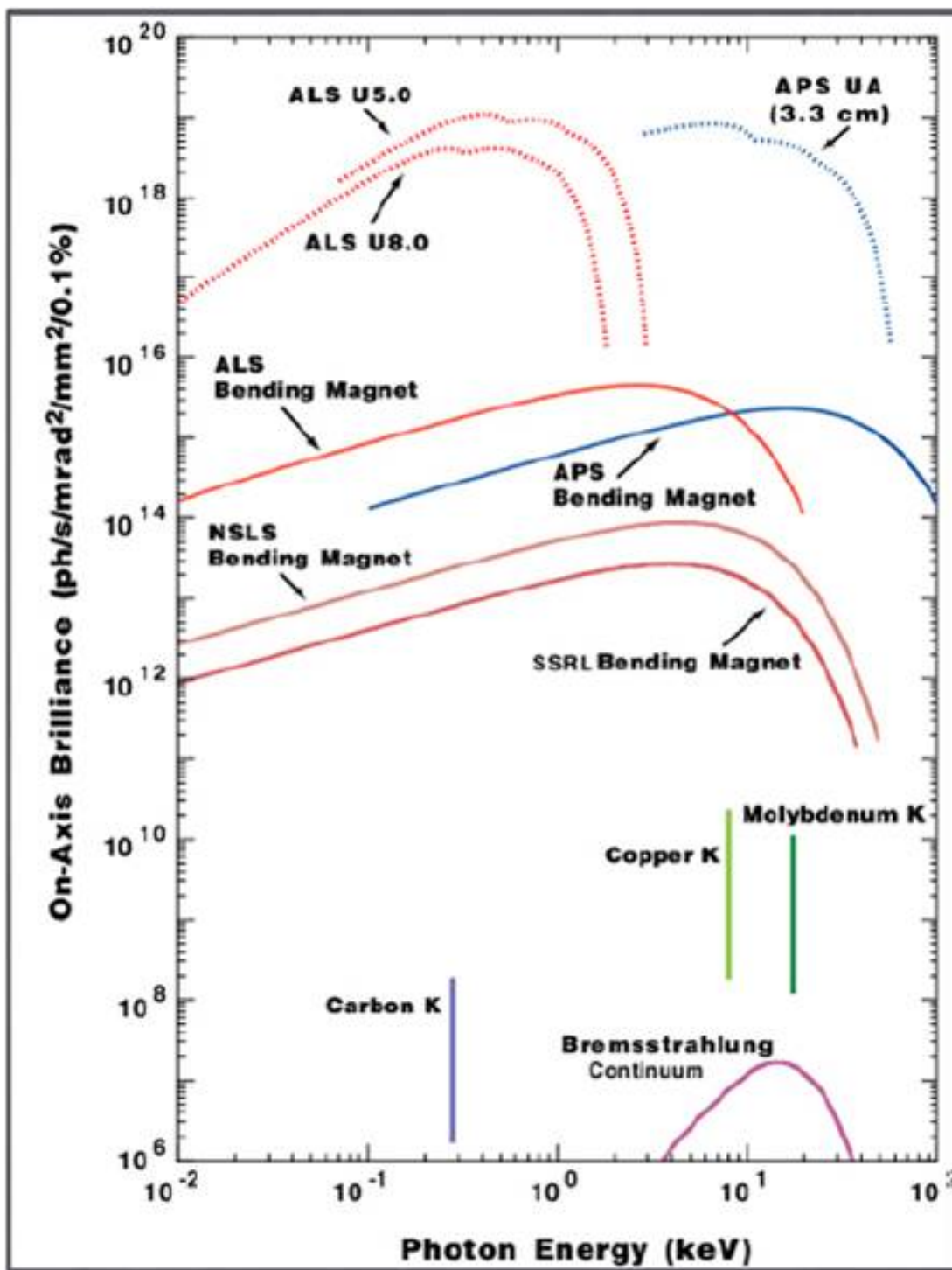
Fig.2.29. Brilliance versus photon energy for several synchrotron sources, alongwith the laboratory based sources for comparison.

2.7.2. Neutron Diffraction

Neutron diffraction is often used as a complementary technique to x – ray diffraction. Neutron has a spin ½, zero charge and a magnetic moment of -1.913 μ_n where μ_n is nuclear magneton. The zero electric charge of neutrons along with a magnetic moment makes them an useful tool to detect atomic magnetic moments without any interference from Coulomb interaction. The zero electric charge also helps them in penetrating to a greater distance. Unlike x – ray scattering, where the scattering amplitude is proportional to the number of electrons (Z) in an atom/ion, for neutrons the nuclear scattering cross – section is governed by a short range nuclear interaction which is independent of Z. This allows one to locate lighter atoms even in the presence of heavier atoms.

The neutron – matter interactions have two major parts, namely nuclear scattering and magnetic scattering. The first is the interaction of the neutrons with the nuclei of the target via short range ($\sim 10^{-12}$ cm) nuclear forces. This scattering is isotropic since the nuclear force is short – ranged. The second arises from the electromagnetic interaction of the magnetic moment of neutrons with the electrons.

Nuclear Bragg Scattering: The coherent scattering cross – section from a crystalline sample is given by $\left(\dfrac{d\sigma}{d\Omega} \right)_{coherent} = \dfrac{(2\pi)^3 N}{V} \sum_{\tau} \delta(Q - 2\pi\tau)|F_\tau|^2$, where, V is the volume of the unit cell. This equation indicates that coherent electron scattering arises only when the wave vector transfer Q suffered by the neutrons corresponds to one of the reciprocal lattice vectors. This is the condition for Bragg scattering of neutrons. Here F_τ is the nuclear structure factor and is defined as $F_\tau = \sum_{l} \langle b_l \rangle e^{i2\pi\tau \cdot \rho_l} e^{-w_l}$, where, e^{-w_l} is the Debye – Waller temperature factor and ρ_l is the coordinate of the lth atom in the unit cell. If h,k,l are the Miller indices associated with a particular reciprocal vector τ, the nuclear structure factor F_{hkl} for the hkl Bragg reflection is then given by $F_{hkl} = \sum_{m} \langle b_m \rangle e^{2\pi i (hx_m + ky_m + lz_m)} e^{-w_m}$, where, x_m, y_m, z_m are the fractional coordinates of the mth atom in the unit cell. The diffracted intensity for a nuclear Bragg peak with Miller indices (hkl) is given by $I_{hkl} = S j L |F_{hkl}|^2$, where, S is a constant scale factor which depends on the amount of sample in the beam, neutron beam flux, detector efficiency etc., j is the multiplicity of the (hkl) plane and L is the Lorentz factor (a geometrical factor to take into account the sample shape).

Magnetic Bragg Scattering: The magnetic Bragg scattering arises from the electromagnetic interaction $\mu_n \cdot \mathbf{H}(\mathbf{r},t)$, where, $\mathbf{H}(\mathbf{r},t)$ is the local magnetic field of an atom at position $\mathbf{r}$ as seen by the neutrons. The interaction of the neutron's magnetic moment with the nuclear magnetic moment (if any) can be neglected as the interaction is $\sim 10^3$ times weaker than the electronic - $\mu_n \cdot \mathbf{H}(\mathbf{r},t)$ contribution. The neutron magnetic scattering has an angular dependence since the radial extent of the unpaired electrons (which are responsible for the atomic moment) is comparable with the neutron wavelength (~ 1 Å). This angular dependence is represented by the magnetic form factor f($\mathbf{Q}$) for an atom or ion. The magnetic scattering amplitude p (in cm) is given by 0.269 X 10^{-12} μ f($\mathbf{Q}$). Here, μ is atomic magnetic moment in Bohr magneton [= μ_B (**L** + 2**S**)] due to unpaired electrons with orbital angular momentum **L** and spin angular momentum **S**. **Q** is the wave vector transfer = (**k$_0$** – **k$_f$**), **k$_0$** and **k$_f$** being the wave vectors of the scattered and

the incident neutrons respectively. The magnetic scattering is effectively governed by the term $\mathbf{q}p$. $\mathbf{q}$ is the magnetic interaction vector and is defined as $\mathbf{k}(\mathbf{k}\cdot\mathbf{K}) - \mathbf{K}$, where, $\mathbf{k} = \mathbf{Q}/|\mathbf{Q}|$ is the unit scattering vector and $\mathbf{K}$ is the unit vector in the direction of the atomic magnetic moment. Thus, the magnetic interaction vector provides information about the orientations of the atomic magnetic moments with respect to the crystal axes. From the definition of $\mathbf{q}$ it can be seen that the component of μ normal to scattering vector $\mathbf{Q}$ is effective in determining the magnitude of magnetic scattering. $f(Q)$ is normalized to unity at $\mathbf{Q} = 0$ and decreases with increasing scattering angle of Q. Thus, unlike nuclear scattering amplitude (a scalar quantity), the magnetic scattering amplitude (a vector quantity) is not isotropic.

In a magnetically ordered crystal with a regular alignment of atomic spins in the crystal lattice, we can define the magnetic elastic differential cross – section as

$$\left(\frac{d\sigma}{d\Omega}\right)^{magnetic}_{coherent} = \frac{(2\pi)^3 N}{V} \sum_{\tau_m} \delta(Q - 2\pi\tau_m) q^2 \left|F_\tau^{mag}\right|^2, \quad \text{where,} \quad F_\tau^{mag} = \sum_j p_j e^{i2\pi\tau_j \cdot \rho_j} e^{-w_j}. \quad \text{Here,} \quad V \text{ is}$$

the volume of the magnetic unit cell. The above equation for $\left(\dfrac{d\sigma}{d\Omega}\right)^{magnetic}_{coherent}$ is valid for any

magnetically ordered crystal (ferromagnet, ferrimagnet or antiferromagnet) provided that the proper sign of the magnetic scattering amplitude is taken into account. If h,k,l are the Miller indices of a particular magnetic reciprocal vector τ_m, then $F_{hkl}^{mag} = \sum_j p_j e^{2\pi i\left(hx_j + jy_j + lz_j\right)} e^{-w_j}$, where,

x_j, y_j and z_j are the fractional coordinates of the jth magnetic atom in the magnetic unit cell.

Thus, the total coherent elasting scattering cross – section that determines the Bragg intensities due to the nuclear and magnetic scattering of the incident beam is

$\left(\dfrac{d\sigma}{d\Omega}\right)^{total}_{coherent} \propto F_{nuclear}^2 + q^2 F_{magnetic}^2$. The diffracted intensity for a Bragg peak with Miller indices

(hkl) is given by $I_{hkl} = S\,j\,L\left(\left|F_N\right|^2 + \left|F_M\right|^2\right)$. $F_N(Q)$ is the nuclear structure factor, and

$F_M(Q) = \sum_j q_j p_j e^{2\pi i\left(hx_j + ky_j + lz_j\right)}$.

Neutrons are typically produced by either of two processes:

1. *Fission process*: Neutrons (thermal neutrons) are produced from the radioactive decay of uranium atom in a nuclear reactor. The typical thermal energies of these neutrons lie between $10 – 100$ meV so that their de Broglie wavelengths can range from $2.86 – 0.905$ Å. These wavelengths are comparable to the interatomic spacing in materials, and hence, neutrons can be used as a probe to study atomic positional correlations in matter.

2. *Spallation process*: Neutrons are produced by high energy collisions between a proton beam and a heavy nucleus. Typically each proton generates $10 – 15$ neutrons. These neutrons then pass through a moderator (often water) to reduce their energy to a level comparable with thermal neutrons from a reactor.

The wavelength distribution for the neutrons produced by the two sources is also different. A schematic representation of the two processes are shown in Fig.2.30 and the wavelength distribution of the neutrons produced by them are shown in Fig.2.31.
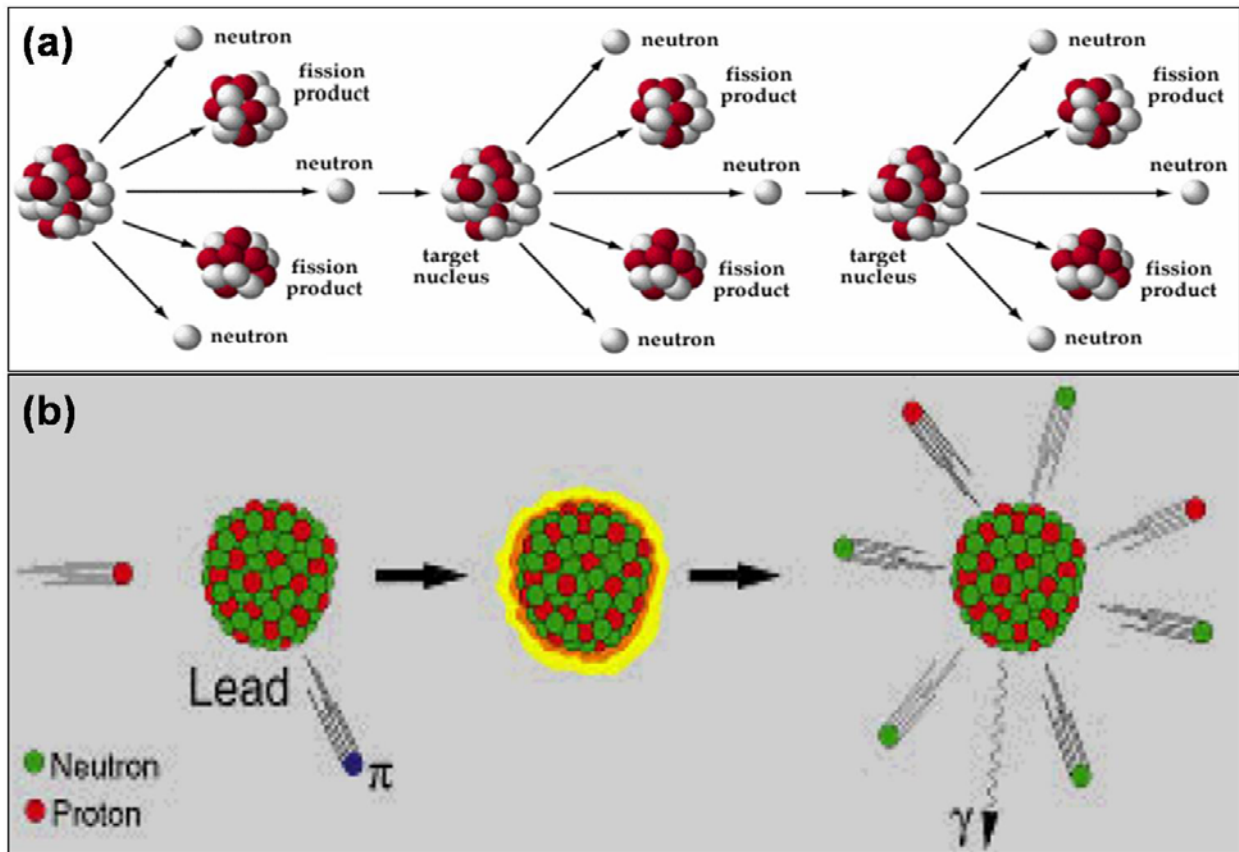
Fig.2.30. Schematic representation of production of neutrons by (a) Fission process and (b) Spallation process (reproduced from [21,22]).
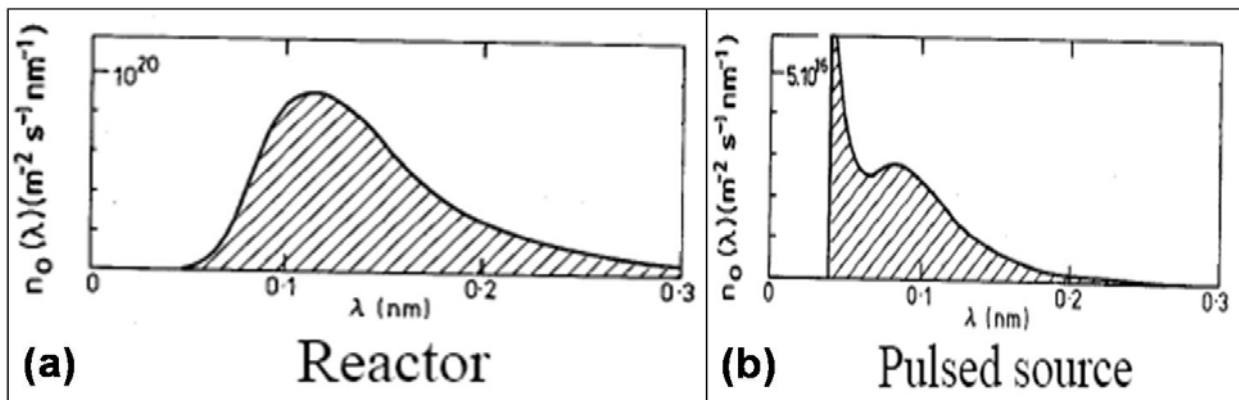
Fig.2.31. Schematic representation of the wavelength distribution of the neutrons produced in a (a) Reactor and (b) Pulsed source (reproduced from [23]).

The same Bragg's law $\left(2d_{hkl}\sin\theta = n\lambda\right)$ which governs x – ray diffraction (covered in Section 2.7.1.1) also governs neutron diffraction. The objective in any diffraction experiment is to measure d_{hkl}. In x – ray powder diffraction, λ is always constant and θ is variable. Neutron diffractometers give us two options: (i) to keep λ constant and vary θ or (ii) to keep θ constant and vary λ. Thus, there are two kinds of neutron diffractometers:

1. *Constant wavelength diffractometer*: This is essentially an extension of the x – ray powder diffractometer, with the added advantage of neutron being the probe, so that magnetic refinements are possible and structural parameters can be determined with more precision than that from x – ray data (Fig.2.32 (a)).

2. *Time – of – flight diffractometer*: This takes advantage of the full "white" spectrum. Combining the two equations $\lambda = \dfrac{h}{mv}$ and $v = \dfrac{L}{t}$ (where, m and v are the mass and the velocity of the neutron respectively, L is the length of flight path and t is the time of flight of neutron), we get, $\lambda = \dfrac{ht}{mL} = 2d\sin\theta$, so that, $t = \dfrac{2mL}{h}d\sin\theta$. L is a constant for the detector and h and m are also constants so that $t \propto d$. Thus, the d – spacings are calculated by measuring the time of arrival of the diffracted neutrons at the detector. Neutrons are separated in energy after traveling over a fixed path length (L). This permits neutrons of many different energies and wavelengths to be used for the experiment. Typically, many separate detectors are used and the counts recorded in each of them are summed to give the total intensity.

Schematic representations of the two kinds of neutron diffractometers are shown in Fig.2.32.
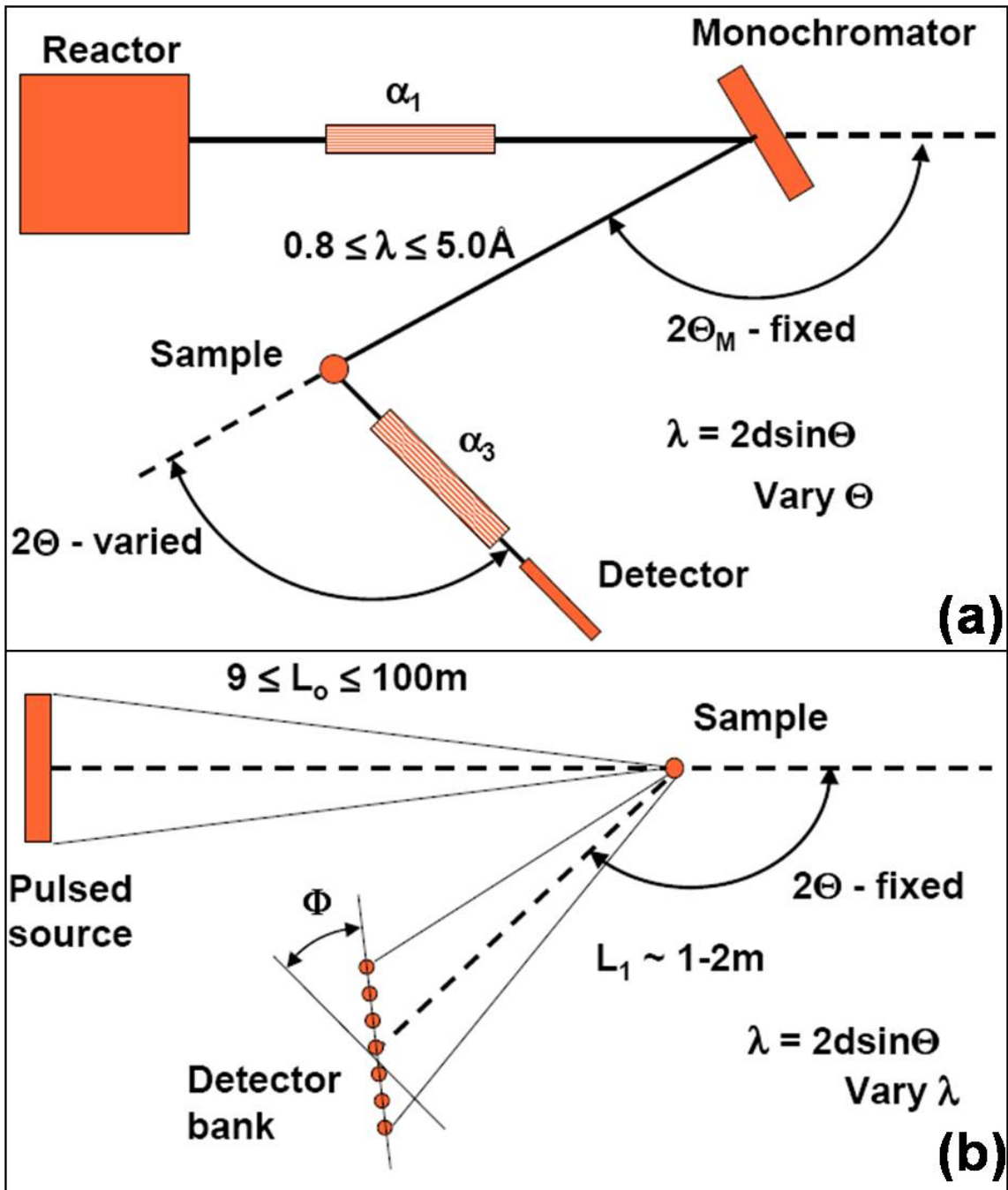
Fig.2.32. Schematic representation of (a) Constant wavelength and (b) Time of flight neutron diffractometers (reproduced from [23]).

The neutron diffraction experiments on $La_{0.67}Ca_{0.33}MnO_3$ reported in Chapter 3 were carried out at the Dhruva reactor (beam port T1013) in Trombay, India. The wavelength used was 1.249 Å and the scattering angular range covered was $2\theta = 10^0$ to 140^0 with a step size of 0.05^0. The powders were packed in a Vanadium can of height 60 mm and diameter 6 mm. For low temperature scans, a closed cycle refrigerator was used. This spectrometer has a flux of 8.5

X 10^5 neutrons/cm^2/sec and a beam size of 4 cm X 1.5 cm. There are a total of 5 detectors which allows the Q range to vary from 0.4 Å^{-1} to 9.4 Å^{-1}. The typical resolution achieved is $\Delta d/d \approx$ 0.8%.

Before moving on to the other experimental techniques used, we end this section by tabulating the relative advantages and disadvantages of x – ray data and neutron data.

Table 2.3 A comparison of neutrons and x – rays.

Neutrons	X – rays
Neutron beams are highly penetrating (penetration depth ~ cm). This ensures that the beams are diffracted from the entire sample and the values are less susceptible to surface and absorption effects. However, larger samples are needed (optimal sample volume ~ 10 cm^3).	X – rays are highly attenuated by matter (penetration depth ~ microns to mm). Smaller volume of sample is sufficient.
Neutrons are scattered from the nuclei. This ensures that the neutron scattering factors are independent of sinθ/λ and do not fall off with 2θ. Thus, the intensities of the high angle peaks are more reliable allowing for more reliable structure determination.	X – rays are scattered by electrons. The form factor decreases with sinθ/λ and the diffracted intensity decreases at higher scattering angles
Neutron scattering power varies irregularly with atomic number and mass number. This ensures that neutrons are more sensitive to light atoms and isotope distributions. This allows one to locate lighter atoms even in the presence of heavier atoms.	X – ray scattering power varies smoothly with atomic number. Hence, the diffracted intensities are dominated by heavier atoms
Neutrons have an intrinsic magnetic moment and hence can be used to determine ordered magnetic structures.	X – rays have no magnetic moment.
Production of neutrons is more costly.	Production of x – rays (laboratory – based sources) is much less expensive.

2.7.3 Imaging tools – Transmission Electron Microscopy

The Transmission Electron Microscope (TEM) is a versatile instrument, capable of characterizing the internal structure of materials with a wide range of imaging and analytical methods. It uses diffraction of electrons to image materials. In transmission electron microscopy, a beam of electrons (with a typical wavelength of less than 1 Å) is sent through a thin specimen (to image powder samples, a very dilute solution of the powder in ethanol is dispersed on a TEM grid). A fraction of the electrons in the beam get either elastically or inelastically scattered. The elastically scattered (diffracted) electrons contribute to the image contrast. Thus, while passing through the specimen, the electron beam undergoes diffraction according to Bragg's law. The non – diffracted as well as the diffracted beams are focused on the back focal plane of the objective lens (which is the first lens below the specimen), resulting in an electron diffraction pattern. The diffraction pattern of the back focal plane undergoes an inverse Fourier transformation and a highly magnified image is formed. In *amplitude or diffraction contrast imaging*, an objective aperture (a small hole in a metallic plate) is introduced into the beam in the

back focal plane. Thus, a significant amount of electrons are removed from the beam before further magnification. This results in an intensity contrast in the final image.

HRTEM: The other basic imaging mode is *phase contrast imaging or high resolution TEM (HRTEM) imaging* mode. It can show structures at the atomic scale, lattice fringes, and hence can be used to look at the arrangement of atoms in a crystal. Here, the aperture in the back focal plane is larger (sometimes the aperture is dispensed with altogether) and multiple beams are allowed to contribute to the final image. One or more diffracted beams interfere with the directly transmitted beam to form the image, and the image contrast depends on the relative phases of the various beams. HRTEM, thus, requires interference of the unscattered and the scattered beams.

Indexing of the diffraction patterns: For small angle of diffraction θ, $\sin\theta$ in the Bragg's law can be replaced by θ. Using this reduced Bragg condition, we get $\lambda = 2d_{hkl}\theta$. Now, if L is the distance between the screen and the sample and R is the distance of the diffracted spot of interest from the central spot, then $\tan 2\theta = \dfrac{R}{L}$. This can be seen in Fig.2.33. Again for small θ, $\tan 2\theta \approx 2\theta$. Thus, $\lambda L = Rd_{hkl}$. The effective length L in the presence and absence of imaging lenses are shown in Fig.2.33. For ring patterns, the radius of each ring can be converted into interplanar spacing by the above equation. For spot patterns (as in our case), the distances of the diffracted spots from the central spot is measured. These distances correspond to the interplanar spacing of the diffracting planes. Thus, by measuring R and calculating the corresponding plane spacing (d_{hkl}), the diffraction pattern can be indexed.
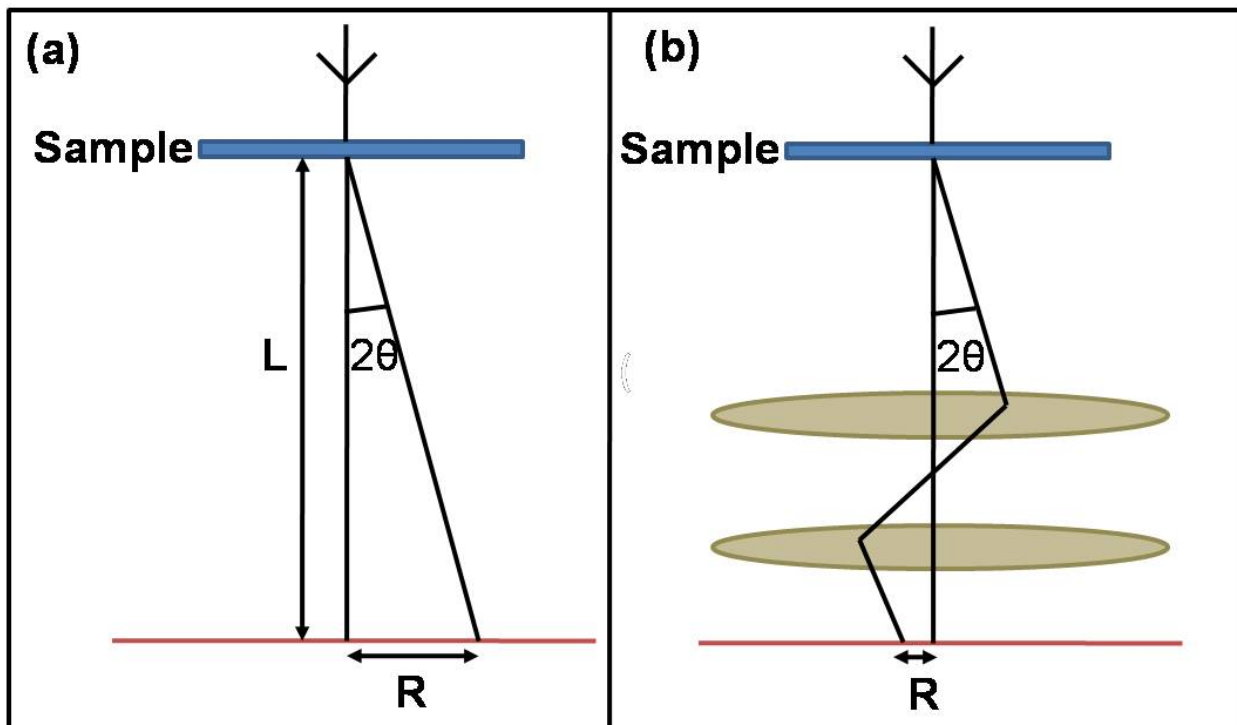
Fig.2.33. Camera length L in the presence and absence of imaging lenses.

EDXS: The technique of energy dispersive x – ray spectroscopy (EDXS) utilizes the characteristic spectrum of x – rays that is emitted by a sample following initial excitation of an inner shell electron to a vacant higher energy level by the high energy electron beam. Highly localized information about the elemental composition of the sample can be obtained, with the spatial resolution determined primarily by the probe size. EDXS is a relatively straightforward technique experimentally, but it requires pre – calibration of the specific EDXS analysis system using standards of known composition.

2.7.4 Tools for stoichiometry checks

2.7.4.1 Inductively Coupled Plasma Atomic Emission Spectroscopy (ICPAES) technique

ICPAES is an analytical technique for the qualitative as well as quantitative determination of the elemental composition in a sample. It is a type of emission spectroscopy that uses an inductively coupled plasma (a type of plasma source in which the energy is supplied by electrical currents produced by electromagnetic induction) to produce excited atoms and ions from the sample which then emit electromagnetic radiation at wavelengths characteristic of that particular element when they return to the ground state. The intensity of the emission is indicative of the amount of the element in the sample. Thus, by determining which wavelengths are emitted by a sample and by determining their intensities, the elemental composition of the sample can be quantified with respect to a reference standard. In general, qualitative information (what elements are present) is related to the wavelengths at which the radiation is absorbed or emitted, and quantitative information (concentration) is related to the amount of electromagnetic radiation that is emitted or absorbed.

The standards used in the analysis are prepared by dissolving high purity metals or salts with high purity acids or other appropriate reagents and then diluting to obtain the desired concentrations. When preparing mixed standards i.e. standards containing a known concentration of more than one element, one must make sure that the elements of interest are compatible with the other species in the solution so that precipitation of the standard elements does not occur. This analysis requires the sample to be in solution. It should be ensured that the same solvent is used both for the standards and the sample. In our case, the oxides were dissolved in concentrated HCl for the ICPAES test.

Quantitative information i.e. how much of the element is in the sample is obtained using calibration curves which are essentially plots of emission intensity versus concentration. An example of a calibration curve is shown in Fig.2.34. The calibration curves are obtained using the standard solutions (solutions with known concentrations of the elements of interest). The standard solutions are first measured and the intensity of the characteristic emission for each element is then measured. These intensities can then be plotted against the concentrations of the standards to form a calibration curve for each element. Next the sample is measured and the emission intensity is checked against that element's calibration curve to determine the concentration corresponding to that intensity. Since calibration curves are generally linear over four to six orders of magnitude in ICPAES, it is usually necessary to measure only one or two standard solutions, along with a blank solution, to obtain the calibration curve.
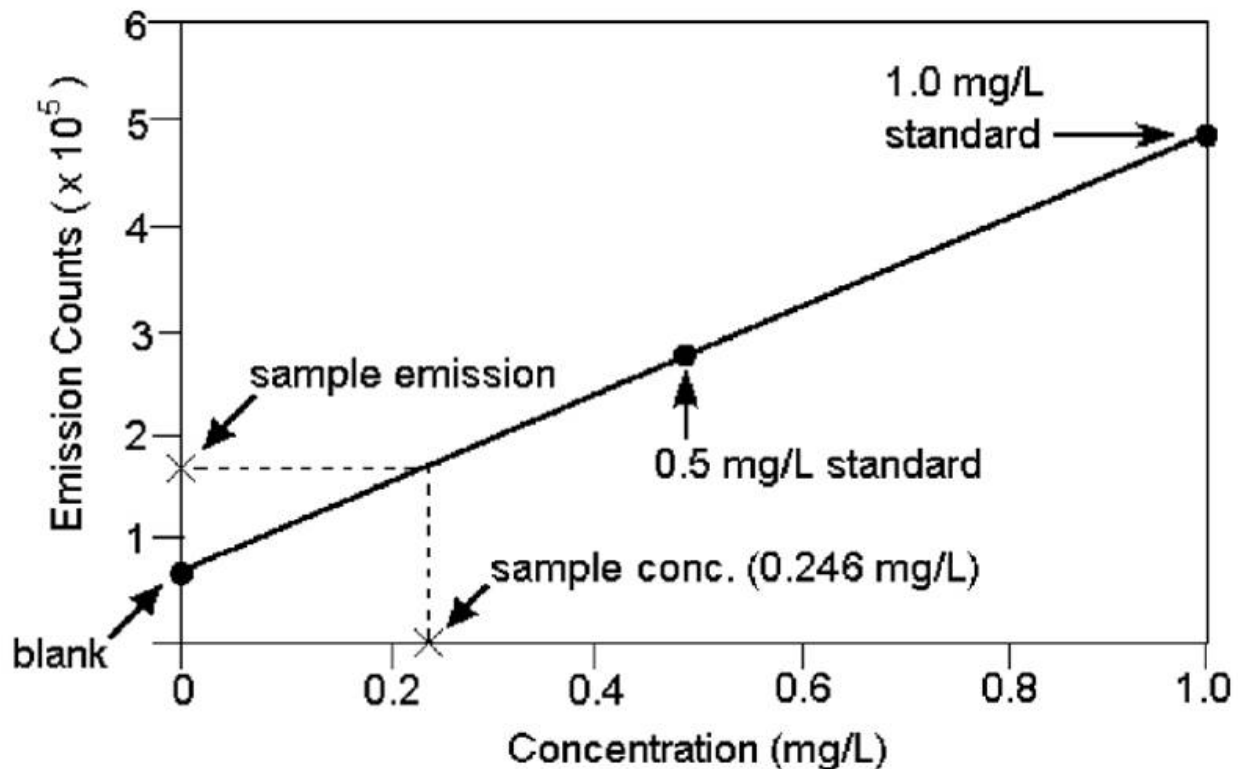
Fig.2.34. Calibration curve used in ICPAES (reproduced from [24]).

2.7.4.2 Iodometric titration to check the oxygen stoichiometry

If the oxides have oxygen deficiency (or oxygen excess), then the molecular formula of LCMO, for example, can be written as $La_{0.67}^{3+}Ca_{0.33}^{2+}Mn_{1-x}^{3+}Mn_x^{4+}O_{3+\delta}^{2-}$ where we have shown the valencies as superscripts. Ideally, $x = 0.33$ and $\delta = 0$. However, for an oxygen deficient (or excess) sample, $\delta \neq 0$ and $x \neq 0.33$. In such cases, the value of x and thereby δ can be extracted by doing a titration measurement.

The strategy is to dissolve a known weight (say, m) of the sample in concentrated HCl, add it to a KI solution (of known normality, say, N), and then titrate with sodium thiosulphate solution. The process is then repeated with a blank solution (i.e. without the oxide sample). The difference in volume (V) of sodium thiosulphase solution needed in the two processes gives the amount of sodium thiosulphate solution used by the sample. Oxidation state of Mn before titration is $3(1 - x) + 4x = 3 + x$. After the titration is completed Mn^{2+} is obtained. Thus, change in oxidation state of Mn during titration $= 1 + x$. The molecular weight of the sample is also known (say, M). Then x can be calculated from the following condition for equilibrium: $MV\dfrac{N}{1000}(1+x)=m$. Now, from the charge balance of $La_{0.67}^{3+}Ca_{0.33}^{2+}Mn_{1-x}^{3+}Mn_x^{4+}O_{3+\delta}^{2-}$, we have,

$3+\delta = \dfrac{5.67 + x}{2}$. Thus, knowing x we can calculate δ. A positive value of δ indicates an excess of oxygen while a negative value of δ implies that the samples are oxygen deficient.

2.7.5 Magnetization measurements

Most of the magnetic measurements were carried out using a commercial vibrating sample magnetometer (VSM)[25] and a Quantum Design superconducting quantum interference device (SQUID) magnetometer[26].

2.7.5.1 Vibrating Sample Magnetometer (VSM)

A vibrating sample magnetometer (VSM) operates on Faraday's Law of Induction which tells us that a changing magnetic field will produce an electric field. This electric field can be measured and can give us information about the changing magnetic field. Thus, the sample is placed in a constant magnetic field and oscillated with a fixed frequency near a set of detection (pickup) coils. If the sample is magnetic, the constant magnetic field induces a magnetic dipole moment in the sample. This magnetic dipole moment creates a magnetic field around the sample. As the sample is oscillated, this magnetic flux changes as a function of time and the voltage induced (proportional to the rate of change of flux) in the pickup coils is synchronously detected. The voltage will also be proportional to the magnetic moment of the sample. In Fig.2.35 we show (a) schematic of VSM and (b) detailed configuration near the pick up coils.
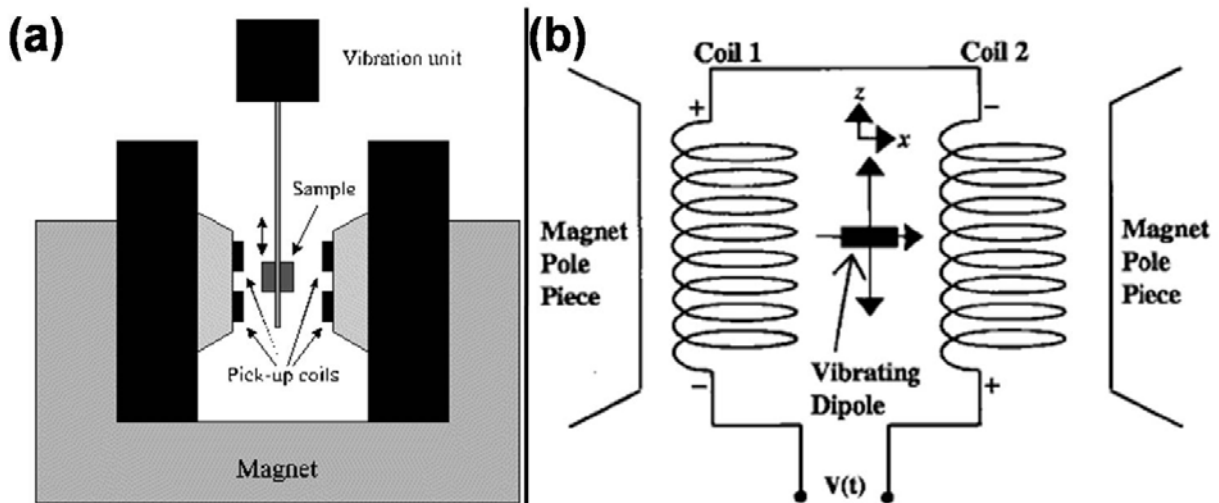
Fig.2.35. Schematic illustration of (a) VSM and (b) details near the pickup coils.

The system detection capability can be maximized by optimizing the geometry of the pickup coils (Fig.2.36), and by having an oscillation amplitude that is relatively large (1 – 3 mm peak). The time – dependent voltage induced in the pickup coils is given by $V_{induced} = \dfrac{d\phi}{dt} = \left(\dfrac{d\phi}{dz}\right)\left(\dfrac{dz}{dt}\right)$, where, φ represents the magnetic flux, the axis of oscillation of the sample is conventionally chosen to be the z – axis, and z, therefore, represents the position of the sample along this axis and t is the time. If the sample is made to oscillate sinusoidally, then the induced voltage in the pickup coils will have the form $V_{induced} = cmA\omega\sin\omega t$, where, c is a

coupling constant, m is the DC magnetic moment of the sample, A is the amplitude of oscillation, and $\omega = 2\pi f$, where, f is the frequency of oscillation of the sample. The detection of the magnetic moment of the sample, thus, amounts to measuring the coefficient of sinusoidal voltage response induced in the detection coil.
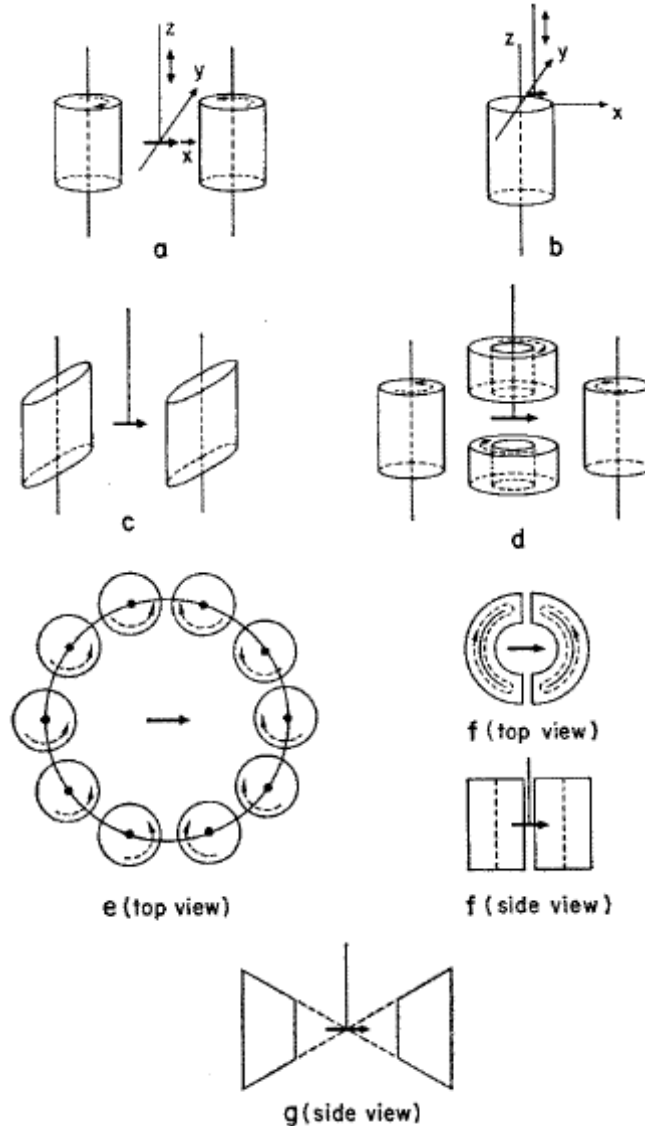
Fig.2.36. Examples of different pickup coil arrangements. The sample, indicated by the heavy arrow, is vibrated along the z – direction. (Reproduced from [27]). The VSM that we have used[25] has the coil arrangement shown in (a).

2.7.5.2 SQUID Magnetometer

SQUID magnetometers have a higher sensitivity than VSMs (the resolution obtained in a SQUID magnetometer is of the order of 10^{-8} emu as compared to a resolution of only 10^{-6} emu for VSM). As such, we used SQUID magnetometer for measuring those samples which have a

lower magnetic moment (specially those samples showing an antiferromagnetic and charge ordering transition). The working principle of a SQUID is based on the quantum interference of wave functions that describe the state of the superconducting charge carriers (the Cooper pairs). A SQUID is based on an interferometer loop in which two weak links (Josephson contacts) are established. A weak link is established by interrupting a superconductor by a very thin insulating barrier. The function of the SQUID is to link the quantum mechanical phase difference of the Cooper pairs wave functions over a weak link with the magnetic flux penetrating the interferometer loop.

The components of a SQUID magnetometer typically consist of the following: a detection coil which senses changes in the external magnetic field and transforms them into an electrical current, an input coil which transforms the resulting current into a magnetic flux in the SQUID sensor, electronics which transform the applied flux into a room temperature voltage output and acquisition hardware and software for acquiring, storing and analyzing data. Both the SQUID amplifier and detection coils are superconducting devices.

Superconducting detection coil: The detection coil used in a SQUID is a single piece of superconducting wire in a set of three coils configured as a second order gradiometer. The coil arrangement is shown in Fig.2.37. The coil sits outside the sample space within the liquid helium bath. The upper coil is a single turn would clockwise, the centre coil comprises two turns wound counter-clockwise and the bottom coil is a single turn wound clockwise. The coils are positioned at the centre of the superconducting magnet outside the sample chamber such that the manetic field from the sample couples inductively to the coils as the sample is moved through them. The gradiometer configuration is used to reduce noise in the detection circuit caused by fluctuations in the large magnetic field of the superconducting magnet. It also minimizes background drifts in the SQUID detection system caused by relaxation in the magnetic field of the superconducting magnet. Ideally, if the magnetic field is relaxing uniformly, the flux change in the two turn centre coil will be exactly cancelled by the flux change in the single turn top and bottom coils. On the other hand, the magnetic moment of the sample can still be measured by moving the sample through the detection coils because only the counterwound coil set measures the local changes in magnetic flux density produced by the dipole field of the sample.
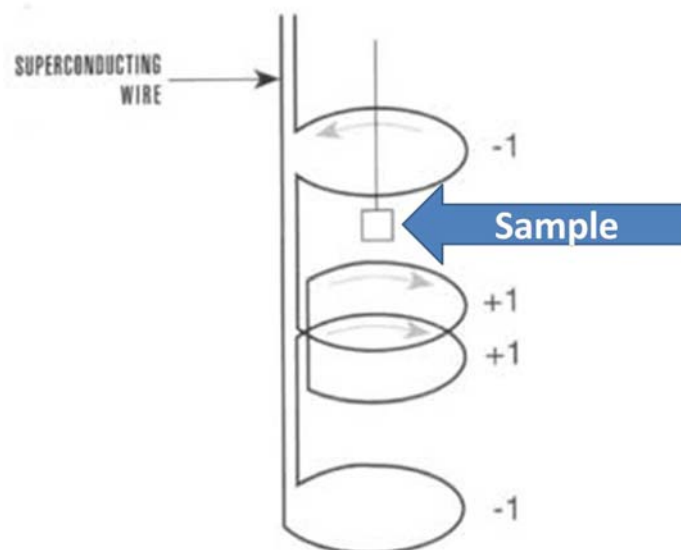
Fig.2.37. Second order gradiometer coil configuration (reproduced from [28]).

2.8 The Rietveld refinement technique

In this section, we introduce the basics of the Rietveld refinement technique. This technique has been used extensively during the course of this thesis for the refinement of both x – ray as well as neutron data in order to extract structural information (including the magnetic structure) of the nanoparticles.

The Rietveld refinement technique has been named after its inventor, Hugo M. Rietveld, who first introduced the technique for structural refinement from neutron data[29,30]. Later the technique was extended for refinement of x – ray data also. The Rietveld refinement technique is specially designed for analysis of powder diffraction data and successfully overcomes the problem of peak overlap. This method is based on the principle of refining user – selected parameters in order to minimize the difference between an experimental pattern (which is the observed data) and a model based on the hypothesized crystal structure and instrumental parameters (which is the calculated pattern). Thus, this method can only refine a structure and is not meant for structure solution. The initial structural model must be known before starting the refinement. Thus, the Rietveld refinement technique has the following requirements:

1. A high quality experimental diffraction pattern
2. An initial structural model. Thus, the symmetry of the crystal (correct space group), the dimensions of the unit cell (approximate lattice parameters) and the positions of the atoms within the unit cell have to be known. The structural parameters for most compounds are available in several standard databases. We used the International Centre for Diffraction Data (ICDD) database[31] for obtaining the initial starting model of our compounds.
3. A Rietveld refinement program. There are several Rietveld programs (both free as well as commercial) which one can use for the fitting procedure. We have used the FullProf Suite [32] which is a software freely available on the internet.

The Rietveld method refines a structure by minimizing the quantity $\chi^2 = \sum_{i=1}^{n} w_i \{y_i - y_{c,i}(\alpha)\}^2$ through a Newton – Raphson algorithm. Here, y_i is the observed intensity at a certain 2θ, $y_{c,i}$ is the calculated intensity at the same angle, $w_i = 1/y_i$ (weighting factor to take care of low intensity peaks), $\alpha = (\alpha_1 \, \alpha_2 \, ... \, \alpha_p)$ are the parameters to be refined. The minimum necessary condition to be satisfied is $\frac{\partial \chi^2}{\partial \alpha} = 0$. A Taylor expansion of $y_{c,i}(\alpha)$ around α permits one to transform the problem into determination of the shifts ($\delta\alpha$) that are solutions of a linear system of equations. The calculated shifts of the parameters are then added to the starting parameters giving rise to a new set of parameters which can then be used for a new cycle. This process is iterated till a convergence criterion is satisfied and a fairly good agreement with the measured x – ray pattern is achieved.

The x – ray pattern is calculated by considering the observed background intensity and all the reflections pertaining to all possible phases present in the sample. The symmetry of the crystal (which is incorporated via the space group) gives the positions of all possible Bragg peaks (irrespective of whether they are observable in the experimental diffraction pattern or not).

Thus, $y_{c,i} = y_{b,i} + \sum_p \sum_k G_{ik}^p I_k$. Here, G is the profile function and I is the intensity of the kth reflection. The summation is performed over all phases p, and over all reflections contributing to the respective point. The profile function G can be written as $G = s|F|^2 mLP$, where s = scale factor for a particular phase, F is the structure factor for a particular reflection, m is the multiplicity of the reflection, L is the correction factor on the intensity and P is the peak shape function which is a convolution of sample and instrumental effects.

The least squares procedure provides (when it converges) the value of the parameters constituting the local minimum closest to the starting point. As such, a set of good starting values are required for all the parameters. If the initial model is bad, then the least squares procedure diverges instead of converging. The refinable parameters include instrumental parameters, the background function, lattice parameters, peak profile (including peak shape and peak width), the atomic positions and atom occupancies and temperature factors. Theoretically, if there are n diffraction peaks, then the number of refinable parameters can go up to n-1. Parameters which cannot be refined are the symmetry of the crystal (i.e. the space group), the chemical composition, the wavelength of radiation used and the intensity ratio in $K_{\alpha 1}$, $K_{\alpha 2}$ doublet. The full width at half maximum (FWHM) of the peaks is defined using the relation $H^2 = W + V \tan\theta + U \tan^2\theta$, where, U, V and W are refinable parameters. This function describes the line broadening due to stress, strain, particle size etc.

The goodness of fit can be estimated visually from the difference pattern as well as quantitatively from the reliability (R) factors. The R – factors are defined as follows:

1. *Profile R – factor* (R_p): $R_p = \dfrac{\sum_i |y_{i0} - y_{ic}|}{\sum_i y_{i0}}$

2. *Weighted profile R – factor* (R_{wp}): $R_{wp} = \left[\dfrac{\sum_i w_i (y_{i0} - y_{ic})^2}{\sum_i w_i y_{i0}^2} \right]^{\frac{1}{2}}$

3. *Expected R – factor* (R_{exp}): $R_{exp} = \left[\dfrac{N - P + C}{\sum_i w_i y_{i0}^2} \right]^{\frac{1}{2}}$. Here, N is the total number of points

   used in the refinement, P is the number of refined parameters, C is the number of constraint functions so that N-P+C is the number of degrees of freedom

4. *Goodness of fit parameter* (χ^2): $\chi^2 = \dfrac{\sum_i w_i (y_{i0} - y_{ic})^2}{N - P + C} = \left(\dfrac{R_{wp}}{R_{exp}} \right)^2$

However, the convergence of the least squares calculation alone does not give a guarantee that the model is physically meaningful. For instance, large values of temperature factors and negative FWHM values may indicate that the refinement is not correct, even if good R – factors are observed. Thus, certain precautions have to be taken in order to extract relevant physical information from the fits.

77

Magnetic structures: The magnitude and direction of the moments of magnetic atoms/ions with respect to the crystalline axes, *a*, *b* and *c* define the magnetic structure in a magnetically ordered material with underlying crystalline lattice. The magnetic unit cell is the building block of the magnetic crystal. Below the magnetic ordering temperature of ferromagnets, ferrimagnets or antiferromagnets there is a regular periodicity of vector moments of magnetic atoms/ions which manifest itself as magnetic Bragg peaks in addition to the Bragg peaks due to regular positional arrangements of atoms/ions in the crystalline solids. The knowledge of the nuclear structure is a pre-requisite for the magnetic structure determination. This is obtained either from x – ray diffraction measurements or by carrying out neutron diffraction experiments at temperatures above the magnetic ordering temperature or at higher Q where magnetic scattering is very small due to its form factor dependence. In the case of ferromagnetic and ferrimagnetic materials, the magnetic unit cell is isomorphous with the chemical unit cell. This amounts to an occurrence of magnetic Bragg intensity at the same Q as that of the nuclear Bragg peak causing an enhancement of Bragg peak intensities below the ordering temperature. On the other hand, in antiferromagnetic materials Bragg peaks other than the chemical peaks appear depending upon the symmetry of the magnetic periodicity.

As examples, we show the XRD pattern of $La_{0.5}Ca_{0.5}MnO_3$ nanoparticle taken at 5 K using synchrotron x – ray source and the neutron diffraction pattern of $La_{0.67}Ca_{0.33}MnO_3$ nanoparticle taken at 20 K in Fig.2.38 and Fig.2.39 respectively. The red curve shows the experimental data, the black curve gives the calculated pattern and the blue curve gives the difference pattern. The position of the Bragg peaks are also shown by green lines. In Fig.2.39, the structural as well as magnetic Bragg peaks are shown, but since the material is ferromagnetic, there is no appearance of any superlattice peaks. The R – factors of the two fits are shown in the figure captions.
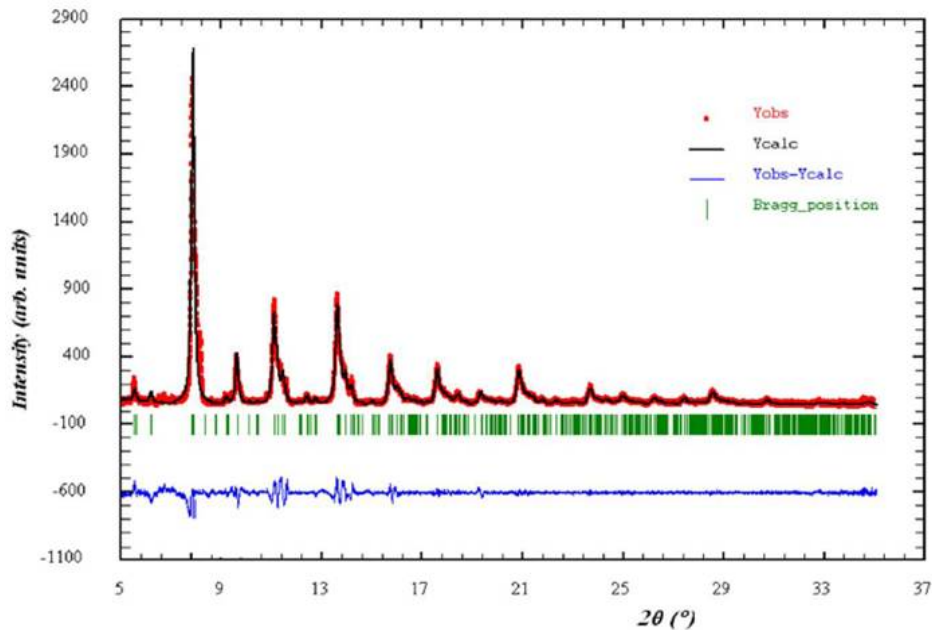
Fig.2.38. XRD pattern (along with the fits) for $La_{0.5}C_{0.5}MnO_3$ nanoparticle taken at T = 5 K. The difference pattern and the position of the Bragg peaks are also shown. The R – factors obtained were R_p = 9.42%, R_{wp} = 12.5%, R_{exp} = 9.12%.
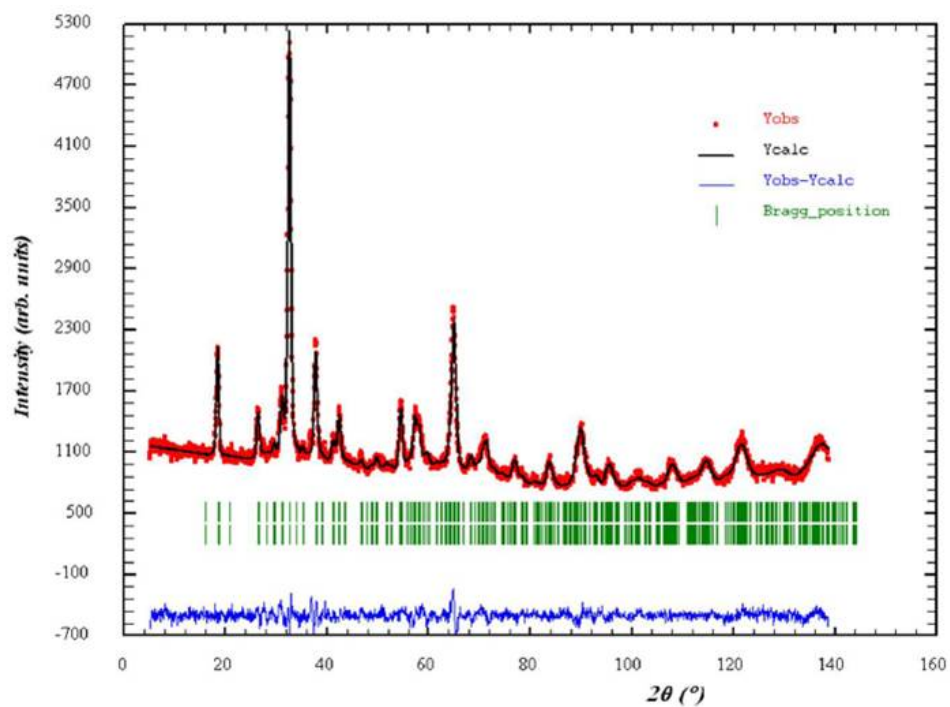
Fig.2.39. Neutron diffraction pattern (along with the fits) for $La_{0.67}C_{0.33}MnO_3$ nanoparticle taken at T = 20 K. The difference pattern and the position of the structural and magnetic Bragg peaks are also shown. The R – factors obtained were R_p = 2.97%, R_{wp} = 3.79%, R_{exp} = 3.08%.

REFERENCES

[1] J. Sundrica, Inter. J. of Powder Metallurgy and Technology, **17**, 291 (1981)

[2] C.N.R.Rao and J.Gopalakrishnan, Acc. Chem. Res., **20**, 228 (1987)

[3] Rustum Roy, Science, **238**, 1664 (1987)

[4] http://www.chem.hanyang.ac.kr:8001/hanyang/professor6/upload/Sol-Gel%20Science.pdf

[5] Ashok K. Ganguli, Sonalika Vaidya and Tokeer Ahmad, Bull. Mater, Sci., **31**, 415 (2008)

[6] M.P.Pileni, J. Phys. Chem., **97**, 6961 (1993)

[7] *The Chemistry of Nanomaterials: Synthesis, Properties and Applications*, edited by C.N.R.Rao, A.Muller and A.K.Cheetham, VCH Wiley (2004)

[8] Sigma – Aldrich, Inc. 3050 Spruce Street, St. Louis, MO 63103, USA

[9] K. Shantha Shankar and A.K.Raychaudhuri, J. Materr. Res., **21**, 27 (2006)

[10] JASCO International Co Ltd., 4 – 21, Senin – cho 2 – chome, Hachioji, Tokyo, 193 – 0835, Japan

[11] PANanalytical B.V., Lelyweg 1, 7602 EA Almelo, The Netherlands

[12] PerkinElmer, Life and Analytical Sciences, 710 Bridgeport Avenue, Shelton, CT 06484 – 4794 USA

[13] Kirby Dwight and Norman Menyuk, Phys. Rev, **119**, 1470 (1960)

[14] http://www10.zzu.edu.cn/taoci/jpkc/solid%20state%20sintering%20.ppt

[15] G.K.Williamson and W.H.Hall, Acta Metall., **1**, 22 (1953)

[16] JEOL Ltd., 1 – 2, Musashino 3 – chome Akishima Tokyo 196 – 8558, Japan

[17] FEI Company, North America NanoPort 5350 NE Dawson Creek Drive Hillsboro, Oregon 97124 USA

[18] N.Gayathri, A.K.Raychaudhuri, X.Q.Xu, J.L.Peng and R.L.Greene, J. Phys.: Condens. Matter, **10**, 1323 (1998)

[19] R.Vidya, P.Ravindran, P.Vajeeston, A.Kjekshus and H.Fjellvåg, Phys. Rev. B, **69**, 092405 (2004)

[20] P.Adler, A.Lebon, V.Damljanović, C.Ulrich, C.Bernhard, A.V.Boris, A.Maljuk, C.T.Lin and B.Keimer, Phys. Rev. B, **73**, 094451 (2006)

[21] http://www.ansto.gov.au/__data/assets/pdf_file/0005/16961/Using_Neutron_Scattering.pdf

[22] http://www.chemistry.ohio-state.edu/~woodward/complimentary.pdf

[23] http://web.chemistry.gatech.edu/~wilkinson/Class_notes/CHEM_6181_spring_2003/Radiation_sources_and_instrumentation.pdf

[24] *Concepts, Instrumentation and Techniques in Inductively Coupled Plasma Optical Emission Spectroscopy*, Charles B. Boss and Kenneth J. Fredeen, Perkin Elmer (Second Edition)

[25] Lake Shore Cryotronics, Inc., 575 Mc Corkle Blvd, Westerville, OH 43082, USA

[26] MPMS SQUID magnetometer, 6325 Lusk Boulevard, San Diego, CA 92121 – 3733, USA

[27] Simon Foner, Rev. Sci. Instr., **30**, 548 (1959)

[28] http://www.nanomagnetics.org/instrumentation_and_characterization/

[29] H.M.Rietveld, Acta Crystallogr., **22**, 151 (1967)

[30] H.M. Rietveld, J. Appl. Crystallogr., **2**, 65 (1969)

[31] http://www.icdd.com

[32] http://www.ill.eu/sites/fullprof/

CHAPTER 3. EFFECT OF SIZE REDUCTION ON THE FERROMAGNETIC METALLIC STATE IN MANGANITES AND COBALTATES

3.1 Introduction and Motivation

The physics of size reduction in hole – doped manganites is the main subject of study in this thesis. As the phase diagram of manganites suggests, the hole doping changes the nature of the ground state in a qualitative way. As mentioned in Chapter 1, the multitude of ground states brought about by changing the hole concentration makes the system so much more interesting.

The principal motivation of this chapter is to investigate what happens to the ferromagnetism and the nature of the ferromagnetic transition in LCMO when the size is reduced. For this study, we have chosen the optimum hole concentration at $x = 0.33$ where the ferromagnetic T_C is highest (≈ 265 K) in the bulk.

This chapter will mainly focus on the magnetic studies while in Chapter 5 we will discuss the transport properties. The next chapter (Chapter 4) discusses the effect of size reduction in yet another hole concentration range (half – doped; $x = 0.5$) where the ground state (in bulk sample) is the charge – ordered antiferromagnetic insulator.

The physics of ferromagnetic nanoparticles encompasses a number of issues like finite size scaling, single domain particles, superparamagnetism etc. which we have discussed in Chapter 1. We will see, however, that in manganite nanoparticles one obtains a different set of questions which may not fit into the general trend of other oxides. Below we list some of these effects again to bring out the unsolved issues which we try to understand:

a) **Finite size scaling effect:** Size reduction, very often, leads to a decrease in T_C in magnetic materials. This change is quantified using the scaling law for $T_C(d)$[1] (see Section 1.12 of Chapter 1). However, in nanocrytsalline $La_{0.67}Ca_{0.33}MnO_3$, there have been reports of an enhancement of the Curie temperature up to 300 K[2]. Nevertheless, the cause of this observation of rise in T_C in nanocrytsalline $La_{0.67}Ca_{0.33}MnO_3$ is still considerably ambiguous. For example, some other studies report an opposite trend of decrease in T_C with a decrease in the particle size[3], and yet others show an irregular variation of T_C with particle size[4]. Fig.3.1 shows a plot of T_C versus particle size for $La_{0.67}Ca_{0.33}MnO_3$ as reported in these past studies. The fact that such contradictive reports exist itself calls for a more detailed investigation into these nanoparticles. Size reduction in these oxide nanoparticles may introduce more than one competing effects, and the final T_C probably depends on which of these effects win over.
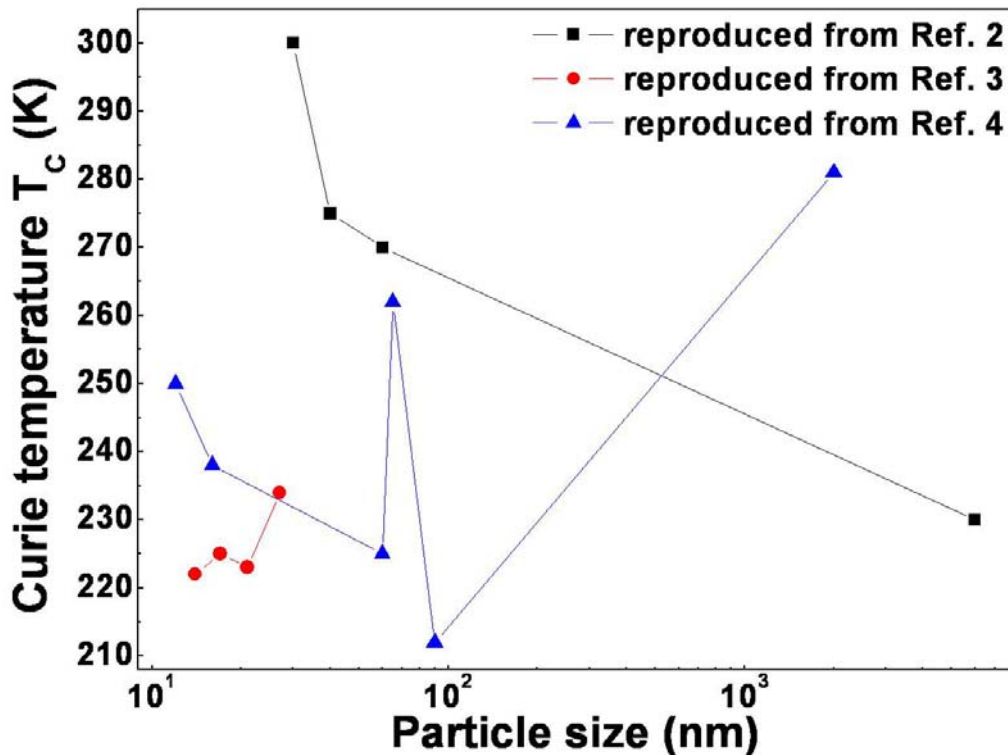
Fig.3.1. Variation of T_C with particle size for $La_{0.67}Ca_{0.33}MnO_3$ as reported in references 2, 3 and 4.

b) **Structural effects:** As has been emphasized in Chapter 1, the crystal structure often dictates the physical properties in these oxides. Also, size reduction often works in a way which is equivalent to increasing the externally applied hydrostatic pressure. Hence, it is expected that size reduction might lead to changes in the crystal structure (as a response to the pressure effect) which might be large enough to change the ground state/physical properties of the system. This particular effect has never been carefully looked into in the previous studies on nanocrystalline manganites.

c) **Core shell structure:** Most magnetic nanoparticles form a core shell structure with a magnetically ordered core and a magnetically disordered shell. The disordered shell leads to a decrease in the value of magnetization, and the extent of decrease depends on the ratio of the core diameter to the shell width. An increase in the surface to volume ratio leads to an increase in the number of broken bonds in the nanoparticles which in turn can lead to a decrease in the ferromagnetic ordering temperature.

d) **Single domain effects and superparamagnetism:** A decrease in the particle size causes a transition from a multi domain particle to a single domain particle. A further reduction in the

particle size may cause the particles to become superparamagnetic and lose their ferromagnetic properties.

e) **Nature of the ferromagnetic to paramagnetic transition:** The nature of the FM-PM transition has been known to show a sensitivity to effects such as site and surface disorder[5,6]. Finite size effects may also lead to the rounding off of a first order FM-PM transition and may even change its nature.

f) **The magnetic structure and spin order:** It is appreciated that in materials like the perovskite oxides, the physics is indeed complex. In fact, if the nature of the interaction that leads to ferromagnetism in these oxides differ, then one would expect that the effect of size reduction will also be different in them. Since this is indeed an important issue, we have compared the physics of size reduction in two different ferromagnetic oxides, namely $La_{0.67}Ca_{0.33}MnO_3$ (LCMO, x = 0.33) and $La_{0.5}Sr_{0.5}CoO_3$ (LSCO, x = 0.5) both of which have comparable $T_C \approx$ 250 K – 270 K in the bulk state.
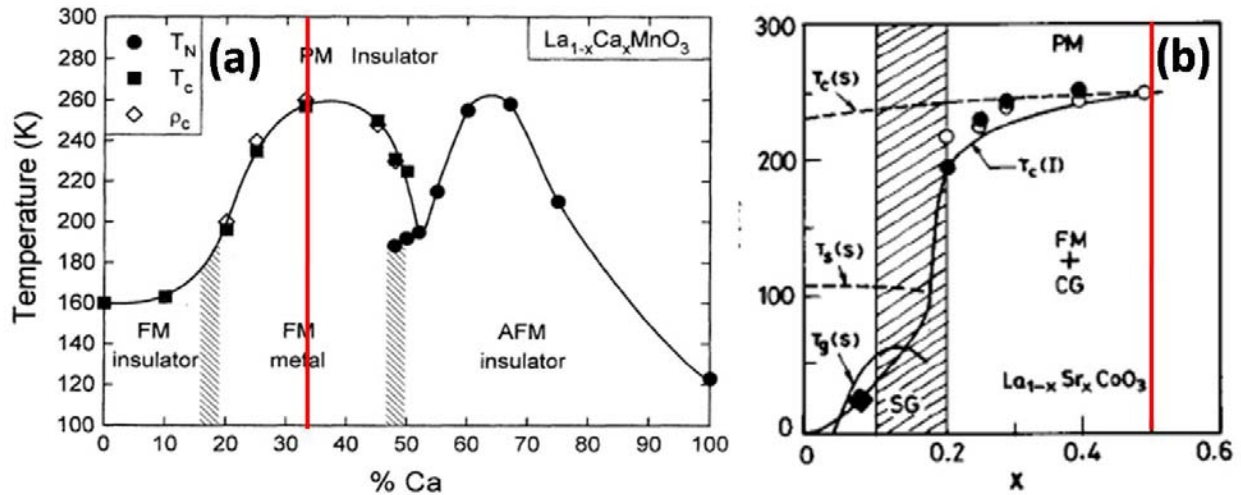
Fig.3.2. Phase diagram of (a) $La_{1-x}Ca_xMnO_3$ (reproduced from [7]) and (b) $La_{1-x}Sr_xCoO_3$ (reproduced from [8]).

The most obvious similarity between the two (as can be seen from their phase diagrams given in Fig.3.2) is that their ferromagnetic Curie temperatures are comparable to each other (T_C (LCMO) = 265 K and T_C (LSCO) = 250 K). Also, in both oxides, the ferromagnetic state is coupled with the metallic state i.e. both show a metallic nature below their respective T_C. Despite these apparent similarities, many differences also crop up on further scrutiny. We list these differences below:

1. Even though both $La_{0.67}Ca_{0.33}MnO_3$ and $La_{0.5}Sr_{0.5}CoO_3$ arise via hole doping (by substitution of divalent Ca^{2+} and Sr^{2+} in place of trivalent La^{3+}) in the parent compounds, $LaMnO_3$ and $LaCoO_3$ respectively, but the resulting spin structures in the two systems differ from each other. We have already given details of the spin structure of the two systems (highlighting the differences) in Section 1.9 of Chapter 1.

83

2. The difference in the spin structure leads to a difference in the mechanism through which ferromagnetism arises in the two systems. While ferromagnetism in the manganites arises from the double exchange mechanism between the Mn^{3+} and Mn^{4+} ions (the double exchange mechanism has been detailed in Section 1.5 of Chapter 1), in the cobaltates, the superexchange interaction between Co^{IV}-O-Co^{3+} or Co^{4+}-O-Co^{3+} is the cause of ferromagnetism. Unlike in the case of manganites, the cobaltates do not have a half – filled t_{2g} level (see Fig.1.14 of Chapter 1). Thus, the core spin is absent in the cobaltates which in turn leads to a less strong Hund's coupling. This favours the superexchange mechanism over the double exchange mechanism in cobaltates. Another difference arises from the fact that no thermal variation of the spin state of the Mn ion is known. In contrast, in the cobaltates, thermal excitation can provide a transition from the low spin to the high spin state. We have highlighted the differences in the spin structure in the two oxides in details in Section 1.9 of Chapter 1.

3. The nature of the ferromagnetic state obtained on cooling below the ordering temperature is also different for the two oxides. While in LCMO, the resulting state below T_C is a long range ferromagnet, LSCO below T_C does not have a long range ferromagnetic order. Rather, we get a cluster glass like state with ferromagnetic regions embedded in a nonferromagnetic matrix.

4. The nature of the ferromagnetic to paramagnetic (FM-PM) phase transition also differs in the two oxides. While the FM-PM phase transition in bulk LCMO in the composition range of interest ($x \approx 0.33$) is of a first order type, in bulk LSCO the FM-PM transition is of a second order type.

In this chapter we will explore the above issues in nanocrystals of these materials.

The above discussion was done to explain the principal motivation of this chapter and also to point out the types of issues we will discuss. Below we itemize the specific issues that we will investigate:

1. What happens to the ferromagnetic Curie temperature in the complex oxide nanoparticles on size reduction? Does it increase or decrease, and what are the reasons either way? Can the finite size scaling law describe the change in T_C in these complex oxides?

2. Does size reduction lead to any change in the crystal structure symmetry? If yes, then how does the symmetry change, and if no, then are there any changes in the values of the structural parameters (lattice parameters, bond lengths, bond angles etc.)? More importantly, how does the change in the structure (if any) affect the physical properties (specifically, the magnetic state) of the system? In particular, we explore the ferromagnetic order as seen through magnetic neutron scattering.

3. Do the nanoparticles of LCMO and LSCO show any core shell structure? To what extent does the disordered shell (if present) affect the magnetic properties of the nanoparticles?

4. Are the nanoparticles studied in this chapter small enough to show single domain effects and superparamagnetism? Is there any difference between the two systems when they are in these size ranges?

5. How does the nature of the ferromagnetic to paramagnetic phase transition change as a result of size reduction? This study is done only in the context of LCMO (which shows a first order FM-PM transition in the bulk state).

This chapter has been organized in two distinct parts. In the first part we discuss the case of LCMO (x = 0.33) nanocrystals and in the second part we discuss the LSCO (x = 0.5) nanocrystals followed by a comparison of these two systems.

3.2 $La_{0.67}Ca_{0.33}MnO_3$

3.2.1 Experimental and Observed Results

3.2.1.1 Samples

Before going into details of the experimental results, we make a list of the samples which have been studied. These samples were prepared using the chemical solution deposition (CSD) technique and were characterized using x – ray diffraction and imaging tools like transmission electron microscopy (TEM) and field emission gun scanning electron microscopy (FEG-SEM). The synthesis and characterization details have already been given in Chapter 2, and will not be repeated here. We simply give a list of the samples alongwith their average particle size, size distribution, oxygen deficiency ε ($La_{0.67}Ca_{0.33}MnO_{3-\varepsilon}$) and ferromagnetic Curie temperature in Table 3.1 below. The average particle sizes for samples A, B and E were estimated from TEM images and XRD data, and for samples C and D, the size was estimated from SEM images.

Table 3.1 Sample ID, average particle size, size distribution, oxygen deficiency and ferromagnetic Curie temperature of $La_{0.67}Ca_{0.33}MnO_3$ samples

Sample ID	Particle size (d) (nm)	Δd/d (%)	ε	Curie temperature (T_C) (K)
A	15 ± 2	13 %	0.02	242
B	50 ± 15	30 %	0.04	294
C	300 ± 40	13 %	0.03	277
D	21500 ± 2000	9 %	0.05	265
E	23 ± 5	21 %	0.02	259

Note: Samples A – D were used for detailed structural (crystal as well as magnetic structure) studies, while sample E was used for detailed magnetic studies.

As can be seen from the above table, sample B showed a large enhancement of the Curie temperature (by ~ 30 K). The size distribution of this sample was also greater than the average size distribution of 15 %. This prompted us to look more carefully into this size region to see whether the non monotonous dependence of T_C on the particle size can be reproduced. For this

purpose we synthesized a second batch of samples in the size range of 15 – 600 nm. This second batch of samples were prepared and the magnetic measurements on them were done by Mr. Hitesh P. Chauhan, M. S. University of Baroda, Vadodara as part of his M.Sc. project. A list of these samples is given in Table 3.2 along with the average particle size.

Table 3.2 Average particle size and ferromagnetic Curie temperature of 2nd batch of $La_{0.67}Ca_{0.33}MnO_3$ samples ($\Delta d/d \sim 10\%$)

Particle size (d) (nm)	Curie temperature (T_C) (K)
12	235
30	262
46	266
115	268
150	272
175	275
190	271
220	274
310	275
575	276

3.2.1.2 Determination of T_C

Before proceeding with any other study, it was essential to check the Curie temperatures of the samples. This was necessary in order to establish that the samples that we are working with remain ferromagnetic even after size reduction of almost four orders of magnitude. This concern arises from the fact that magnetic properties at the nanoscale might be quite different from those observed in the bulk material. As emphasized earlier, finite size effects and enhanced surface to volume ratio can often change material properties drastically. Thus, a preliminary check of the ferromagnetic Curie temperatures was made by measuring the zero field cooled (ZFC) M versus T curves for the samples at a low field of H = 1 mT. The ZFC curves for the samples listed in Table 3.1 are shown in Fig.3.3. The ZFC curves for samples A – D were also used to determine the temperatures at which the neutron diffraction scans were taken. The neutron diffraction measurements were done to probe the crystal and magnetic structure of the sample, which we come to in the next section. The ZFC curves for some of the samples listed in Table 3.2 are shown in Fig.3.4 (the curves for all the samples are not shown for the purpose of clarity).
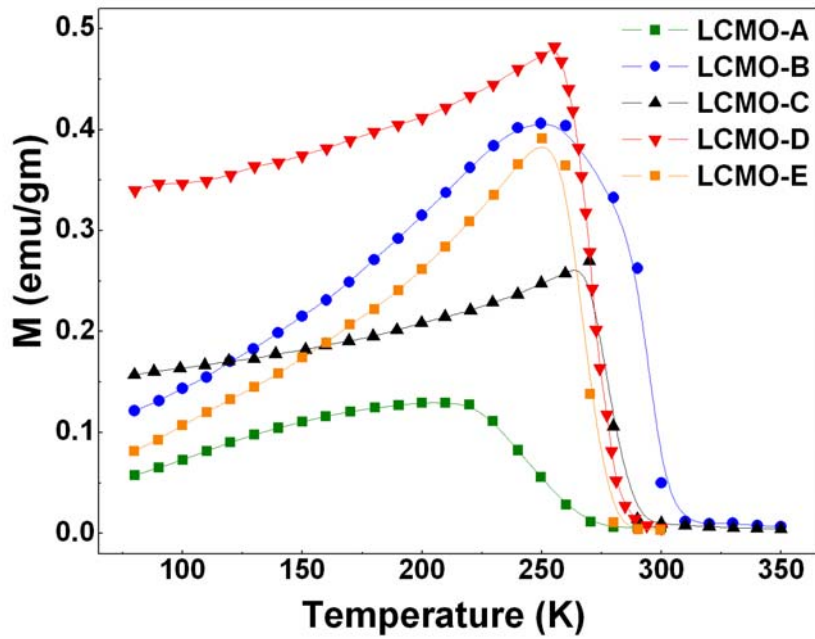
Fig.3.3. Zero field cooled M vs T curves taken under a magnetizing field of H = 1 mT for La$_{0.67}$Ca$_{0.33}$MnO$_3$ samples listed in Table 3.1.
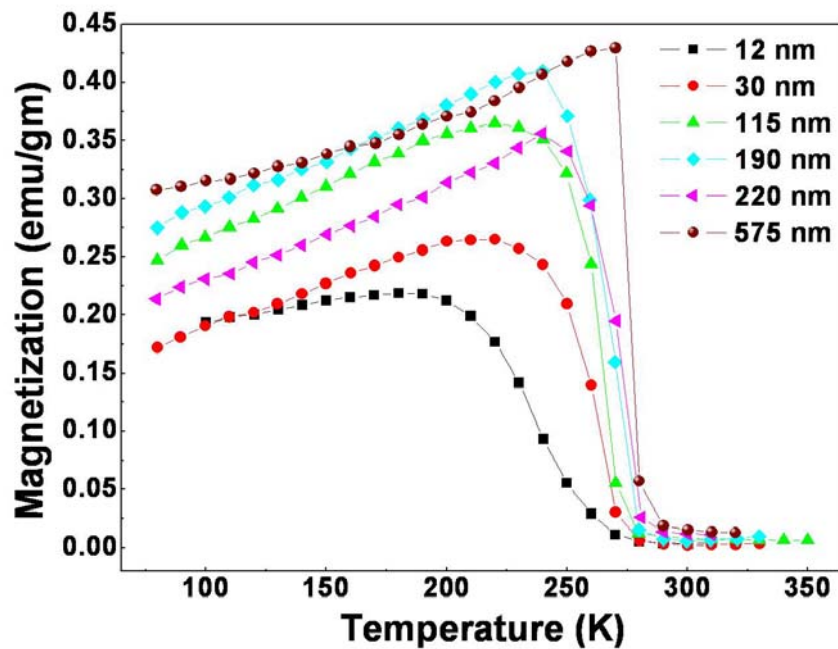
Fig.3.4. Zero field cooled M vs T curves taken under a magnetizing field of H = 1 mT for La$_{0.67}$Ca$_{0.33}$MnO$_3$ samples listed in Table 3.2.

In Fig.3.5, we show the variation of T_C with particle size (d). The curve shows a maximum at d = 50 nm. We will come back to this point and discuss it in details later in this chapter. As mentioned earlier, a very careful measurement of size dependence of T_C was needed fbecause of this non – monotonic dependence of T_C on the diameter (d) of the sample for which we prepared the second batch of samples. The T_C obtained in these samples are also shown in Fig.3.5 (as a red curve). Though this second batch of samples did not show the 10 % increase in T_C that we had obtained in sample B, but it is clear from Fig.3.5 that there is a transition region around d = 50 nm (marked by an arrow in the figure). It can be seen that there is a small but finite increase in T_C as the particle size is decreased to ~ 200 nm, below which the downturn occurs. Below 50 nm, the value of T_C becomes smaller than bulk T_C. A comparison of Fig.3.5 with Fig.3.1 (where we have shown the variation of T_C with particle size for LCMO nanoparticles obtained by other groups), show that our batch of samples covers a wider spectrum of particle sizes so that we reproduce the behavior of Ref 2 and Ref 3. Here, we note that the samples in Ref 4 were prepared by ball milling and so might have a lot of oxygen vacancy. Due to the difference in the method of preparation, the samples in Ref 4 cannot be strictly compared with our samples.
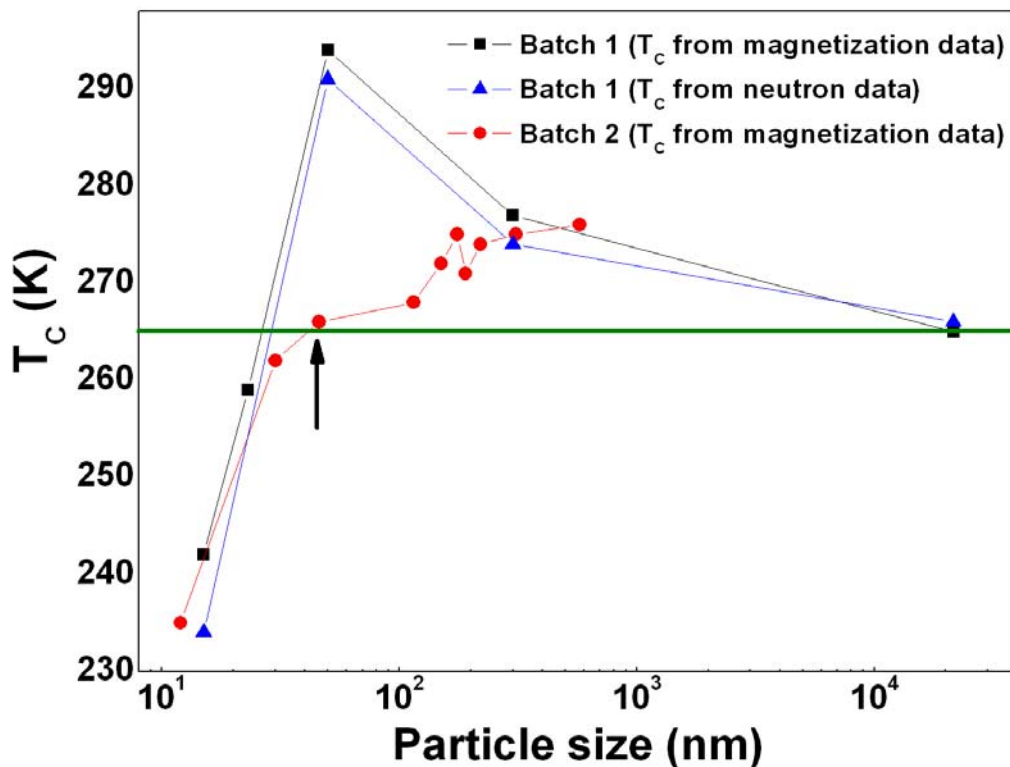
Fig.3.5. Variation of T_C vs d for $La_{0.67}Ca_{0.33}MnO_3$ samples. The blue line marks the most observed T_C values of bulk LCMO.

The typical good "bulk" polycrystalline samples of LCMO (x = 0.33) show T_C in the range $\approx$ 260 – 270 K. In epitaxial films, the T_C is dependent on strain and can vary considerably depending on the residual strain in the film. In good low strain epitaxial films of LCMO (x = 0.3) grown on lattice matched $NdGaO_3$ substrates, T_C (or T_P) $\approx$ 268 K[9]. In Fig.3.5, we have marked the most observed T_C values of bulk LCMO by a green line. The enhancement of T_C on size reduction is obvious for d $\geq$ 50 nm. For d $\leq$ 50 nm, T_C again decreases (with respect to the bulk T_C). This critical size ($d_{critical}$) is marked by an arrow in Fig.3.5. In Fig.3.6, we show finite size scaling plots for LCMO (both nanoparticles as well as film) using the relation $\frac{T_C(\infty) - T_C(d)}{T_C(\infty)} = \pm \left(\frac{d}{\xi_0} \right)^{-\lambda}$, where $T_C(\infty)$ corresponds to the bulk Curie temperature and ξ_0 should be of the order of a characteristic microscopic dimension. For the nanoparticles, we have plotted data only for those samples where $T_C(d) < T_C(\infty)$ i.e. for the samples where T_C decreases with respect to the bulk sample. The LCMO film follows the finite size scaling relation with λ = 0.9 $\pm$ 0.06 and ξ_0 = 1.5 nm. The nanoparticles, on the other hand, show a very large value of λ (= 2.6 $\pm$ 0.1) and ξ_0 = 2.1 nm.
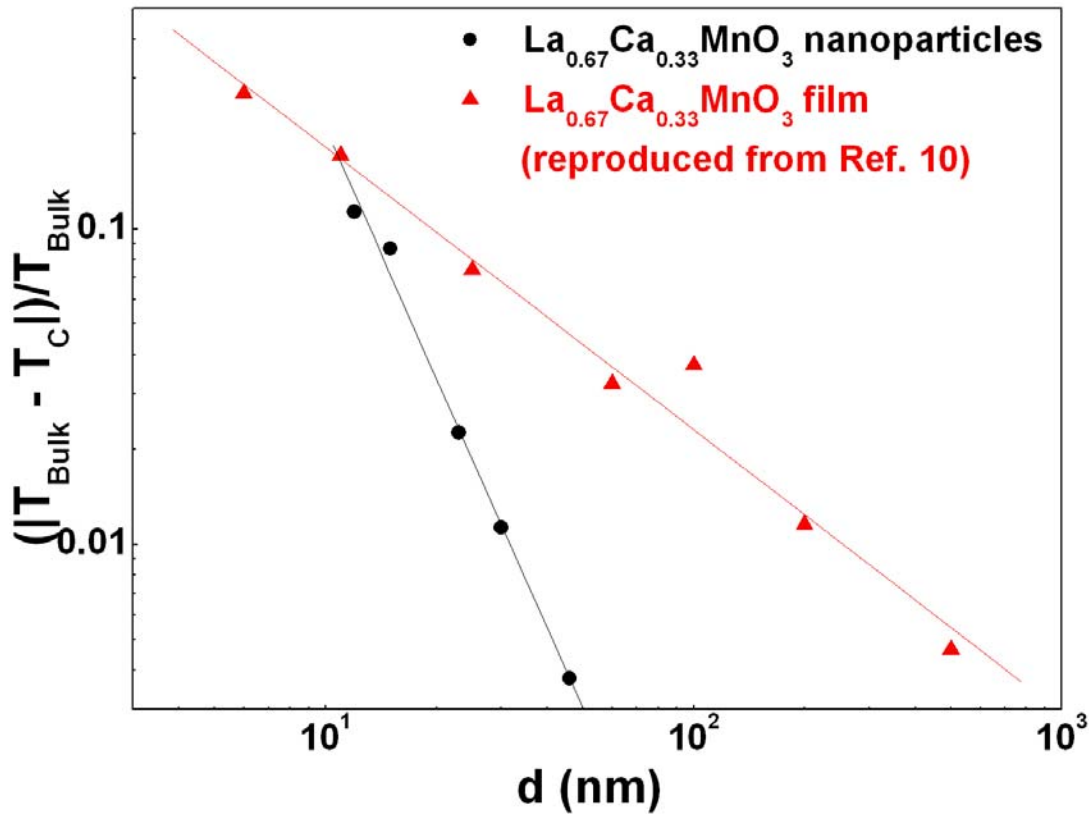
Fig.3.6. Finite size scaling plots for LCMO nanoparticles and LCMO film.

3.2.1.3 Neutron diffraction data

The structural analysis, including magnetic structural analysis, were done for samples A – D using neutron diffraction data. This gave us a dual advantage of being able to obtain the crystal as well as the magnetic structure. The neutron powder diffraction measurements were carried out at the Dhruva reactor (beam port T1013) at Trombay, India. A wavelength of 1.249 Å was used and a scattering angular range of $2\theta = 5^0 - 140^0$ was covered. The beam was made monochromatic by using a Germanium crystal monochromator ((331) reflecting plane). The typical neutron flux was 8.5 X 10^5 neutrons/cm^2/sec and a beam size of 4 cm X 1.5 cm was used. The powders were packed in a Vanadium can of height 60 mm and diameter 6 mm. The measurements were done with no external magnetic field and at different temperatures between 20 K and 320 K. For low temperature scans, a closed cycle refrigerator was used. The scans for all four samples for all temperatures are shown in Fig.3.7, Fig.3.8, Fig.3.9 and Fig.3.10. A detailed analysis of the neutron data are done in subsequent sections. This part of the work was done in collaboration with the group of Dr. S. M. Yusuf of BARC, Trombay, India.
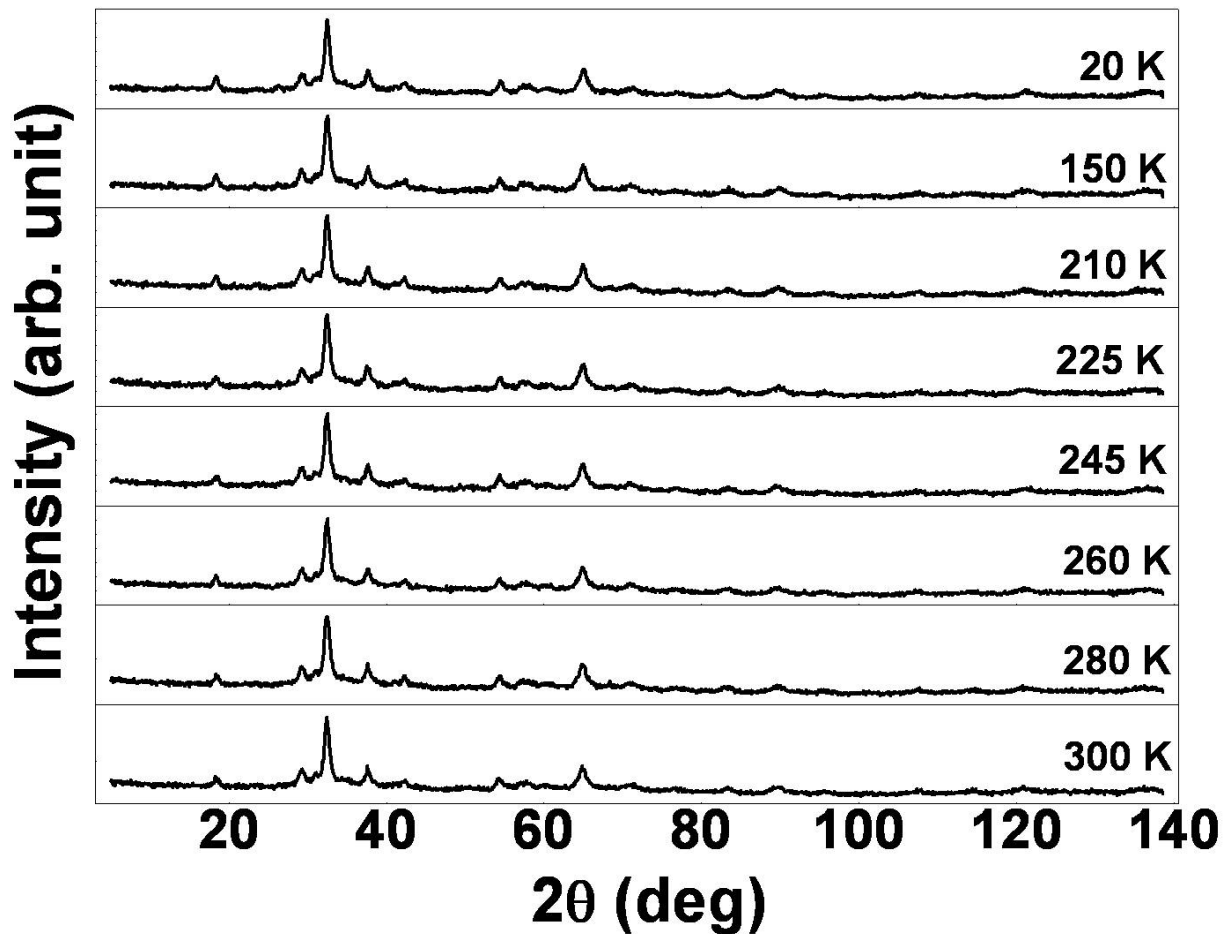
Fig.3.7. Neutron diffraction patterns for LCMO-A taken at different temperatures between 20 K and 300 K.
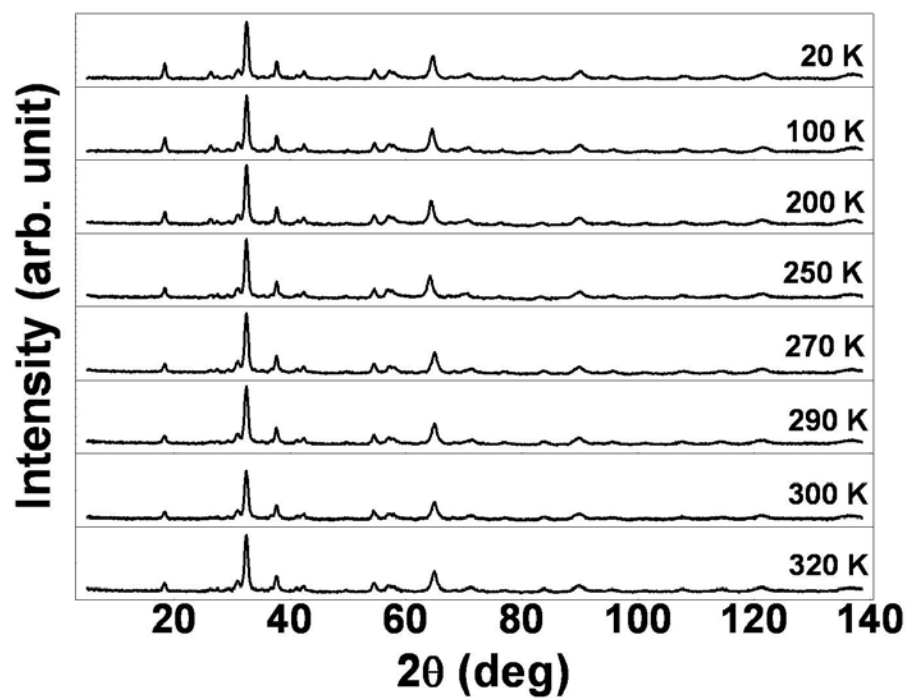
Fig.3.8. Neutron diffraction patterns for LCMO-B taken at different temperatures between 20 K and 320 K.
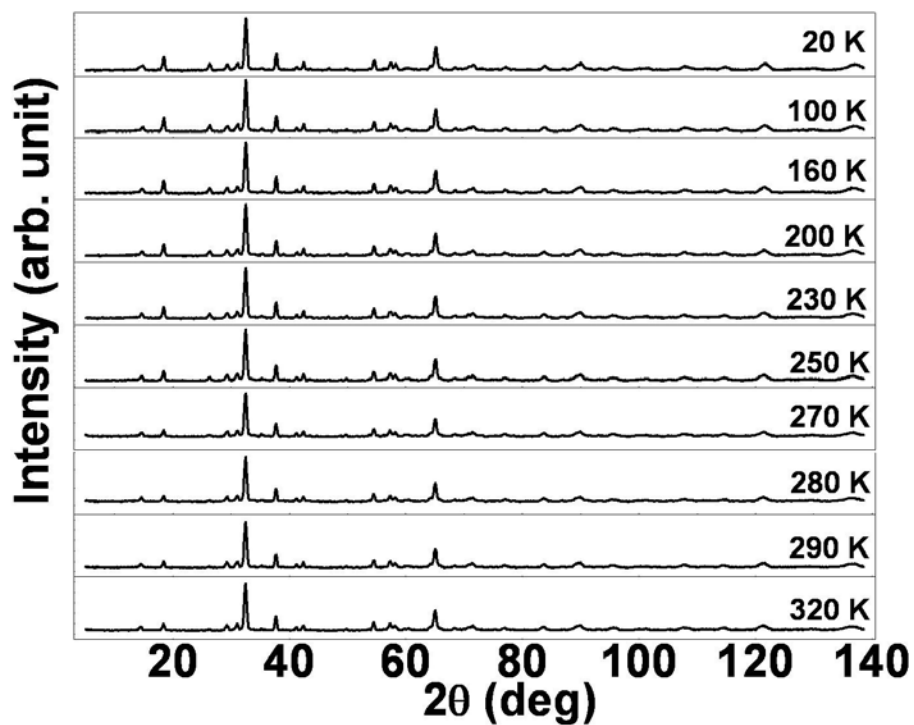
Fig.3.9. Neutron diffraction patterns for LCMO-C taken at different temperatures between 20 K and 320 K.
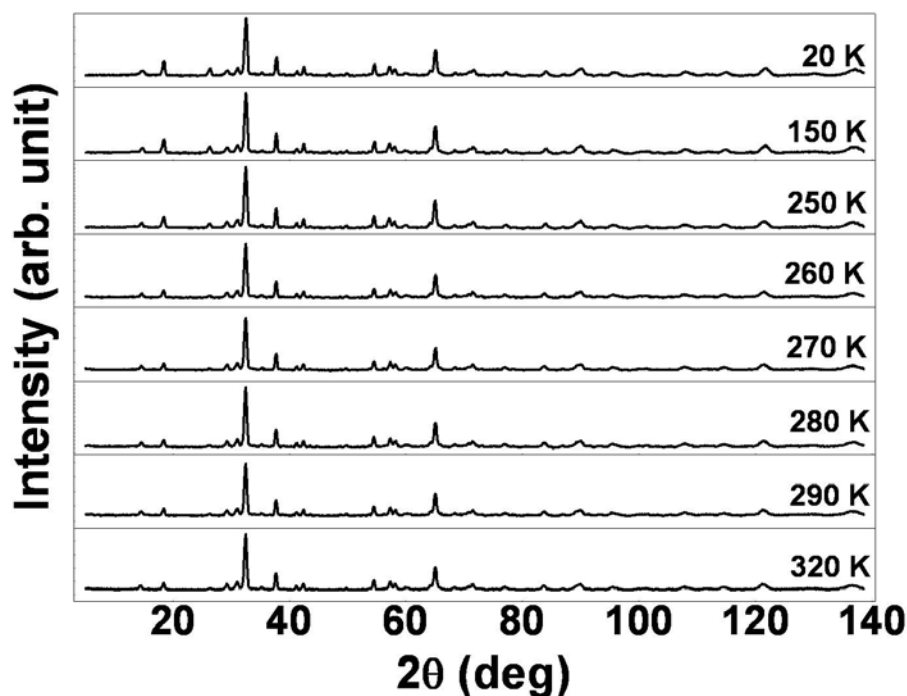
Fig.3.10. Neutron diffraction patterns for LCMO-D taken at different temperatures between 20 K and 320 K.

3.2.1.4 Magnetization data

The detailed magnetization data in these materials have been acquired in two stages. In the first stage, we observed the M-H and M-T data over a wider temperature range to study the variation of M_S and the coercive field (H_C) with size. In the second stage, we studied the M-H and M-T data close to T_C to study the nature of the magnetic phase transition. In this part we present only the first stage data. This also includes detailed zero field cooled (ZFC) and field cooled (FC) studies of magnetization at different fields on sample E (size $\approx 23 \pm 5$ nm). Sample E was specifically chosen for detailed magnetization measurements because it has a transition temperature very close to the bulk T_C, but a particle size less than 4 orders smaller than the bulk sample (sample D).

The M-H curves taken at T = 80 K for a number of samples of different particle sizes are shown in Fig.3.11. The data for the samples which have been tabulated in Table 3.1 are shown in Fig.3.11(a) and those for the samples listed in Table 3.2 are shown in Fig.3.11(b).

92
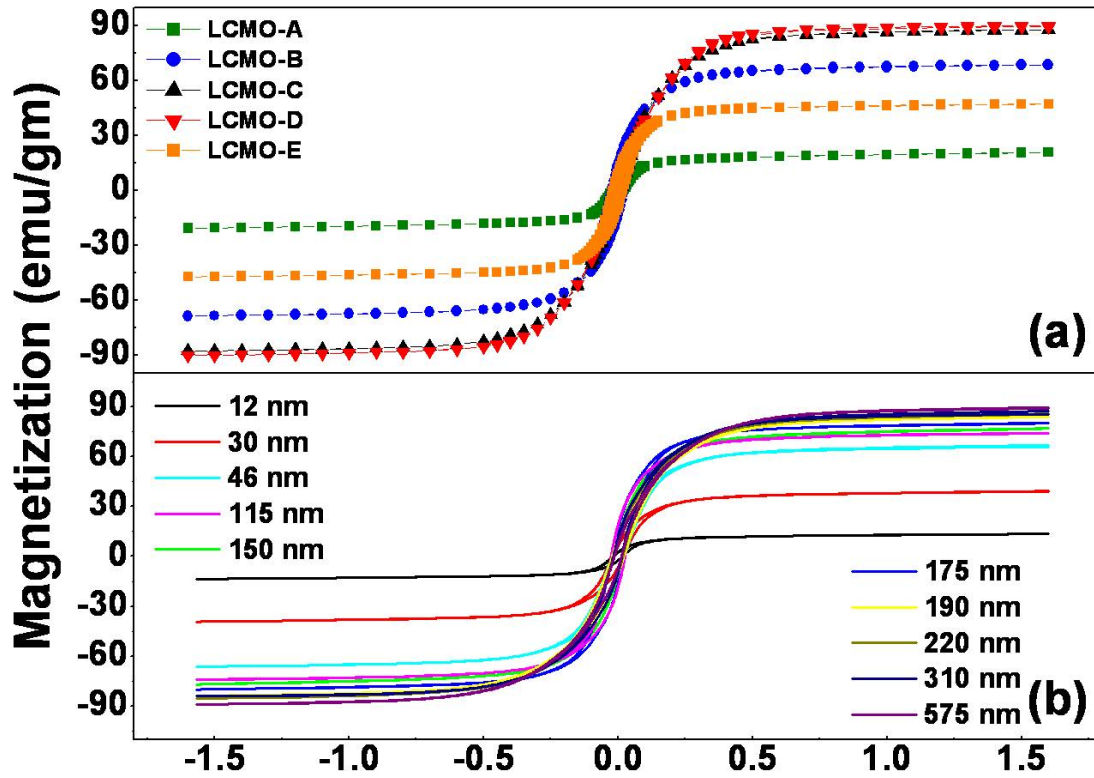
Fig.3.11. M-H curves taken at T = 80 K for LCMO samples of different particle size (a) for samples of batch 1 (Table 3.1) and (b) for samples of batch 2 (Table 3.2).

The value of the magnetization (M) at H = 1.6 T taken at T = 80 K is around 85 % of the saturation magnetization M_S. Thus, a plot of M (at H = 1.6 T and T = 80 K) as a function of particle size (d) will reflect the dependence of M_S on d. This is shown in Fig.3.12. The magnetization is almost size independent down to d = 200 nm, followed by a shallow dip, and below d = 100 nm it reduces sharply. In the same graph, we show the spontaneous moment at T = 20 K determined from the neutron data as a function of the particle size d. The local moment does not show the shallow dip below 200 nm. It retains its value till ~ 50 nm below which it goes down sharply. We show later that the drop of the magnetization (and likely that of T_C, as seen in Fig.3.4) is a consequence of the "magnetic" core – shell structure of the nanoparticles.
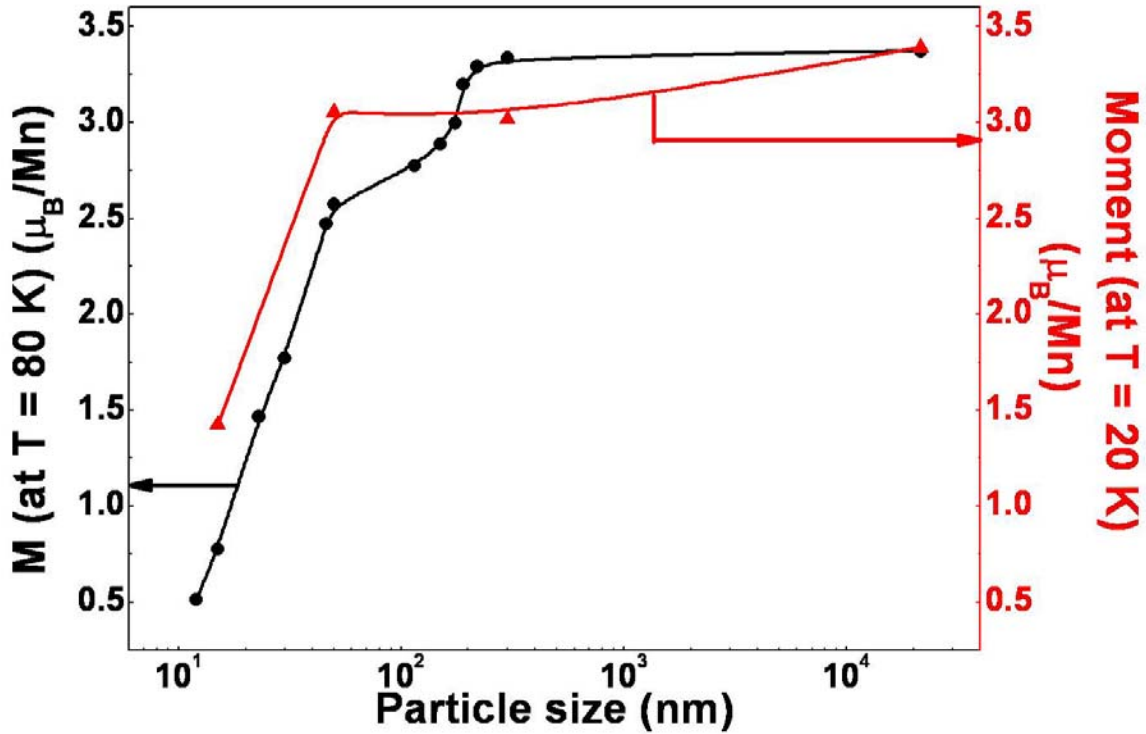
Fig.3.12. Plot of magnetization at T = 80 K (black curve) and spontaneous moment at T = 20 K (red curve) as a function of the average particle size (d).

In Fig.3.13 we show the field cooled (FC) and zero field cooled (ZFC) magnetization data for different values of applied field ranging from 1 mT to 1 T for LCMO-E (the ZFC curves are shown by continuous lines while the FC curves are shown by symbols + lines). We see typically three kinds of behaviours depending upon the value of the applied field. At very low fields (H < 0.05 T), the ZFC curves show a broad maximum. The position of this maximum is shifted to lower temperatures as H increases. At intermediate field values (0.05 T < H < 0.1 T), the ZFC magnetization is characterized by an abrupt increase at low temperatures, followed by a smooth evolution to a plateau before merging with the FC curve. For higher values of H, the ZFC and FC curves are superimposed, saturating at low temperature. It takes an applied field as high as 1 T to close the gap between the FC and ZFC curves. For comparison, in Fig.3.14, we show the FC and ZFC magnetization data taken at H = 1 mT and 0.1 T for LCMO-D (which is taken as the bulk reference). It is seen that in the bulk sample (unlike that in the nanoparticle sample), an applied field of 0.1 T is sufficient to close the gap between the FC and ZFC curves. This field is one order less than what was required for the ZFC curves of the nanoparticle sample to saturate.
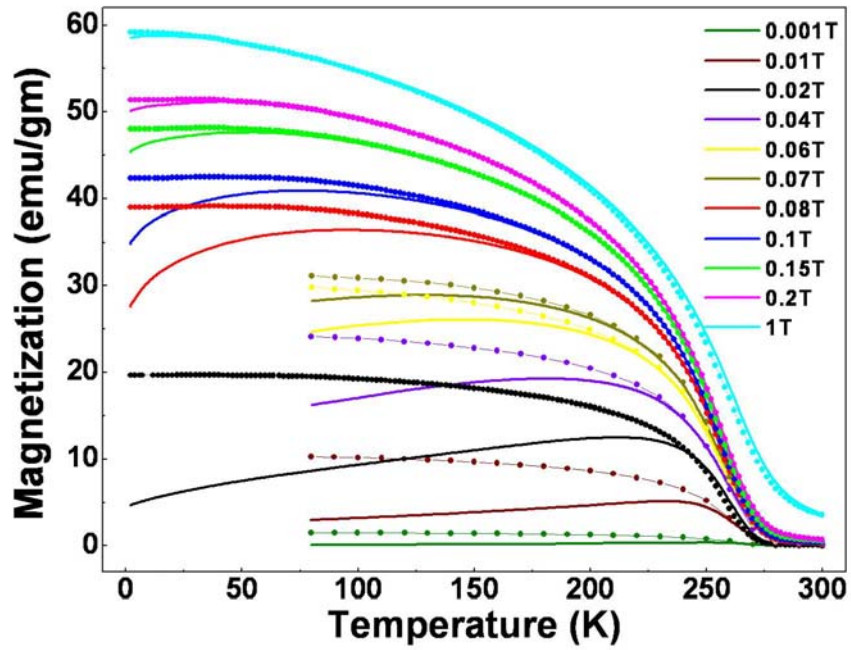
Fig.3.13. ZFC and FC curves for LCMO-E (d ≈ 23 ± 5 nm) taken under different magnetic fields.
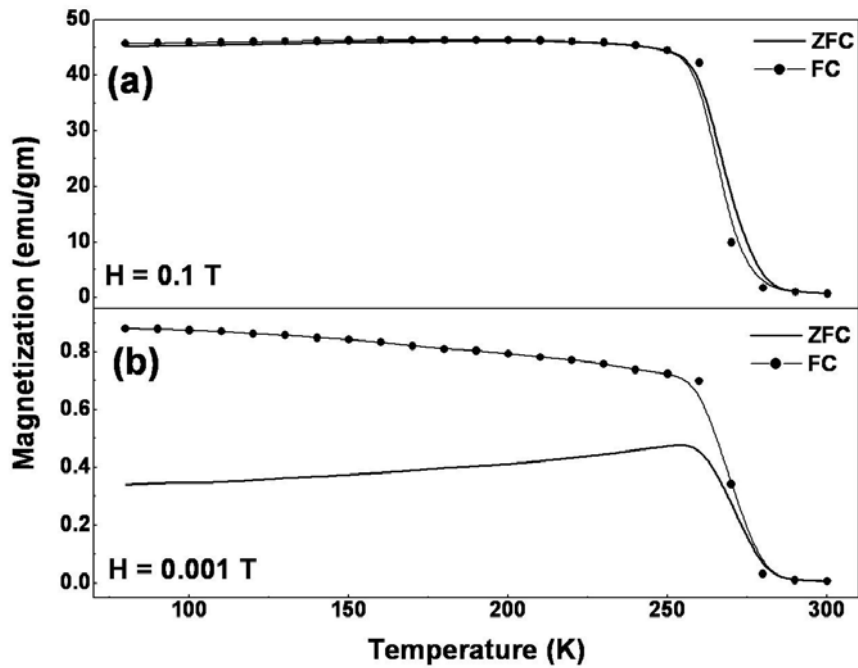
Fig.3.14. ZFC and FC curves for LCMO-D taken under (a) H = 0.1 T and (b) H = 0.001 T.

The two characteristic temperatures, T_B (where the FC and ZFC magnetization curves bifurcate) and T_P* (where the ZFC magnetization shows a peak), are shown in the inset of Fig.3.15 for a typical curve. T_B marks the temperature above which the system is in the same ferromagnetic state in both the ZFC and FC processes. Below T_B, the magnetization is irreversible, and the magnetic state of the sample depends on the externally applied field. This irreversibility between M_{ZFC} and M_{FC} can arise either due to a large magnetocrystalline anisotropy or from a spin glass like nature of the sample. In Fig.3.15, we show the variation of T_B and T_P* as a function of applied field H for the nanoparticle sample (LCMO-E). In Fig.3.16, we show the variation of the coercive field H_C as a function of the particle size (d) (Fig.3.16 (b)) as well as a function of T (for the nanoparticle sample, LCMO-E, Fig.3.16 (a)).
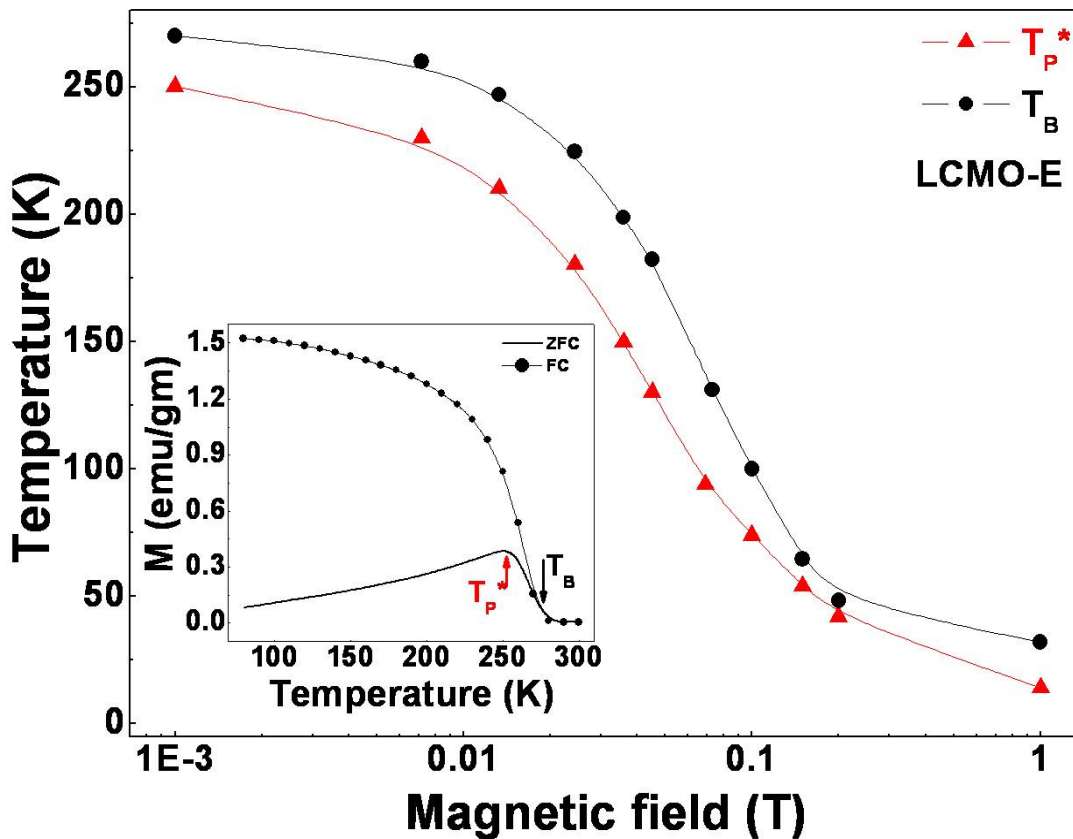
Fig.3.15. Variation of T_B and T_P* as a function of the applied magnetic field for LCMO-E. The inset shows a typical magnetization curve indicating the positions of T_B and T_P*.
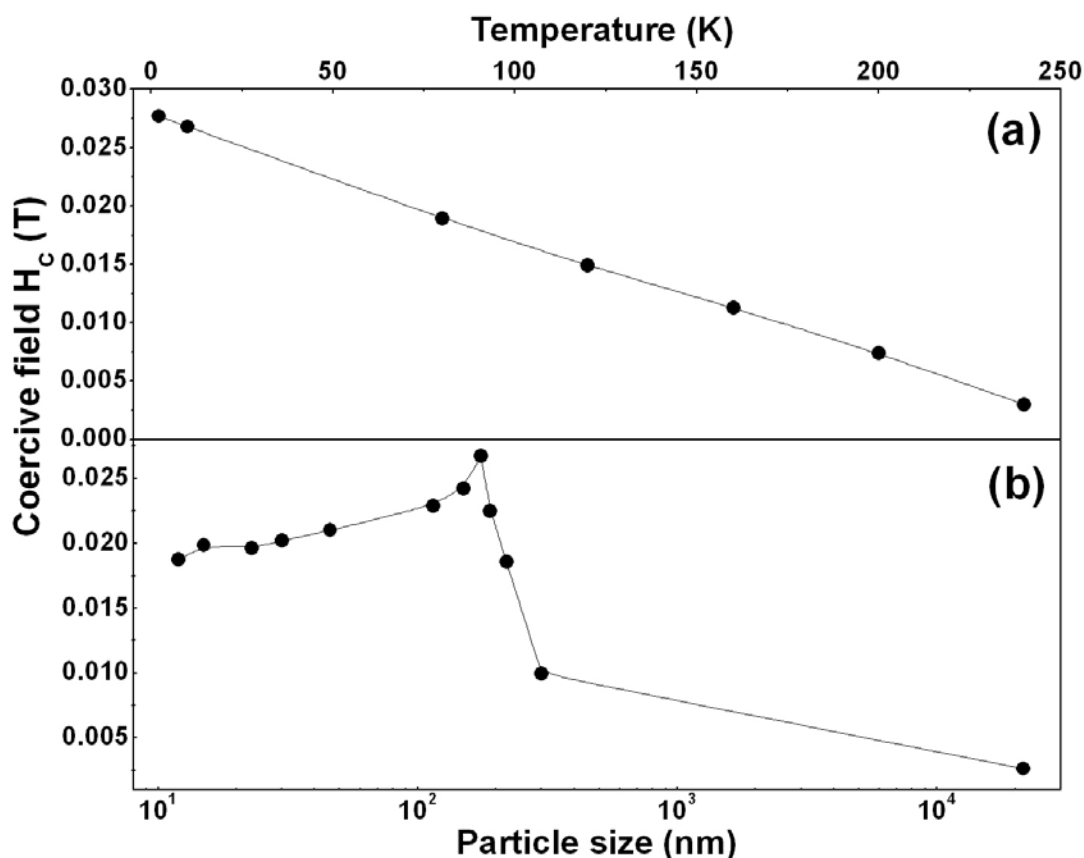
Fig.3.16. Variation of coercive field for LCMO samples as a function of (a) temperature (for LCMO-E) and (b) particle size.

The extensive magnetization data taken on these materials show that nanoparticles of manganites are rather distinct from nanoparticles of other ferromagnets like Fe_3O_4[11] and Ni[12]. We discuss these issues in details later.

3.2.2 Analysis of results and Discussions

3.2.2.1 Neutron data

A detailed two – phase Rietveld analysis (with a structural phase and a magnetic phase) was done to extract the various structural and magnetic parameters. The space group *Pnma* was used for both the phases. The line profiles were modeled using a Pseudo – Voigt profile shape function. The Rietveld analysis was done using the FullProf Suite software[13]. As an example of the fits obtained, we show, in Fig.3.17, the neutron diffraction pattern of LCMO – A (alongwith the fits) taken at the lower most temperature of T = 20 K. In the inset, we show the expanded region between $2\theta = 16^0 - 27.5^0$ to show the two magnetic Bragg peaks. (By magnetic Bragg peaks we refer to those Bragg peaks that are also related to magnetic order.) In contrast to

antiferromagnetic order, in ferromagnetic materials the magnetic order is commensurate with structural order. Hence no extra peaks are seen in ferromagnetic materials when the samples are cooled below the ferromagnetic to paramagnetic phase transition. The temperature evolution of the intensity of the two magnetic Bragg peaks are shown in Fig.3.18 (a) and (b) respectively. For comparison, we also show the temperature evolution of a peak which is not linked to magnetic order ((422) at $2\theta = 65.2^0$) in Fig.3.18 (c). The intensity of this peak remains essentially temperature independent.
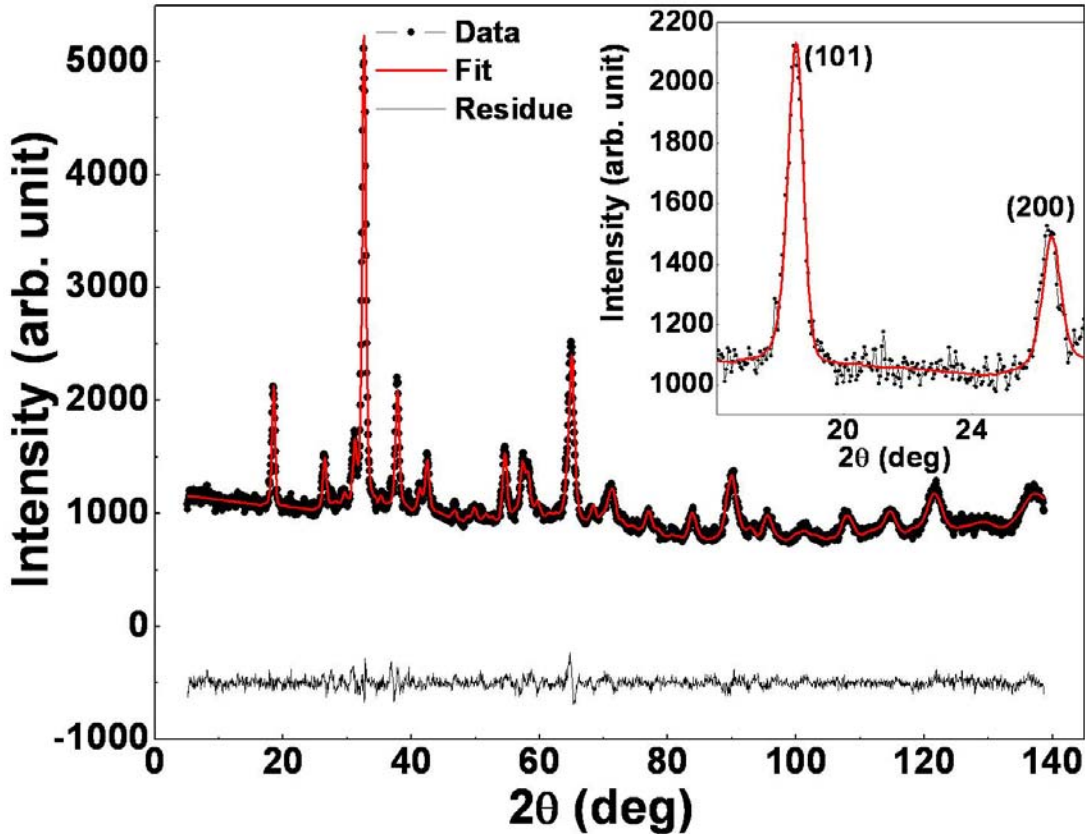
Fig.3.17. Neutron diffraction patterns for LCMO-A (alongwith the fits) taken at T = 20 K. The inset shows the expanded region between $2\theta = 16^0 - 27.5^0$ which shows two peaks ((101) and (200)) which are related to magnetic order.
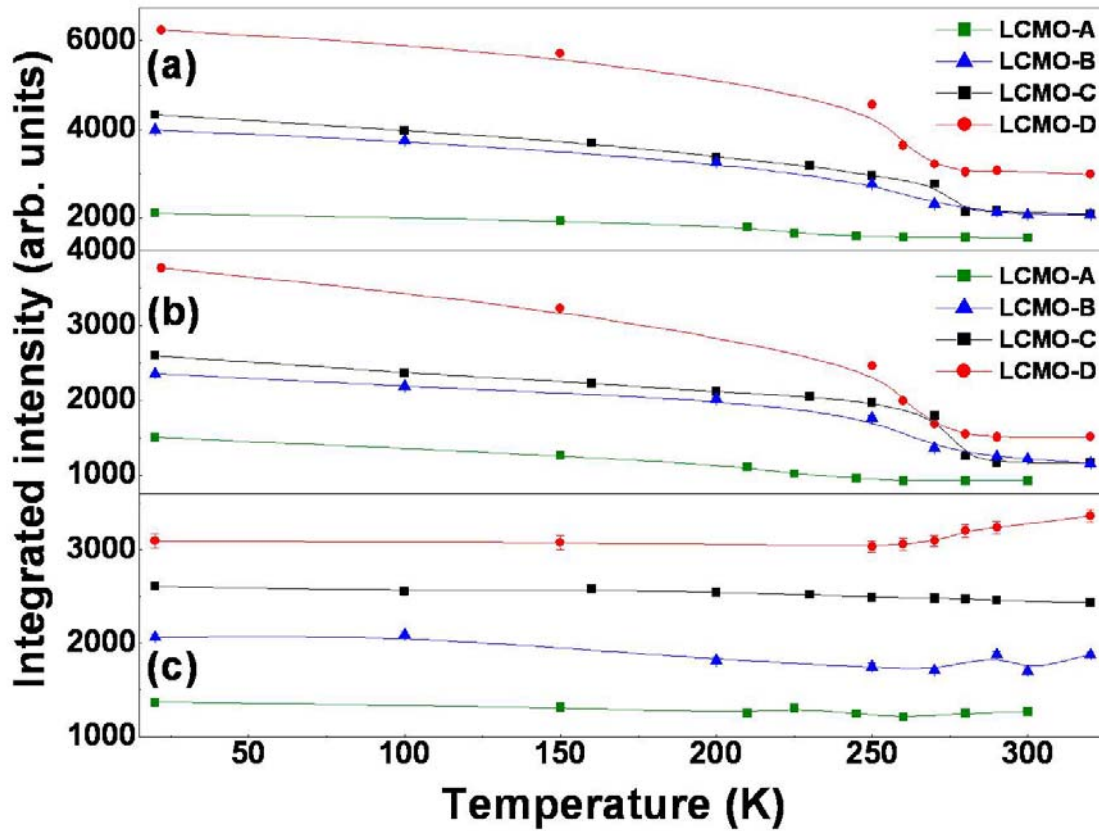
Fig.3.18. Temperature evolution of the intensity of (a) (101), (b) (200) and (c) (422) peak.

Magnetic structure information: The refinable parameters included the lattice parameters, the atomic positions as well as the magnetic vectors. Before elaborating on the structural parameters, we show, in Fig.3.19, the temperature evolution of the spontaneous moment in the four samples, which was obtained from the refinement of the magnetic phase in the neutron diffraction data. We note here that the neutron diffraction patterns were taken at zero external magnetic field, and the moment we observe is due to the internal molecular field that drives the material ferromagnetic. In Table 3.3, we compare the T_C obtained from the magnetization measurements and the neutron diffraction data (also shown in Fig.3.5). We note that the large enhancement in T_C of sample B has been seen in both the magnetization data as well as in the neutron measurements. Thus, it is not an artifact. By the end of this chapter, we will explain the peculiar non monotonic trend of T_C vs d as arising from a competition between two effects both of which arise as a result of size reduction. One of these effects is linked to the modification of the lattice structure of the system, and will become obvious from the results shown in the next section.

A very important outcome that arises from the neutron scattering data is the location and alignment of the magnetic moment. This is shown in the inset of Fig.3.19. Although the moment (average) decreases in particles of lowest dimensions, but it remains aligned in the same direction (b – axis) as that in the bulk.
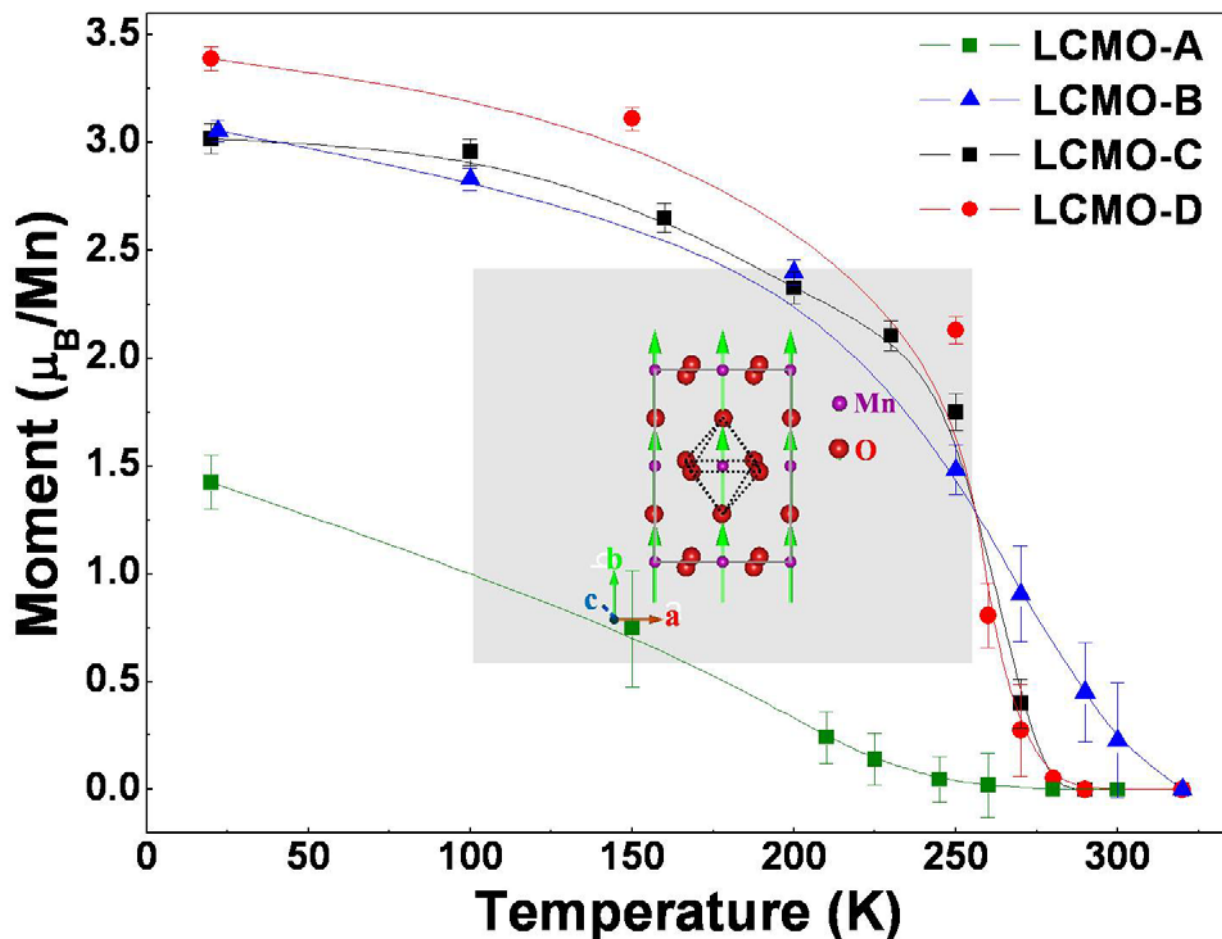
Fig.3.19. Variation of the spontaneous moment with temperature for LCMO-A, LCMO-B, LCMO-C and LCMO-D. Inset shows a schematic representation of the magnetic structure with all the moments aligned along the *b*-axis.

Table 3.3 Comparison of T_C of $La_{0.67}Ca_{0.33}MnO_3$ samples as obtained from magnetization measurements and neutron diffraction data

Sample ID	T_C (from ZFC curves)	T_C (from neutron diffraction data)
LCMO-A	242 K	234 K
LCMO-B	294 K	291 K
LCMO-C	277 K	274 K
LCMO-D	265 K	268 K

Crystal structure information: The temperature evolution of the lattice parameters and unit cell volume of the four samples are shown in Fig.3.20. No drastic change is noticeable in the lattice parameters as a function of size reduction. The only obvious change is a slight increase in the *b*-axis in the sample with the smallest average particle size (the *b*-axis increases by ~ 0.3% in LCMO-A, which leads to an increase of ~ 0.5% in the cell volume of LCMO-A). The

100

temperature dependence of the unit cell shows a small component associated with formation of the ferromagnetic order. This component is present in all the lattice parameters of the orthorhombic unit cell.
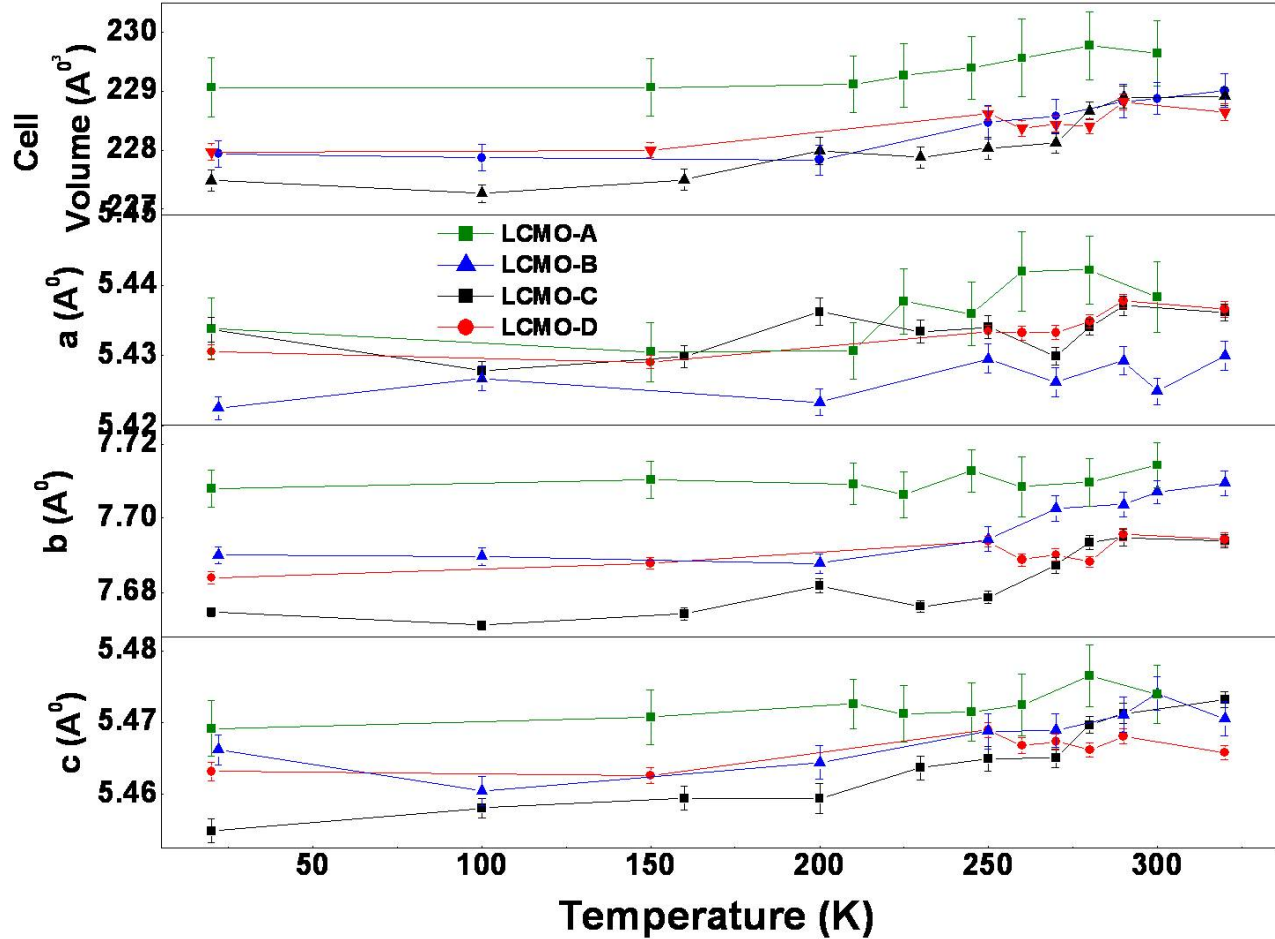
Fig.3.20. Variation of lattice parameters (lower three panels) and unit cell volume (upper panel) with temperature for LCMO-A, LCMO-B, LCMO-C and LCMO-D.

Rather than the lattice parameters, a more relevant feature to examine would be the orthorhombic strains, $OS_\perp$ and $OS_\parallel$. These quantities give a measure of the deviation of the unit cell from the perfect cubic structure. $OS_\parallel$ gives the strain in the ac plane and is defined as $OS_\parallel = \dfrac{2(c-a)}{c+a}$, while $OS_\perp$ gives the strain along the b axis with respect to the ac plane and is defined as $OS_\perp = \dfrac{2(a+c-b\sqrt{2})}{a+c+b\sqrt{2}}$. The orthorhombic distortion is related to the Jahn – Teller distortion that moves the system away from the cubic structure by distorting the MnO_6 octahedron. In certain doping concentrations, these orthorhombic strains become very indicative of what ground state the sample exists in. For example, in $La_{0.5}Ca_{0.5}MnO_3$, a cross-over from a ferromagnetic ground state to a charge – ordered antiferromagnetic ground state is accompanied

by a sudden increase in $OS_\perp$. The orthorhombic distortion in $La_{0.67}Ca_{0.33}MnO_3$ is much less compared $La_{0.5}Ca_{0.5}MnO_3$. We will deal with the half – doped manganite $La_{0.5}Ca_{0.5}MnO_3$ in details in Chapter 4. However, for a quick comparison, we show in Table 3.4, the values of $OS_\perp$ and $OS_{||}$ in LCMO (x = 0.33 and x = 0.5) for bulk as well as nanoparticles at the lowest temperature. As can be seen from the Table, for the bulk samples of LCMO, $OS_\perp$ is one order less for x = 0.33 compound than the x = 0.5 compound. These values of $OS_\perp$ actually reflect the fact in the x = 0.5 doping regime, the structure is more distorted, which in turn causes the ground state to move away from the ferromagnetic region (refer the phase diagram of LCMO shown in Fig.3.2(a)). Alternatively, a lower value of $OS_\perp$ will indicate a more cubic structure and hence a strengthening of the ferromagnetism. With this background in mind we note that $OS_\perp$ in nano $La_{0.67}Ca_{0.33}MnO_3$ has a much lower value than that in the corresponding bulk sample (lower by one order). This immediately points towards a strengthening of ferromagnetism with size reduction in $La_{0.67}Ca_{0.33}MnO_3$.

Table 3.4 Comparison of the values of $OS_\perp$ and $OS_{||}$ in LCMO (x = 0.33 and x = 0.5) at low temperature.

Composition	Particle size	$OS_\perp$	$OS_{||}$
$La_{0.67}Ca_{0.33}MnO_3$	Nano (15 nm)	0.0002	0.006
	Bulk (~ µm)	0.002	0.006
$La_{0.5}Ca_{0.5}MnO_3$	Nano (15 nm)	0.015	0.018
	Bulk (~ µm)	0.026	0.000018

In Fig.3.21, we show $OS_{||}$ (in the lower panel) and $OS_\perp$ (in the upper panel) for samples A – D. While $OS_{||}$ has a more or less similar value for all four samples, $OS_\perp$, while close in value for the four samples, nevertheless, can be distinguished into two groups. These two groups are demarcated by the pink line in the upper panel of Fig.3.21. It is clearly seen that the samples A and B (smaller size particles) have a slightly lower value of $OS_\perp$ than the samples C and D (larger size particles). Thus, the orthorhombic strain along the b-axis tends to decrease with a decrease in the particle size. The result, though quantitatively small, affects the qualitative behavior in an important way. As we have stated earlier, this points towards a tendency of strengthening ferromagnetism with size reduction. This can explain our observation of enhancement of T_C for sample B with respect to the larger particle size samples. Of course, the smallest particle size sample (sample A) again shows a reduced T_C, which we will explain in later sections. [Note: Below T_C, the $OS_{||}$ are higher in nanoparticles, though marginally].
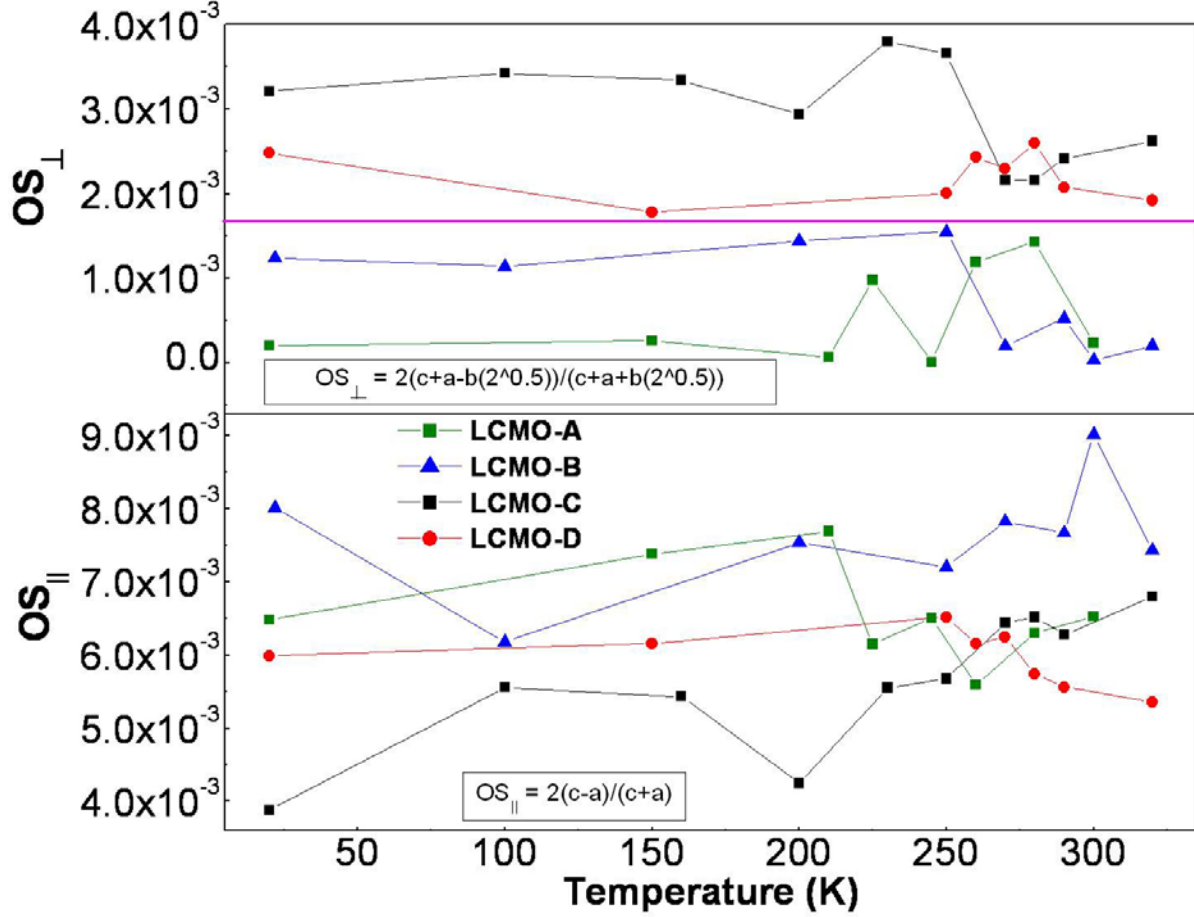
Fig.3.21. Variation of orthorhombic strains, $OS_{\parallel}$ (lower panel) and $OS_{\perp}$ (upper panel) with temperature for LCMO-A, LCMO-B, LCMO-C and LCMO-D. The pink line in the upper panel shows a demarcation between the larger and smaller size particles. (For details, see text).

This demarcation between the values of $OS_{\perp}$ for the larger and the smaller particle size samples is seen in the plots of the *Mn-O-Mn* bond angles (Fig.3.22) and *Mn-O* bond lengths (Fig.3.23) also. The O1 and O2 in the figure axes refer to the apical and equatorial oxygen atoms respectively (Fig.3.24). The bond angles and bond lengths were calculated from the refined atomic positions. The onset of ferromagnetic order increases both the Mn-O-Mn bond angle, especially the apical Mn-O-Mn bond angle by making it closer to 180^0, which tends to increase the band width. As can be seen from the figures, lowering the particle size also increases the bond angles and makes them closer to 180^0. It is more visible for the smallest size particles. On the other hand, size reduction decreases the bond lengths. These two effects work in tandem to make the unit cell more cubic. Since the band width W (in the double exchange model) can be expressed to a first approximation as $W \propto \dfrac{\cos \omega}{d_{Mn-O}^{3.5}}$, with $\omega = \dfrac{1}{2}\left(\pi - \theta_{Mn-O-Mn}\right)$, an increase in the bond angle and a decrease in the bond length means an overall increase in the bandwidth, thereby leading to a strengthening of the ferromagnetic phase. The temperature evolution of the bandwidth of the four samples as calculated from the bond angles and bond lengths are shown in Fig.3.25.

103
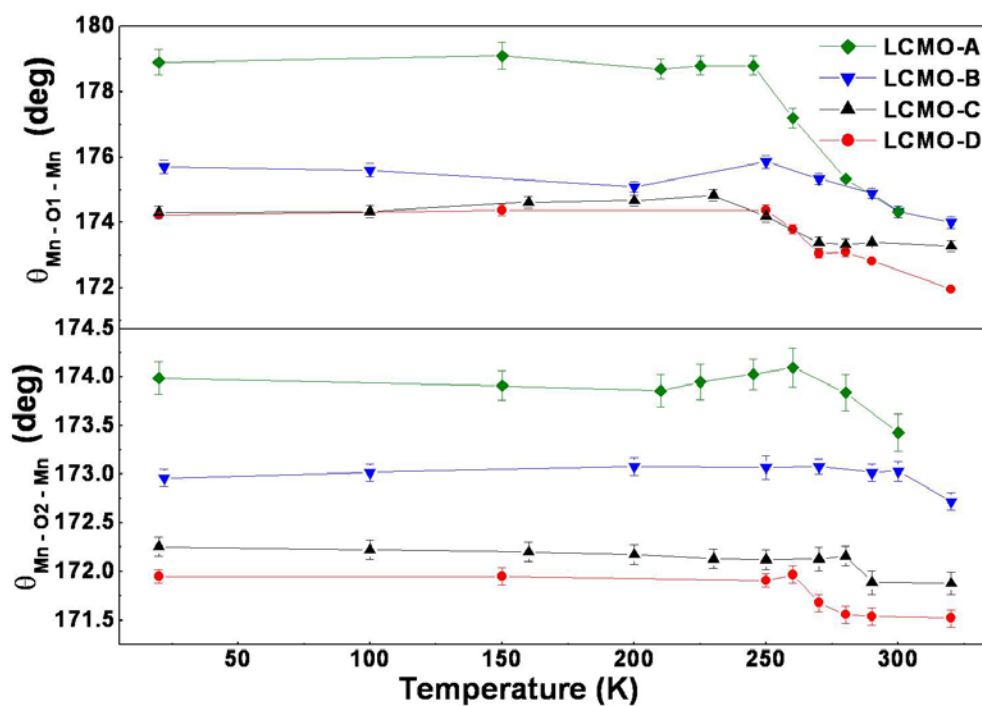
Fig.3.22. Variation of the *Mn-O-Mn* bond angle with temperature for LCMO-A, LCMO-B, LCMO-C and LCMO-D.
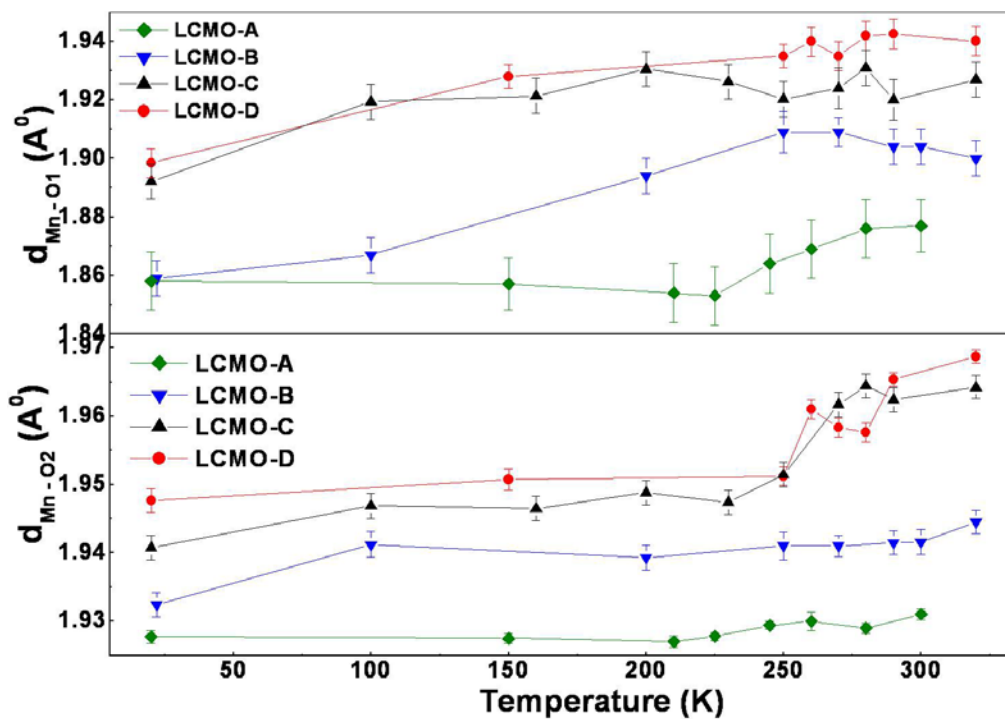
Fig.3.23. Variation of the *Mn-O* bond length with temperature for LCMO-A, LCMO-B, LCMO-C and LCMO-D.

104
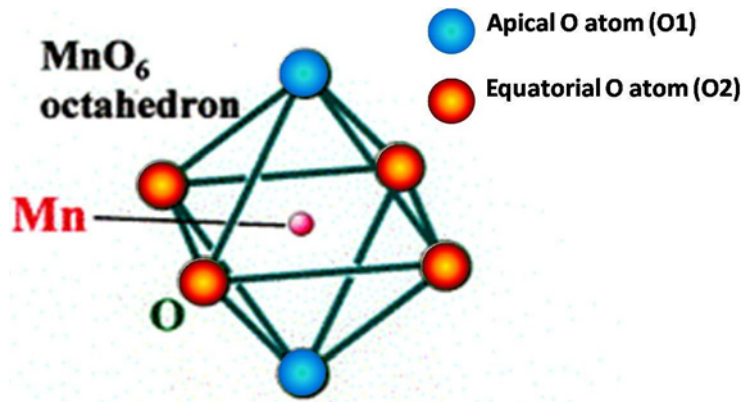
Fig.3.24. Schematic representation of the MnO_6 octahedron showing the apical and equatorial oxygen atoms.
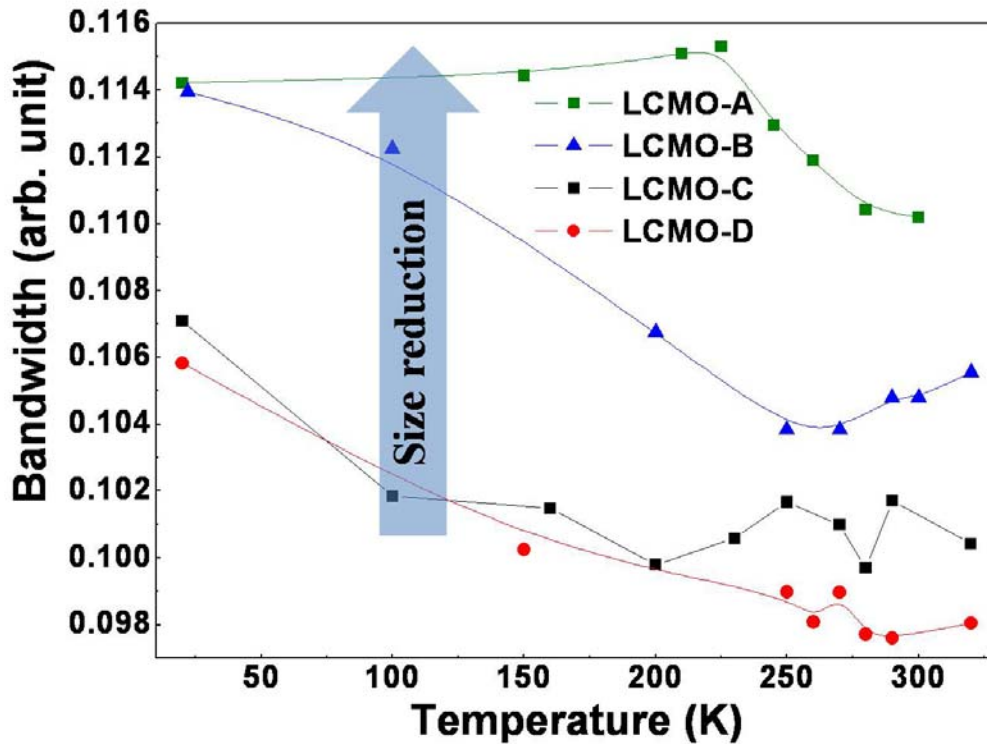
Fig.3.25. Variation of the bandwidth with temperature for LCMO-A, LCMO-B, LCMO-C and LCMO-D.

It is important to note that there is a relative strengthening (increase) of the bandwidth on size reduction. In all the samples (except the smallest size sample), the bandwidth slowly increases on cooling. In the smallest size sample the bandwidth builds up around T_C and then it remains constant.

The analysis based on the simple expression for bandwidth may not be quantitatively rigorous, but it shows a clear trend that there is indeed a strengthening of the ferromagnetism in the bulk of the nanoparticle. A small compaction of the lattice and straightening of apical Mn-O-Mn bond strengthens the ferromagnetism.

3.2.2.2 Variation of T_C with d

The non monotonic behavior of T_C with the particle size has been shown earlier in Fig.3.5and Fig.3.6. This behavior is obviously a result of two competing effects which come into play when the particle size is reduced. One is the finite size scaling effect which we have described in Section 3.1 and also touched upon briefly in Section 3.2.1.2. The finite particle size limits the divergence of the spin-spin correlation length ξ_0 at T_C. This will serve to push down the ferromagnetic T_C in the nanoparticles from its bulk value. The second is the lattice effect (or the bandwidth effect) which we have explained in Section 3.2.2.1. Size reduction changes the structure in a way that the bandwidth is enhanced, thereby strengthening the ferromagnetism and increasing the ferromagnetic T_C in the nanoparticles. The relative strength of these two effects will determine where the turn around will occur. The sensitivity of the transition region will also depend on this. A schematic representation of this dual effect of size reduction on the ferromagnetic T_C is shown in Fig.3.26. [Note: The region of transition ("peak region" in the black curve in Fig.3.26) is very susceptible to the sample synthesis conditions. An increase in the oxygen vacancies will sharply reduce T_C even for samples with similar particle sizes. We fill that this might be a reason for our failure to reproduce the high T_C sample (sample B) that we obtained in Batch 1, when we attempted to make a 2nd. Batch of samples].
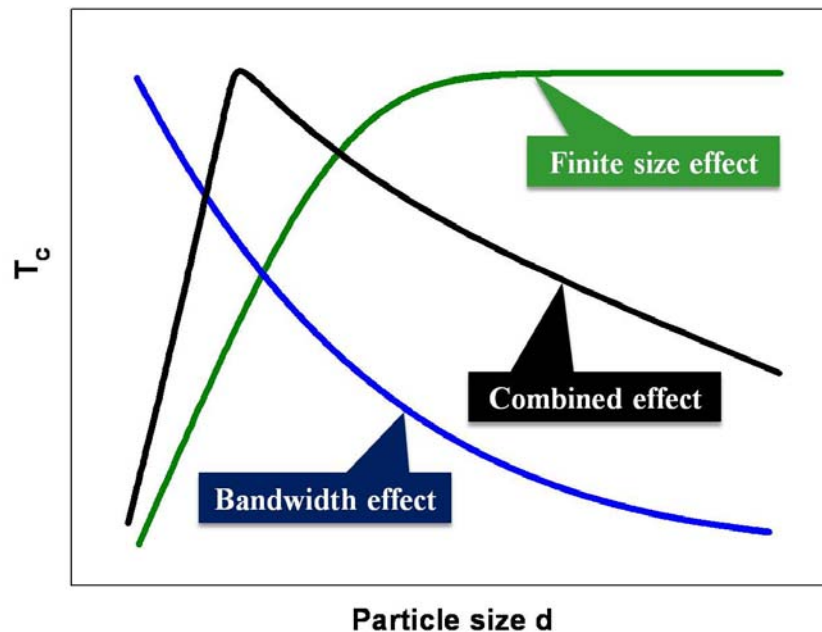
Fig.3.26. Schematic representation of the dual effect of size reduction in LCMO on the ferromagnetic T_C.

3.2.2.3 Variation of H_C with d and T

The variation of H_C with particle size (d) and temperature T (for LCMO-E) has been shown in Fig.3.16. The coercive field shows a very peculiar trend which cannot be explained by our conventional knowledge of single domain particles. As a function of particle size, it shows a peak at d ≈ 175 nm, below which size the coercivity starts falling. This indicates that below a size of 175 nm, the particles enter a single domain regime. (From the known values of ferromagnetic coupling constant J (≈ 0.3 eV) and the magnetocrsytalline anisotropy constant K (~ 10^5 J/m^3) for manganites, we can estimate the particle size below which the system should enter the single domain regime. This value is ~ 70 nm, which turns out to be lower than our observed value of 175 nm. A possible explanation for this discrepancy is that the samples have a large size distribution, and although the average particle size is ~ 175 nm, a certain fraction of particles are smaller in size and have entered the single domain regime.) At the smallest particle size of ~ 15 nm, the coercivity is almost one order larger than the coercivity value for the "bulk" (micron size) samples. This indicates that although the smaller size particles (d < 175 nm) have entered the single domain regime, but they are still not small enough to become superparamagnetic (where $H_C \sim 0$, see Fig.1.25 of Chapter 1 for further clarification).

However, the unusual behavior of the nanomanganites becomes apparent when we look at the temperature dependence of the coercivity (Fig.3.16 (a)). Instead of following the $T^{1/2}$ dependence $\left[H_C = \alpha \frac{2K}{M_S} \left\{ 1 - \left(\frac{T}{T_b} \right)^{\frac{1}{2}} \right\} \right]$, which is how single domain particles typically behave[14], the nanomanganites show a linear dependence of H_C with T. As we will see later on in this chapter, this is quite distinct from the behavior of the nanocobaltates, which show a more conventional $H_C - T$ dependence.

3.2.2.4 Variation of T_B and T_P* with H

The variation of T_B and T_P* with the applied magnetic field has been shown in Fig.3.15. In the figure, the magnetic field axis is in log scale which shows that when the field is increased from 1 mT, both T_B and T_P* show a rapid response till H = 0.2 T, but above 0.2 T, the response is much slower. The fact that a low enough field of 0.2 T is sufficient to produce the maximum response in these samples indicates the absence of any domain wall pinning and spin glass like situation. We will come back to this point when we do a comparative study of the nano manganites and nano cobaltates and note the difference between the two.

3.2.2.5 Variation of M_S with d

The variation of the magnetization (at T = 80 K) as well as the spontaneous moment (as obtained from the neutron diffraction data) as a function of the particle size have been shown in Fig.3.12. We see a sharp drop in both when the particle size goes below 50 nm. This is also the same size ($d_{critical}$) above which the samples show an enhancement in T_C (with respect to the bulk T_C) and below which they show a reduction in T_C. We can explain the decrease in the

107

magnetization for smaller size samples from a core – shell model. According to this model, all the samples have a core having ordered and aligned spins, and a disordered shell where the spins are randomized in direction and hence contribute zero (or very small) magnetic moment. As the particle size is reduced, an increase in the surface to volume ratio ensures that the effect of the shell becomes increasingly prominent. For the bulk samples, the thickness of the shell (δ) is much smaller than the particle size which makes it pretty much insignificant. A schematic representation of the core – shell structure is shown in Fig.3.27.
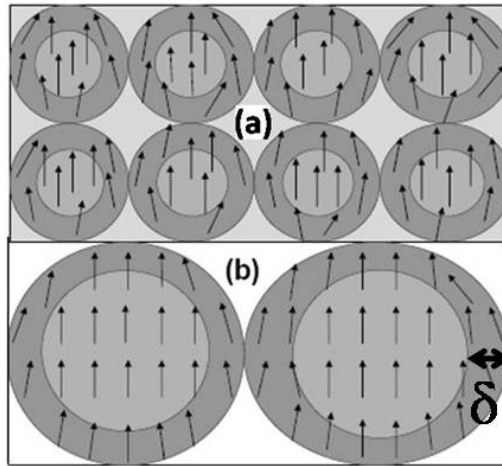
Fig.3.27. Schematic representation of the core – shell structure in (a) smallest size nanoparticles and (b) intermediate size samples.

The thickness of the disordered shell (δ) can be estimated from the suppression of the magnetization with respect to the bulk magnetization value. In the core – shell model, we assume that M_S is proportional to the volume fraction of the core i.e. $M_S = M_{0S}\left(\dfrac{\left(d/2\right)-\delta}{d/2}\right)^3$, where M_{0S} is the bulk saturation magnetization. Expanding the cube and ignoring higher powers of δ/d, we get the equation $M_S = M_{0S}\left(1 - \dfrac{6\delta}{d}\right)$. This relation gives us a more or less constant value of the shell thickness for smaller size particles (d < 50 nm), and the value of δ for these samples turns out to be ~ 2 nm. For samples with larger particle size the shell thickness falls off drastically as expected. The variation of δ with d is shown in the inset of Fig.3.28. But the increasing importance of the disordered shell for the smaller size particles becomes apparent when we compare δ to the diameter of the particles (d). We do this in Fig.3.28, where we have plotted δ/d as a function of the particle size (d). It is seen that the ratio δ/d starts increasing slowly when the particle size goes below 200 nm, but it shows a very sharp rise when the particle size is reduced below 50 nm. This can account for the sharp drop of M_S for samples with particle size below 50 nm (Fig.3.12).

This shell of disordered spins on the surface can also explain the higher value of coercivity for the nanoparticle samples as compared to the coercivity value in the "bulk" (micron

size) samples. The disordered shell leads to surface spin freezing and hence, a spin glass like state and pinning on the surface, which in turn leads to an increased surface anisotropy. This effectively increases the magnetocrystalline anisotropy which in turn increases the coercivity of the nanoparticle samples.

. We also note that the magnetic behavior of the smaller size samples become dominated by the surface magnetic properties. Broken bonds at the grain boundary (i.e. breaking of the *Mn-O-Mn* paths at the grain surface) might hinder the double exchange mechanism and weaken the ferromagnetism, thereby reducing T_C. Thus, the surface phase has a notably reduced temperature of magnetic ordering. The crystallographic structure as described in the earlier sections essentially gives a picture of the inner core. The shell, on the other hand, might have faults in this crystallographic structure.
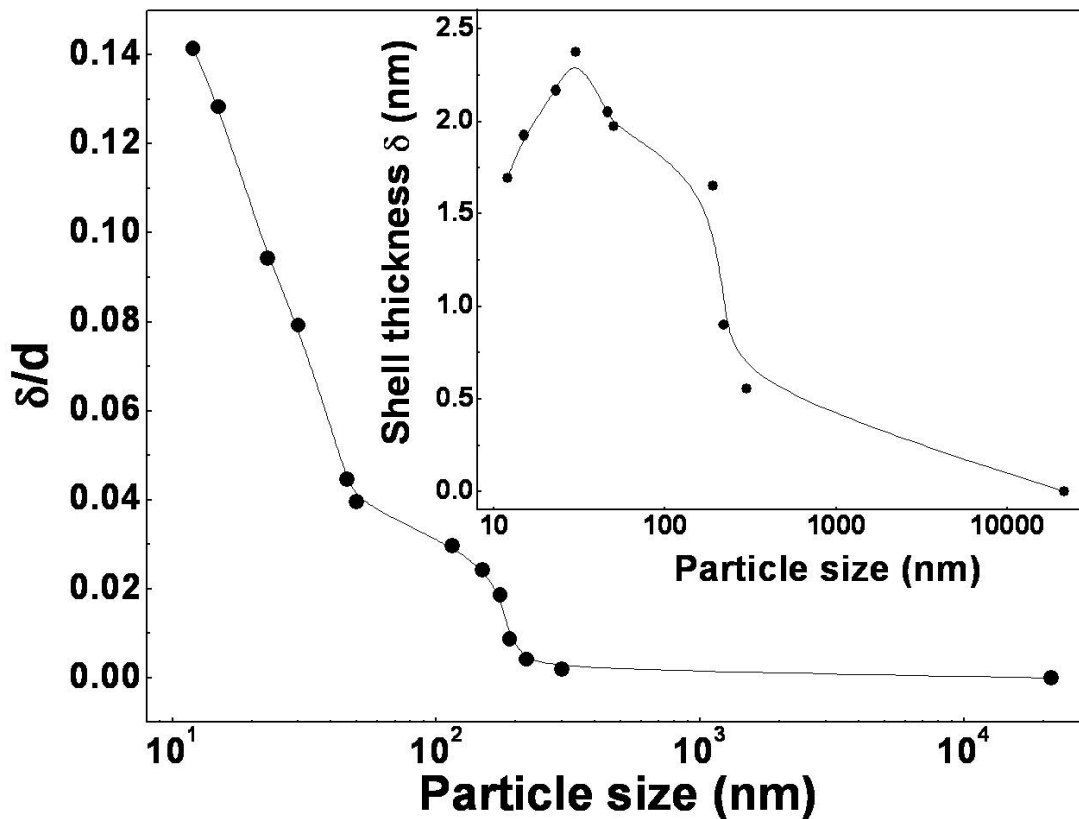
Fig.3.28. Variation of δ/d as a function of the particle size in LCMO (for details see text).

3.2.2.6 Role of pressure on size reduction

The ferromagnetic state, at least down to a certain size range, is stabilized by size reduction. Below 200 nm, the formation of the shell becomes important. We would like to explore whether the size reduction can lead to an effective hydrostatic pressure that can tune the physical properties of the nanomanganites. We had mentioned this concept, that size reduction

109

can induce an external pressure, briefly in Chapter 1 (in Section 1.11). Here we elaborate on it. Assuming the particles to be spherical in shape, we can estimate the surface pressure, $P = \dfrac{2S}{d}$, where, d is the diameter of the particle and S is the surface tension. We argue that this surface pressure acts in a way which is equivalent to externally applied hydrostatic pressure. In other words, size reduction, in certain cases, should give the same result as external application of hydrostatic pressure.

For complex oxides, there are uncertainties in the exact value of S but it is in the range of few tens of N/m. Thus, using, as a rough estimate, $S \approx 50$ N/m[15], we can easily convert d into P. As an example, in Fig.3.29, we show the variation of T_C as a function of the particle size as well as the equivalent surface pressure. The particle size (d) is plotted in the bottom axis while the surface pressure (P) is plotted in the top axis. Thus, a larger particle size (bulk sample) corresponds to a very low surface pressure and vice versa. In the inset of Fig.3.29, we have shown T_C versus measured hydrostatic pressure in bulk $La_{0.67}Ca_{0.33}MnO_3$. The data has been reproduced from Neumeier et.al. (Phys. Rev. B, 52, R7006 (1995)). The parallel between the pressure axis in the inset and the pressure axis corresponding to the equivalent surface pressure (top axis of Fig.3.29) is very clear.

This plot can be utilized to calculate $\dfrac{dT_C}{dP}$ and see how the derivative evolves as a function of particle size. This has been shown in Fig. 3.30. The value of the derivative decreases as the particle size is reduced. We argue that such a reduction in the value of $\dfrac{dT_C}{dP}$ occurs as the effective pressure on the nanoparticles is increased on size reduction. In manganites, it has been observed that as the pressure is increased, the $T_C - P$ curve reached a broad peak for pressures close to 4 GPa[16 − 17] $\left(\dfrac{dT_C}{dP} \to 0 \right)$. Beyond that T_C decreases slowly as P increases showing that $\dfrac{dT_C}{dP}$ has actually changed sign. It has been argued from structural studies done under pressure[17] that at low pressure (P < 2 GPa), the enhancement of T_C with pressure is due to the enhancement of overlap of electron wavefunctions due to lattice compaction. However, for P > 3 GPa, there is an enhancement of the Jahn − Teller distortion that halts the increase of T_C with P. In nanoparticles, it is expected that a surface generated equivalent pressure acts on the particles due to the reduction in size[18].

In the next section, where we study the magnetic phase transition in LCMO, we will show that this decrease in the value of dT_C/dP has a very important effect on the nature of the transition. The derivative shows a crossover from a positive value to a negative value at ~ 56 nm (shown by an arrow in Fig.3.30). We also note that the value of dT_C/dP which we obtain for the bulk sample using this method ≈ 20.2 K/GPa, which is very close to the value of dT_C/dP reported for bulk LCMO (20 K/GPa[19]).

We will see further in Chapter 4 that a hydrostatic pressure effect can indeed be generated by size reduction.
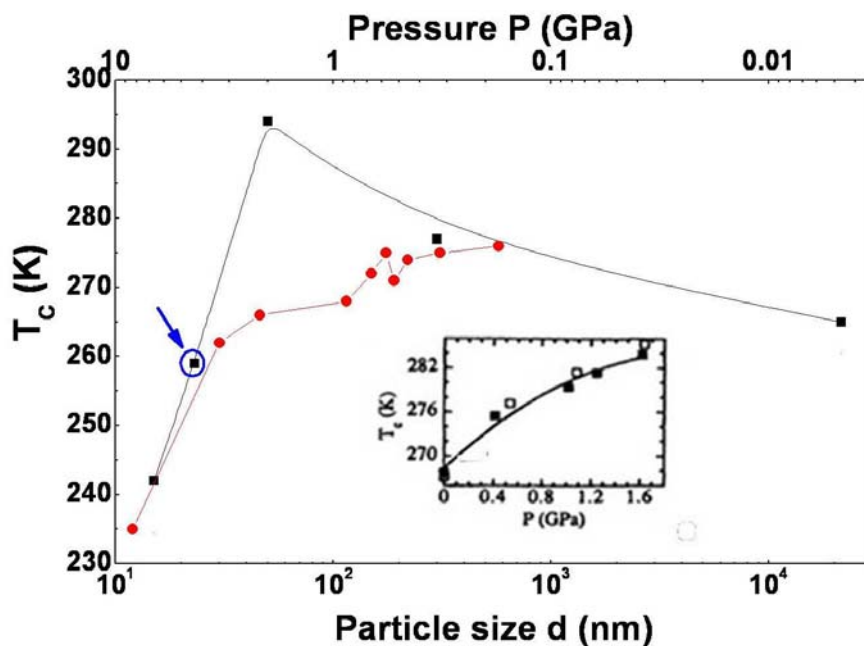
Fig.3.29. Variation of T_C as a function of the particle size (bottom axis) and equivalent surface pressure (top axis) in LCMO. The inset shown variation of T_C vs hydrostatic pressure in LCMO (data Neumeier et.al. (Phys. Rev. B, 52, R7006 (1995)).
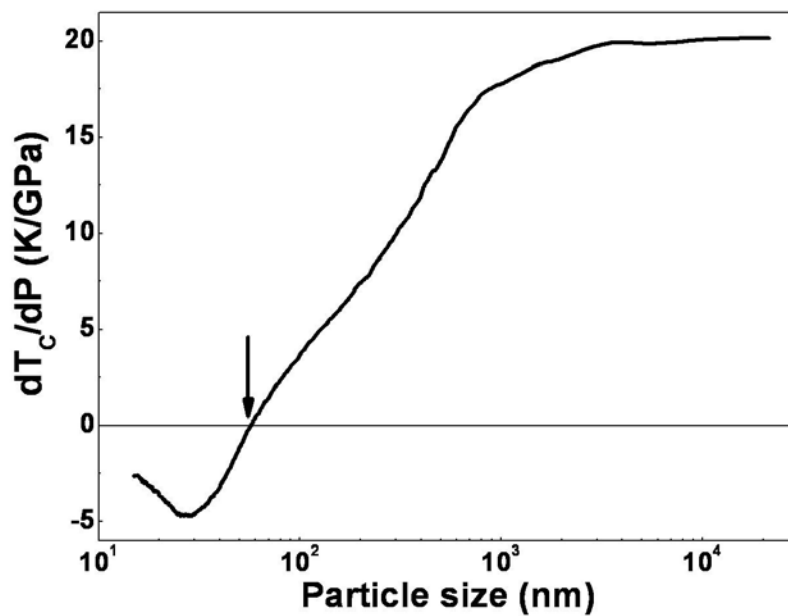
Fig.3.30. Variation of dT_C/dP as a function of the particle size in LCMO.

111

3.2.3 Nature of the magnetic phase transition

In this subsection, we show that size reduction also changes the nature of magnetic phase transition in LCMO (x = 0.33) nanoparticles. In fact, the nature of the magnetic phase transition poses an interesting problem in the case of the bulk doped manganites also (even without introducing the added dimension of size reduction). While in most doped manganites (A = Sr, Ba etc.; A being the divalent cation) with wider bandwidth the phase transition is second order, in narrow bandwidth $La_{0.67}Ca_{0.33}MnO_3$ the transition has been found to be first order[20 − 22]. The issue of the nature of magnetic phase transition in the $La_{1-x}Ca_xMnO_3$ system as the hole concentration x is changed is a topic of considerable interest and has not been understood yet, although experimentally it has been observed that the transition is first order for $x \approx 0.2 - 0.4$ and is a continuous one for x outside this regime. For $x = 0.4$, in particular, there is a tricritical point at the ferromagnetic T_C[23]. In the Ca substituted manganites which have a smaller bandwidth, the effect of the electron lattice coupling is stronger and presumably it can play a very dominant role in deciding the nature of the transition in addition to the contribution arising from the double exchange interaction which is the cause of ferromagnetism in these materials. As we have seen in the earlier sections, size reduction in LCMO does alter the lattice structure to some extent and appears to strengthen the ferromagnetic interactions. Hence, it might have an effect on the nature of the phase transition as well. In fact, as we proceed to show in this section, the first order phase transition in $La_{0.67}Ca_{0.33}MnO_3$ does change to a second order transition when the particle size is brought down to the nanometer regime. In this change-over, the hole concentration (i.e. x) is kept fixed and the change-over occurs solely due to factors that arise from size reduction.

Before we elaborate our studies on the nature of phase transition in nano LCMO, we briefly review the available current knowledge regarding the nature of the phase transition in other doped manganites. Thus, in manganites other than LCMO (like $La_{0.67}Sr_{0.33}MnO_3$[20,22], $Nd_{0.6}Pb_{0.4}MnO_3$[24]), the magnetic transition is a continuous transition. The critical exponents are close to what one would expect from a 3D Heisenberg model with short range interactions. Interestingly, the first order transition observed in bulk $La_{0.67}Ca_{0.33}MnO_3$ can be made a continuous transition by substitution of Ca in the A − site by a small amount of Ba or Sr[20,21] (increase in internal pressure), or substitution in Mn sites by Ga[5] (increase in magnetic disorder). The critical exponents obtained in these cases were also what one would expect in a 3D Heisenberg model. The basic magnetic system in the manganites with double exchange interaction is, thus, a 3D magnetic system. There are causes like strong coupling to other modes that makes the transition in LCMO in the special hole concentration region ($x = 0.2 - 0.4$) a first order transition. It has been suggested that the transition in LCMO is a fluctuation driven first order transition[25]. The change-over to a second order (continuous) transition on small substitution by Ba or Sr at the Ca site, or by Ga at the Mn site is generally thought of as arising from random disorder that rounds off the first order transition to a second order transition[26]. In this context, the observation of a size reduction induced continuous transition is an important observation because the system has the same chemical composition (no change in hole concentration, or dilution of the magnetic interaction), and the only difference is the size of the system. We have chosen a particular nanoparticle sample which has a T_C close to the bulk T_C but a particle size more than 4 orders smaller than the bulk sample (sample E, shown by a blue circle and arrow in Fig.3.29). Thus, the change-over in the order of the phase transition happens with

no significant change in the value of the transition temperature. Substitution of Sr and Ba enhances T_C while dilution of Mn site by Ga reduces T_C significantly.

The nature of the magnetic transition can be obtained experimentally from the slopes of the isotherm plots of H/M vs M^2, M being the experimentally observed magnetization and H, the magnetic field. This criterion of deciding the nature of the transition is generally referred to as the Banerjee criterion[27] and has been used widely to experimentally determine the order of the magnetic phase transition. Briefly, a positive or a negative slope of the experimental H/M vs M^2 curve indicates a second order or first order transition respectively. We have used samples E and D for this investigation (the latter serving as the bulk reference), and found striking differences in the magnetic behavior of the two samples near T_C.

To apply the Banerjee criterion, the first step was to measure initial magnetization isotherms in the vicinity of the critical temperature. These magnetization isotherms were measured in applied fields up to 1.6 T with a temperature control better than $\pm$ 0.05 K. Before each run, samples were heated above their T_C and cooled to the measuring temperature under zero field in order to ensure a perfect demagnetization of the samples. The magnetization isotherms for the two samples are shown in Fig.3.31.
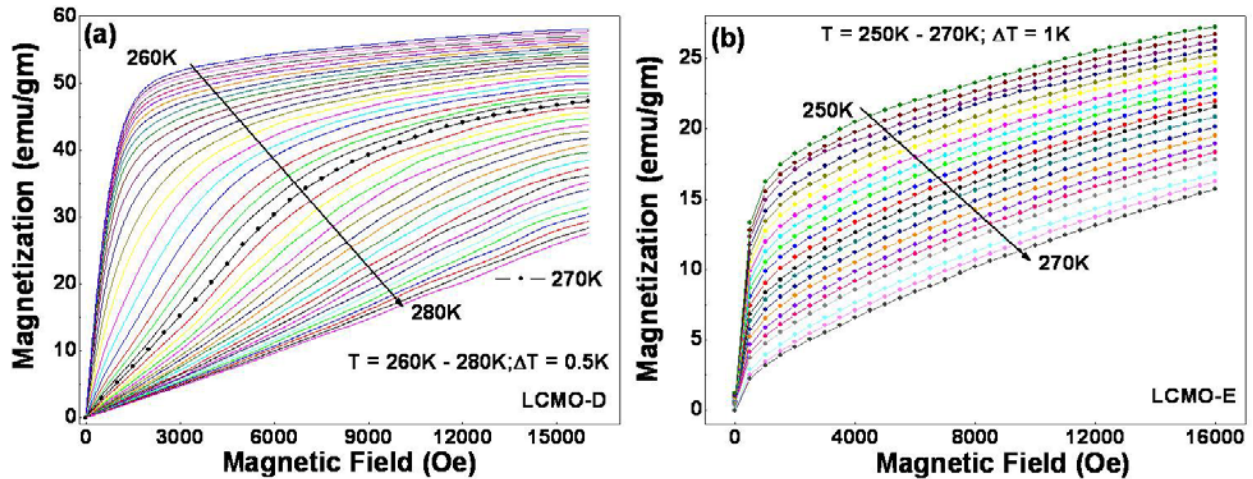
Fig.3.31. Magnetization isotherms for (a) LCMO-D and (b) LCMO-E taken around their respective Curie temperatures.

In Fig.3.32, we plot M^2 versus H/M isotherms (Arrott plots) for the two samples. For the bulk sample (Fig.3.32 (a)), it is clear that the isotherms present negative slopes in some parts which, according to the criterion used here, is an indication of the first order character of the transition. The observation of a first order transition in the bulk sample is in agreement with past studies[20,21]. The magnetization isotherms for the nanoparticles (Fig.3.32 (b)) do not display the anomalous change of slope as seen in the bulk sample. Here, we find a positive slope throughout the range of M^2. Nano LCMO, thus, shows a second order magnetic phase transition at T_C.
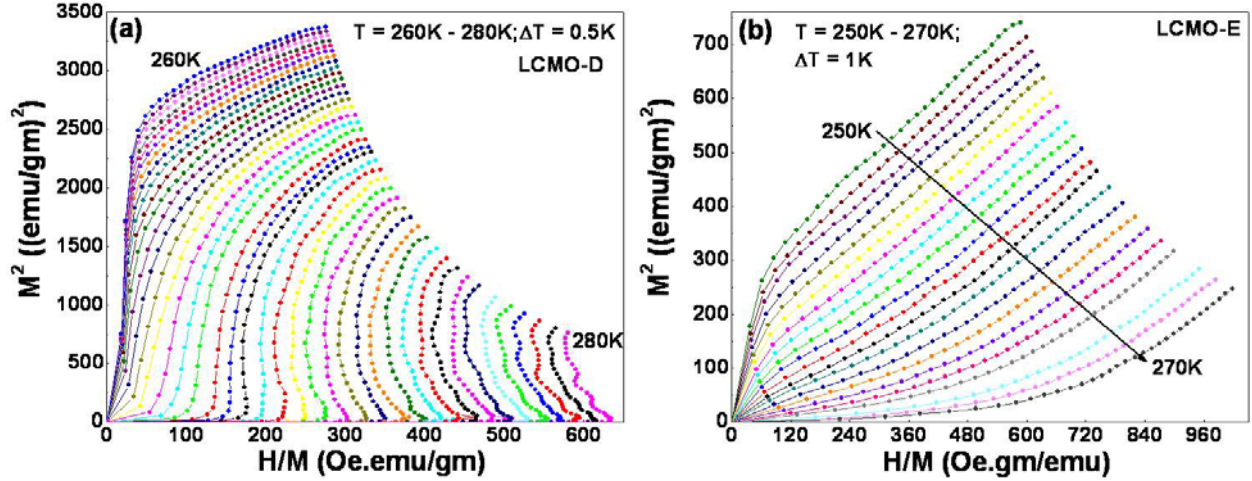
Fig.3.32. Arrott plots for (a) LCMO-D and (b) LCMO-E.

The second order magnetic phase transition near the Curie temperature is characterized by a set of critical exponents, β (associated with the spontaneous magnetization), γ (associated with the initial susceptibility) and δ (related to the critical magnetization isotherm). They are defined as

$$M_S(T) = M_0(-\varepsilon)^{\beta}, \quad \varepsilon < 0$$

$$\chi_0^{-1}(T) = \left(\frac{h_0}{M_0}\right)\varepsilon^{\gamma}, \quad \varepsilon > 0$$

$$M = A_0(H)^{\frac{1}{\delta}}, \quad \varepsilon = 0$$

where, $\varepsilon = \dfrac{T - T_C}{T_C}$ and M_0, h_0/M_0 and A_0 are the critical amplitudes. The exact values of the critical exponents β and γ and the exact Curie temperature T_C were determined from a modified Arrott plot (Fig.3.33) by taking β, γ and T_C as refinable parameters. The exact values of $\beta = 0.47 \pm 0.01$ and $\gamma = 1.06 \pm 0.03$ come out to be close to the mean field values ($\beta = 0.5$, $\gamma = 1$). T_C was found to be 259 K. The mean field value of the exponent δ can be derived using the relation $\delta = 1 + \dfrac{\gamma}{\beta}$. We find $\delta = 3.26 \pm 0.16$. One can also obtain δ directly from the plot of M versus H at T_C (see inset of Fig.3.33). From such a plot we obtain $\delta = 3.10 \pm 0.13$. A comparison of the critical exponents show that the magnetic transition is not only second order, but the exponents are close to the mean field values: $\beta = 0.5$, $\gamma = 1$ and $\delta = 3$. The critical exponents obtained from the various fits as described above are listed in Table 3.5.
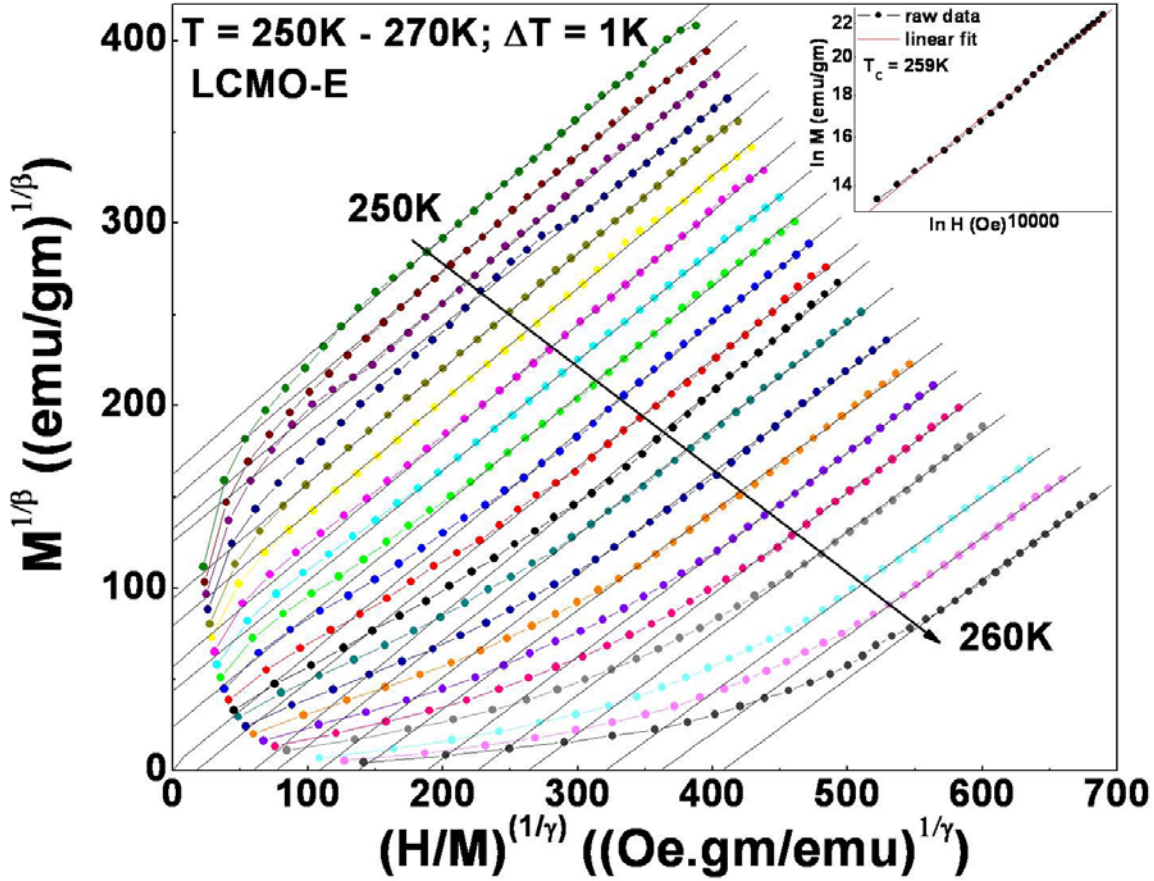
Fig.3.33. Modified Arrott plot for LCMO-E. Inset gives the plot of ln M vs ln H at T = 259 K.

Table 3.5 Critical exponents of nano LCMO obtained experimentally and compared with theoretical (mean field) values.

Critical exponent	Experimental value	Mean field theory	$\delta = 1+\gamma/\beta$
β	0.47 ± 0.01	0.5	—
γ	1.06 ± 0.03	1.0	—
δ	3.26 ± 0.16	3.0	3.10 ± 0.13

The critical exponents of the transition can be equivalently determined by scaling plots of

the form $\dfrac{M}{|\varepsilon|^{\beta}} = f_{\pm}\left(\dfrac{H}{|\varepsilon|^{\gamma+\beta}}\right)$, where, $\varepsilon = \dfrac{T-T_C}{T_C}$ and $f_{\pm}$ is a scaling function with the plus and

minus sign corresponding to the ferromagnetic and paramagnetic regions respectively. By appropriate selection of the parameters T_C, β and γ, the data should collapse on two different branches for $T > T_C$ and $T < T_C$. We construct scaling plots (Fig.3.34) to prove the validity of our choice of β, γ and T_C. A convincing scaling of the data points on the two branches of the scaling function $f_{\pm}$ can be seen.
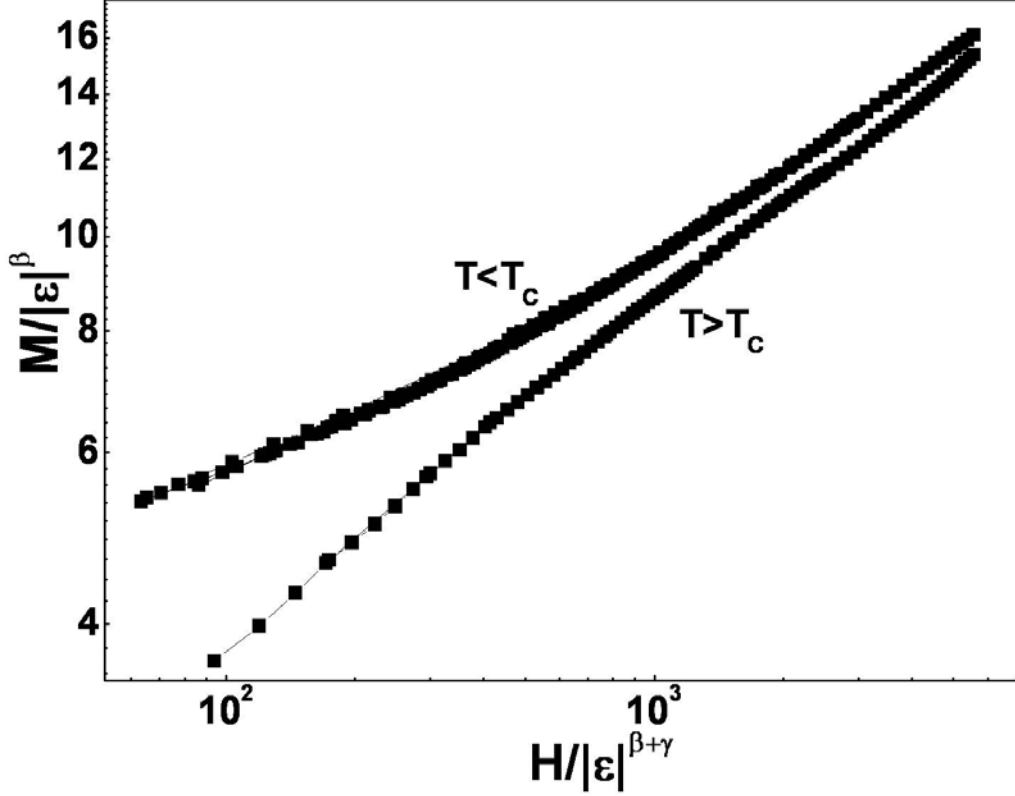
Fig.3.34. Scaling plots for LCMO-E.

We have, thus, observed a very clear change in the nature of the magnetic phase transition in LCMO from first order to second order when the particle size is brought down from bulk to nano. The nature of the magnetic transition in double exchange ferromagnets has been investigated theoretically before. The model is an extension of the compressible spin model of Bean and Rodbell[28]. It has been found that the change-over from the first order to second order transition can be parameterized by a quantity η[19], where, $\eta = K \dfrac{1}{T_C} \left(\dfrac{dT_C}{dP} \right)^2$, with $K = \dfrac{35S(S+1)}{6(S-1)(3S+1)} \dfrac{Nk_B}{\kappa T}$, N being the number of magnetic ions/unit volume, κ, the compressibility and S, the spin. This parameter η can be obtained experimentally from the $m_s - t$ curve, where, $m_s = \dfrac{M_S(T)}{M_S(T=0)}$ and $t = \dfrac{T}{T_C}$. M_S is the saturation magnetization. For $\eta < 1$, the transition if of the second order, while for $\eta \geq 1$, the transition is of the first order. We obtained the value of η from the $m_s - t$ curves for both the samples (Fig.3.35) using the recipes given in ref 19. For the bulk sample, we obtain $\eta = 0.75$. This agrees very well with the value of $\eta = 0.77$ obtained by past studies. The proximity of η to 1 makes the transition first order as expected. However, a similar fit of the $m_s - t$ data for the nanoparticle sample gives $\eta \approx 0.03$, which is much less than that seen in the bulk sample and is close to $\eta = 0$. The change-over from first order to second order transition is, thus, reflected in the parameter η. The important question is

116

what causes this reduction of η or the change-over. We now proceed to discuss some of the plausible scenarios that can make this happen.
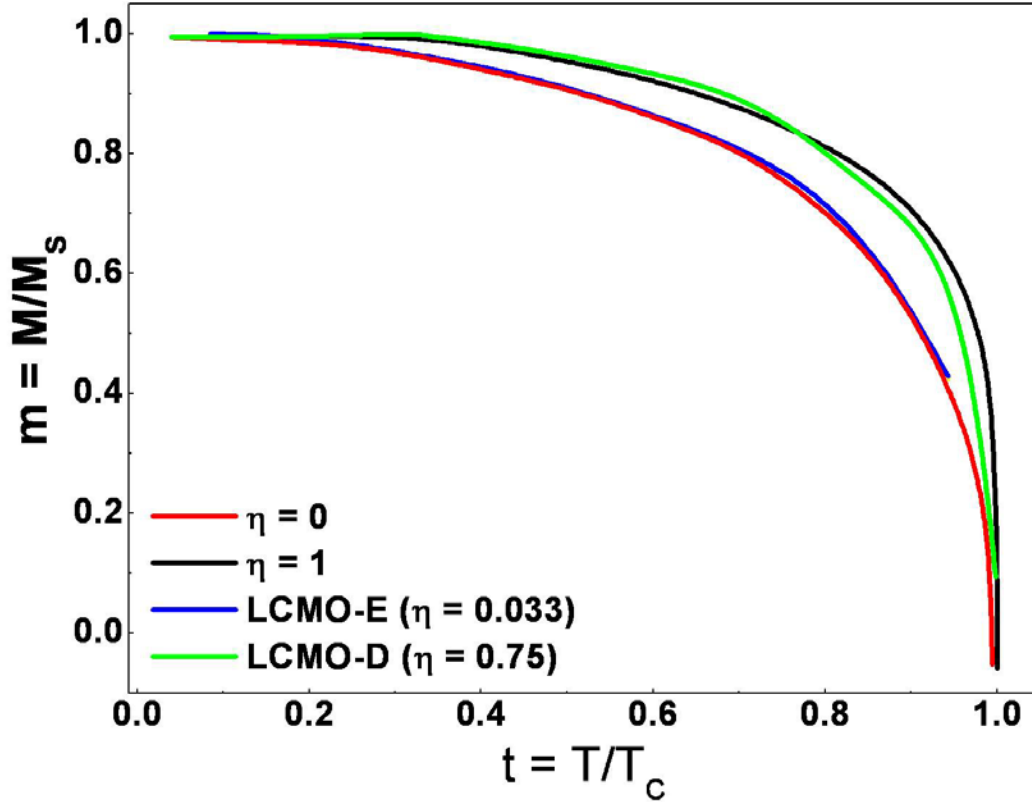
Fig.3.35. m vs t curves for LCMO-D and LCMO-E. The curves for $\eta = 0$ and $\eta = 1$ have been reproduced from [24].

Alternatively, the value of η in the two samples can also be calculated from the values of dT_C/dP from Fig.3.29. Thus, $\left(\dfrac{dT_C}{dP}\right)_{Bulk} \approx 20.2 \ K/GPa$ which gives $\eta = 0.80$. On the other hand, $\left(\dfrac{dT_C}{dP}\right)_{nano} \approx 4.2 \ K/GPa$ (value corresponding to d = 23 nm as read out from Fig.3.29), which gives $\eta = 0.035$ (which is quite close to the value of η obtained from the m-t curves in Fig.3.35). This provides additional proof of the fact that our hypothesis relating to the size reduction giving rise to an enhanced surface pressure is quite correct, and this is the primary reason for the change in the nature of the phase transition.

Two features of our results are noteworthy. First, the change in T_C for sample E is extremely small with respect to the bulk T_C ($\approx 2 \%$) in view of the fact that the size changes by nearly 4 orders. For itinerant ferromagnets like Ni such size reduction shifts T_C by much larger fractions. We note here that in the cobaltate system (LSCO), a similar size reduction changes the T_C by 60 K (a change of $\sim 25\%$). (The LSCO system will be dealt with in details later in this chapter). Thus, the ferromagnetic transition in LCMO is more stable under size reduction. As we have seen earlier, for certain size ranges, the ferromagnetic transition in LCMO actually gets

strengthened. Secondly, the critical exponents obtained for the transition are very close to the mean field values and the spin system is isotropic.

Another important effect that can cause the change-over is random strain. The nanoparticles have a hydrostatic pressure caused by the surface pressure as argued before. However, they also have a local random strain. A Williamson Hall plot[29] of the XRD data of the nanocrystals gave a large random strain of $\approx 8\%$. This random strain can cause rounding off of the first order transition. It is quite likely that the random local strain causes the same physical effect as random substitution because the random substitution due to mismatch of ionic size can also lead to random local strain. Given the susceptibility of the first order transition to random substitution, this can also be a likely cause. The two plausible causes, the spin compressibility under pressure created by size reduction as well as the random strain might occur in tandem and cause the change-over.

Since T_C is very critically dependent on the size, a slight increase in the size distribution might also lead to a spread in the transition.

3.3 La$_{0.5}$Sr$_{0.5}$CoO$_3$ (LSCO, x = 0.5)

3.3.1 General background

In the first part of this chapter we have discussed, in details, the effects of size reduction on a double exchange ferromagnet, LCMO (x = 0.33). To benchmark this with a conventional superexchange based ferromagnet, we now investigate the effect of size reduction on ferromagnetic La$_{0.5}$Sr$_{0.5}$CoO$_3$.

According to the phase diagram of La$_{1-x}$Sr$_x$CoO$_3$ (Fig.3.2 (b)), La$_{0.5}$Sr$_{0.5}$CoO$_3$ belongs to the cluster glass phase[30]. The cobaltate system contains a mixture of low spin Co^{III} (t$_{2g}^6$), low spin Co^{IV} (t$_{2g}^5$), and some high spin Co^{3+} (t$_{2g}^4$e$_g^2$) and high spin Co^{4+} (t$_{2g}^3$e$_g^2$). The exchange interaction Co^{IV} – O – Co^{3+} or Co^{4+} – O – Co^{3+} is known to be ferromagnetic whereas the superexchange interactions between the ions with the same valency state are antiferromagnetic[31 – 33]. The competition between the ferromagnetic and antiferromagnetic interactions leads to spin glass states observed for $0 < x \leq 0.18$. When the ferromagnetic exchange interactions just overcome the antiferromagnetic ones, the cluster glass phase appears with short range ferromagnetic ordering ($0.18 \leq x \leq 0.5$)[34]. Thus, in La$_{0.5}$Sr$_{0.5}$CoO$_3$, one sees the onset of a ferromagnetic transition at $T_C \approx 250$ K. Here, each Co^{3+} in the lattice is surrounded by six Co^{4+} neighbours, which gives maximum Co^{3+} - Co^{4+} ferromagnetic interactions. However, the resulting ferromagnetic state does not have a long range order. Rather it becomes like clusters of ferromagnetic regions embedded in a non-ferromagnetic matrix. The cluster glass like features of La$_{0.5}$Sr$_{0.5}$CoO$_3$ have been attributed to its magnetocrystalline anisotropy[35]. In the following sections, we elaborate on the magnetic properties of LSCO nanoparticles, see how they differ from the bulk LSCO sample and also from the LCMO nanocrystals having roughly the same size (LCMO-E).

3.3.2 Samples

In this chapter, we have focused on two $La_{0.5}Sr_{0.5}CoO_3$ samples: the nanoparticle sample and the bulk sample. We have listed the average particle size and the cell dimensions of these samples in Table 3.6. The cell dimensions were extracted from a Rietveld refinement of laboratory – based XRD data (taken at room temperature) using the FullProf Suite software[13]. We used the rhombohedral space group R-3c[36]. The x-ray diffraction patterns (along with the fits) for both samples (taken at T = 300 K) are shown in Fig.3.36.

<u>Note:</u> Crystals having the rhombohedral space group can be described in two ways, either through a rhombohedral unit cell (a = b = c; $\alpha = \beta = \gamma$), or through a hexagonal unit cell (a = b ≠ c; $\alpha = \beta = 90^0$, $\gamma = 120^0$). Although these two descriptions are entirely equivalent (with the volume of the unit cell in the rhombohedral representation being a third of the volume of the unit cell in the hexagonal representation), but the FullProf Suite software requires that only the hexagonal description of the unit cell can be used. In Table 3.5 we have listed the cell parameters both in the hexagonal description (which were obtained directly from the fittings) as well as in the rhombohedral description (which were obtained by converting the corresponding hexagonal cell parameters).

A comparison of the two data shows that there is a clear small compaction of the unit cell (~ 1 %) when the size is reduced. Also the deviation of the rhombohedral cell angle from 60^0 is slightly more (~ 0.4 %) for the nanoparticle sample than the bulk sample. In contrast, for nano LCMO, the smallest size nanoparticle sample (sample A) showed a small expansion (~ 0.4 %) in the unit cell volume.

Table 3.6 Sample ID, average particle size (d), lattice parameters (at 300 K), unit cell volume and Curie temperature of $La_{0.5}Sr_{0.5}CoO_3$ samples.

Sample ID	Average particle size (nm)	Hexagonal description			Rhombohedral description			T_C (K)
		a (Å)	c (Å)	Cell Volume ($Å^3$)	a (Å)	α $(^0)$	Cell Volume ($Å^3$)	
LSCO-A	36 ± 15	5.3602 (0.0003)	12.982 (0.001)	323.014	5.32	60.50	107.67	190
LSCO-B	3000 ± 1000	5.3718 (0.0002)	13.078 (0.001)	326.824	5.35	60.27	108.94	250
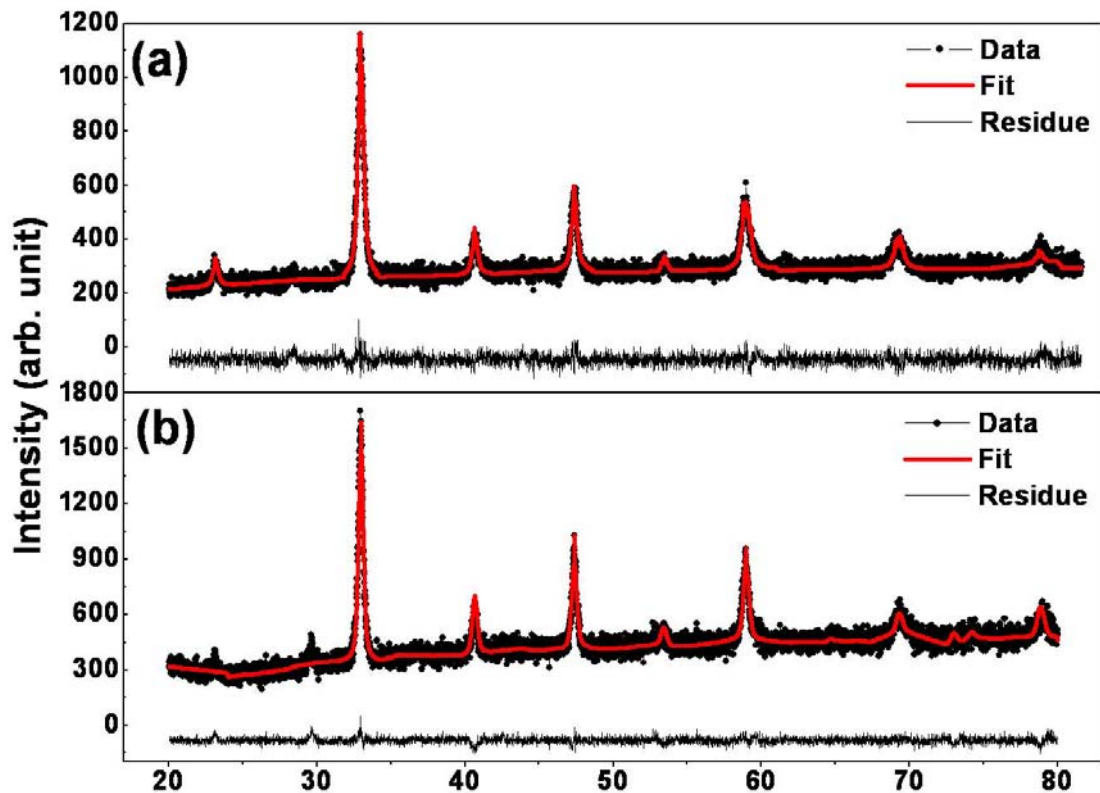
Fig.3.36. X – Ray diffraction patterns for (a) LSCO-A (nanoparticle sample) and (b) LSCO-B (bulk sample) (along with the fits) taken at T = 300 K.

3.3.3 Magnetic properties of $La_{0.5}Sr_{0.5}CoO_3$ nanoparticles

The Curie temperatures of the two samples listed in Table 3.6 were estimated from M versus T curves taken under a low magnetizing field of H = 1 mT. These curves are shown in Fig.3.37. The insets in the figure show the dM/dT versus T curves whose inflection points give the respective Curie temperatures.
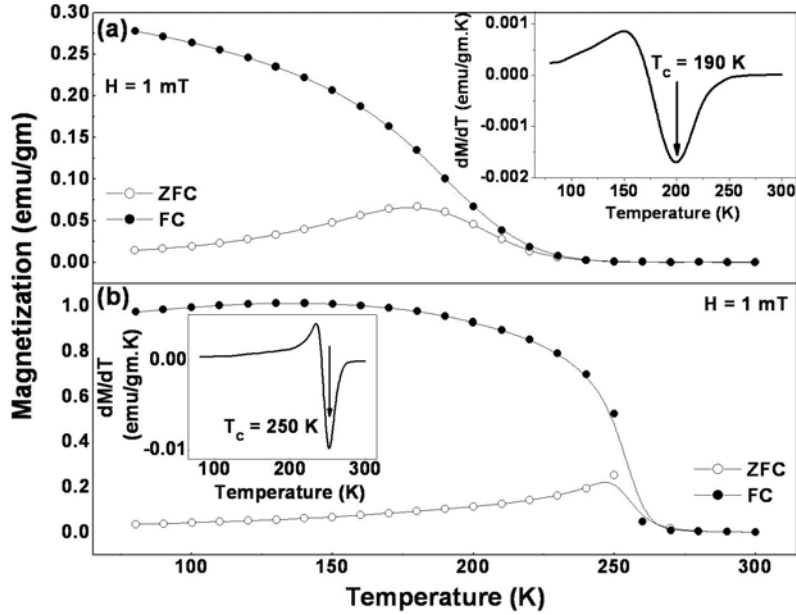
Fig.3.37. ZFC and FC curves for (a) LSCO-A and (b) LSCO-B taken under a magnetizing field of H = 1 mT. The insets show the dM/dT vs T curves for the two samples.

The variation of T_C with d have been determined for a series of nanoparticles from low field (H = 1 mT) ZFC curves (Fig.3.38 (a)). The variation of T_C with d is shown in Fig.3.38 (b). The T_C continuously decreases on size reduction.
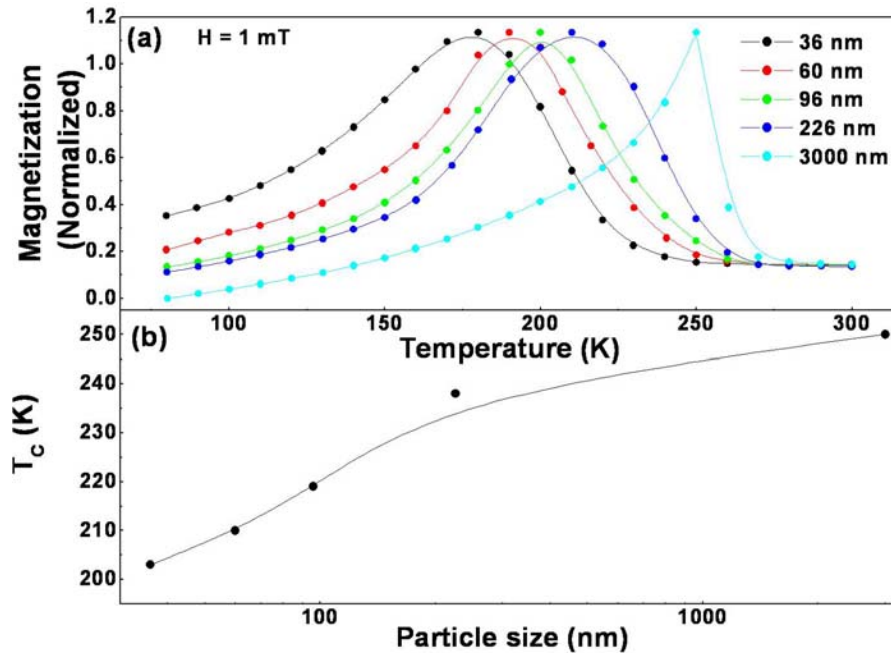
Fig.3.38. (a) Zero field cooled magnetization vs temperature curves for LSCO samples taken under a magnetizing field of 1 mT, (b) Variation of T_C as a function of the particle size for LSCO.

We have made finite size scaling plots for LSCO (both nanoparticles as well as film) using the relation $\dfrac{T_C(\infty) - T_C(d)}{T_C(\infty)} = \pm \left(\dfrac{d}{\xi_0} \right)^{-\lambda}$, where $T_C(\infty)$ corresponds to the bulk Curie temperature. These are shown in Fig.3.39. Both obey the scaling relation. The values of λ and ξ_0 are also quoted in Fig.3.39. We obtain slightly lower values of λ than is expected from mean field theories ($\lambda = 1$).
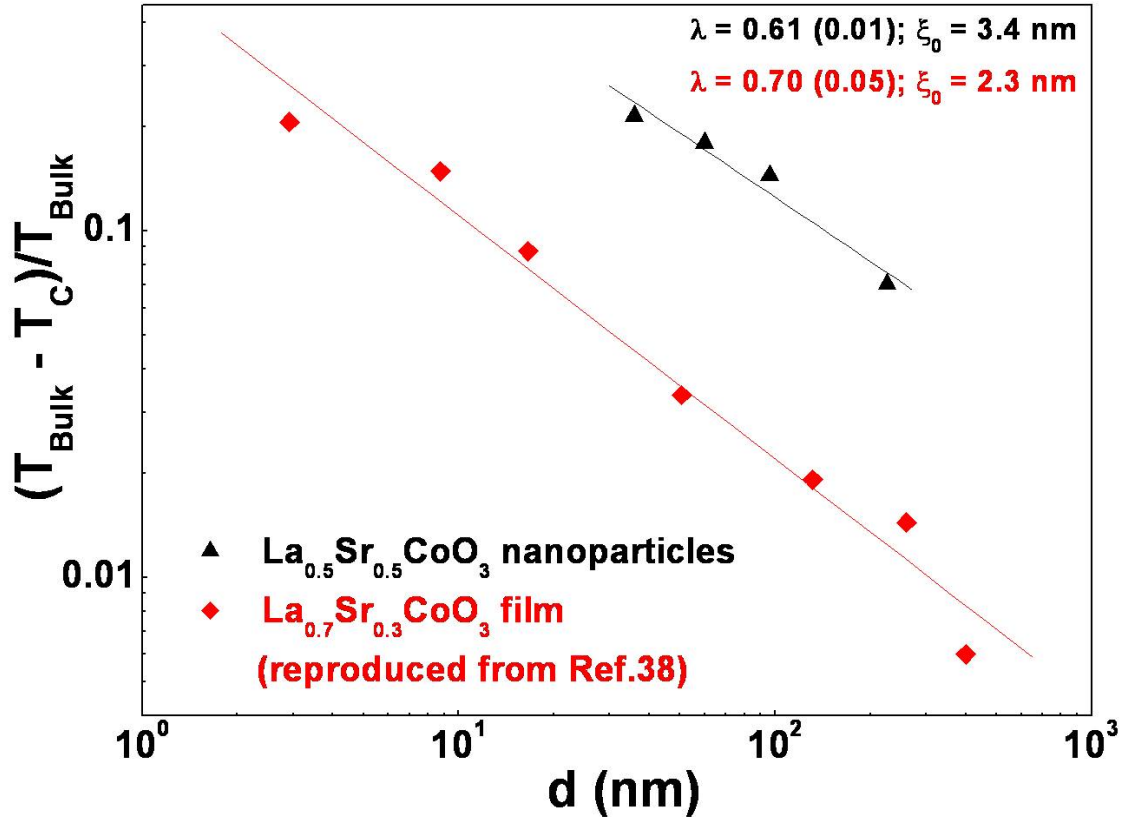
Fig.3.39. Finite size scaling plots for LSCO nanoparticles and LSCO film.

In Fig.3.40, we show the ZFC curves for LSCO-A taken under magnetizing fields ranging from 1 mT to 1 T. The ZFC curves do not saturate even for the highest field of 1 T. Also, even at H = 1 T, the FC and ZFC curves are not superimposed (see inset of Fig.3.40).

122
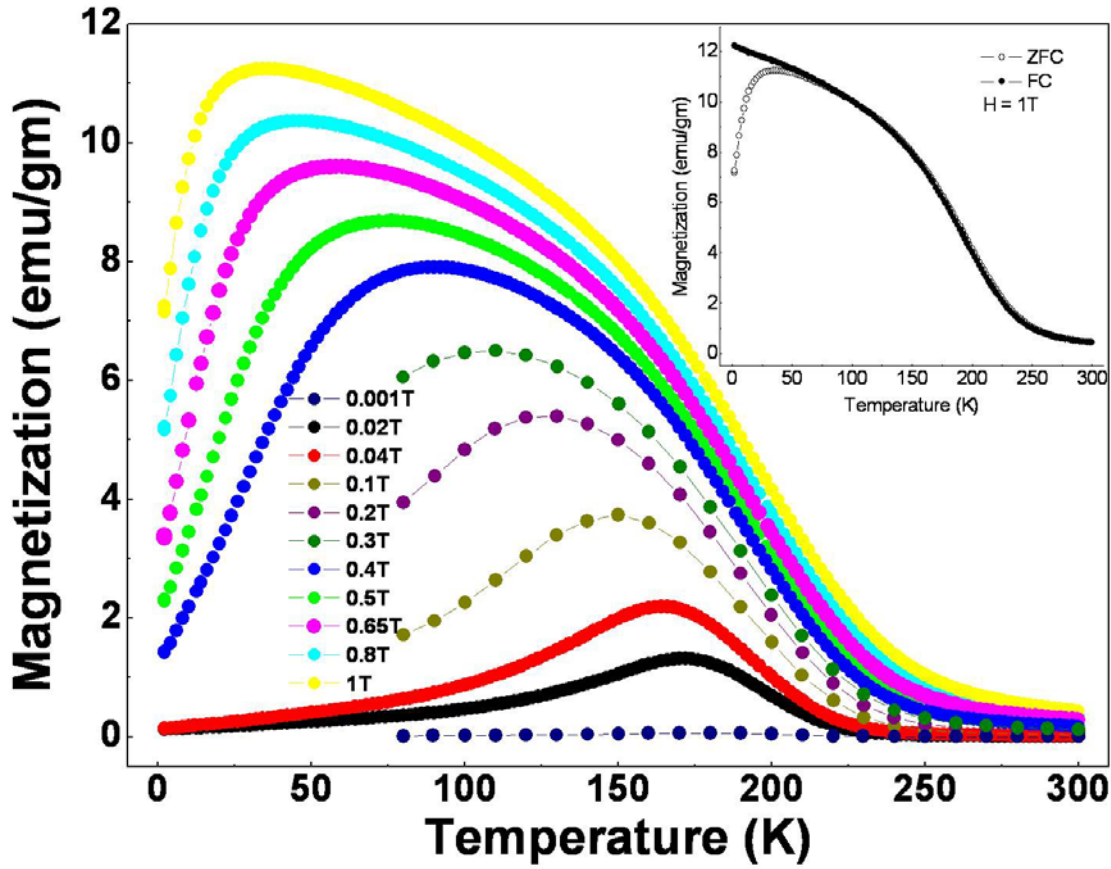
Fig.3.40. Zero field cooled magnetization vs temperature curves for LSCO-A taken under magnetizing fields ranging from 1 mT to 1 T. The inset shows both FC and ZFC curves taken under magnetizing fields of 1 T.

In Fig.3.41, we show the variation of the coercive field (H_C) as a function of particle size (d) (Fig.3.41 (b)) as well as temperature (T) (Fig.3.41 (a)). As the particle size is reduced, H_C first increases, reaches a maximum for d = 60 nm (this is much closer to our estimate of single domain particle size ($\sim$ 70 nm)), and then decreases. This indicates that LSCO-A (d = 36 nm) has entered the single domain regime. The coercive field of LSCO-A also follows the $T^{1/2}$

dependence $\left(H_C = \alpha \dfrac{2K}{M_S} \left\{ 1 - \left(\dfrac{T}{T_b} \right)^{\frac{1}{2}} \right\} \right)$ of single domain particles (also shown in Fig.3.41).

Here, M_S is the saturation magnetization, K is the anisotropy constant, α is a dimensionless constant and T_b is the blocking temperature. The value of T_b has been extracted from the slope of the linear fit. We get T_b = 159 K.

In Fig.3.42, we show the variation of T_B and T_P* for LSCO-A as a function of the applied magnetic field. The definitions of T_B and T_P* have been given earlier (see inset of Fig.3.15).
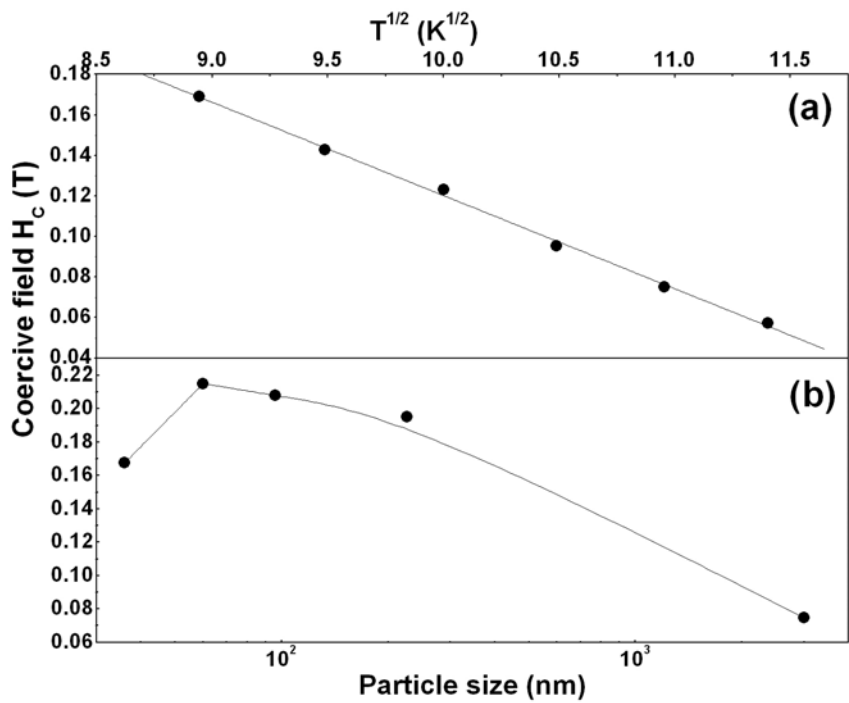
Fig.3.41. Variation of coercive field for LSCOO samples as a function of (a) temperature (for LSCO-A) and (b) particle size.
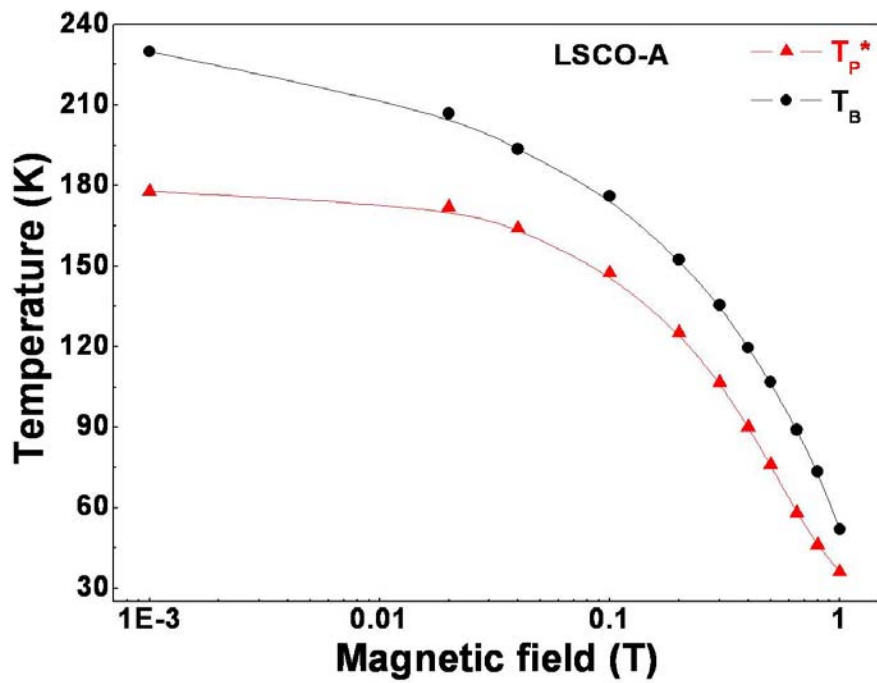
Fig.3.42. Variation of T_B and T_P* as a function of the applied magnetic field for LSCO-A.

3.3.3.1 Core – shell structure in LSCO nanoparticles

In Fig.3.43 (a), we plot the magnetization values of LSCO samples of different particle sizes at H = 1.6 T. These have been taken from MH curves taken at T = 80 K. Although the samples do not reach full saturation at this temperature, but the variation of M (at T = 80 K) with particle size (d) does mirror the variation of saturation magnetization with d. Thus, we can use these values to evaluate the shell thickness (δ) to particle size (d) ratio using the formula $M_S = M_{0S}\left(1 - \dfrac{6\delta}{d}\right)$. We have done this, and the variation of δ/d with d is shown in Fig.3.43 (b).

A comparison with Fig.3.28 (where we have shown the variation of δ/d with particle size for LCMO) will show that, while in LCMO the δ/d ratio is moderately low at $d \sim 100$ nm and starts to pick up very sharply below $d \approx 100$ nm, in LSCO, the rise in δ/d ratio occurs at a size much above $d \approx 100$ nm. At $d \approx 100$ nm, the δ/d ratio is quite high in LSCO, and increases only slightly below $d \sim 100$ nm. This is one of the reasons why the ferromagnetism in LCMO is more stable under size reduction.
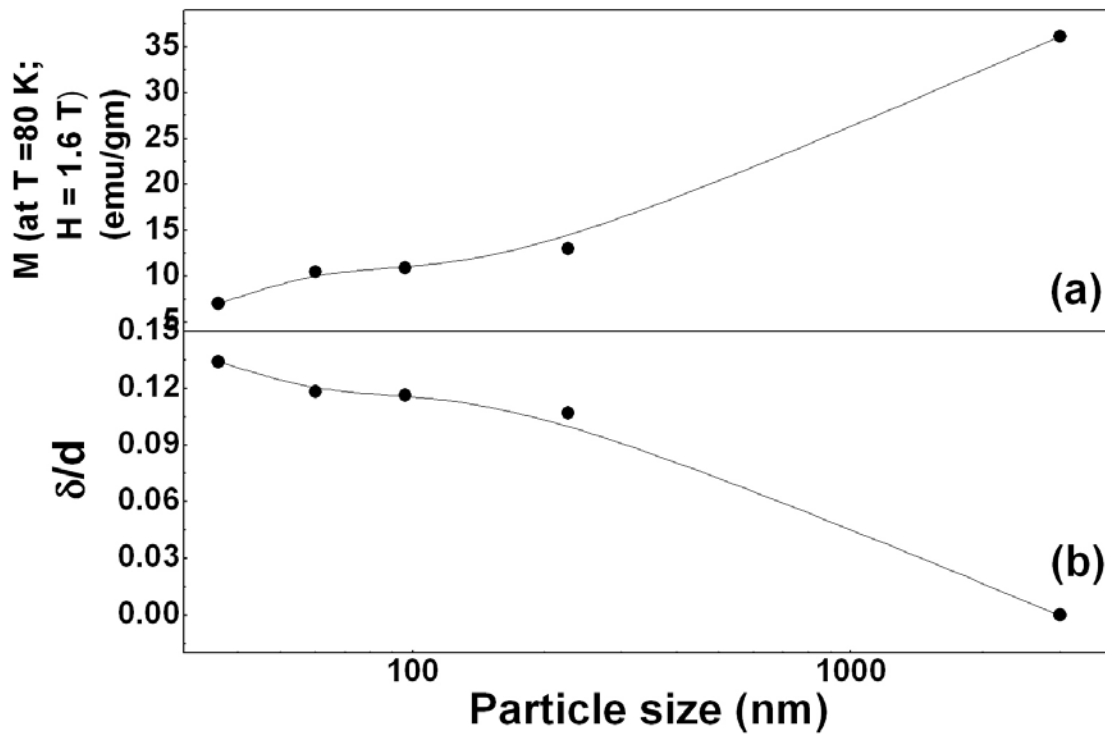
Fig.3.43. Variation of (a) M (at T = 80 K; H = 1.6 T) and (b) δ/d with particle size for LSCO (for details, see text).

3.4 Nanocrystalline $La_{0.67}Ca_{0.33}MnO_3$ and $La_{0.5}Sr_{0.5}CoO_3$ – a comparative study

In this section, we compare the magnetic state of nano LCMO with that in nano LSCO. In the bulk form, both $La_{0.67}Ca_{0.33}MnO_3$ and $La_{0.5}Sr_{0.5}CoO_3$ are ferromagnets and have Curie temperatures close to each other (T_C(LCMO) = 265 K and T_C(LSCO) = 250 K). However, as we have seen, on reducing the particle size to the nanometer regime, several differences can be seen in their magnetic behavior. In this section, we make a comprehensive list of these differences:

1. A size reduction to approximately the same regime brings down the Curie temperature of LSCO (d ~ 36 nm) by 60 K, while for LCMO (d ~ 23 nm), it decreases only by 10 K. The ferromagnetic interaction in LCMO is more stable under size reduction. For LCMO, T_C initially increases, reaches a maximum and then it reducesagain as d is decreased. In LSCO, the decrease in T_C is monotonous. The transition to the ferromagnetic state on cooling through T_C is more sharp in the manganite sample than the cobaltate sample ($\Delta T_{1/2}$(LCMO) $\approx$ 27 K and $\Delta T_{1/2}$(LSCO) $\approx$ 36 K). This probably happens because even in the bulk form, $La_{0.5}Sr_{0.5}CoO_3$ exists in a cluster glass like state with absence of long range ferromagnetic order. On the other hand, LCMO in the bulk form is a double exchange mediated long range ferromagnet.

2. The magnetization of the manganite nanoparticle sample saturates at low temperature. However, for nano LSCO, there is no magnetic saturation at low temperatures even at a high field of 1 T. This is an indication that in the nanometer regime, LSCO retains its cluster glass like behavior. Here, we note that a lack of saturation at high magnetic fields might also arise due to a spin – disordered shell in the nanoparticles. However, the surface to volume ratio being higher in smaller particles, we expect the disordered surface spins to have more influence on the manganite nanoparticles (which have an average diameter $d =$ 23 nm) than the cobaltate nanoparticles (which have an average diameter d = 36 nm). The fact that just the reverse of this occurs i.e. the magnetization of nano LCMO saturates whereas nano LSCO shows a lack of magnetic saturation leads us to the conclusion that the LSCO nanoparticles retain the cluster glass like behavior of the bulk system.

3. The two systems also respond in a different way to applied magnetic field. This can be seen in Fig.3.44 where we have shown the variation of T_B and T_P* as a function of the applied magnetic field for both nano LCMO and nano LSCO. In nano LCMO, a field of 0.2 T is sufficient to push down both T_B and T_P* to ~ 15 % of their value at H = 0 T. Above H = 0.2 T, T_B and T_P* do not change much. On the other hand, for nano LSCO, at a field of 0.2 T, T_B and T_P* are still at 70 % of their value at H = 0 T. Above H = 0.2 T, T_B and T_P* keep decreasing continuously and do not reach any kind of saturation. This again indicates the spin glass nature of the magnetic state in LSCO.
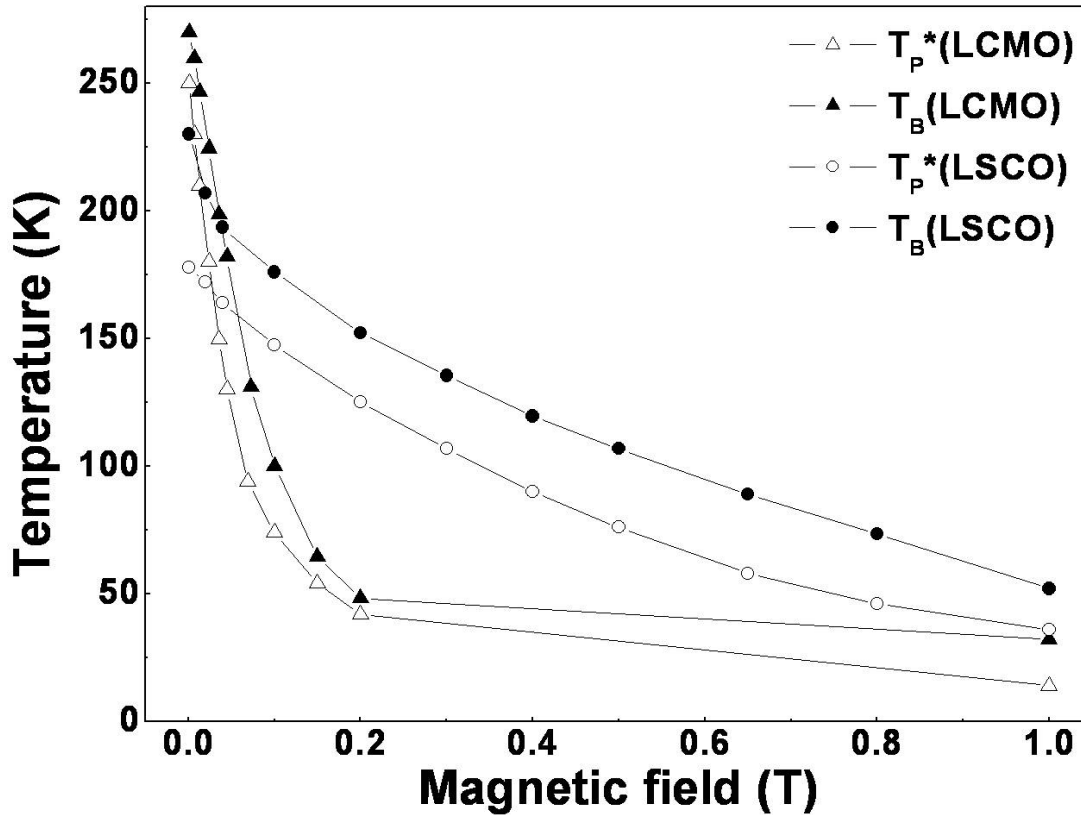
Fig.3.44. Variation of T_B and T_P^* as a function of the applied magnetic field for LCMO-E ($d \sim$ 23 nm) and LSCO-A ($d \sim$ 36 nm).

4. In Fig.3.45, we show the MH loop of nano LCMO and nano LSCO taken at T = 2 K. The most striking difference between the two lies in the value of the coercive field (H_C). While the manganite sample has a very small coercive field of $\sim$ 0.03 T (see inset of Fig.3.45(a)), nano LSCO has a much higher $H_C \approx 0.15$ T. This can also be seen in Fig.3.46, where we have plotted T vs H_C for nano LCMO and nano LSCO. Apart from that, in $La_{0.67}Ca_{0.33}MnO_3$, the magnetization more or less saturates at high field, whereas in $La_{0.5}Sr_{0.5}CoO_3$, the magnetization keeps on increasing and does not saturate even at the highest measured field of 5 T. (This lack of magnetic saturation was observed earlier from the field cooled curves also). Though the absolute value of the remanent magnetization (M_r) is of the same order in both the samples (M_r(LCMO) = 17 emu/gm and M_r(LSCO) = 10 emu/gm), the difference between the two becomes evident when we extract the values M_r/M(5 T) for both samples. M_r/M(5 T) for LCMO $\approx$ 0.27 and M_r/M(5 T) for LSCO $\approx$ 0.59.
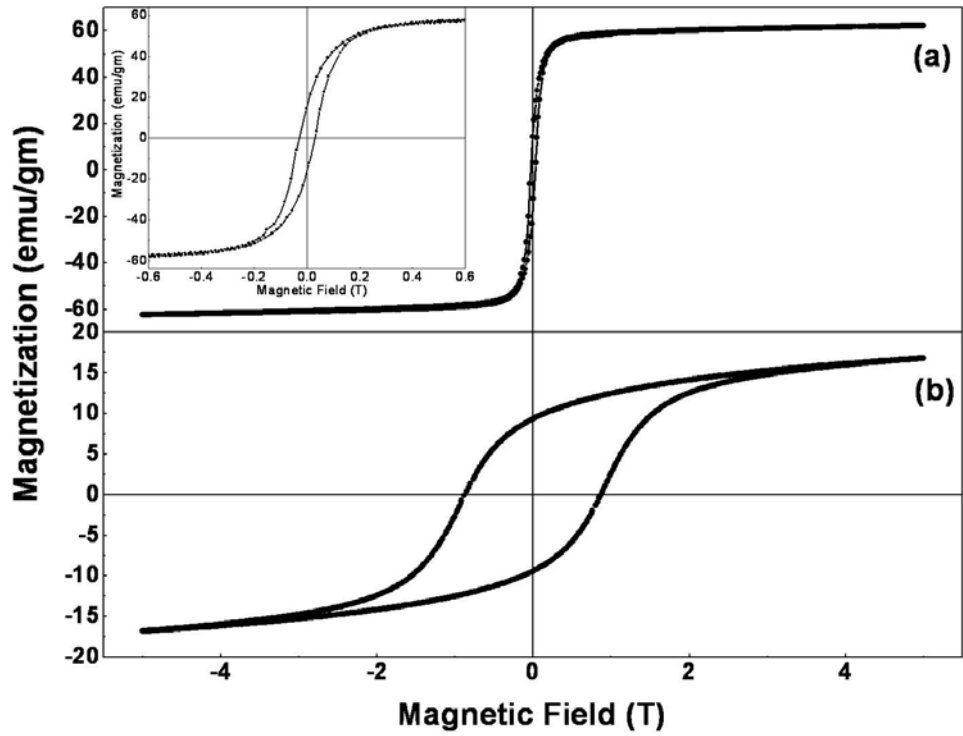
Fig.3.45. M vs H loop for nano (a) LCMO and (b) LSCO taken at T = 2 K. The inset shows an expanded region of the MH loop of nano LCMO around the origin.
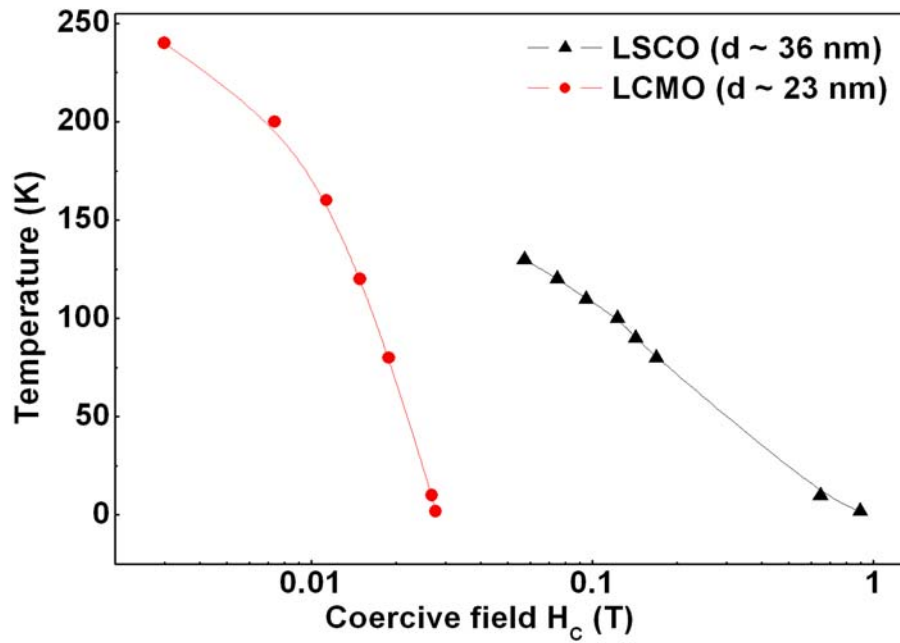
Fig.3.46. T vs H_C for LCMO-E ($d \sim 23$ nm) and LSCO-A ($d \sim 36$ nm)

5. A study of the temperature variation of the coercive fields of the two samples reveals that the difference goes much deeper than simply the absolute value of the two. While nano LSCO follows the $T^{1/2}$ dependence $\left(H_C = \alpha \dfrac{2K}{M_S} \left\{ 1 - \left(\dfrac{T}{T_b} \right)^{\frac{1}{2}} \right\} \right)$ of single domain particles, nano LCMO shows a more unusual linear dependence of the coercivity on temperature. These have been shown in Fig.3.16 and Fig.3.41.

3.5 Summary of results

We end this chapter by recapitulating the main results that have been obtained so far:

1. We have presented the effects of size reduction on two different kinds of perovskite oxides, $La_{0.67}Ca_{0.33}MnO_3$ (which, in the bulk state, is a double exchange ferromagnet) and $La_{0.5}Sr_{0.5}CoO_3$ (which, in the bulk state, lacks long range ferromagnetic order and shows cluster glass like behavior below the Curie temperature).

2. In $La_{0.67}Ca_{0.33}MnO_3$, size reduction introduces two competing effects. The first one arises from a change in the unit cell structure which becomes more cubic with a reduced orthorhombic strain, and tends to strengthen the ferromagnetism, and the second one arises from the outer disordered shell in the nanoparticles, which tends to weaken the ferromagnetism and whose effect increases drastically for very small size particles. The final phase of the system depends on which of these two effects win over.

3. The magnetic phase transition in LCMO changes from first order to second order when the size is reduced from the micron regime to the nanometer regime. We attribute this change in the order of the transition to a lowering of the value of $\dfrac{dT_C}{dP}$ due to an increased pressure in the nanoparticles (surface pressure), and also because of a rounding off effect due to random strain. Critical exponents, β, γ and δ have also been determined for nano LCMO. The critical exponents come out close to the mean field values for an isotropic system.

4. Finally, we have ended the chapter by making a comparative study of the magnetic properties of LCMO and LSCO nanoparticles both of which have comparable average particle sizes but show many differences in their magnetic properties.

References

[1] M.N.Barber in *Phase Transitions and Critical Phenomena*, edited by C.Domb and J.L.Lebowitz (Academic, New York, 1983)

[2] K.Shantha Shankar, Sohini Kar, G.N.Subbanna and A.K.Raychaudhuri, Solid State Comm., **129**, 479 (2004)

[3] P.Dey and T.K.Nath, Phys. Rev. B, **73**, 214425 (2006)

[4] R.N.Bhowmik, Asok Poddar, R.Ranganathan and Chandan Majumdar, arXiv:0810.0090v1 [cond-mat.mtrl-sci] 1 Oct 2008

[5] S.Robler, U.K.Robler, K.Nenkov, D.Eckert, S.M.Yusuf, K.Dorr and K.H.Muller, Phys. Rev. B, **70**, 104417 (2004)

[6] Yoseph Imry and Michael Wortis, Phys. Rev. B, **19**, 3580 (1979)

[7] P.Schiffer, A.P.Ramirez, W.Bao and S.-W.Cheong, Phys. Rev. Lett., **75**, 3336 (1995)

[8] R.Mahendiran and A.K.Raychaudhuri, Phys. Rev. B, **54**, 16044 (1996)

[9] Mandar Paranjape, A.K.Raychaudhuri, N.D.Mathur and M.G.Blamire, Phys. Rev. B, **67**, 214415 (2003)

[10] M.Ziese, H.C.Semmelhack, K.H.Han, S.P.Sena and H.J.Blythe, J. Appl. Phys., **91**, 9930 (2002)

[11] Jun Wang, Kai Zhang, Zhenmeng Peng and Qianwang Chen, J. Crystal Growth, **266**, 500 (2004)

[12] Aparna Roy, V.Srinivas, S.Ram, J.A.De Toro and J.P.Goff, J. Appl. Phys, **100**, 094307 (2006)

[13] http://www.ill.eu/sites/fullprof/

[14] W.C.Nunes, W.S.D.Folly, J.P.Sinnecker and M.A.Novak, Phys. Rev. B, **70**, 014419 (2004)

[15] Z.H.Zhou, X.S.Gao, J,Wang, K.Fujihara, S.Ramakrishna and V.Nagarajan, Appl. Phys. Lett., **90**, 052902 (2007)

[16] Congwu Cui and Trevor A. Tyson, Phys. Rev. B, **70**, 094409 (2004); Congwu Cui, Trevor A. Tyson and Zhiqiang Chen, Phys. Rev. B, **68**, 214417 (2003)

[17] Congwu Cui, Trevor A. Tyson, Zhong Zhong, Jeremy P.Carlo and Yuhai Qin, Phys. Rev. B, **67**, 104107 (2003)

[18] Tapati Sarkar, Barnali Ghosh, A.K.Raychaudhuri and Tapan Chatterji, Phys. Rev. B, **77**, 235112 (2008)

[19] P.Novak, M.Marysko, M.M.Savosta and A.N.Ulyanov, Phys. Rev. B, **60**, 6655 (1999)

[20] J.Mira, J.Rivas, F.Rivadulla, C.Vazquez-Vazquez and M.A.Lopez-Quintela, Phys. Rev. B, **60**, 2998 (1999)

[21] N.Moutis, I.Panagiotopoulos, M.Pissas and D.Niarchos, Phys. Rev. B, **59**, 1129 (1999)

[22] K.Ghosh, C.J.Lobb, R.L.Greene, S.G.Karabashev, D.A.Shulyatev, A.A.Arsenov and Y.Mukovskii, Phys. Rev. Lett., **81**, 4740 (1998)

[23] D.Kim, B.Revaz, B.L.Zink, F.Hellman, J.J.Rhyne and J.F.Mitchell, Phys.Rev.Lett., **89**, 227202 (2002)

[24] M.Sahana, U.K.Rossler, Nilotpal Ghosh, Suja Elizabeth, H.L.Bhat, K.Dorr, D.Eckert, M.Wolf and K.H.Muller, Phys. Rev. B, **68**, 104408 (2003)

[25] Daniel J.Amit and G.Parisi, J. Phys. C: Solid State Phys., **16**, 1385 (1983); Marcia C.Barbosa, Phys. Rev. B, **46**, 3672 (1992)

[26] Michael Aizenman and Jan Wehr, Phys. Rev. Lett., **62**, 2503 (1989)

[27] B.K.Banerjee, Phys. Lett., **12**, 16 (1964)

[28] C.P.Bean and D.S.Rodbell, Phys. Rev. **126**, 104 (1962)

[29] G.K.Williamson and W.H.Hall, Acta Metall., **1**, 22 (1953)

[30] S.Mukherjee, R.Ranganathan, P.S.Anilkumar and P.A.Joy, Phys. Rev. B, **54**, 9267 (1996)

[31] G.H.Jonker and J.H.Van Santen, Physica, **191**, 120 (1953)

[32] V.G.Bhide, D.S.Rajoria, C.N.R.Rao, G.Rama Rao and V.G.Jadhao, Phys. Rev. B, **12**, 2832 (1975)

[33] R.Mahendiran and A.K.Raychaudhuri, Phys. Rev. B, 54, **16044** (1996)

[34] M.Itoh, I.Natori, S.Kubota and K.Motoya, J. Phys. Soc. Jpn., **63**, 1486 (1994)

[35] P.S.Anil Kumar, P.A.Joy and S.K.Date, J. Phys.: Condens. Matter, **10**, L487 (1998)

[36] V.G.Sathe, A.V.Pimpale, V.Siruguri and S.K.Paranjpe, J. Phys.: Condens. Matter, **8**, 3889 (1996)

CHAPTER 4. DESTABILIZATION OF CHARGE ORDER IN $A_{0.5}Ca_{0.5}MnO_3$ (A = La, Pr) NANOPARTICLES

4.1 A brief review of the charge ordered state in half – doped manganites

The charge – ordered phase in manganites has been introduced in Section 1.6 of Chapter 1 of this thesis. Since the present chapter deals exclusively with this phase, we begin the chapter by revisiting the traditional charge – ordered state once again. This brief review will enable us to put our own investigations into proper perspective, and help us to establish the importance of the results obtained by us.

Formally, Rao et. al.[1] have defined charge ordering as a phenomenon observed in solids wherein electrons become localized due to the ordering of cations of differing charges on specific lattice sites. In this scenario of real space ordering of the charge carriers in the lattice, the Coulomb repulsion becomes predominant over the kinetic energy of the electrons and this renders the material insulating. In mixed valence manganites, these 'cations of differing charges' are the Mn^{3+} and Mn^{4+} cations. Historically, the occurrence of charge ordering in the manganites was first observed by Wollan and Koehler[2] through a series of systematic neutron scattering experiments. They used the series of $La_{1-x}Ca_xMnO_3$ oxides for these studies.

Charge ordering is favoured in half – doped manganites where equal number of Mn^{3+} and Mn^{4+} ions are present. However, it is not restricted to $x = 0.5$, but is also found in various compositions in the range $0.3 < x < 0.75$, depending on the A and B ions. The charge ordered phases are novel manifestations arising from the interactions between the charge carriers and the phonons wherein the Jahn – Teller distortions play a significant role. Charge ordering arises because the carriers are localized into specific sites below the charge ordering temperature (T_{CO}), giving rise to long range order throughout the crystal structure. Furthermore, the Mn^{3+} (e_g) orbitals and the associated lattice distortions also develop long range order, giving rise to orbital ordering. The magnetic exchange interactions between the Mn ions become anisotropic and give rise to complex magnetic ordering in these structures. We have, in Chapter 1, shown the possible magnetic structures commonly found in the manganese oxides (see Fig.1.6). The charge ordered state is typically accompanied by an antiferromagnetic ordering of spins, which is called the CE type[3], and is shown in Fig.4.1 (a). This is actually a mixture of the C – phase with the E – phase. In the antiferromagnetic state, the $Mn^{3+}O_6$ octahedra get distorted with the Mn-O bonds in the ab plane being longer than the Mn-O bonds in the c direction (Fig.4.2(b)).
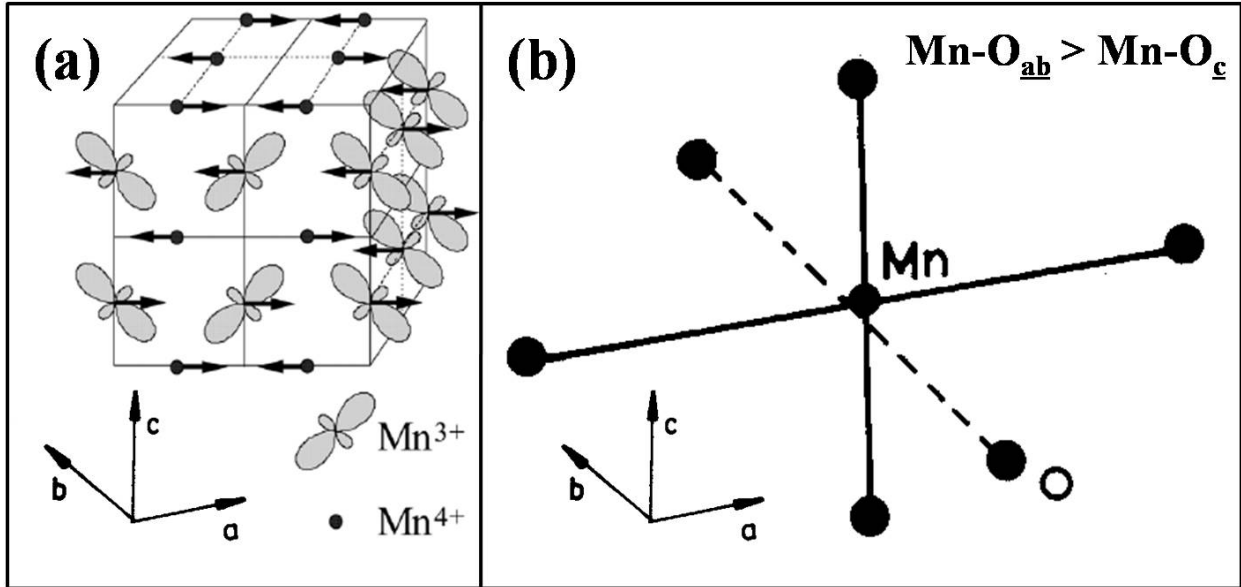
Fig.4.1. (a) Spin, charge and e_g orbital ordering pattern of the CE – type observed for most half – doped manganites (reproduced from [4]), (b) Distortion in $Mn^{3+}O_6$ octahedra in the antiferromagnetic state (reproduced from [1]).

The long range ordering mentioned before is often visible as "charge stripes" in transmission electron microscopy (TEM) images. In $La_{1-x}Ca_xMnO_3$ (x = 2/3), TEM images show pairs of $Mn^{3+}O_6$ stripes, with large lattice contractions due to the Jahn – Teller effect, separated by uniform stripes due to the $Mn^{4+}O_6$ octahedra[5] (Fig.4.2). Paired Jahn – Teller distorted stripes or bi-stripes have been suggested to be the basic building blocks of the charge ordered state. High resolution lattice images of $La_{0.5}Ca_{0.5}MnO_3$ show the CO state to involve a mixture of paired and unpaired Jahn – Teller distorted Mn^{3+} stripes, the unpaired stripes arising from the disordering of the d_z^2 orbitals concerned[6]. Although these stripes in electron microscope images have received much attention, it must be noted that these are essentially lattice images. It is not fully clear why the dark contrast arises.
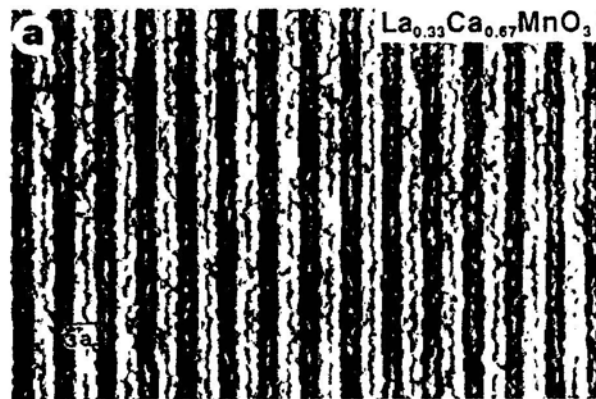
Fig.4.2. Electron microscope lattice image taken at 95 K showing $Mn^{3+}O_6$ Jahn – Teller distorted stripes in $La_{0.33}Ca_{0.67}MnO_3$ (reproduced from [1]).

133

However, some recent studies have shown that the superstructure that evolves in these oxides at low temperature cannot always be explained through Mn^{3+}/Mn^{4+} charge ordering. Daoud – Aladine et. al.[7] have shown that the pattern of atom displacements in these oxides suggests the trapping of electrons within pairs of Mn sites, involving both a local double exchange and a polaronic – like distortion. The two mechanisms act together to form vibronic localized electronic states – the Zener polarons. These studies were reported on $Pr_{0.6}Ca_{0.4}MnO_3$ single crystal data.

4.2 Stability of the charge ordered phase

One major issue that is still a matter of intense investigation is the stability of the charge – ordered phase in the manganite oxides. As has been emphasized earlier, a complicated balance of the ferromagnetic double exchange mediated by charge carriers of e_g nature and antiferromagnetic superexchange interactions between localized magnetic moments of t_{2g} nature coupled to lattice distortion effects and orbital degrees of freedom leads to this especially complex phase at x ~ 0.5. The charge ordered phase is mostly located at phase boundaries between insulating and metallic states with different magnetic order. This makes it very prone to getting affected by a variety of external perturbations. Studies have revealed that the charge – ordered ground state is highly sensitive to a variety of external factors like the average size of the A – site cations[8,9], pressure[10,11], magnetic[12] and electric fields[13,14], as well as isotopic[15] and chemical substitutions. A slight perturbation in any of the above forms can destabilize the charge – ordered ground state and give rise to a ferromagnetic metallic state. This fine sensitivity rises from the fact that the charge – ordered insulating state and the ferromagnetic metallic state are energetically almost degenerate. Thus, destabilization of the charge ordered state gives rise to a ferromagnetic metallic phase (in preference to a paramagnetic metallic or paramagnetic insulating state). Here, we note that in contrast to the various factors mentioned above, cation size disorder (the definition of cation size disorder, and how it is quantified can be found in Chapter 1) does not seem to have much of an effect on the charge ordered state of half – doped manganites. Vanitha et. al.[16] have shown that the charge ordering transition temperature (T_{CO}) is not very sensitive to the size mismatch.

However, what is relatively less explored is the effect of size reduction of the particles to the nanometer regime on the traditional charge – ordered phase. A handful of studies do report the effect of size reduction on half – doped manganites[17-19], but these studies were done with particle sizes which were much larger than those used in the present thesis (in some cases, in excess of 100 nm). These studies have reported some modification of the charge – ordered state in these systems. However, no clear analysis of the crystal structure was done, and the physics underlying the modification of the ground state was not explored unambiguously. The motivation behind the work reported in this chapter was to see whether size tuning of the ground state is a possibility in the half – doped manganites, and if so, then to state unambiguously the underlying physics behind the observed effect. In particular, it is noted that structure plays a very important role in stabilizing the CO-OO state, and hence, any investigation of the stability of a charge ordered phase necessarily requires a study of the structure of the system. In this context, the earlier reports on nanoparticles of half – doped manganites were woefully inadequate. In the present work, we have focused on how the structure evolves on size reduction and leads to a destabilization of the CO-OO state.

In Fig.4.3, we illustrate schematically the effect of external perturbations on the charge – ordered ground state, and the motivation behind the work reported in this chapter.
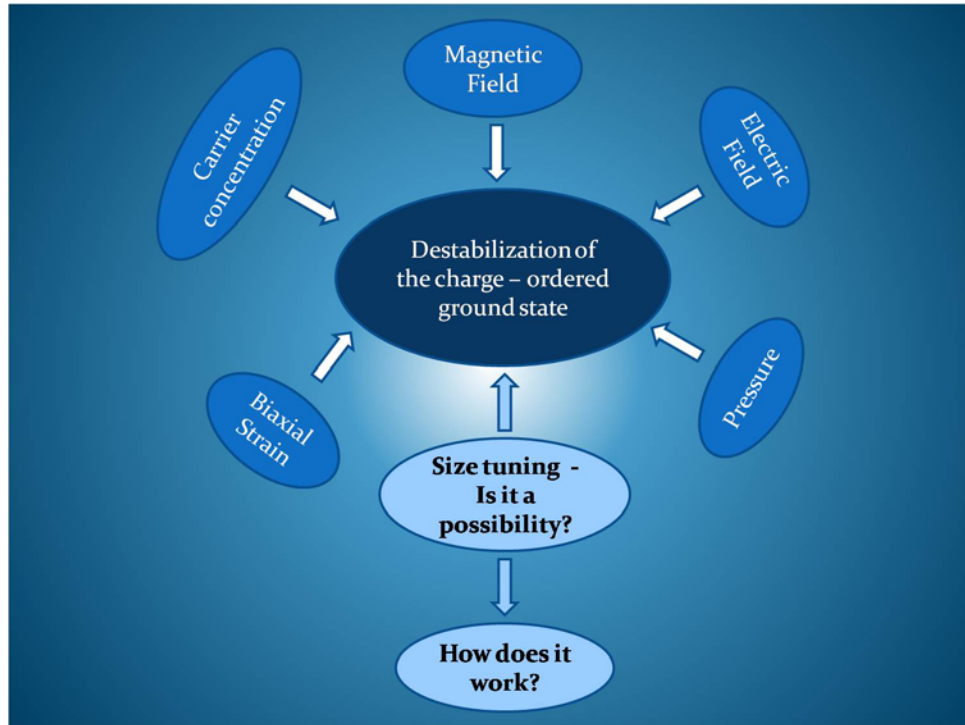
Fig.4.3. Effects of external perturbations on the charge – ordered ground state.

4.3 The traditional charge – ordered state in bulk half – doped manganites

The studies reported in this chapter have been done on two half – doped systems, $La_{0.5}Ca_{0.5}MnO_3$ (LCMO) and $Pr_{0.5}Ca_{0.5}MnO_3$ (PCMO). In Fig.4.4, we show the phase diagrams of $La_{1-x}Ca_xMnO_3$ (Fig.4.4 (a)) and $Pr_{1-x}Ca_xMnO_3$ (Fig.4.4 (b)). Our regions of interest have been marked by red lines in the phase diagrams. As can be seen from the phase diagrams, when $La_{0.5}Ca_{0.5}MnO_3$ is cooled from room temperature, it first encounters a paramagnetic to ferromagnetic phase transition at around ~ 225 K. On further cooling, it encounters a second phase transition from the ferromagnetic to charge ordered antiferromagnetic state at ~ 150 K. We also note that $La_{0.5}Ca_{0.5}MnO_3$ lies at the boundary line of the ferromagnetic (x < 0.5 region) and charge ordered antiferromagnetic (x > 0.5) region. Thus, the charge ordered antiferromagnetic state in $La_{0.5}Ca_{0.5}MnO_3$ is more susceptible to destabilization. This brings us to the second oxide ($Pr_{0.5}Ca_{0.5}MnO_3$). The major difference between $La_{0.5}Ca_{0.5}MnO_3$ (LCMO) and $Pr_{0.5}Ca_{0.5}MnO_3$ (PCMO) is that while the former is an intermediate bandwidth oxide, the latter is a low bandwidth oxide. Thus, PCMO should have a weaker ferromagnetic interaction which in turn means that the competing interaction (i.e. charge ordering) should be strengthened. This can be seen in the phase diagram of PCMO, which shows that unlike the case of LCMO, $Pr_{1-x}Ca_xMnO_3$ compositions do not show ferromagnetic metallic states at any temperature. However, at low hole doping range, it shows a ferromagnetic insulating state. Thus, on cooling $Pr_{0.5}Ca_{0.5}MnO_3$ from room temperature, it first encounters a phase transition from a paramagnetic insulating state

to a charge ordered insulating state at ~ 250 K, followed by a transition to an antiferromagnetic insulating state at a lower temperature.
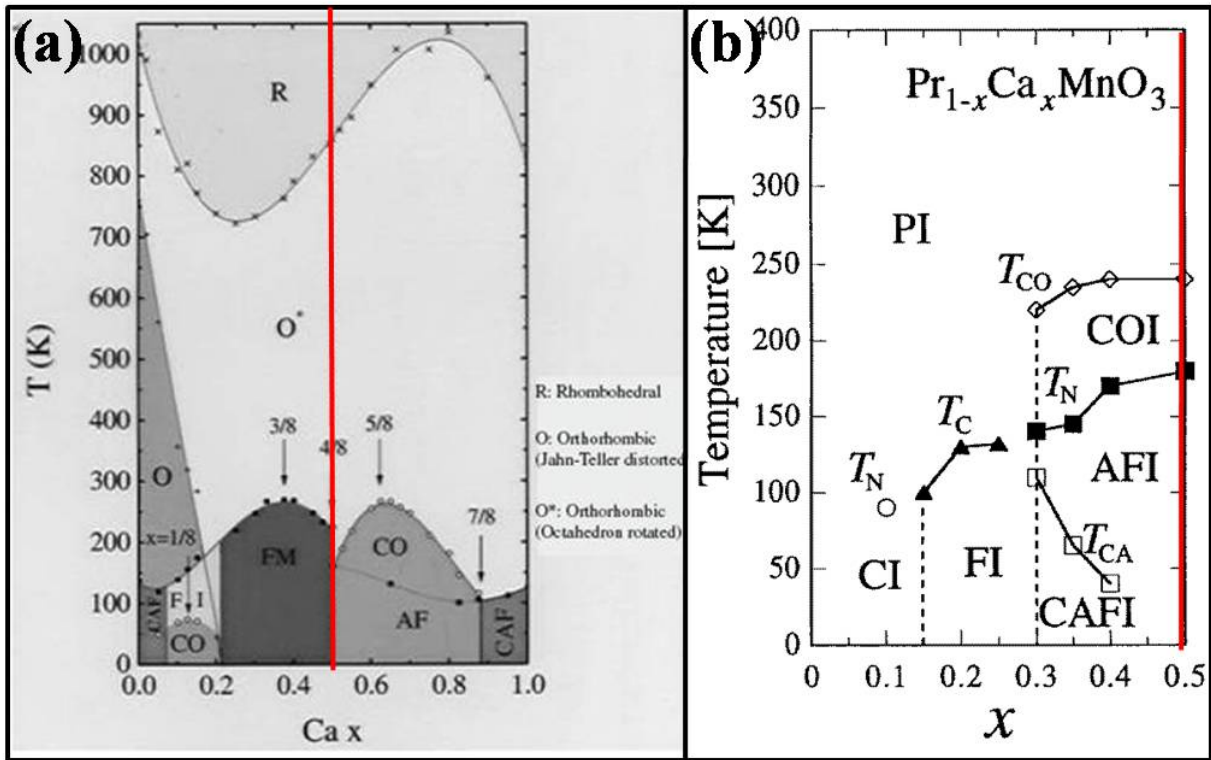
Fig.4.4. Phase diagrams of (a) $La_{1-x}Ca_xMnO_3$ (reproduced from [20]) and (b) $Pr_{1-x}Ca_xMnO_3$ (reproduced from [21]).

In the following subsections, we briefly review the salient features of these two systems in the bulk state. The bulk samples of LCMO and PCMO show features which are typical of all charge – ordered systems like rapid changes in the lattice parameters around the charge ordering temperature and existence of an antiferromagnetic and insulating ground state. The bulk samples on which the measurements (described in the subsequent sections) have been done are polycrystalline samples prepared by annealing the nano powder at 1300^0C and have particle sizes in excess of 3 μm. The details of the sample preparation method and characterization of the samples have been dealt with in details in Chapter 2 and will not be repeated here.

4.3.1 La$_{0.5}$Ca$_{0.5}$MnO$_3$

At high temperatures, $La_{0.5}Ca_{0.5}MnO_3$ is a paramagnetic insulator, and upon cooling, it first becomes ferromagnetic at T_C ~ 225 K, and then antiferromagnetic at T_N ~ 155 K. The existence of these two phases has been attributed to the competition between ferromagnetic double exchange and antiferromagnetic superexchange coupling. The antiferromagnetic transition at 155 K is accompanied by a charge ordering transition (T_{CO} ~ 155 K). The magnetic structure of $La_{0.5}Ca_{0.5}MnO_3$ was first reported by Wollan et.al.[2], and is quite complex: it entails

a quadrupling of the volume of the original orthorhombic unit cell and consists of two magnetic sublattices. Following this observation, Goodenough[3] proposed that the two sublattices result from charge ordering between the Mn^{3+} and Mn^{4+} ions. In Goodenough's model, charge ordering is accompanied by orbital ordering, whereby the d_z^2 Mn^{3+} orbitals (associated with long Mn^{3+} - O bonds in the Jahn – Teller distorted $Mn^{3+}O_6$ octahedra) would order, forming zig – zag chains in the $a – c$ plane. Later on, more complete structural studies were done by Radaelli et.al.[22] from high resolution synchrotron x – ray and neutron powder diffraction measurements. They showed that the development of magnetic ordering in $La_{0.5}Ca_{0.5}MnO_3$ is associated with the appearance of weak extra reflections in the x-ray diffraction patterns, which are signatures of small structural distortions due to charge and orbital ordering. The appearance of these satellite peaks are shown in the insets of Fig.4.5. In Fig.4.5, we show the XRD patterns of LCMO bulk sample taken at (a) 300 K and (b) 5 K. The insets show the expanded regions between $2\theta = 13.4^0$ and 14.2^0, which clearly show the appearance of an extra reflection (240) when the sample is cooled below its charge ordering temperature.
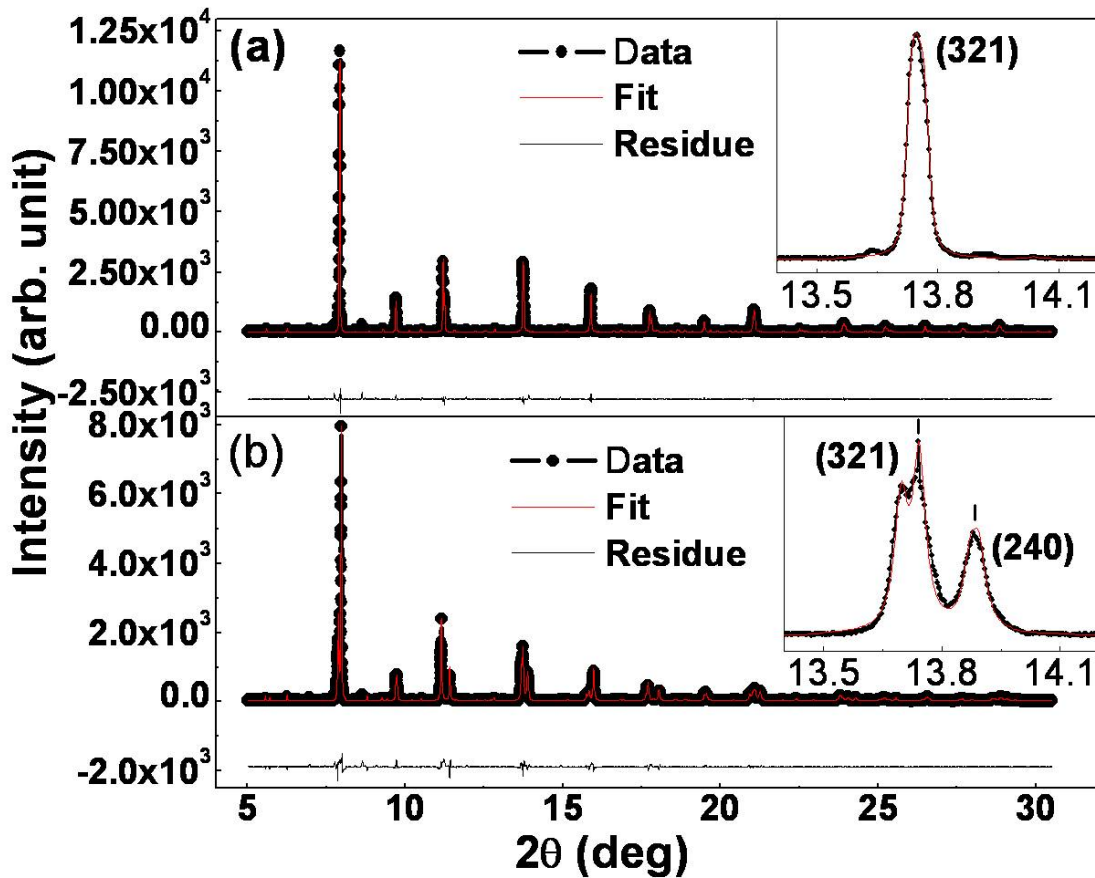
Fig.4.5. XRD patterns (along with the fits) of bulk $La_{0.5}Ca_{0.5}MnO_3$ (average particle size ~ 3.6 μm) taken at (a) 300 K and (b) 5 K. Insets show the expanded regions between $2\theta = 13.4^0$ and 14.2^0.

137

The x-ray patterns shown in Fig.4.5 were taken using high resolution synchrotron radiation source at the European Synchrotron Radiation Facility, Grenoble, France using the BM-01B beamline and a wavelength of 0.375 Å. The samples were in powder form and were kept in a borosilicate capillary. The calibration was done using standard Si samples. Fig.4.3 also shows the Rietveld fits (red lines) alongwith the residues of the patterns. The Rietveld analysis of the lattice structure was done using the FullProf suite software[23]. For these structural refinements, we used nearly 5000 – 6000 points/scan using six detectors. The Rietveld refinement uses a profile fitting technique to obtain the crystal structure parameters. The x – ray line profiles were modeled using a pseudo – Voigt profile shape function. The lattice parameters of bulk $La_{0.5}Ca_{0.5}MnO_3$ as extracted from the Rietveld fits are shown in Fig.4.6. To extract the temperature evolution of the lattice parameters, we took x – ray diffraction data at 11 temperatures over the range 5 K – 300 K (all the x – ray patterns are shown in Fig.4.7). As can be seen from Fig.4.6, the lattice parameters display large changes in the region $T_{CO} < T < T_C$. At 300 K, the three axes have similar size. With cooling, the *b* axis decreases drastically, and the *a* and *c* axes increase correspondingly. The changes become more pronounced below 200 K and they become nearly temperature independent for $T < T_{CO}$. These changes in the lattice parameters are associated with the structural changes which occur as the bulk sample undergoes the charge ordering transition. Radaelli et.al.[22] have found that these structural changes constitute a large Jahn – Teller distortion of the $Mn^{3+}O_6$ octahedra, while the $Mn^{4+}O_6$ octahedra remain almost undistorted. Another important point to note is that below the charge ordering temperature, the structure of bulk LCMO undergoes an orthorhombic to monoclinic transition, which reduces the crystallographic symmetry from *Pnma* to *P2$_1$/m*[22]. This is because the charge ordered structure is characterized by a large J – T distortion of the $Mn^{3+}O_6$ octahedra, while the $Mn^{4+}O_6$ octahedra remain almost undistorted. Thus, we get two independent magnetic sublattices which would necessarily entail a reduction of the crystallographic symmetry (in this case from orthorhombic to monoclinic) since there must be two inequivalent Mn sites in the unit cell.
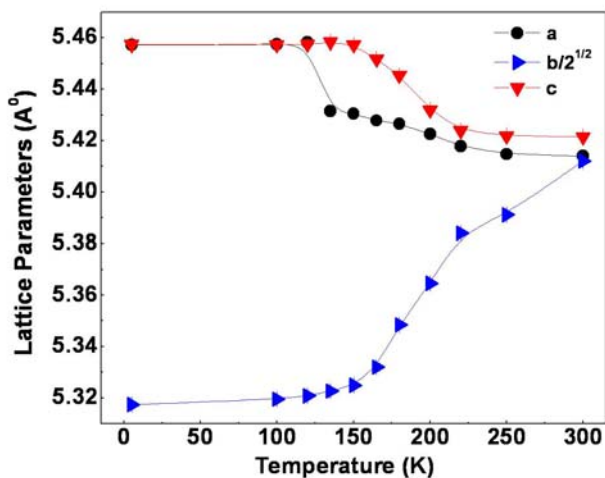
Fig.4.6. Temperature evolution of lattice parameters for bulk LCMO. Error bars, where not visible, are smaller than the symbols.
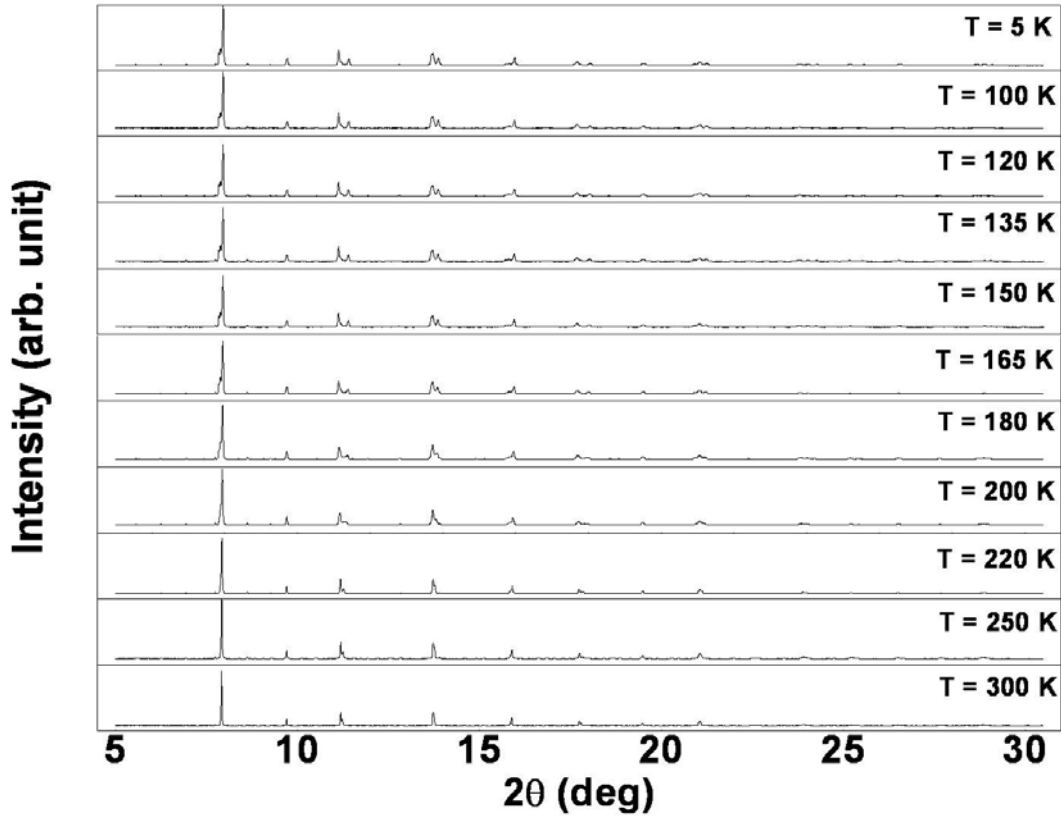
Fig.4.7. Synchrotron x – ray diffraction patterns for bulk LCMO taken at different temperatures.

As stated earlier, charge ordering in bulk LCMO is accompanied by spin ordering. As such, the structural changes which are detailed above are accompanied by distinct changes in the magnetic properties of the sample. The spin ordering is an antiferromagnetic transition to CE – type ordering with the Néel temperature $T_N \approx 155$ K. Fig.4.8 shows the ac susceptibility vs temperature plot (taken by mutual inductance bridge) for bulk LCMO. As is clear from the figure, the antiferromagnetic transition shows up as a drop in the susceptibility following the high temperature transition from paramagnetic to ferromagnetic state at $T_C \approx 225$ K. These measurements were made using a homemade low field ac susceptibility bridge working at 33.33 Hz. An important point to note is the hysteresis present in the ac susceptibility near T_{CO}. During cooling (black curve), the susceptibility starts to decrease at $T \approx 150$ K, and the transition is mostly over by $T \approx 135$ K. The warming curve (red curve) shows a single peak at ~ 210 K. The presence of this hysteresis between the heating and cooling runs is a typical signature of the charge ordering transition.
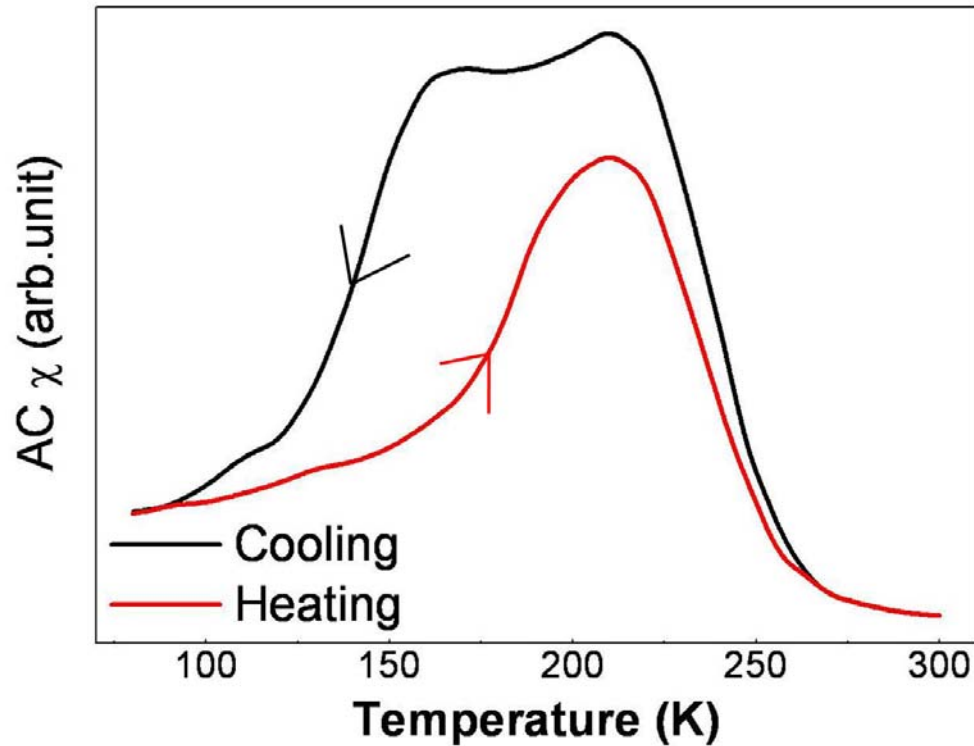
Fig.4.8. AC susceptibility versus temperature plot for bulk LCMO.

Electrical resistivity also provides a strong evidence for the charge and orbital ordering transition when the sample enters an insulating state on cooling. Often the charge ordering transition is reflected as a change in slope in the resistivity plot. In Fig.4.9, we show the resistivity versus temperature plot for bulk LCMO. The sample shows an insulating behaviour throughout the temperature range and the resistivity rises rapidly as the sample is cooled through the charge ordering transition. The charge ordering transition is reflected as a change in slope in the resistivity plot. This can be seen in the inset of Fig.4.9, where we plot *dlnρ/d(1/T)* versus *T*, which gives the transport activation energy at temperature *T*. We find a clear change in slope (at T ≈ 150 K) showing hardening of the transport gap on cooling through the charge ordering temperature.
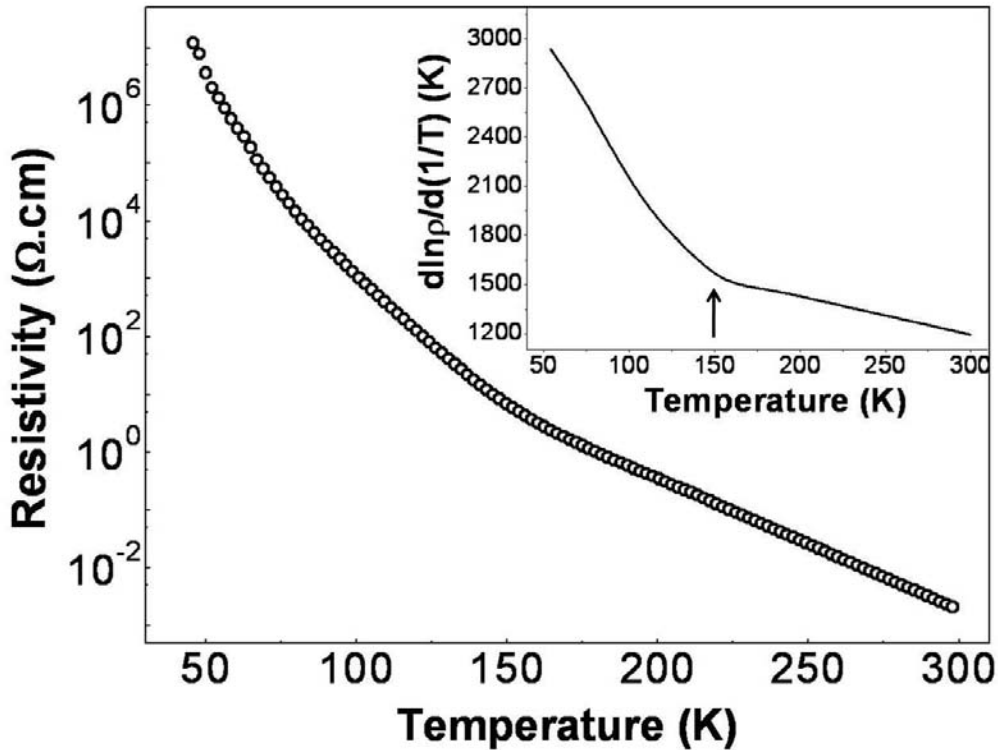
Fig.4.9. Resistivity versus temperature plot for bulk LCMO. The inset shows a plot of
dlnρ/d(1/T) versus *T*.

4.3.2 $Pr_{0.5}Ca_{0.5}MnO_3$

$Pr_{1-x}Ca_xMnO_3$ is a low bandwidth perovskite and shows insulating properties for the entire range of Ca concentration ($0 \leq x \leq 1$). In this respect, $Pr_{1-x}Ca_xMnO_3$ is quite different from $La_{1-x}Ca_xMnO_3$ which shows a wide range of x having ferromagnetic metallic ground state. The difference arises from the fact that the tolerance factor of $Pr_{1-x}Ca_xMnO_3$ is lower than that of $La_{1-x}Ca_xMnO_3$ (the ionic radius of Pr^{3+} being smaller than that of La^{3+}). The tolerance factor (*f*) expresses the mismatch of the ionic radii with respect to the ideal cubic perovskite structure. The more the *f* – value declines from 1, the stronger is the deformation of the crystal structure. Lowering the symmetry from cubic and increasing the structural deformation results in a narrower e_g – band.

Although the charge – ordered phenomenon is optimized at x = 0.5, but this phase is seen in $Pr_{1-x}Ca_xMnO_3$ even when there is a deviation of x from 0.5. Thus, the charge – ordered phase is particularly robust for the range $0.3 \leq x \leq 0.5$[24]. The specific case of $Pr_{0.5}Ca_{0.5}MnO_3$ has a charge – ordering transition around 250 K[21]. This phase is particularly robust, and a magnetic field as high as 20 T is needed to destabilize ("melt") the CO state. The smaller ionic radius stabilizes the CO-OO state and the CO-OO state is more stable in this material compared to that

seen in LCMO (x = 0.5) system. Fig.4.10 shows a schematic representation of the ordering of manganese moments in $Pr_{0.5}Ca_{0.5}MnO_3$ at 5 K.
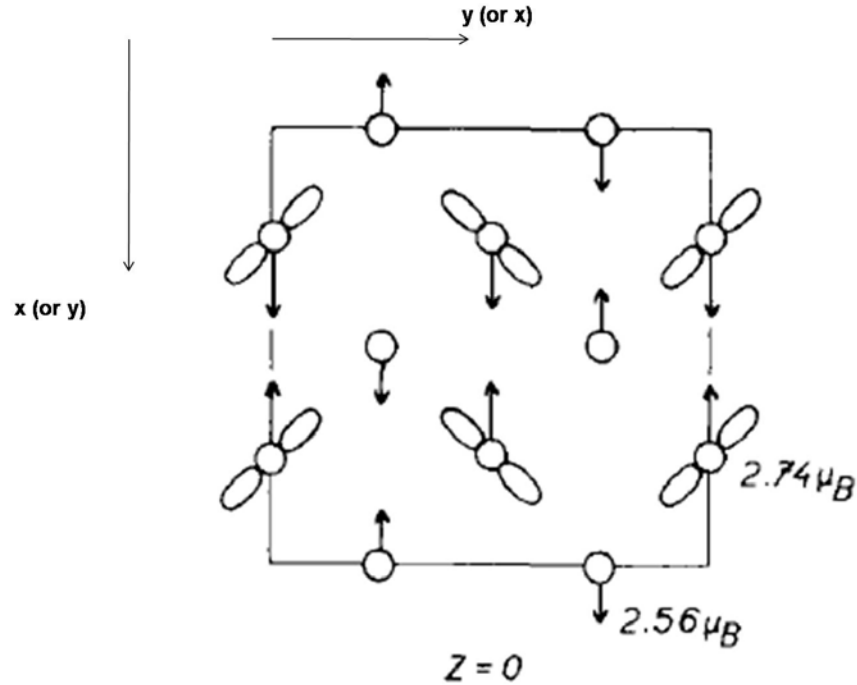
Fig.4.10. Ordering of manganese moments in $Pr_{0.5}Ca_{0.5}MnO_3$ at 5 K. The plane z = ½ is identical, but with spins reversed (reproduced from [25]).

In Fig.4.11, we show the XRD patterns (along with the fits) of bulk PCMO taken at 300 K and 5 K (the appearance of satellite peaks on cooling through the charge ordering temperature are shown in the insets), and Fig.4.12 shows the temperature evolution of the lattice parameter, magnetization and resistivity of bulk $Pr_{0.5}Ca_{0.5}MnO_3$. The lattice parameters have been extracted from synchrotron x – ray data taken at different temperatures (similar to bulk LCMO). These x – ray patterns are shown in Fig.4.13.
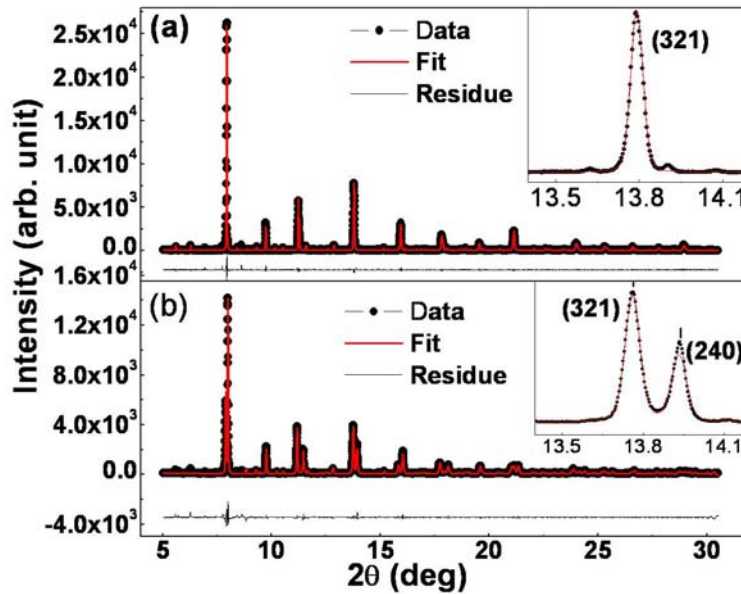
Fig.4.11. XRD patterns (along with the fits) of bulk $Pr_{0.5}Ca_{0.5}MnO_3$ (average particle size ~ 3.6 μm) taken at (a) 300 K and (b) 5 K. Insets show the expanded regions between $2\theta = 13.4^0$ and 14.2^0.
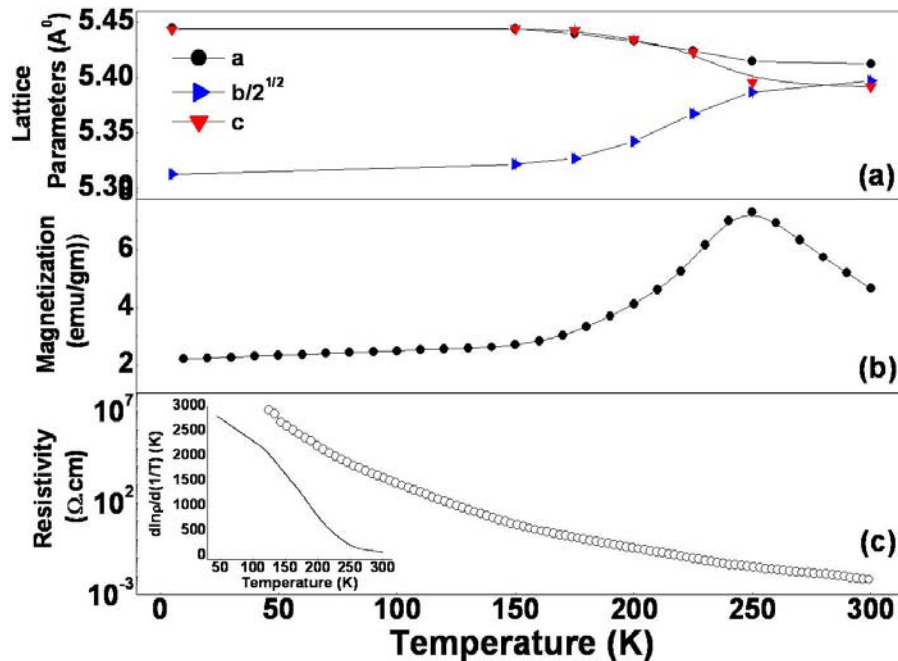
Fig.4.12. Temperature evolution of (a) lattice parameters, (b) magnetization and (c) resistivity of bulk $Pr_{0.5}Ca_{0.5}MnO_3$ The inset in (c) shows a plot of *dlnρ/d(1/T)* versus *T*.

143
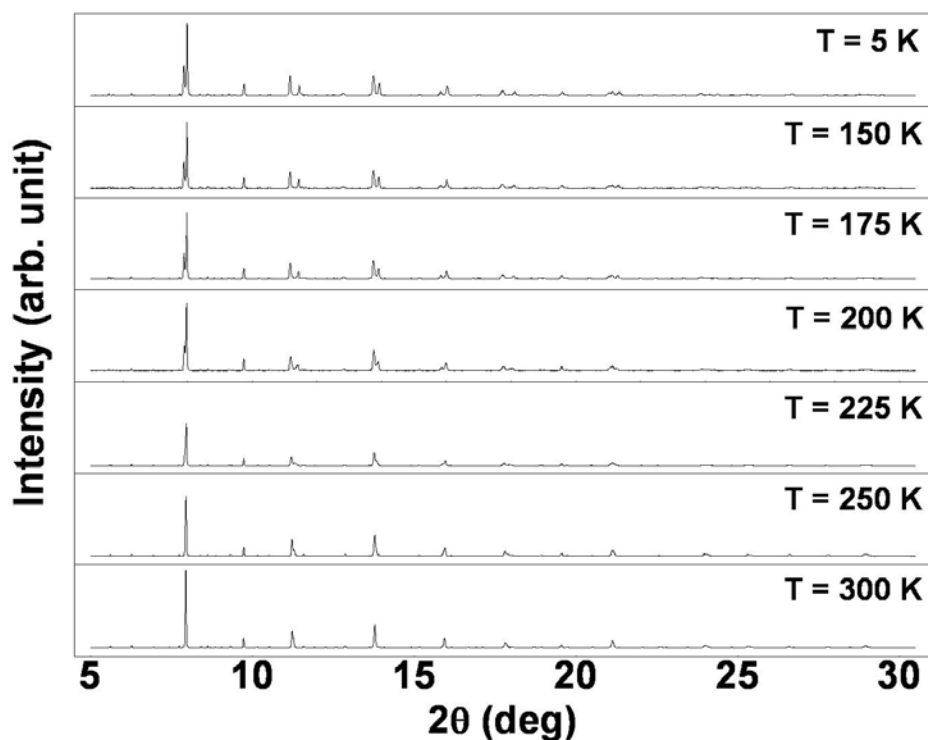
Fig.4.13. Synchrotron x – ray diffraction patterns for bulk PCMO taken at different temperatures.

As is seen from Fig.4.12 (a), the lattice parameters of bulk PCMO show similar large changes around the charge – ordering transition temperature as seen in bulk $La_{0.5}Ca_{0.5}MnO_3$. The charge – ordering transition is also clearly seen as a peak at T = 250 K in the M – T curve. The resistivity curve, which rises rapidly as the sample is cooled though $T_{CO} \approx 250$ K, also reflects the CO transition as a change in slope at ~ 250 K. This is highlighted in the inset of Fig.4.12 (c) where we have shown a plot of the derivative *dlnρ/d(1/T)* versus T. The derivative gives the transport activation energy at any temperature T. We find a clear change in slope at the CO temperature of T = 250 K showing hardening of the transport gap on cooling through the CO temperature. The bulk sample, thus, shows an insulating behaviour throughout the temperature range and the continuous increase in the activation energy on cooling can be seen through enhancement of *dlnρ/d(1/T)* on cooling.

4.4 Size reduction: Change in properties when the particle size is progressively reduced

After having recapitulated the properties of bulk compounds in the preceding sections, we now proceed to the main objective of this work i.e. to see what happens to the charge – ordered phase when the particle size of these oxides is progressively reduced. The studies were carried out with 6 samples of each oxide having particle size in the range of ~ 15 nm to greater than 3 μm (Table 4.1). The sample preparation method and characterization techniques have been detailed in Chapter 2.

144

Table 4.1. List of samples used along with the particle size.

Chemical formula	Sample ID	Particle size (nm)
$La_{0.5}Ca_{0.5}MnO_3$	LCMO – A	15 ± 2
	LCMO – B	43 ± 8
	LCMO – C	141 ± 15
	LCMO – D	378 ± 50
	LCMO – E	600 ± 70
	LCMO – F	3660 ± 600
$Pr_{0.5}Ca_{0.5}MnO_3$	PCMO – A	15 ± 2
	PCMO – B	38 ± 7
	PCMO – C	128 ± 13
	PCMO – D	287 ± 40
	PCMO – E	870 ± 100
	PCMO – F	3318 ± 500

LCMO – F and PCMO – F are the "bulk" samples which replicate the behaviour of $La_{0.5}Ca_{0.5}MnO_3$ and $Pr_{0.5}Ca_{0.5}MnO_3$ single crystals respectively. The data shown in the preceding figures have been taken on these two samples. They serve as references.

4.4.1 Crystal structure analysis

In Chapter 3 we have seen how size reduction modifies the crystal structure in $La_{0.67}Ca_{0.33}MnO_3$ nanoparticles. Unlike $La_{0.67}Ca_{0.33}MnO_3$, which does not show any structural transition in the bulk state, $La_{0.5}Ca_{0.5}MnO_3$, in the bulk state, shows an orthorhombic to monoclinic transition associated with the charge ordering transition. Thus, it is expected that the structure will play an even more vital role in the case of $La_{0.5}Ca_{0.5}MnO_3$ nanoparticles than it did for the $La_{0.67}Ca_{0.33}MnO_3$ nanoparticles.

The structural analysis of the $La_{0.5}Ca_{0.5}MnO_3$ nanoparticle samples was done using temperature dependent diffraction data taken using high resolution synchrotron radiation source at the European Synchrotron Radiation Facility, Grenoble, France using the BM-01B beamline and a wavelength of 0.375 Å. The experimental conditions for the nanoparticle samples were the same as those for the bulk (which have been detailed in Section 4.3.1). We show the x – ray patterns for LCMO-A taken at different temperatures in Fig.4.14.
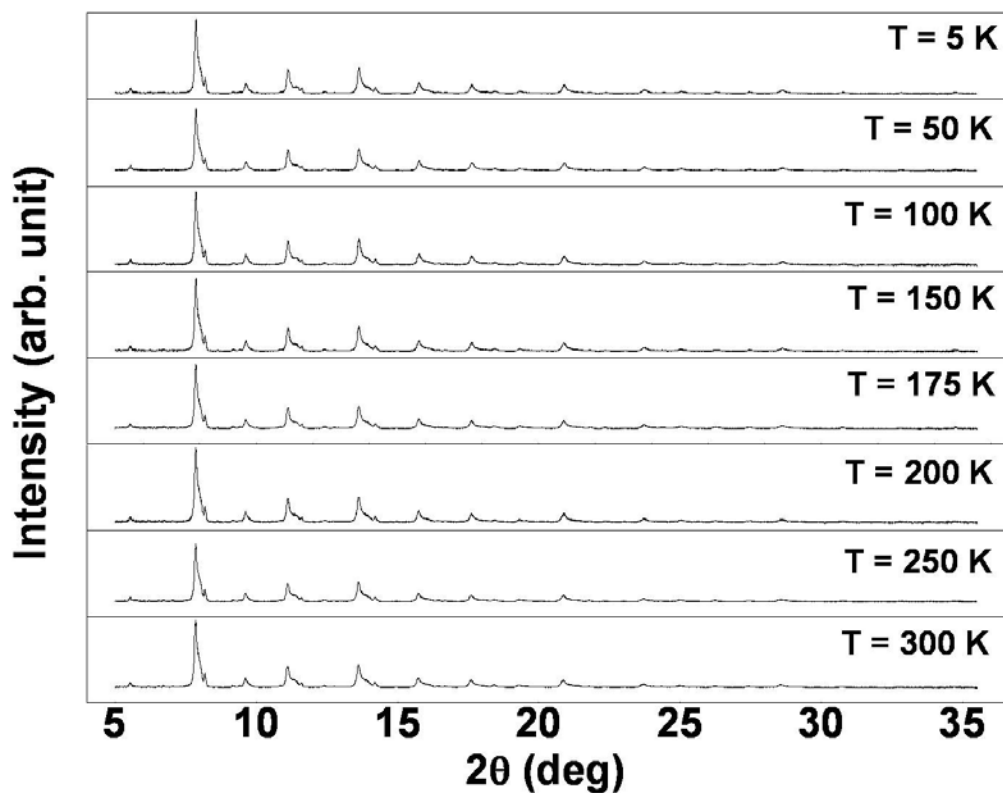
Fig.4.14. Synchrotron x – ray diffraction patterns for LCMO-A taken at different temperatures.

In Fig.4.5, we have shown the XRD patterns of bulk LCMO taken at two temperatures, one below the charge ordering transition temperature (5 K), and the other above the charge ordering transition temperature (300 K), which clearly showed the appearance of satellite peaks in the XRD patterns when the sample is cooled below the CO transition temperature. In Fig.4.15, we show the corresponding XRD patterns for the nanoparticle sample (LCMO – A). The figure clearly shows that the diffraction pattern of the nanocrystal remains virtually unchanged throughout the temperature region scanned i.e. the scan taken at 300 K is virtually the same as that taken at 5 K with no appearance of any extra peaks. This is the first indication we get that the structure of the nanocrystals fails to evolve as it should on lowering the temperature if charge and orbital ordering have to set in.
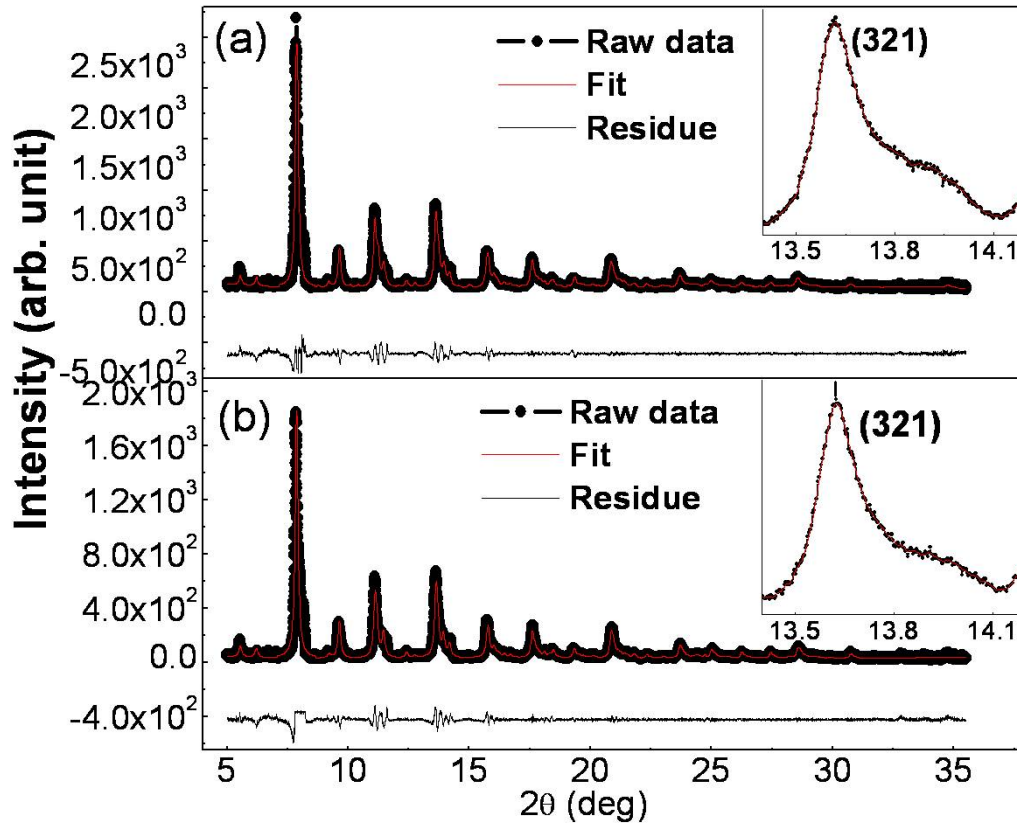
Fig.4.15. XRD patterns (along with the fits) of LCMO – A (average particle size ~ 15 nm) taken at (a) 300 K and (b) 5 K. Insets show the expanded regions between $2\theta = 13.4^0$ and 14.2^0.

Here, we note that one obvious difference arising due to size reduction is in the shape of the peaks, the peaks in the nanoparticle sample being more broad and asymmetric than those in the bulk sample. This difference in the line shape is taken care of during the refinement process through the asymmetry parameter β. Thus, we get $\beta_{bulk} = 0.08$ and $\beta_{nano} = 0.61$ at T = 300 K. With cooling, β increases for both samples, ($\beta_{bulk} = 0.21$ and $\beta_{nano} = 0.66$ at T = 5 K), but the increase is much more in the bulk sample than that in the nanoparticle sample. We also note that we did the analysis using the higher symmetry space group *Pnma* at all temperatures. As we have stated earlier, below the charge ordering temperature the structure of the bulk sample undergoes an orthorhombic to monoclinic transition, which reduces the crystallographic symmetry from *Pnma* to *P2₁/m*. However, we report the refined values of the lattice parameters only (and not the atomic positions), and so the reported values are quite reliable. In fact, fitting the low temperature data using the space group *P2₁/m* changes the refined values of the lattice parameters by only ~ 0.0016% (we do not report these values here). This change is lower than the percent error of 0.03%. So, effectively the values of the lattice parameters become independent of whether we use the space group *Pnma* or *P2₁/m*.

The temperature evolution of the lattice parameters of LCMO – A (the sample with the smallest average particle size) are shown in Fig.4.16. In the same graph, we once again show the temperature evolution of the lattice parameters of LCMO – F for comparison. The variations of the lattice constants with temperature are sharply different in the nanocrystals and the bulk sample. For the nanocrystals, throughout the temperature range studied, all the lattice constants remain essentially unchanged. Unlike the bulk sample, there are no systematic changes in the lattice constants on cooling. At room temperature, the nanocrystals have the *a* axis smaller by ≈ 1% compared to the bulk. The compaction in the *b* axis is ≈ 2% while the *c* axis expands by ≈ 1%. At the lowest temperature (5 K) due to the large changes in the lattice constants of the bulk sample, the lattice constants *a* and *c* become comparable in the bulk sample while the *b* axis becomes smaller. The absence of any temperature variation of the lattice constants of the nanocrystals indicates that the room temperature structure is arrested in the nanocrystals. This arrest of the room temperature structure in the nanocrystals prevents the evolution of the low temperature charge – ordered phase.
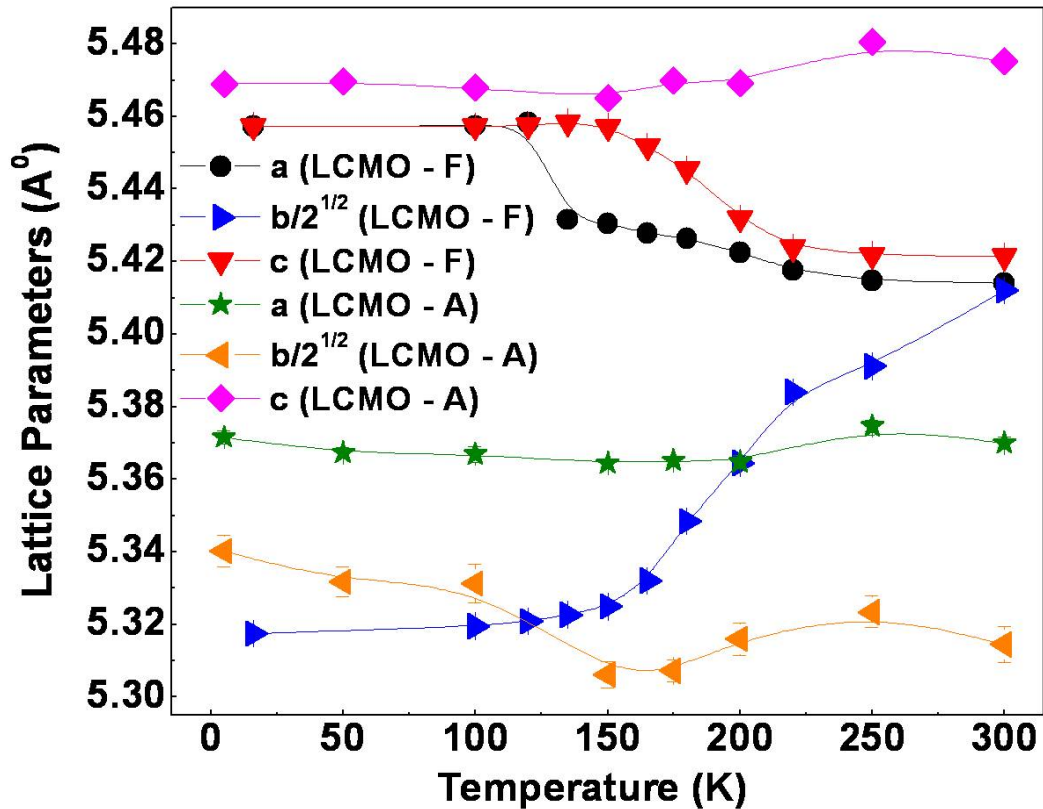
Fig.4.16. Variation of lattice parameters for LCMO – A and LCMO – F. Error bars, where not visible, are smaller than the symbols.

The unit cell volume of the nanoparticle sample is about 1% smaller than that of the bulk sample, and this difference remains almost constant throughout the temperature range scanned

(Fig.4.17 (a)). In the lower panel of Fig.4.17, we show the variation of the unit cell volume at room temperature as a function of the particle size. It is seen that there is a sort of cross – over of the cell volume and this change occurs in the range of 100 – 200 nm.
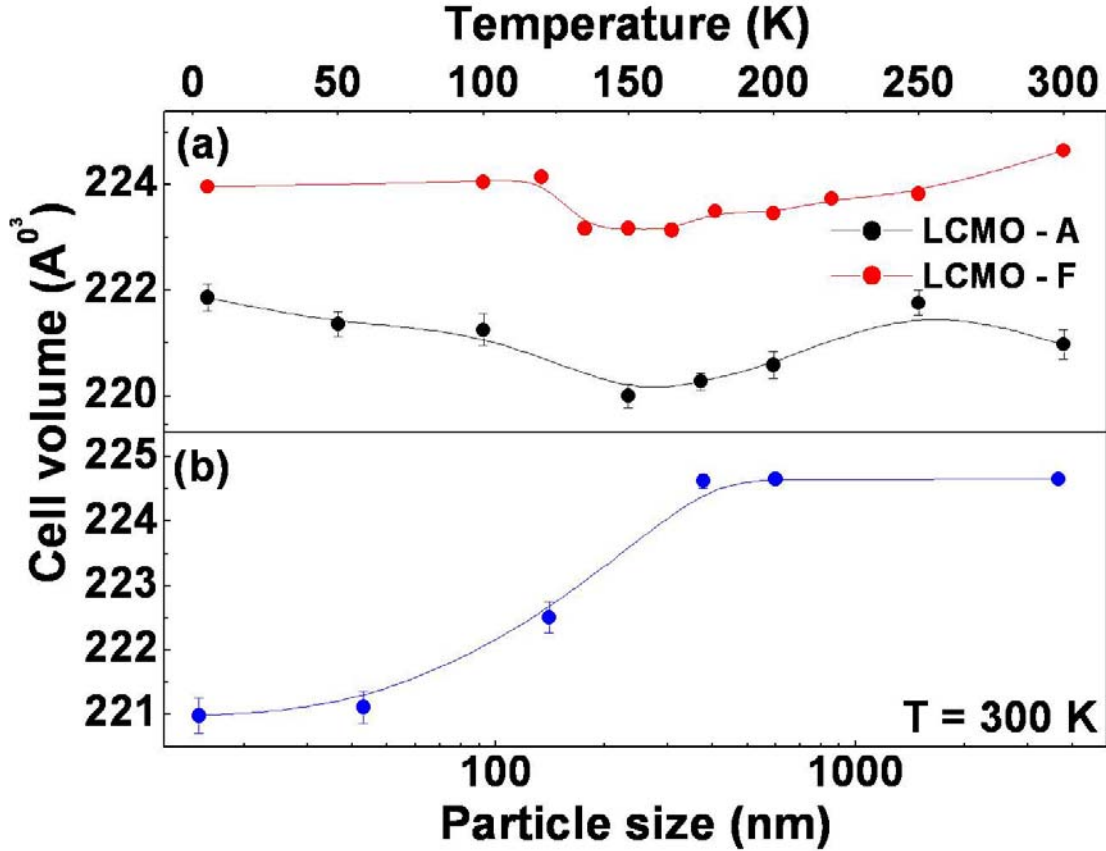
Fig.4.17. Variation of the unit cell volume (a) of LCMO – A and LCMO – F as a function of temperature and (b) as a function of the average particle size at T = 300 K.

One important quantity that changes due to size reduction are the orthorhombic strains ($O_{S\parallel}$ and $O_{S\perp}$). These are shown for the two samples (LCMO – A and LCMO – F) in Fig.4.18. The orthorhombic strain $O_{S\parallel}$ gives the strain in the *ac* plane and is defined as $OS_{\parallel} = \dfrac{2(c-a)}{c+a}$, while $O_{S\perp}$ gives the strain along the *b* axis with respect to the *ac* plane and is defined as $O_{S_{\perp}} = \dfrac{2(a+c-b\sqrt{2})}{a+c+b\sqrt{2}}$. In the bulk sample, the largest change occurs in $O_{S\perp}$, which increases substantially as the sample is cooled and reaches a saturation value of ≈ 0.026 below the charge ordering temperature T_{CO}. On the other hand, $O_{S\parallel}$ shows a rather small value over the whole temperature range while showing a small enhancement in the temperature range where the CO sets in but again becoming negligible for $T < T_{CO}$. In the nanocrystal, since the lattice constants are more or less temperature independent, both $O_{S\perp}$ and $O_{S\parallel}$ are temperature independent over

149

the whole temperature range, and they have similar magnitudes. The rapid change of the orthorhombic strains in the bulk sample at T ≈ T_{CO} is completely absent in the nanocrystals, and as stated before, the $O_S\perp$ and $O_{S\parallel}$ remain locked at their room temperature values. It is interesting to note that the orthorhombic strain in the nanoparticles is the same in both directions, so it is "isotropic". However, in the bulk sample in which the CO-OO occurs, the orthorhombic strain is anisotropic, being very large in the ⊥ direction. Thus, it is clear that just any type of orthorhombic distortion is not sufficient to stabilize the charge ordered state. Rather, the system needs a particular kind of distortion with strong anisotropy to stabilize the CO-OO phase.
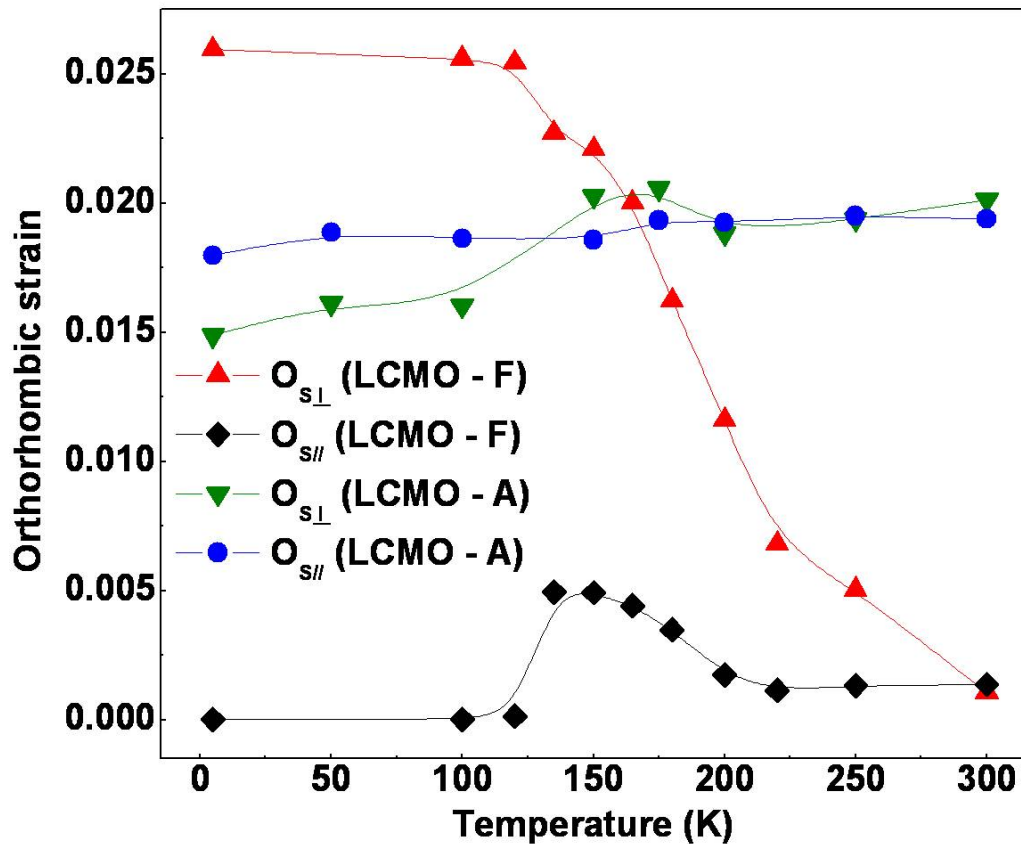
Fig.4.18. Variation of the orthorhombic strains for LCMO − A and LCMO − F. Error bars, that are not visible, are smaller than the symbols.

The $Pr_{0.5}Ca_{0.5}MnO_3$ system also shows similar effects on size reduction vis − a − vis its crystal structure. In Fig.4.19, we show the synchrotron x − ray patterns of PCMO-A which were used for study of the lattice structure.
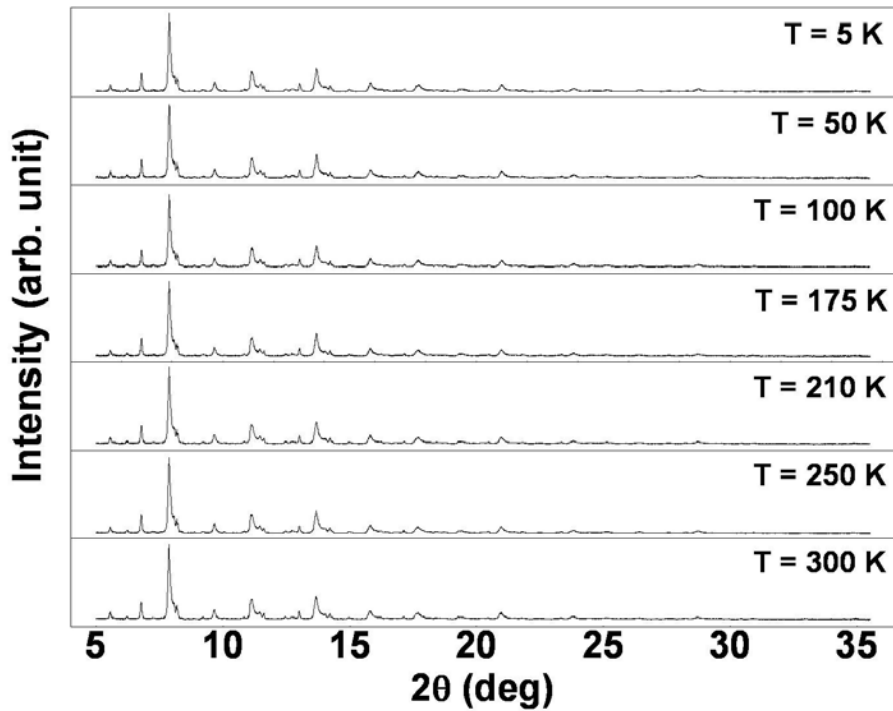
Fig.4.19. Synchrotron x – ray diffraction patterns for PCMO-A taken at different temperatures.

In Fig.4.20, we show the variation of the lattice parameter as a function of temperature for PCMO-A and PCMO-F, and in Fig.4.21 we show the variation of the (a) cell volume and (b) orthorhombic strains of the two samples as calculated from the lattice parameters.
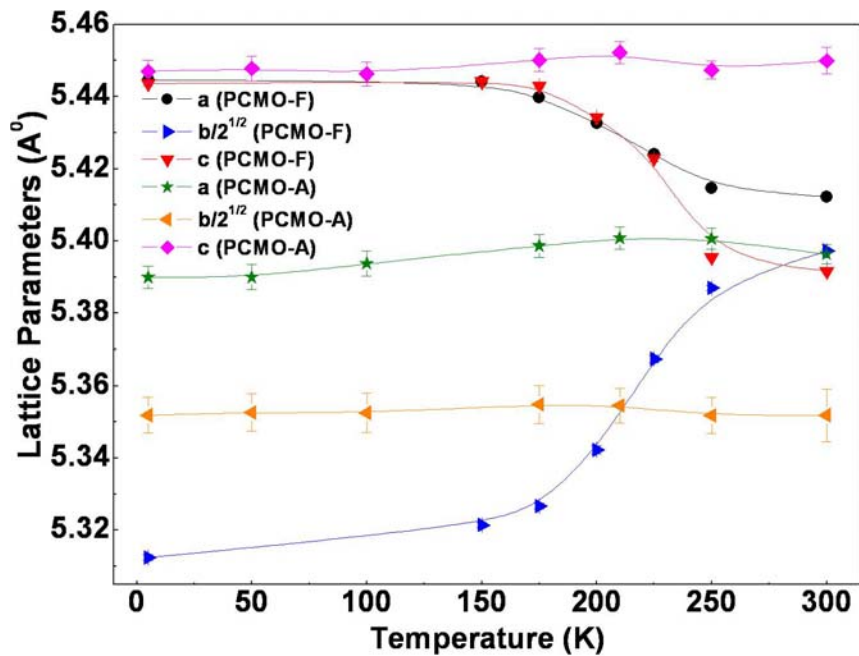
Fig.4.20. Variation of lattice parameters for PCMO – A and PCMO – F. Error bars, where not visible, are smaller than the symbols.
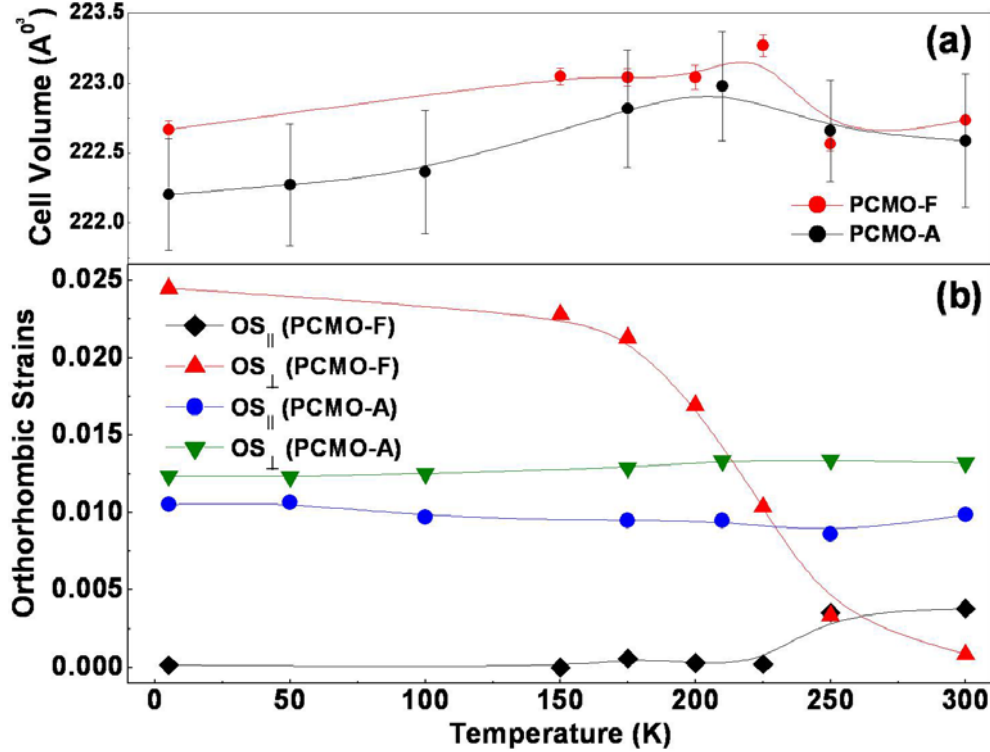
Fig.4.21. Variation of (a) unit cell volume and (b) orthorhombic strains of PCMO – A and PCMO – F as a function of temperature. Error bars, where not visible, are smaller than the symbols.

In the preceding sections, we have seen that there is a qualitative similarity of the changes in the lattice constants that occur in the two systems (LCMO and PCMO) on size reduction. The need for a definite type of orthorhombic distortion to stabilize the CO-OO phase is also similar in both the systems. In the nanocrystals, the temperature independent strain is very similar in both the systems. The detailed structural investigations that we have undertaken thus establish that the destabilization of the CO-OO phase on size reduction has a very clear structural origin.

4.4.2 Magnetic measurements

4.4.2.1 LCMO (x = 0.5)

The size reduction is accompanied by distinct changes in the magnetic properties of the samples. The magnetic behavior of bulk LCMO (through the temperature dependence of the low field a.c. susceptibility) has been shown earlier in Fig.4.8. In Fig.4.22, we show the temperature dependence of the low field a.c. susceptibility of all the LCMO samples of different particle size (LCMO-A to LCMO-F). All the samples undergo a transition from paramagnetic to ferromagnetic state at around 230 K – 250 K (we identify the T_C by the inflection points in the dM/dT versus T plots). Interestingly, the T_C increases with size reduction signifying strengthening of the ferromagnetic interaction in smaller size particles. We had observed a similar strengthening of the ferromagnetic interaction in the case of $La_{0.67}Ca_{0.33}MnO_3$ nanoparticles also (details given in Chapter 3). As the temperature is decreased further, the

susceptibility of the bulk sample starts to decrease at T ≈ 150 K, and the transition is mostly over by T ≈ 135 K. This is the signature of the onset of the antiferromagnetic order accompanying the charge order. Such a drop in the susceptibility at lower temperatures is absent in nanocrystals of size ≤ 150 nm. This would imply that the antiferromagnetic order that accompanies the charge order is absent in nanocrystals with sizes smaller than 150 nm.
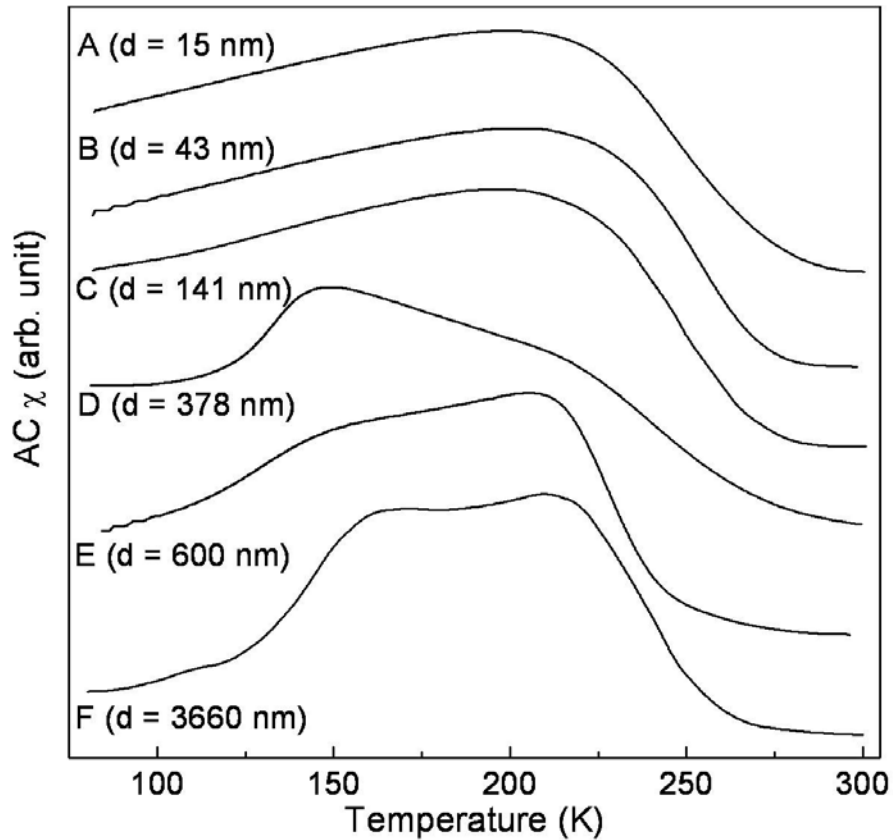
Fig.4.22. AC susceptibility vs temperature for LCMO-A to LCMO-F.

In Fig.4.23, we plot (a) T_C, (b) T_{CO} and the ferromagnetic fraction as determined from the mgnetization data (magnetization data shown later on) as a function of the particle size. It is clearly seen that both T_{CO}, as well as the ferromagnetic fraction, show a transition when the particle size goes below 150 nm. T_{CO} varies abruptly from 300 nm to 150 nm. Below 100 nm, there is no T_{CO} (i.e. the transition from the ferromagnetic phase to charge ordered antiferromagnetic phase is completely absent). The magnetization essentially shows a two phase behavior over the whole size range. The ferromagnetic fraction is below 25 % for d ≥ 1000 nm and above 80 % for d ≤ 100 nm. (Interestingly, it has been observed that at a local scale (~ few tens of nm), the AFM (CO-OO) phase does coexist with a FM phase.) The size reduction, thus, inhibits formation of the charge – ordered state, and the ferromagnetic state is stabilized.
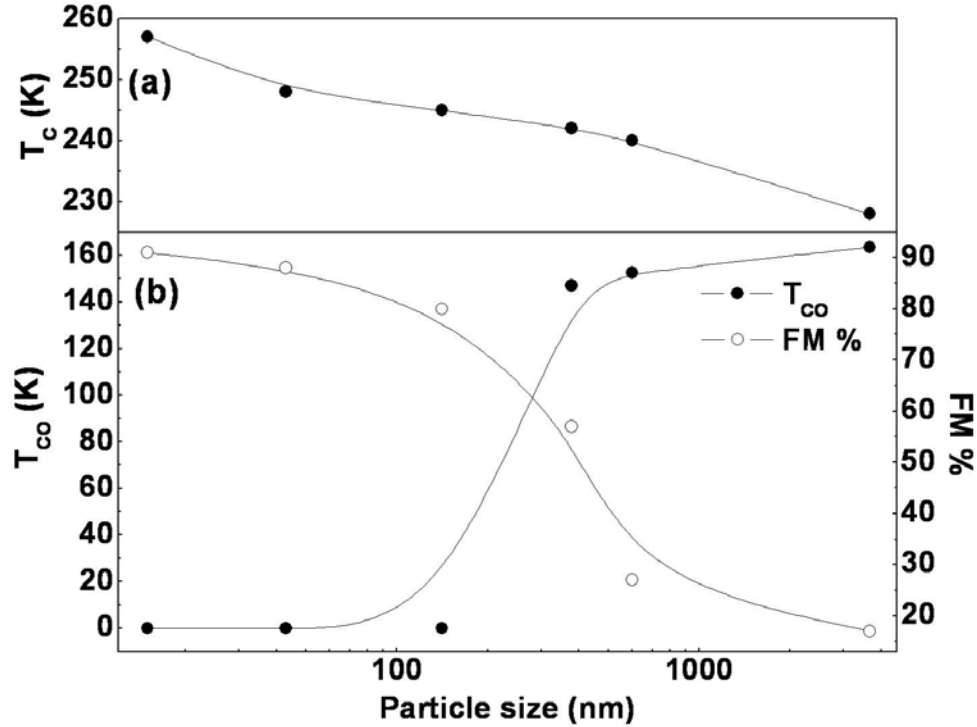
Fig.4.23. Variation of (a) T_C, (b) T_{CO} and FM % as a function of the particle size in La$_{0.5}$Ca$_{0.5}$MnO$_3$.

The magnetization data support the observation as made in the a.c. susceptibility. The magnetization data taken on LCMO-F (bulk sample) and LCMO-A (nanocrystals) under two magnetizing fields (0.01 T and 5 T) are shown in Fig.4.21. LCMO-F (lower panel) shows the transition from paramagnetic to ferromagnetic state, where the magnetization rises, and then on further cooling as the antiferromagnetic order sets in, it falls as seen in the a.c. susceptibility data. At lower field (0.01 T), there is a clear separation of the zero field cooled and field cooled data, which occurs close to the temperature where the magnetization shows a peak. This is a signature of irreversibility that may arise due to remanent spin disorder in the sample. The magnetic moment at 10 K at a field of 5 T $\approx$ 0.6 μ_B/f.u. This is substantially less than that expected from fully ferromagnetically aligned moments. However, it is not zero either as one would expect for a good antiferromagnet. This indicates that there is a presence of a small yet finite ferromagnetic moment in these samples. This coexistence of the ferromagnetic metallic state and antiferromagnetic insulating state in bulk La$_{0.5}$Ca$_{0.5}$MnO$_3$ has been recently looked into by Banerjee et.al.[26,27]. Nevertheless, in our samples the antiferromagnetic order that sets in along with the charge ordering transition is stable down to the lowest temperature in the bulk sample in a field of 5 T.

In contrast to the bulk sample, the nanocrystals do not show any magnetic transition below the paramagnetic to ferromagnetic transition. The magnetization of the nanocrystals at H = 5 T rises monotonically (for both FC and ZFC cases) and approaches toward saturation at the lowest temperature. The magnetization at 10 K ~ 3.18 μ_B/f.u. This is ~ 91% of M$_S$ (= 3.5 μ_B/f.u., calculated assuming full ferromagnetic alignment of the spins for La$_{0.5}$Ca$_{0.5}$MnO$_3$). The saturation moment determined from the magnetization has been shown in Fig.4.23 before.

154
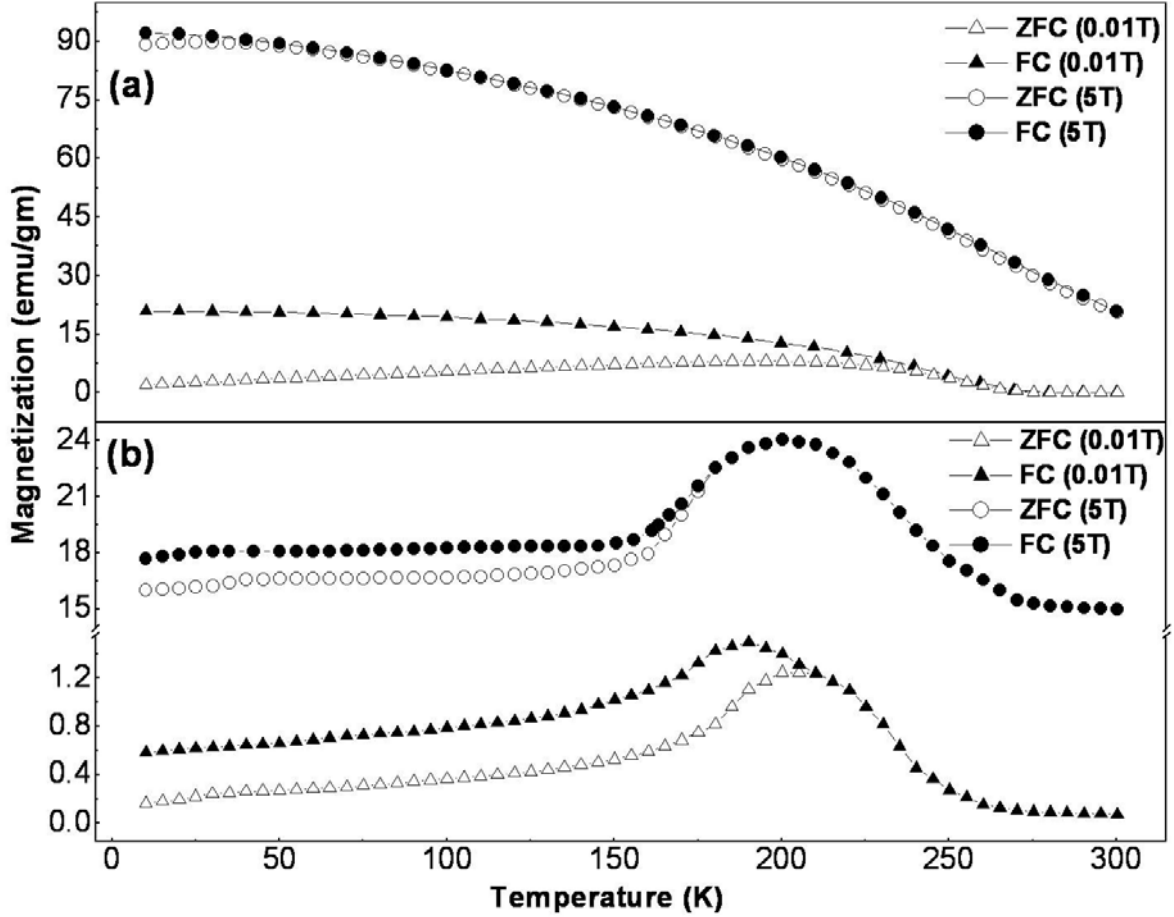
Fig.4.24. Magnetization vs temperature for (a) LCMO-A and (b) LCMO-F taken under magnetizing fields of 0.01 T and 5 T.

A plot of inverse susceptibility versus temperature for the samples in the paramagnetic region show a Curie – Weiss kind of behavior $\left[\chi = \dfrac{C}{T - \theta} \right]$, where, C is the Curie constant and θ is the Weiss temperature. This plot is shown in Fig.4.25. The Curie temperatures in all the samples are ferromagnetic. From the Curie constant C, we could calculate the effective magnetic moment μ_{eff} using the relation $C = \dfrac{\mu_{eff}^2 \mu_B^2}{3k_B}$, where, k_B is the Boltzmann constant. For the bulk sample, $\mu_{eff} \approx 4.14 \ \mu_B$, and for the 15 nm nanocrystal, $\mu_{eff} \approx 4.36 \ \mu_B$. The value of θ is positive for both samples and quite close in value ($\theta_{Bulk} = 202$ K, $\theta_{nano} = 203$ K). This establishes that the paramagnetic state of LCMO is not much affected by the particle size. The main effect arises on cooling below the first transition from paramagnetic to ferromagnetic state and the subsequent presence or absence of the antiferromagnetic transition. The magnetic moment enhancement of the nanocrystals at low temperatures distinguishes the two ground states seen in the bulk and nanoparticle samples.

155
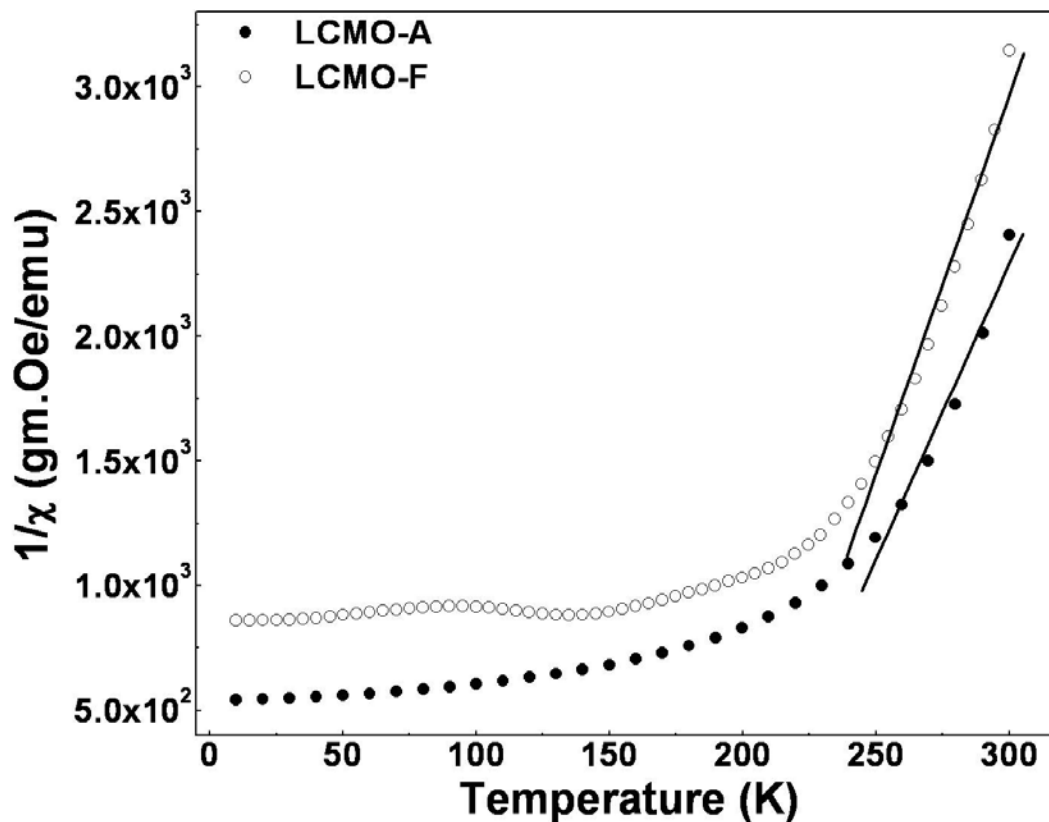
Fig.4.25. Curie – Weiss plot for LCMO-A and LCMO-F.

In Fig.4.26, we show the magnetization vs magnetic field (M-H) curves for the bulk and nanoparticle samples taken at T = 5 K. Compared to the bulk sample, which shows no hysteresis in the MH loop, the nanoparticle sample shows a considerable hysteresis with a coercive field of ~ 0.05 T and a remanence magnetization of ~ 16 emu/gm (inset of Fig.4.26). In contrast, there is no remanence or coercive field in the bulk sample.
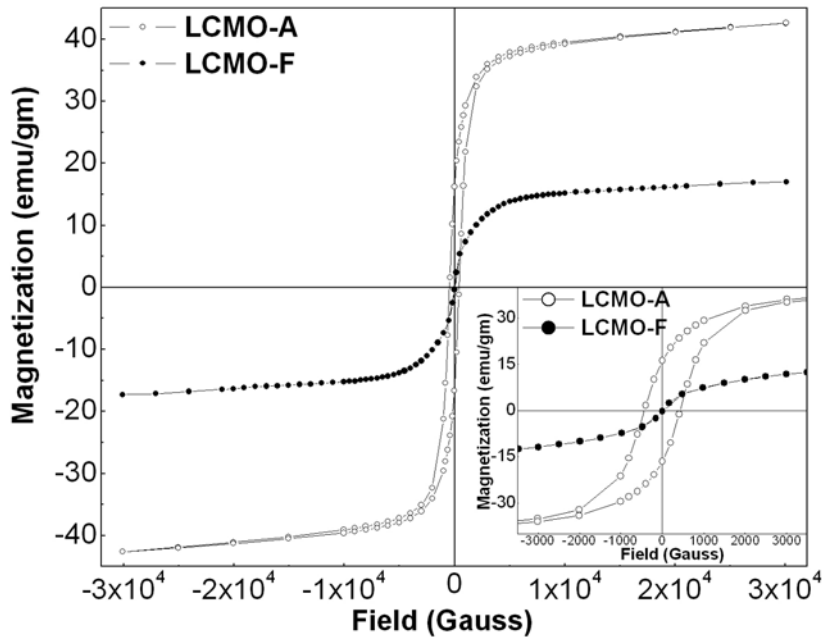
Fig.4.26. Magnetization vs magnetic field LCMO-A and LCMO-F taken at T = 5 K. The inset shows an expanded portion of the MH loop near the origin.

The magnetization data of $La_{0.5}Ca_{0.5}MnO_3$ show that the nanocrystals retain their ferromagnetic state as they are cooled to lower temperatures unlike the bulk sample that shows the antiferromagnetic transition. The data also show that there is a significant enhancement of the ferromagnetic moment in the nanocrystals. In Table 4.2, we compare the saturation magnetization (M_S), coercive field (H_C), remanence magnetization (M_r), μ_{eff} and θ for nanocrystals of LCMO (both x = 0.5 and x = 0.33) having the same average particle size (~ 15 nm). It is seen that the ferromagnetic state that arises in $La_{0.5}Ca_{0.5}MnO_3$ due to the destabilization of the CO-OO state is remarkably similar to the ferromagnetic state of $La_{0.67}Ca_{0.33}MnO_3$ nanocrystals having the same average particle size.

Table 4.2 Saturation magnetization (M_S), coercive field (H_C), remanence magnetization (M_r), μ_{eff} and θ for nanocrystals of LCMO (x = 0.5 and x = 0.33) nanocrystals (particle size ~ 15 nm)

Sample	M_S (emu/gm) (M at H = 3 T and T = 5 K)	H_C (T) (at T = 5 K)	M_r (emu/gm) (at T = 5 K)	μ_{eff} (μ_B)	θ (K)
LCMO Nano (x = 0.5)	42.6	0.05	16	4.36	203
LCMO Nano (x = 0.33)	61.06	0.03	17	4.67	270

In fact, the magnetic superlattice Bragg peaks of the ferromagnetic order in $La_{0.5}Ca_{0.5}MnO_3$ nanoparticles obtained from neutron scattering experiments were found to have the same indices and approximately same d – spacing as that seen in ferromagnetic $La_{0.67}Ca_{0.33}MnO_3$. In Fig.4.27, we show the intensity of the magnetic superlattice peaks at Q = 1.64 Å^{-1} and Q = 2.31 Å^{-1} for $La_{0.5}Ca_{0.5}MnO_3$ nanoparticles (which have a Curie temperature ~ 250 K) obtained from the neutron scattering experiments. For comparison, in the inset of Fig.4.27, we show the neutron diffraction pattern for $La_{0.67}Ca_{0.33}MnO_3$ nanoparticles between Q = 1.25 Å^{-1} to 2.44 Å^{-1} at T = 20 K which shows the two magnetic Bragg peaks at the same Q values. (This inset shows the same pattern as that shown in the inset of Fig.3.17 of Chapter 3 with the x – axis represented in Q instead of 2θ).
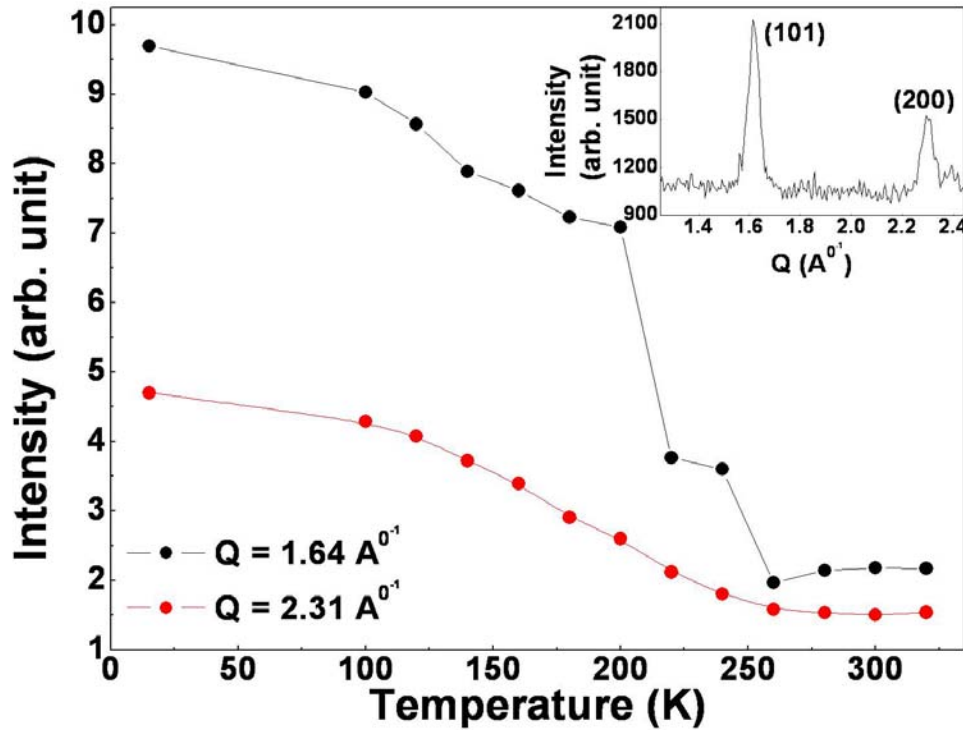
Fig.4.27. Temperature evolution of the magnetic superlattice peaks in $La_{0.5}Ca_{0.5}MnO_3$ nanoparticle. The inset shows the neutron diffraction pattern of $La_{0.67}Ca_{0.33}MnO_3$ nanoparticle between the region Q = 1.25 Å^{-1} to 2.44 Å^{-1}.

4.4.2.2 PCMO (x = 0.5)

The magnetic measurements on the $Pr_{0.5}Ca_{0.5}MnO_3$ samples lead us to similar conclusions. In Fig.4.28, we show the temperature dependence of magnetization of PCMO-A and PCMO-F taken under a magnetizing field of H = 2 T. The charge ordering transition is clearly seen in the bulk sample (PCMO-F) as a peak at T = 250 K. This is similar to that reported in $Pr_{0.5}Ca_{0.5}MnO_3$ samples with particle size larger than 1 μm prepared by conventional ceramic route[28,29]. In contrast, for the nanoparticle sample, the magnetization rises monotonically as the temperature is lowered with a small shoulder in the vicinity of T = 250 K. PCMO-A does not show a peak in the magnetization that is observed in the charge ordered sample. We thus observe

that for the nanoparticle the magnetization is distinct from that seen in the bulk sample and there is a large enhancement of the moment at low temperatures. However, we note that while the magnetization does increase as the temperature is lowered, the M-T curve is not exactly what one would expect for a ferromagnet with a proper long range order where one sees a sharp transition at the ferromagnetic Curie temperature. It is likely that the resulting phase in PCMO-A is a disordered ferromagnet or there are two coexisting phases. One is an antiferromagnetic phase that forms at a higher temperature ($T_N \sim 160$ K), and the other, a ferromagnetic phase that forms at a lower temperature. An approximate way to describe the magnetization in the ferromagnetic phase (T < 100 K) is to use the relation $M = M_0\left(1 - \dfrac{T}{T_C}\right)^{\beta}$. We find that $\beta = 0.33 \pm 0.02$ and T_C

= 136 ± 4 K can describe the data well (the fit is shown as a red curve in Fig.4.28). This T_C is close to the T_C found in the low x ferromagnetic insulating phase (see Fig.4.4 (b)). In between T_C and T_N, χ follows an approximate Curie Weiss law where the ferromagnetic moment builds up (marked by an arrow in inset of Fig.4.28). In this context it is different from the $La_{0.5}Ca_{0.5}MnO_3$ nanoparticles where the ferromagnetism obtained as a result of destabilization of the charge ordered state is a long range ferromagnetism remarkably similar to ferromagnetic $La_{0.67}Ca_{0.33}MnO_3$.
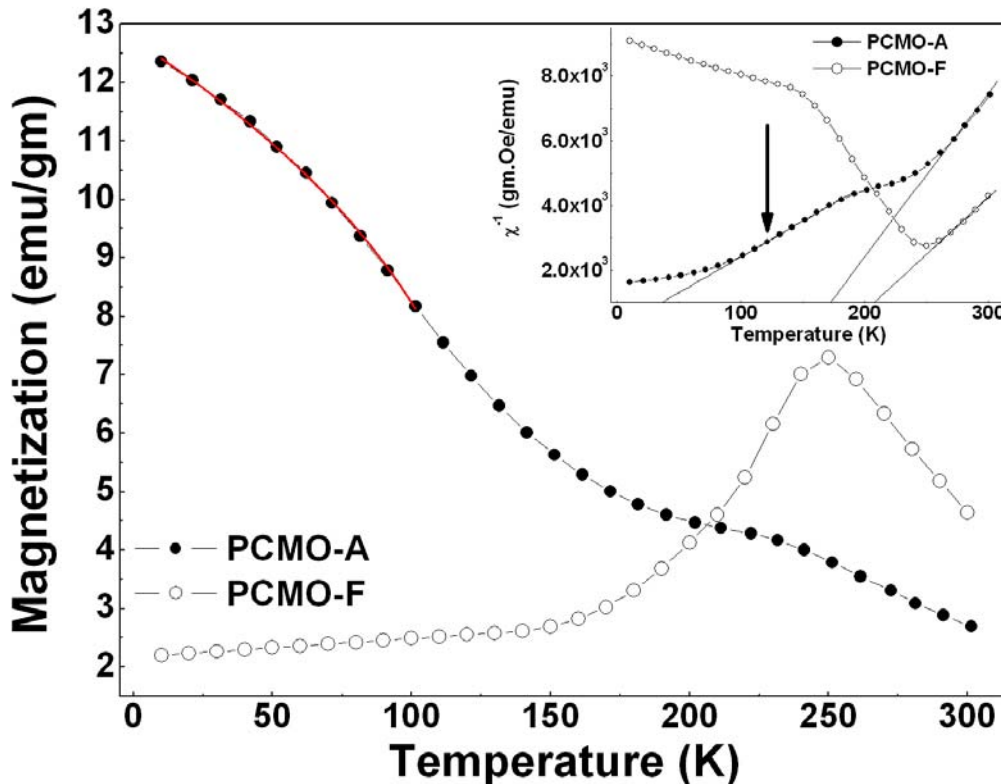
Fig.4.28. Magnetization vs temperature for PCMO-A and PCMO-F taken under a magnetizing field of 2 T. The inset shows the Curie Weiss plot for the two samples.

In the inset of the Fig.4.28, we have shown a plot of inverse susceptibility $1/\chi$ versus temperature for the two samples (PCMO-A and PCMO-F). We have taken $\chi = \dfrac{M}{H}$. In the paramagnetic region, the data is fitted to the Curie – Weiss law (the fits are shown as straight lines). The paramagnetic Curie temperature in both samples is nearly identical and positive. The θ for the bulk sample $\approx$ 229 K and that for the nanoparticle sample $\approx$ 231 K. The effective magnetic moment μ_{eff} (calculated from the Curie constant C) is $\mu_{eff} \approx 3.72 \mu_B$ (for the bulk sample), and $\mu_{eff} \approx 3.51 \mu_B$ (for the nanoparticle sample). This is comparable to μ_{eff} in most manganites. This establishes that the paramagnetic state of PCMO is not much affected by the particle size. The main effect arises below the charge ordering transition and the magnetic order (or its absence) at low temperatures distinguishes them. Here, we again emphasize that the two samples (PCMO-A and PCMO-F) are chemically identical and have nearly identical paramagnetic state, but the bulk sample (PCMO-F) becomes charge ordered while the nanoparticle sample (PCMO-A) has larger moment and leads to a disordered ferromagnet.

While there is an enhancement of the magnetic moment in the $Pr_{0.5}Ca_{0.5}MnO_3$ nanoparticles as revealed through the magnetization, it is apparent that there is an absence of a proper long range ferromagnetic order. This absence of long range ferromagnetic order can also be seen in the hysteresis curve shown in Fig.4.29. The MH loops (at T = 5 K) for PCMO-A and PCMO-F are shown. The magnetic field has been varied from - 5 T to + 5 T. The nanoparticle shows a small hysteresis loop which closes at ~ 1 T. (There is a small shift in the fourth quadrant of the MH loop which arises due to thermal drift). There is a small coercive field, $H_C \approx 0.1$ T. However, the magnetization does not saturate even at a field of 5 T which is another signature of spin disorder in the resulting ferromagnetic state. The bulk sample, in contrast, does not show any such hysteresis loop. It has a small moment of 0.16 μ_B/f.u. even at 5 T. For the nanoparticle sample, the observed moment (at H = 5 T) is much larger (0.80 μ_B/f.u.). However, this is smaller than the moment ($\approx 3.5 \mu_B$/f.u.) seen in ferromagnetic manganites such as $La_{0.67}Ca_{0.33}MnO_3$. The reduction in moment is likely due to large contribution of disordered spins in the surface as well as in the grain boundaries that constitute a good fraction of the nanoparticle sample. It can also arise because the coexisting phase is an antiferromagnetic phase and this phase does not show any moment. The important point, however, is that we get nearly $1/4^{th}$. of the expected saturation moment when size is reduced, and this leads to a ferromagnetic order.
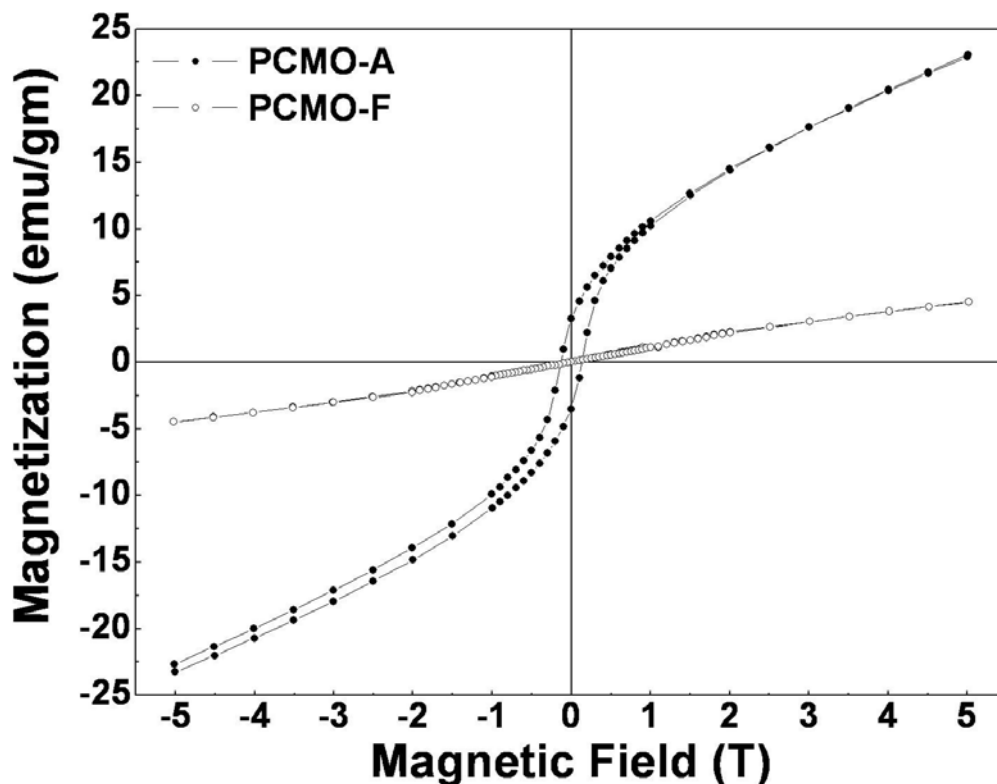
Fig.4.29. Magnetization vs magnetic field for PCMO-A and PCMO-F taken at T = 5 K.

To summarize, we find that in $Pr_{0.5}Ca_{0.5}MnO_3$, there is a rather strong enhancement of the ferromagnetic moment in the nanoparticles that are not charge ordered but the resulting state, though containing a ferromagnetic fraction, has substantial disorder that presumably prevents formation of long range order. We contrast this with LCMO (x = 0.5), which like PCMO (x = 0.5) show similar structural distortion on size reduction but shows much stronger ferromagnetic moment as well as ferromagnetic order. This difference is most likely related to the difference in the bandwidth of these two systems. LCMO, with a larger bandwidth, gives rise to a more ordered ferromagnetic state upon destabilization of the charge ordered state. The smaller bandwidth of PCMO is responsible for the fact that a ferromagnetic metallic phase never forms in this material, and for $0.15 \leq x \leq 0.3$, when a ferromagnetic insulating state does form, its T_C is rather low (~ 130 K). The lack of a proper long range ordered ferromagnetic phase formation in the nanoparticle of PCMO (x = 0.5) can thus, predominantly be linked to a smaller bandwidth.

4.4.3 Electrical transport and magnetoresistance

4.4.3.1 LCMO (x = 0.5)

The electrical transport data for bulk LCMO has already been shown in Fig.4.9 where the charge ordering transition is reflected as a change in slope in the resistivity plot. The charge ordered phase also shows a very strong magnetoresistance in some of the manganites as the insulating state is destabilized by an applied magnetic field which leads to creation of a ferromagnetic metallic state. In this investigation, particularly for the nanocrystals, the particle

161

size being small, the transport experiments have interference from the presence of a large contribution of grain boundaries in the electrical as well as magnetotransport behavior. However, we find that despite the interference, one can distinguish the electrical and magnetotransport behaviours in samples that have large grains and those that have nanocrystals. We now proceed to elaborate on this. In particular, we show that on destabilization of the CO-OO state, the insulating behavior is also destabilized. The ferromagnetic state formed in the nanocrystals have much higher conductivity.

The temperature dependence of the resistivities of LCMO-A and LCMO-F from 4.2 K to 300 K are shown together in Fig.4.30. The data are shown in the log scale. In the nanoparticles (LCMO-A), the resistivity at room temperature is about 3 orders higher than that of the bulk sample (LCMO-F). In this temperature range both the samples are in a charge and orbitally disordered paramagnetic state. The higher resistance of LCMO-A reflects the enhanced grain boundary contribution. In the bulk sample, however, the resistivity rises rapidly as the sample is cooled through the charge ordering transition, and at 50 K the resistivity in the bulk sample becomes more than 6 orders higher than that in the nanoparticles. In contrast, the nanocrystals show much less sensitivity to temperature, and the resistivity does not vary much on cooling (within one order). The resistivity also shows a shallow peak at $T_P \sim 160$ K (seen more clearly in the inset of Fig.4.31). In conventional ferromagnetic manganite ($La_{0.67}Ca_{0.33}MnO_3$), a metal – insulator transition occurs close to the ferromagnetic transition. Thus, a peak in the resistivity occurs close to T_C. However, for nano $La_{0.5}Ca_{0.5}MnO_3$, T_P is significantly lower than T_C ($T_C \sim$ 257 K). Such a behavior is expected when the material is not a homogeneous metallic phase, but is percolative in nature because of a large number of grain boundaries or the presence of an insulating phase coexisting with the metallic phase. The resistance again starts to rise below 55 K, presumably due to predominant contribution of the insulating grain boundaries to the overall current transport. Such behavior has been reported in nanostructured ferromagnetic films of manganites also[30]. We will discuss the low temperature electrical transport behavior of ferromagnetic nanoparticles in details in Chapter 5.
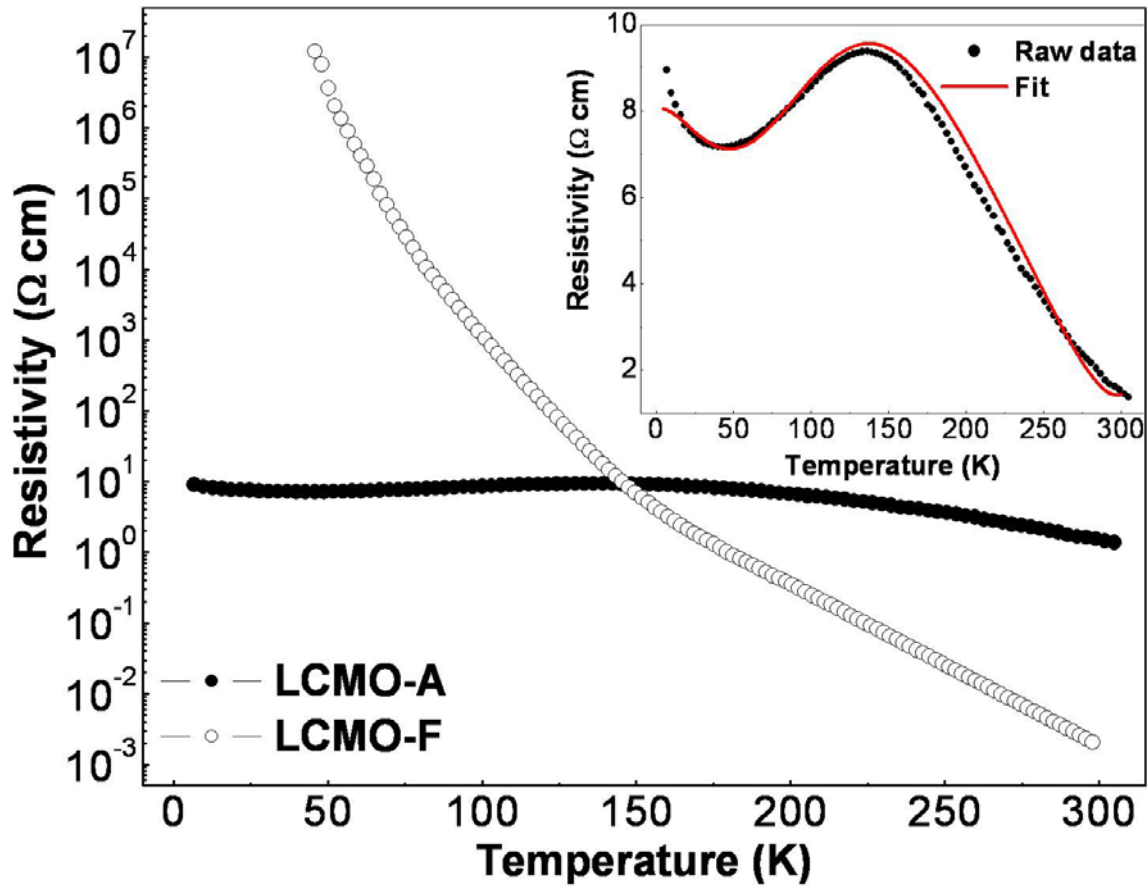
Fig.4.30. Resistivity vs temperature for LCMO-A and LCMO-F. Inset shows the resistivity of LCMO-A on an extended scale.

Fig.4.31 shows the plot of $\dfrac{d \ln \rho}{d\left(\dfrac{1}{T}\right)}$ versus temperature for LCMO-A and LCMO-F which gives the transport activation energy at temperature T. The bulk sample shows a clear change in slope at T ≈ 150 K (marked by a red arrow) showing hardening of the transport gap on cooling through the charge ordering temperature. For the nanoparticle sample, there is no clear change at around 150 K which one would expect if the system showed a charge ordering transition. If anything, it shows a gradual decrease in slope.
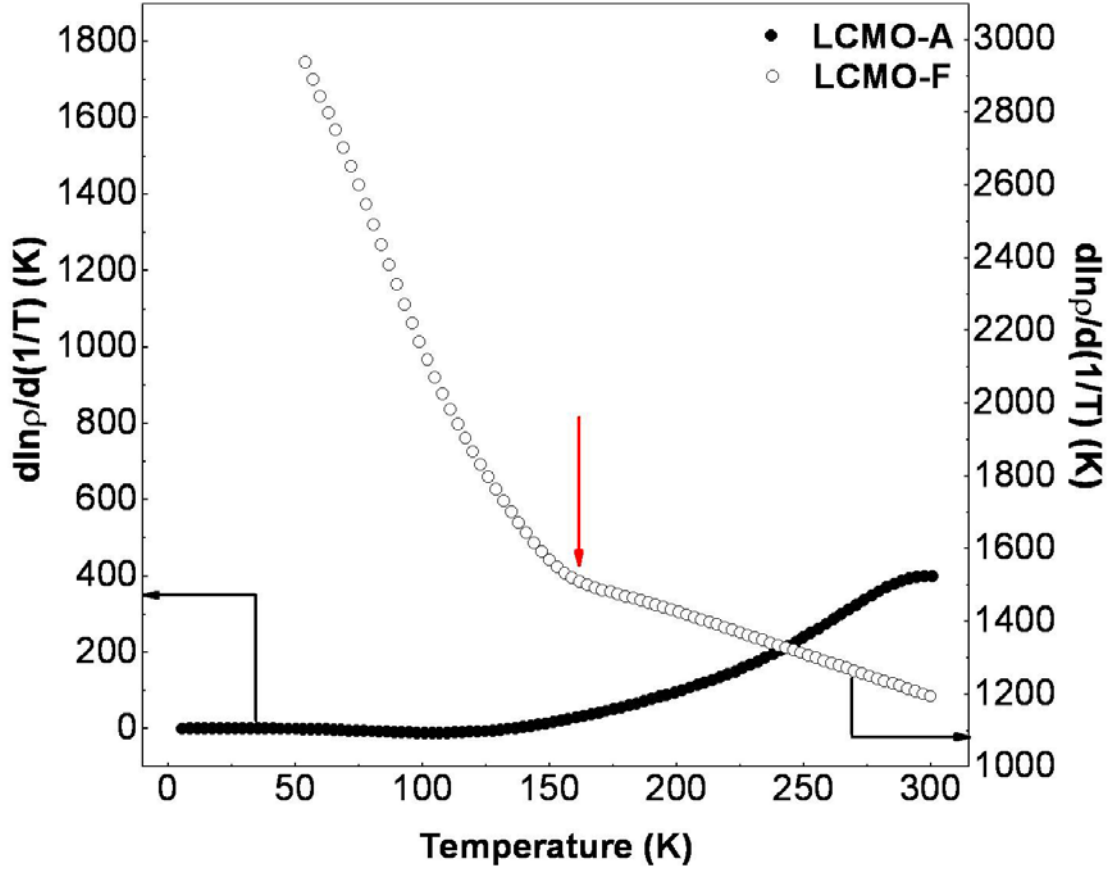
Fig.4.31. $\dfrac{d \ln \rho}{d\left(\dfrac{1}{T}\right)}$ vs temperature for LCMO-A and LCMO-F.

       The observations above clearly show that in the nanocrystlas of LCMO (x = 0.5) the resistivity is lower (or conductivity is higher) although there is a perceptible interference from the grain boundary transport. We have already noted that the ferromagnetic state seen in the nanocrystals is not a homogeneous phase. The resistivity data shows a clear signature of the existence of a high resistance phase along with the metallic phase which makes the transition percolative and pushes T_P to a very low value. (Part of the high resistance phase may be in the grain boundary and part may be within the grain of a nanocrystal that may be phase separated.) To get a rough estimate of the metallic and insulating fraction of the samples, we modeled the transport phenomena occurring in the nanoparticle sample as occurring through two channels. Such a phenomenological model has been used in the past to analyze transport in mixed manganites[31]. By using a resistor network model it has been justified that such a simple two channel conduction model indeed captures the essential physics of the mixed transport and can reproduce the fraction of conduction through the two channels. We used this model of two channel conduction where the two parallel channels: (a) insulating channels which have a resistivity ρ_i and (b) percolating metallic channels having a resistivity ρ_m. We further assume that ρ_i has a functional form similar to that of the bulk sample, and ρ_m is given by $\rho_m = \rho_{m0} + \alpha T^n$.

164

Thus, the total resistivity of the nanoparticle sample can be written as $\dfrac{1}{\rho} = \dfrac{A_i}{\rho_i} + \dfrac{A_m}{\rho_m}$. Fitting the resistivity of the nanoparticle sample using this equation (the fit is shown in the inset of Fig.4.30), we can estimate the relative fraction of the metallic and insulating parts in the sample. The value of $\dfrac{A_m}{A_i}$ for LCMO-A $\approx$ 1.5 (i.e. 60%). This shows that the phase in the nanocrystals that has been obtained by destabilizing the charge ordered insulating phase has significant electrical inhomogeneity and it shows electronic phase separation. The fraction of ferromagnetic component in the nanoparticle sample as estimated from the value of the magnetization at 10 K is almost 90% (details given in Section 4.4.2.1). This higher fraction of the insulating phase as estimated from the transport data probably arises due to the contribution of the grain boundaries in the nanoparticle sample whose contribution is also included within the insulating phase fraction. An analysis of the resistivity data, thus, shows that there is indeed a signature of suppression of the charge ordered insulating phase in the nanoparticles, and the phase that forms is metallic in nature although it is a percolative type of bad metal because of the existence of a large number of grain boundaries or even a coexisting insulating phase.

The magnetoresistance (MR) {defined as $100 * \left[\dfrac{\rho(H) - \rho(0)}{\rho(0)} \right]$ with H = 10 T} for LCMO-A and LCMO-F are plotted as a function of temperature in Fig.4.32. In both samples the MR is negative although the value, as well as the temperature dependence, is qualitatively different. The insulating state of the charge ordered bulk sample is completely suppressed on application of 10 T magnetic field. This is due to magnetic field induced destabilization of the charge ordered state that has been seen in many charge ordered systems. The MR at the lower most temperature is nearly 100% for the bulk sample for T < 100 K. In contrast, in the nanoparticle sample, the MR increases slowly as it is cooled and reaches the limiting value of ~ 70%. The behavior of the MR in the nanocrystal is similar to that seen in nanostructured films of ferromagnetic manganites[32,33], which arises predominantly due to the grain boundary contributions. The MR data of the two samples also corroborate with the earlier observation about the predominant phases present in the two samples.

165
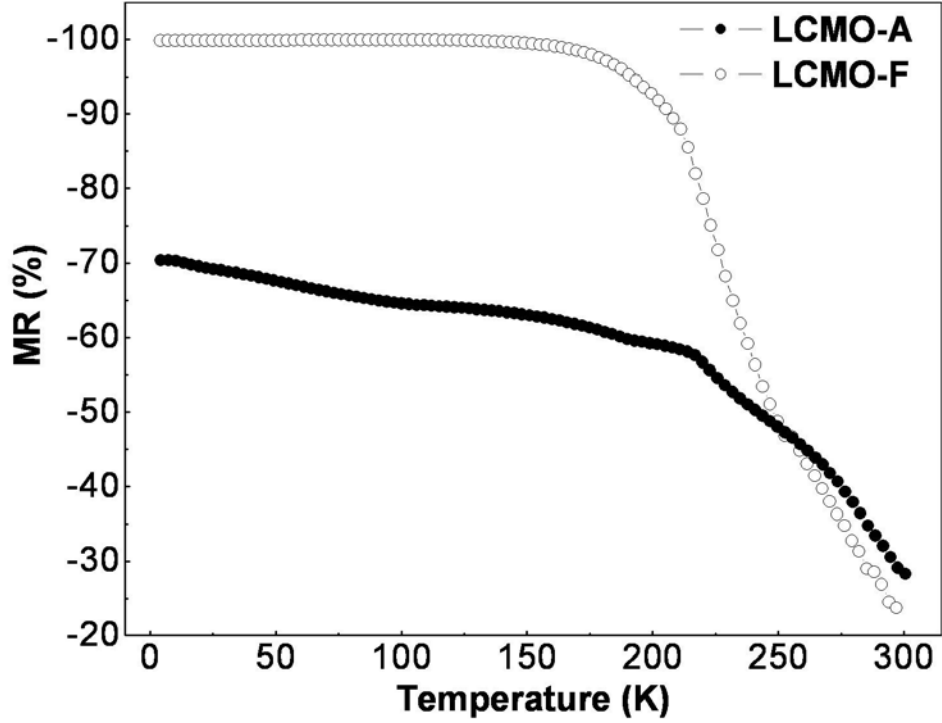
Fig.4.32. MR as a function of temperature for LCMO-A and LCMO-F.

4.4.3.2 PCMO (x = 0.5)

Next we examine the electrical transport properties of $Pr_{0.5}Ca_{0.5}MnO_3$ and find striking parallels with the LCMO case. In Fig.4.34, we show the temperature dependence of the resistivity of PCMO-A and PCMO-F. In the bulk sample (PCMO-F), the resistivity rises rapidly as the sample is cooled through the charge ordering transition at $T \approx 250$ K. Although at room temperature the resistivity of the bulk sample was 3 orders lower than that of the nanocrystals, the bulk sample reaches ρ of the nanoparticle sample at $T \approx 120$ K, and at $T \approx 50$ K, ρ_{bulk} is nearly 5 orders higher than ρ_{nano}. For the nanoparticle sample also, the resistivity rises upon cooling, but the rise is much less rapid and at low temperature the resistivity change actually reverses trend with a shallow maxima and minima (see inset of Fig.4.33). The activated transport with a steep activation energy in the charge ordered bulk sample is strongly suppressed in the nanoparticle sample. To highlight this we show, in Fig.4.34, the temperature dependence of the derivative $\dfrac{d \ln \rho}{d\left(\dfrac{1}{T}\right)}$ which gives the transport activation energy at temperature T. The bulk sample shows an insulating behavior throughout the temperature range and the continuous increase in the activation energy on cooling can be seen through enhancement of $\dfrac{d \ln \rho}{d\left(\dfrac{1}{T}\right)}$ on cooling. The change in slope at 250 K for the bulk sample is marked by a red arrow. The nanoparticle sample has a resistivity that increases as T is lowered but unlike the bulk sample there is no clear change

166

in slope at around 250 K which one would expect if the system showed a charge ordering transition. Like LCMO-A, PCMO-A also shows a gradual decrease in slope with decreasing temperature. It also shows a shallow hump in the resistivity at ~ 65 K beyond which ρ decreases on cooling though not very drastically. The decrease in resistance from 65 K to 50 K is a signature that PCMO-A may have a small metallic fraction which is coexisting with a dominant insulating phase. The metallic fraction is far below the percolation threshold and there is also a large contribution of activated transport through the grain boundaries as a result of which the sample never shows a clear metallic behavior.
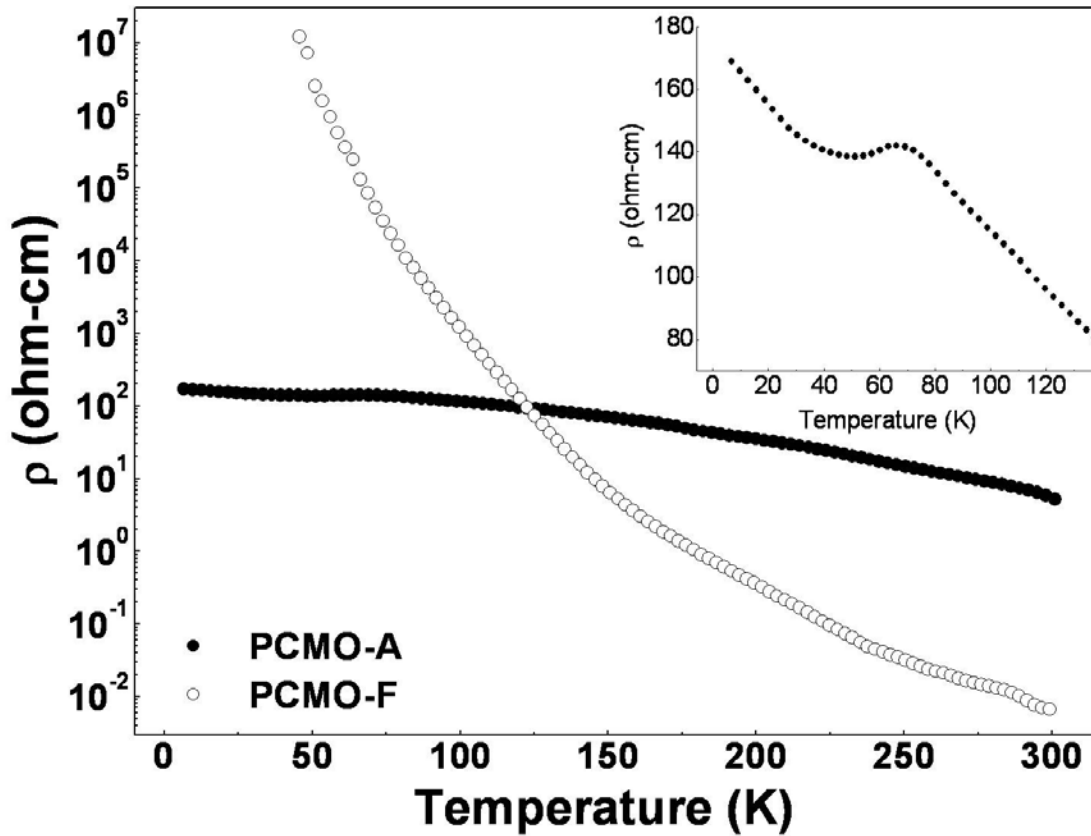
Fig.4.33. Resistivity vs temperature curves for PCMO-A and PCMO-F. The inset shows the resistivity vs temperature curve of PCMO-A in the low temperature region.
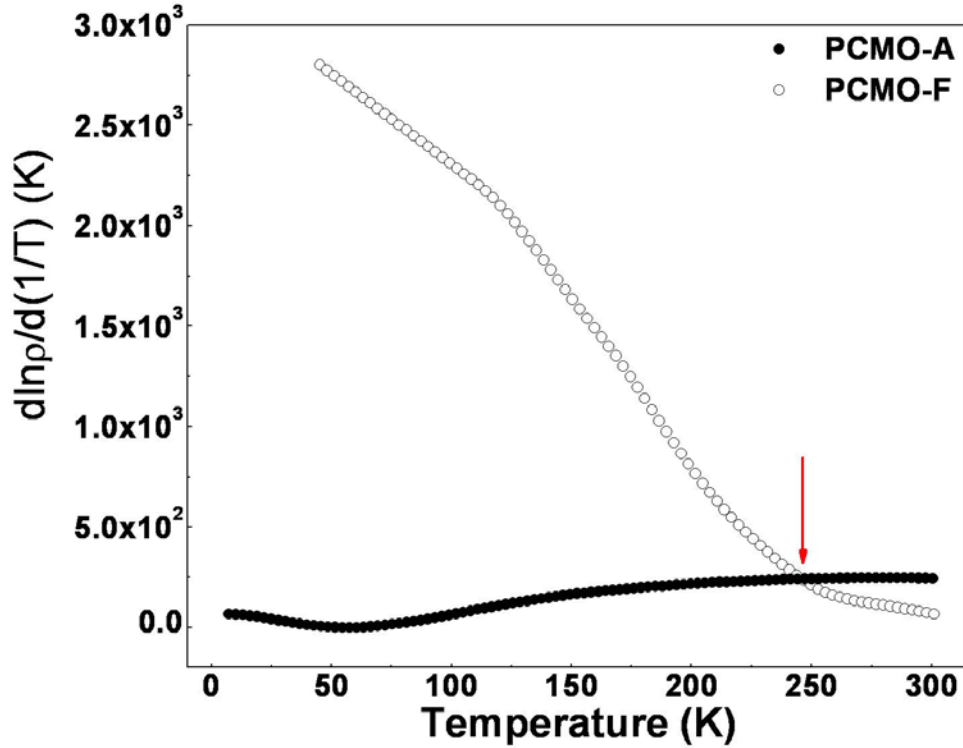
Fig.4.34. $\dfrac{d\ln\rho}{d\left(\dfrac{1}{T}\right)}$ vs temperature for PCMO-A and PCMO-F.

The MR of PCMO-A also shows a change in the dominant characteristics. In bulk PCMO, the charge ordered state is very rugged and fields larger than 20 T are needed to melt the charge order and obtain the metallic phase[34]. In contrast, the nanoparticle sample shows a finite MR even at a field of H = 10 T. The MR values in the temperature range 4.2 K to 300 K are shown in Fig.4.35. The MR is negative. Down to ~ 70 K the magnetic field has very little effect on the resistance and the MR is very low even in a field of 10 T. However, below 70 K the field starts showing its effect, and there is a sharp rise in magnetoresistance. At the lower most temperature of 4.2 K the magnetoresistance reaches a value of ~ -38%. We note that the temperature at which the MR appears (rather suddenly) is the same temperature (65 K) at which there is a small peak in ρ and it then decreases on cooling. The MR in the nanoparticle sample can, thus, be interpreted as a signature of weakening or destabilization of the charge order that pulls down the magnetic field at which the charge order can be made to melt.

The important observation that is noteworthy is that, in PCMO (x = 0.5), a very low resistance phase forms on size reduction. This low resistance phase may not be "metallic" in the strict sense, nevertheless, it is a phase with nearly zero or very small activation energy. Such a phase is not formed anywhere in the zero field phase diagram of PCMO (any x, see Fig.4.4 (b)). It is, thus, truly intriguing that size reduction indeed brings forth such a state.
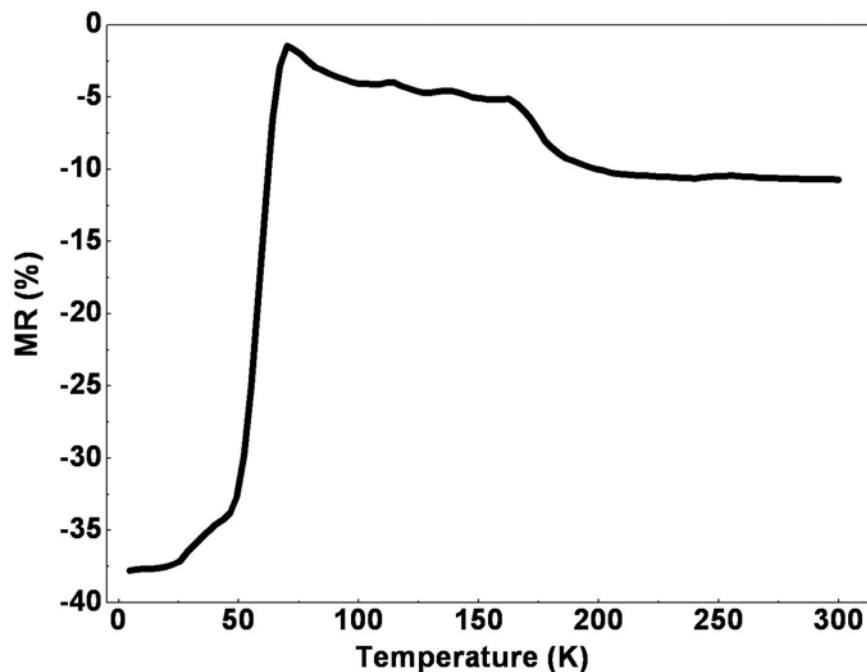
Fig.4.35. MR curve of PCMO-A.

4.5 Reasons behind the destabilization of charge order in the half – doped manganite nanoparticles

The results presented on structural, magnetic and electrical transport data unambiguously establish that, in both LCMO as well as in PCMO, below a certain size range (< 100 nm), the charge order state is <u>not</u> stable. The destabilization, in both cases, leads to phases that have more moment and are ferromagnetically ordered (even if with short range order), and phases that have significantly lower resistivity (even if not metallic). It is also clear that the destabilization of the charge and orbitally ordered state has a structural origin. Below we discuss the main mechanisms which cause the observed destabilization of the charge ordered state in the nanoparticles.

4.5.1 Structure mediated

The onset of charge order needs a particular type of crystal structure (or distortion) to support it. It is, thus, natural to connect the absence of charge order in the nanocrystals to structural factors. The high resolution x – ray diffraction studies have shown a drastic change in the structure of the system on size reduction. At room temperature the nanocrystals are more distorted than the bulk sample, as is evidenced from the higher values of the orthorhombic strains at room temperature in the nanoparticle samples. However, this distortion is temperature insensitive. The room temperature structure does not evolve with temperature unlike the bulk sample. This brings forward the question of whether the structure has a role in preventing the charge order to develop on cooling the sample. To explain this change in the structure on size reduction we make the proposition that the surface pressure makes the nanocrystals behave as material under high hydrostatic pressure which not only changes the structure, but also "locks"

the room temperature structure. This proposition can be justified as follows: we assume our particles to be spherical in shape (in reality the particles are of irregular shape, so an assumption of sphericity gives us an average result). Then the surface pressure acting on the particles can be written as $P_S = \dfrac{2S}{d}$, where, d is the diameter of the particle and S is the surface tension. Using $S \approx 50$ N/m we find that a pressure of $P_S \approx 6$ GPa acts on the sample with average particle size $d \sim 15$ nm. For particles of larger size (≥ 100 nm), the surface pressure will be very small (≤ 1 GPa) and thus will be of no consequence. The hydrostatic pressure leads to reduction in cell volume which has been observed in the nanoparticles also. For example, in LCMO-A, the cell volume changes by $\sim 1.7\%$. Using a typical bulk modulus of manganites as ~ 150 GPa, we find that a hydrostatic pressure of ~ 6 GPa will lead to a reduction in cell volume of $\sim 4\%$, which is similar to but slightly larger than the observed reduction. This simple argument explains that the surface effect can indeed produce enough hydrostatic pressure to explain the change in the unit cell volume.

Since the effect of surface pressure is to produce an effective hydrostatic pressure, it will be worthwhile to see how the crystal structure is modified under applied hydrostatic pressure. For this purpose, we refer to a recent report on the crystal structure of bulk $La_{0.5}Ca_{0.5}MnO_3$ at room temperature and at high pressure[35]. This paper reports a structural transition from orthorhombic to monoclinic phase found at P ~ 15 GPa (at T = 300 K). The authors have done a systematic study of the evolution of the room temperature structure with pressure ranging from 0 to 31 GPa. The evolution of lattice parameter, unit cell volume and orthorhombic strain as functions of pressure are shown in Fig.4.36.
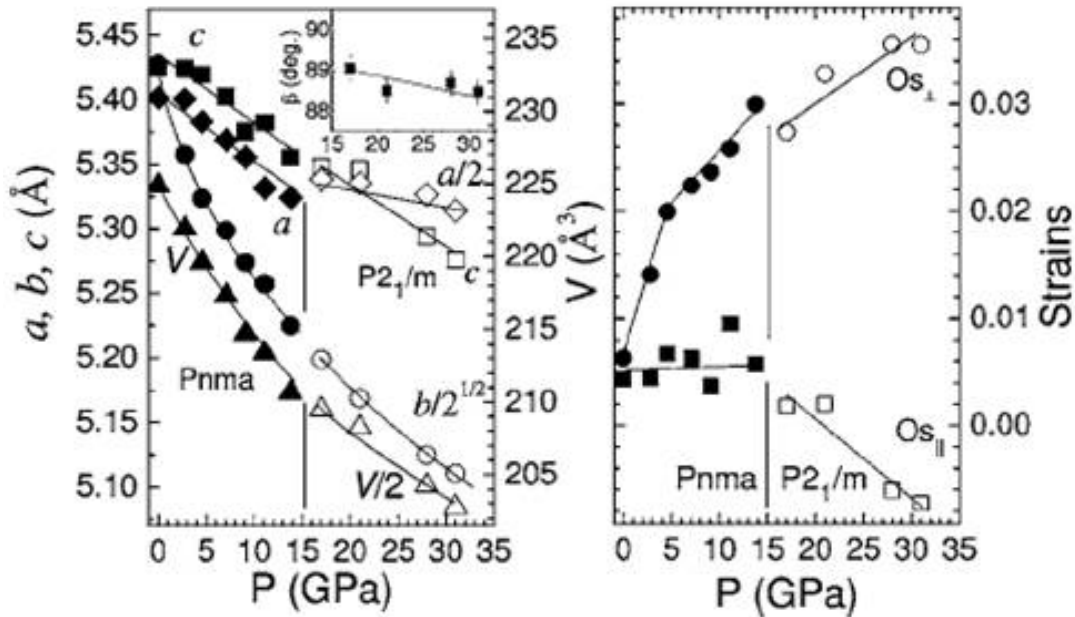
Fig.4.36. Lattice parameters, unit cell volume and orthorhombic strains in bulk $La_{0.5}Ca_{0.5}MnO_3$ as functions of pressure (reproduced from [35]).

Our data for LCMO-A (which we consider to be under an effective pressure of ~ 6 GPa) match very well with the crystal structure data of bulk LCMO measured under directly applied

hydrostatic pressure of the same magnitude. This can be seen from Table 4.3 where we list the room temperature structural parameters of LCMO-A and bulk LCMO at P ~ 7 GPa.

Table 4.3. Comparison of the room temperature structural parameters of nano LCMO and bulk LCMO (hydrostatic pressure = 7 GPa)

	LCMO-A	LCMO-Bulk under hydrostatic pressure of 7 GPa (values reproduced from Ref 29)
a (Å)	5.37	5.37
b/√2 (Å)	5.31	5.30
c (Å)	5.48	5.40
Cell Volume (Å^3)	221	217
OS∥	0.019	0.006
OS⊥	0.020	0.023

Thus, comparison to the hydrostatic pressure data establishes that the nanocrystal samples are under an effective hydrostatic pressure created by surface pressure due to its small size. It is this effective pressure that causes the crystal structure to deviate from the bulk structure. The related issue is what causes the room temperature crystal structure of the nanocrystals not to evolve with temperature as the sample is cooled unlike the bulk sample. We suggest that the effective hydrostatic pressure created by the size reduction acts like a "clamp" that freezes in the room temperature structure. In the bulk sample, the structural evolution on cooling involves expansion of the *a* and *c* axes and contraction of the *b* axis (Fig.4.6 and Fig.4.12 (a)). It is likely that the hydrostatic pressure prevents the lattice expansion. As a rough estimate, using the ~ 1.7% unit cell compaction as a strain due to the effective hydrostatic pressure of 7 GPa (for LCMO-A), we find that the energy involved is ≈ 60 meV, which is larger than the thermal energy. This justifies why the effective hydrostatic pressure freezes in the room temperature structure. Also the onset of charge order requires a particular type of orthorhombic distortion where OS⊥ is substantially larger than OS∥ (Fig.4.18 and Fig.4.21 (b)). This is absent in the nanocrystals where OS⊥ ≈ OS∥. This may prevent the charge order to set in.

Here, we also note that there have been high pressure studies on $Pr_{1-x}Ca_xMnO_3$ (with different x)[36] which have shown that the charge ordered state is suppressed and a ferromagnetic metallic state is induced in these samples. Thus, application of hydrostatic pressure on PCMO produces very similar effects as obtained by size reduction.

4.5.2 Finite size effect

The development of charge order needs creation of a modulated structure and a supercell as has been seen in bulk samples of $La_{0.5}Ca_{0.5}MnO_3$[22]. The propagation vector of the charge ordered modulated structure is (1/2-ε,0,0), where, ε ≈ 0.01 at 20 K. This implies that the periodicity of the supercell is ≈ 200*a* ≈ 106 nm. Thus, if the particle size is less than ~ 100 nm, the supercell modulation needed for the charge order cannot develop. In our case, the smallest size nanocrystals are more than seven times less than this value. It appears that the absence of a

supercell modulation can be another cause why the charge order does not set in in the nanocrystals.

4.5.3 Site/Surface disorder

While disorder can most definitely lead to a destabilization of the charge ordered state, it is not clear why this should lead to an enhancement and strengthening of the ferromagnetic interaction as is observed in the nanocrystals. In fact, as we have shown in Chapter 3, disorder serves to weaken the ferromagnetic interaction and decrease the Curie temperature in $La_{0.67}Ca_{0.33}MnO_3$ nanocrystals. It has been widely observed that both site as well as surface disorder leads to a decrease in the ferromagnetic T_C as well as the ferromagnetic moment[37,38]. In $La_{0.5}Ca_{0.5}MnO_3$, we find just the opposite trend i.e. an enhancement in the ferromagnetic T_C (Fig.4.23 (a)) as well as an increase in the ferromagnetic moment (Fig.4.24) as the particle size is reduced. Thus, disorder as seen in the grain boundary or grain surfaces appear to be an unlikely cause of destabilization of charge order in the nanocrystals. Even if a disordered shell is present on the surface of the particles (which is most likely the case), the fact that T_C increases with size reduction proves that the structural effect takes precedence in these particles (refer to our concept of dual effect of size reduction on LCMO that we had introduced in Chapter 3, see Fig.3.26). The structural modification which serves to strengthen ferromagnetism (and increase T_C) simultaneously weakens, and ultimately destabilizes the charge order in these systems.

The effect of substitutional or site disorder has been studied in a number of experiments[39,40]. It has been proposed that substitution leads to creation of random field that can destabilize the charge ordered state. However, the random field created by substitution destabilizes the ferromagnetic state also[37]. In the present investigation, the destabilization of the charge ordered state is achieved by simple size reduction, keeping the chemistry the same. We argue that the formation of nearly full ferromagnetic moment in the nanocrystals and the fact that the order that forms mimics LCMO (x = 0.33) as established by neutron data rule out much of a disorder or surface related effects. The destabilization occurs in the bulk of the nanocrystals. As a result, random field created by substitution does not have much relevance in our context.

4.5.4 Strain

Biaxial strain as seen in films when they are grown on a substrate mostly stabilize the charge ordered phase although in some cases this may even destabilize the charge ordered phase [41]. Tensile strain can stabilize the orbital ordering which accompanies charge ordering and can even restore the charge order, for example, in Cr substituted samples where the suppression in the Mn site suppresses the charge order. It has been seen that compressive strain may also suppress ferromagnetism although not as strongly as the tensile strain. Even a small biaxial lattice strain (~ 1.5%) can tune the ground state of the charge ordered films. For films grown on substrates, the stabilization of the phase will depend on the extent of the asymmetry between the in – phase and out – of – phase strains. Since biaxial strain actually strengthens the charge ordering transition, it is not expected to play a role in the current phenomenon.

Random local strain arising from inhomogeneous strain, on the other hand, might affect the ground state of the nanocrystals. This can act as a random field that can indeed destabilize the charge ordered state.

4.6 Summary of results

We end this chapter by recapitulating the main results that have been obtained so far:

1. We have studied, in details, the effect of size reduction on the crystal structure and physical properties of half – doped manganite nanocrystals ($La_{0.5}Ca_{0.5}MnO_3$ and $Pr_{0.5}Ca_{0.5}MnO_3$).

2. The major effect of size reduction in these samples is a destabilization of the traditional charge – ordered state seen in the bulk materials and an appearance of a ferromagnetic state with enhanced magnetic moment and metallic type conductivity.

3. The cause of this destabilization can be traced predominantly to changes in the crystal structure on size reduction. The room temperature structure is arrested in the nanocrystals and does not evolve on cooling unlike bulk samples. The change in structure was ascribed to an effective hydrostatic pressure created by surface pressure, which not only changes the structure but also causes the room temperature structure to freeze. Thus, our investigation establishes a structural basis for the destabilization of the charge ordered state in the nanocrystals.

4. Although the experiments have been carried out in the specific context of half – doped manganites, the concept that the surface pressure can act as a change agent may be applicable in other systems whose properties can change substantially with moderate hydrostatic pressure.

5. In almost all other reported oxide systems, size reduction destabilizes the metallic state, and one obtains transition to an insulating state[42]. The results described in this chapter bring to light one of the few known systems where the metallic state (with ferromagnetic interaction) is stabilized by size reduction.

REFERENCES

[1] C.N.R.Rao, Anthony Arulraj, A.K.Cheetham and Bernard Raveau, J. Phys.: Condens. Matter, **12**, R83 (2000)

[2] E.O.Wollan and W.C.Koehler, Phys. Rev., **100**, 545 (1955)

[3] John B. Goodenough, Phys. Rev., **100**, 564 (1955)

[4] Y.Tokura, Rep. Prog. Phys., **69**, 797 (2006)

[5] S.Mori, C.H.Chen and S.-W.Cheong, Nature, **392**, 473 (1998)

[6] S.Mori, C.H.Chen and S.-W.Cheong, Phys. Rev. Lett., **81**, 3972 (1998)

[7] A.Daoud – Aladine, J.Rodríguez – Carvajal, L.Pinsard – Gaudart, M.T.Fernández – Díaz and A.Revcolevschi, Phys. Rev. Lett., **89**, 097205 (2002)

[8] P.M.Woodward, T.Vogt, D.E.Cox, A.Arulraj, C.N.R.Rao, P.Karen and A.K.Cheetham, Chem.Mater., **10**, 3652 (1998)

[9] Anthony Arulraj, P.N.Santhosh, R.Srinivasa Gopalan, Ayan Guha, A.K.Raychaudhuri, N.Kumar and C.N.R.Rao, J. Phys.: Condens. Matter, **10**, 8497 (1998)

[10] D.P.Kozlenko, Z.Jirák, I.N.Goncharenko and B.N.Savenko, J. Phys.: Condens. Matter, **16**, 5883 (2004)

[11] Y.Moritomo, H.Kuwahara, Y.Tomioka and Y.Tokura, Phys. Rev. B, **55**, 7549 (1997)

[12] H.Kuwahara, Y.Tomioka, A.Asamitsu, Y.Moritomo and Y.Tokura, Science, **270**, 961 (1995)

[13] A.Asamitsu, Y.Tomioka, H.Kuwahara and Y.Tokura, Nature (London), **388**, 50 (1997)

[14] Ayan Guha, Arindam Ghosh, A.K.Raychaudhuri, S.Parashar, A.R.Raju and C.N.R.Rao, Appl.Phys. Lett., **75**, 3381 (1999)

[15] M.R.Ibarra, Guo-meng Zhao, J.M.De Teresa, B.García – Landa, Z.Arnold, C.Marquina, P.A.Algarabel, H.Keller and C.Ritter, Phys. Rev. B, **57**, 7446 (1998)

[16] P.V.Vanitha, P.N.Santosh, R.S.Singh, C.N.R.Rao and J.P.Attfield, Phys. Rev. B, **59**, 13539 (1999)

[17] L.Sudheendra, H.D.Chinh, A.R.Raju, A.K.Raychaudhuri and C.N.R.Rao, Solid State Comm., **122**, 53 (2002)

[18] S.S.Rao, S.Tripathi, D.Pandey and S.V.Bhat, Phys. Rev. B, **74**, 144416 (2006)

[19] Anis Biswas, I.Das and Chandan Majumdar, **98**, 124310 (2005)

[20] T.V.Ramakrishnan, J. Phys. Condens. Matter, **19**, 125211 (2007)

[21] Y.Tomioka, A.Asamitsu, H.Kuwahara, Y.Moritomo and Y.Tokura, Phys. Rev. B, **53**, R1689 (1996)

[22] P.G.Radaelli, D.E.Cox, M.Marezio and S-W.Cheong, Phys. Rev. B, **55**, 3015 (1997)

[23] http://www.ill.eu/sites/fullprof

[24] M.R.Lees, J.Barratt, G.Balakrishnan, D.McK. Paul amd M.Yethiraj, Phys. Rev. B, **52**, R14303 (1995)

[25] Z.Jirák, S.Krupićka, V.Nekvasil, E.Pollert, G.Villeneuve and F.Zounová, J. Magn. Magn. Mater., **15**, 519 (1980)

[26] A. Banerjee, Kranti Kumar and P. Chaddah, J. Phys.: Condens. Matter, **20**, 255245 (2008)

[27] P. Chaddah, Kranti Kumar and A. Banerjee, Phys. Rev. B, **77**, 100402(R) (2008)

[28] E.Pollert, S.Krupicka and E.Kuzmicova, J. Phys. Chem. Solids, **43**, 1137 (1982)

[29] Z.Jirák, F.Damay, M.Hervieu, C.Martin, B.Raveau, G.André and F.Bourée, Phys. Rev. B, **61**, 1181 (2000)

[30] Sohini Kar, Jayanta Sarkar, Barnali Ghosh and A.K.Raychaudhuri, Phys. Rev. B, **74**, 085412 (2006)

[31] Matthias Mayr, Adriana Moreo, Jose A. Verges, Jeanette Arispe, Adrain Feiguin and Elbio Dagotto, Phys. Rev. Lett., **86**, 135 (2001)

[32] Mandar A. Paranjape, K. Shantha Shankar and A.K.Raychaudhuri, J. Phys. D, **38**, 3674 (2005)

[33] Barnali Ghosh, Sohini Kar, Loveleen K. Brar and A.K.Raychaudhuri, J. Appl. Phys., **98**, 094302 (2005)

[34] M.Tokunaga, N.Miura, Y.Tomioka and Y.Tokura, Phys. Rev. B, **57**, 5259 (1998)

[35] D.P.Kozlenko, L.S.Dubrovinsky, I.N.Goncharenko, B.N.Savenko, V.I.Voronin, E.A.Kiselev and N.V.Proskurnina, Phys. Rev. B, **75**, 104408 (2007)

[36] Congwu Cui and Trevor A. Tyson, Phys. Rev. B, **70**, 094409 (2004)

[37] S.Robler, U.K.Robler, K.Nenkov, D.Eckert, S.M.Yusuf, K.Dorr and K.H.Muller, Phys. Rev. B, **70**, 104417 (2004)

[38] P.Kameli, H.Salamati and A.Aezami, J. Appl. Phys. **100**, 053914 (2006)

[39] B.Raveau, A.Maignan and C.Martin, J. Solid State Chem., **130**, 162 (1997)

[40] T.Kimura, Y.Tomioka, R.Kumai, Y.Okimoto and Y.Tokura, Phys. Rev. Lett., **83**, 3940 (1999)

[41] Y.Ogimoto, M.Izumi, T.Manako, T.Kimura, Y.Tomioka, M.Kawasaki and Y.Tokura, Appl. Phys. Lett., **78**, 3505 (2001)

[42] Ll.Balcells, B.Martinez, F.Sandiumenge and J.Fontcuberta, J. Phys.: Condens. Matter, **12**, 3013 (2000)

CHAPTER 5. ELECTRONIC TRANSPORT IN COMPLEX OXIDES AT LOW TEMPERATURES

The study of the complex oxide nanoparticles is incomplete without understanding their electrical transport properties. This is because these complex oxides are part of the correlated electron systems where the structural, magnetic and electronic degrees of freedom are intrinsically linked to each other (Fig.5.1). We have already shed light on the structural and magnetic properties of representative complex oxide nanoparticles in the preceeding chapters. In order to complete our understanding of the effect of size reduction on the ground state of these oxides, we turn our attention to their electronic state in this chapter. The three representative oxides that we have chosen are $La_{0.67}Ca_{0.33}MnO_3$, $La_{0.5}Sr_{0.5}CoO_3$ and $LaNiO_3$. The reason for specifically choosing these three systems will become clear when we review their properties in subsequent sections of this chapter. But before that we start this chapter with a brief review of the various transport mechanisms that have been observed in related oxide systems. This will help to put our current investigation in proper perspective.
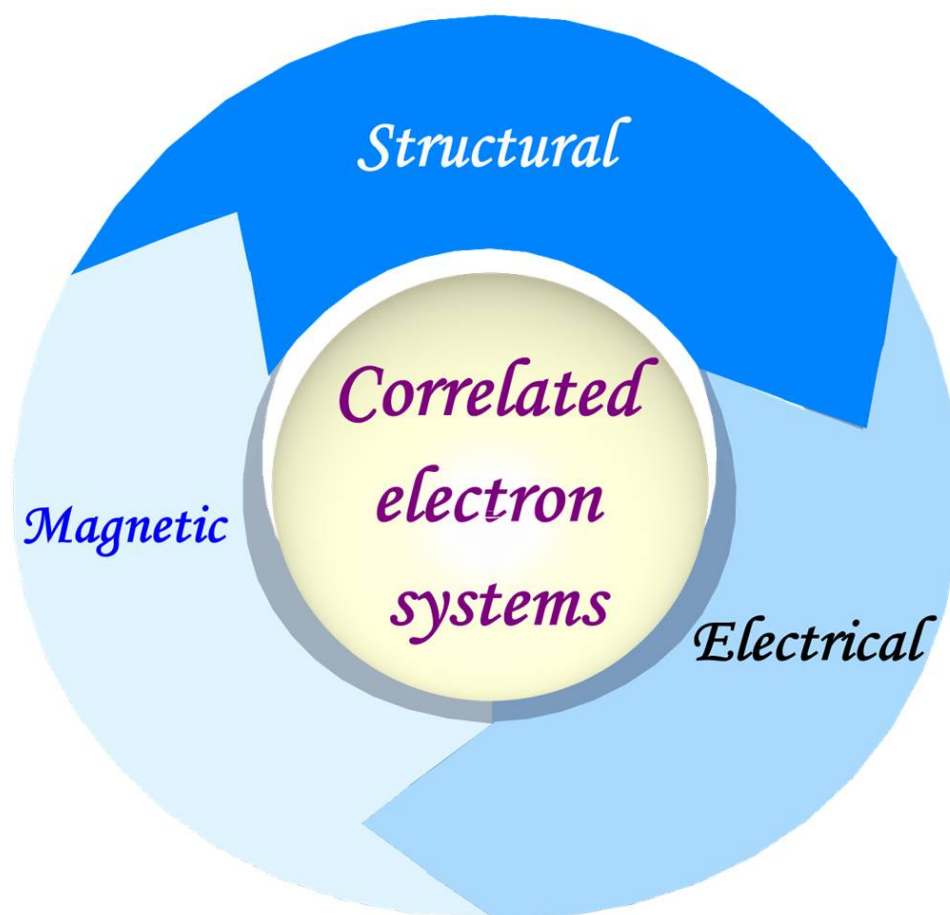
Fig.5.1. Schematic representation showing the concept of correlation in complex oxide systems.

5.1 Temperature dependence of resistivity: various existing models

Various models have been proposed to explain the temperature dependence of resistivity of manganites and other complex oxides. We list these below:

1. **Arrhenius model**[1]: $\rho = \rho_0 \exp\left(\dfrac{E_a}{k_B T}\right)$. This is generally used to model activated behavior due to a band gap E_a. Here, E_a is the average temperature independent activation energy. However, it has to be kept in mind that a pure Arrhenius law is a very crude approximation. In real cases, the resistivity might display a temperature dependent prefactor which the Arrhenius model does not take into account.

2. **Polaron model**[2,3,4]: This model represents the localization of charge carriers on small polarons. The localization is a consequence of a large electron – phonon interaction. In the high temperature regime (paramagnetic region), the magnetic correlations become negligible and the electric charge – lattice interplay is dominant. Nearest neighbor hopping of these polarons leads to a mobility with thermally activated form. In this model, the temperature dependence of electrical resistivity is given as $\rho = \left(\dfrac{\hbar a}{e^2}\right)\left(\dfrac{T}{T_P}\right)^n \left(\dfrac{1}{c(1-c)}\right)\exp\left(\dfrac{\varepsilon_0 + W - \lambda^{3-2n}}{k_B T}\right)$, or $\rho = \rho_P T^n \exp\left(\dfrac{E_P}{k_B T}\right)$. Here, a is the hopping distance (distance between hopping sites), c is the polaron concentration, $2W$ is the polaron formation energy, $k_B T_P$ is a characteristic polaron energy scale which gives the polaron tunneling rate, λ is the transfer integral and ε_0 is the energy required to produce intrinsic carriers. Depending on the magnitude of the optical phonon frequencies, there are two physical limits for these hopping processes: for $k_B T_P \gg \hbar \omega_{ph}$ (ω_{ph} being the characteristic phonon frequency involved in the polaron formation), the hopping is termed adiabatic. In this regime, the relevant optical mode lattice vibration of frequency ω_{ph} is long lived compared to the relevant polaron tunneling event i.e. the charge carrier motion is faster than the lattice vibrations. Here, the exponent $n = 1$. In the other case, for non-adiabatic transport, the electron tunneling event is not necessarily fast compared to the relevant optical mode lattice vibration i.e. the charge carrier motion is slow compared to the lattice vibrations. Here, the exponent $n = 3/2$, and T_P, λ and $2W$ are related as $k_B T_P = \left(\dfrac{\pi \lambda^4}{4W}\right)^{\frac{1}{3}}$.

3. **Mott** [5] **Variable Range Hopping (VRH) model**[5,6]: This describes the low temperature behavior of the resistivity in strongly disordered systems where states are localized near the Fermi level E_F. This model is based on the idea of charge transport by thermally assisted hopping of electrons between states localized near randomly distributed "traps" – potential fluctuations that can bind electrons. Anderson established that in a disordered system, if the randomness of the potential exceeds a certain critical value, the wavefunctions of all the states up to the mobility edge are localized, and such

states are referred to as localized states. Mott showed later that this kind of localization necessarily occurs at the bottom of the conduction band and at the top of the valence band of any disordered material. The conduction occurs in the localized states by a thermally assisted hopping process. Here, the hopping mechanism is not constrained by the condition that it can occur only between nearest neighbor sites (hence the name "variable range"). Rather, the probability of an electron hopping between any two given sites is determined by a competition between the coupling between the sites i.e. the potential energy difference between the sites and the distance between the two sites in question. Under this scenario, the temperature dependence of the resistivity is given by

$$\rho = \rho_\infty \exp\left[\left(\frac{T_0}{T}\right)^{\frac{1}{4}}\right], \text{ with } k_B T_0 = \frac{\lambda}{N(E_F)\xi^3}. \text{ Here, } \lambda \text{ is a dimensionless constant, } \xi \text{ is the}$$

localization length of the electrons and $N(E_F)$ is the density of states at the Fermi level.

4. **Efros Shklovskii (ES) model**[7]: If one allows for long range Coulomb interaction between the hopping electron and the hole formed at the site that the electron formerly occupied, we get the Efros Shklovskii model. This scenario results in an enhancement of localization and appearance of a soft gap in the density of states near the Fermi level E_F. (The derivation of the Mott law was based on the assumption that the density of states near the Fermi level remains constant). The density of states under the ES model can be self consistently shown to be $N(E) = N_0 (E - E_F)^2$, where, $N_0 \approx \frac{\kappa^3}{e^6}$, κ being the dielectric constant of the sample. The increase in localization manifests as an increase in the exponent of temperature to ½. Thus, we get, $\rho = \rho'_\infty \exp\left[\left(\frac{T_0}{T}\right)^{\frac{1}{2}}\right]$, with $T_0 = \frac{C}{\xi(N_0)^{\frac{1}{3}}}$.

Also, the proportionality factor $\rho'_\infty = \rho_\infty T^{\frac{1}{2}}$.

5. **Spin polarized electron conduction**[8]: Conduction electrons in ferromagnetic materials can be considered to reside in two "conduction channels" with the electron being either parallel ("spin – up") or antiparallel ("spin – down") to the magnetization vector. There is no intermixing between the channels if no spin – flip scattering occurs and the conductivities of both channels just add up to the total conductivity. The electronic density of states (DOS) is split into a spin – up and a spin – down sub – band with a relative shift of the spin – down band towards higher energy (Fig.5.2). The difference of the DOS in the two channels ($n\uparrow$; $n\downarrow$) at the Fermi level (E_F) produces the spin polarization of conduction electrons, $P = \frac{n_\uparrow - n_\downarrow}{n_\uparrow + n_\downarrow}$. The spin polarization of a current flowing in a material might differ from P due to a difference in the velocity of $n\uparrow$ and $n\downarrow$ electrons – this is the so called "transport spin polarization". The best known example of spin polarized conduction is the giant magnetoresistance (GMR) effect[9]. In a spin valve

structure, spin – polarized electrons travel through a non – magnetic metal interlayer separating two ferromagnetic layers. Essentially, spin – dependent scattering occurs only at the interfaces. For parallel magnetization directions of both ferromagnetic layers, spin – up electrons can pass with little scattering at both interfaces, thus the resistance of the system is lower than that for anti-parallel magnetization directions. If the interlayer is replaced by an insulator with the thickness of a few nanometers, a magnetic tunnel junction[10] is obtained. In 1975, Julliere proposed an expression for the tunneling magnetoresistance (TMR) in such a trilayer comprising of two ferromagnetic metals and an insulating barrier[10]. The Julliere model connects the TMR with spin polarization of the electrodes and the barrier as such is not envisaged to have any spin polarization or is not expected to be source of spin-flip scattering that makes the electron lose the spin polarization. In this model the TMR defined as: $TMR \equiv \dfrac{R_{AP} - R_P}{R_P} = \dfrac{2P_1P_2}{1 - P_1P_2}$, where P_1

and P_2 are the spin –polarization of the two electrodes and R_{AP} and R_P are the resistances for the configurations when the spins in two electrodes are in anti-parallel (AP) and parallel (P) configurations respectively. In recent years there are reports of TMR exceeding 400% at room temperatures.

The tunnel conductance of an electron is described to be proportional to the product of the occupied density of states in the start electrode (prior to tunneling) and the empty density of states (at same energy and spin) in the final electrode (final state). This applies to both spin-subbands. Among the manganites, $La_{0.7}Sr_{0.3}MnO_3$[11] is a well known example of an oxide with nearly 100% spin polarization.
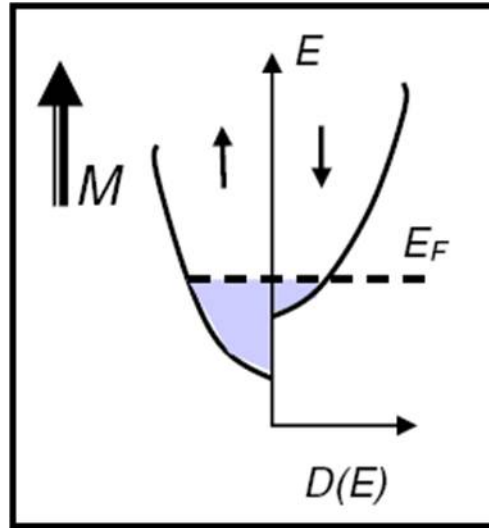
Fig.5.2. Schematic representation of the density of electronic states vs energy of a conducting ferromagnet (reproduced from [8]).

6. **Electronic conduction via percolation in phase separated samples**: Phase separation refers to the coexistence of nanoscale regions representing different phases in a single sample. We have described phase separation in manganites earlier in Section 1.8 of Chapter 1. Here we revisit the idea of phase separation solely from the point of view of

electronic conduction. Most of our samples are phase separated i.e. we have coexistence of metallic and insulating regions (or regions of very different electrical conductivity) in a single sample. In such samples, electrical conductivity can be interpreted using a mixed phase approach. Extended numerical studies by Dagotto and coworkers[12,13] on simulated random resistor networks have established that one can model the transport phenomena in the phase separated samples as occurring through two parallel channels – (a) insulating channels which have a resistivity ρ_i and percolating metallic channels having a resistivity ρ_m. Thus, the total resistivity of the sample can be written as $\frac{1}{\rho} = \frac{A_i}{\rho_i} + \frac{A_m}{\rho_m}$. A_i and A_m give the relative fraction of insulating and metallic parts in the sample. The exact analytical forms for ρ_i and ρ_m depend on the particular sample that is being studied. We have already introduced this idea in Chapter 4 while describing the resistivity behavior of nano $La_{0.5}Ca_{0.5}MnO_3$ (Section 4.4.3). It will be further used in this chapter also in later sections.

5.2 Grain boundaries

In nanomaterials, where the surface – to – volume ratio is much enhanced, the electrical transport has a greater contribution from the grain boundaries. The transport through the grain boundaries is expected to be different from that in the bulk[14-16]. Due to the close correlation between electron transfer and magnetic order in these oxides, magnetic disorder at the grain boundaries is associated with high resistance in the LCMO (x = 0.33) or LSCO (x = 0.5) samples. While the grains might remain metallic, the disordered grain boundary regions are likely to become more resistive. Thus, grain boundaries are the origin of additional resistance in the polycrystalline nanoparticle samples. In some cases, it might even become insulating with activated electrical transport.

5.2.1 Grain boundary transport models in magnetic materials

All grain boundary transport models assume that the magnetic structure of the grain boundary deviates from that of the grains' interior i.e. the grain boundary constitutes of a layer of reduced magnetic order. Thus, the ordering temperature as well as the saturation magnetization of the grain boundary is different from that of the core particle.

Electron transport can occur either by tunneling or by activated conduction. Electron tunneling may proceed directly[15] or via localized magnetic states inside the grain boundary layer[17,18]. Transport across the grain boundaries is typically non – ohmic leading to non – linear I-V characteristics[17,19]. The voltage dependence of the conductance $g(V,T)$ can then be written as

$$g(V,T) = \frac{dI}{dV} = g_0(T) + g_\alpha(T)|V|^{\alpha(T)} \dots\dots\dots\dots\dots\dots\dots\dots\dots\dots\dots\dots\dots\dots(1)$$

The temperature dependent exponent α indicates the dominant tunneling process. Thus, α = 2 (parabolic dependence of g on V) indicates direct tunneling[20,21] through a junction with rectangular energy barrier[22]. Here, the transport is an elastic process and the voltage dependence arises from the voltage dependence of the tunneling barrier transmission probability. Usually the contribution of the voltage dependent term is much weaker than the zero bias

conductance g_0. This mechanism does not include any aspect of spin polarized transport, and hence, is not affected by magnetic field unless the barrier is significantly modified by the field. $\alpha = \dfrac{n+2}{n+1}$ indicates tunneling via n localized states ($n \geq 1$)[17,23]. Paranjape et. al.[19] reported a value of $\alpha = 0.5$, and attributed it to tunneling between disordered electrodes. This kind of dependence is a manifestation of electron-electron interaction in weakly localized disordered solids[24]. The coefficient $g_{0.5}$ is a strong function of temperature and it decreases rapidly as T is increased. This has been experimentally seen in disordered metallic alloys as well as in disordered metallic oxides[25] at low temperatures ($T < 10$ K). Glazman and Mateev[23] proposed a theory for multistep tunneling for conduction in disordered solid. This model gives a generalized expression for voltage dependent dynamic conductance: $g(V) = g_0 + g_{\frac{4}{3}}|V|^{\frac{4}{3}} + g_{\frac{5}{2}}|V|^{\frac{5}{2}} + \cdots\cdots$. Here, the first term g_0 includes elastic tunneling and tunneling via single localized state. $g_{4/3}$ is the contribution by tunneling via two localized states. The tunneling involving more localized states will constitute higher order terms.

5.2.2 Coulomb blockade

At very low temperature and for small grain size, conductivity might be suppressed due to charging of grains. This is the Coulomb blockade phenomenon which might come into existence in the nanoparticle samples at very low temperatures. In this case, the carriers must overcome the charging energy, $E_C \approx \dfrac{e^2}{2C}$ of the metallic grains to be transported through the barrier. (In the above relation, $C = 4\pi\varepsilon_0 r =$ capacitance of the grains of radius r, assuming the grains to be spherical [26-28].) Existence of such an energy will make the transport activated and open up a gap at $T \approx E_C/k_B$, and can cause the resistivity of metallic particles to show an upturn at very low temperatures.

In order for the Coulomb blockade to be observable, the temperature has to be low enough so that the charging energy is at least comparable to the thermal energy of the charge carriers. In case $T >> E_C/k_B$, the thermal energy will make win over the charging energy and the phenomena could not be seen. This requires measurements down to very low temperatures. In the type of systems we study here, we will see that Coulomb blockade becomes observable below $\sim$ 5 K. For a proper understanding of this effect it is necessary to go down to temperatures at least one order below the temperature where Coulomb blockade starts to show. To this purpose, we have made measurements down to 0.3 K. To our knowledge, this is the first studies of electrical transport in these complex oxides down to such low temperatures where issues related to Coulomb charging can be addressed to unambiguously.

5.3 Samples

Having reviewed the various known mechanisms of electron transport in these materials, we now turn our attention to the specific oxide systems that we investigate in this work. We have chosen three different systems: $La_{0.67}Ca_{0.33}MnO_3$ (LCMO), $La_{0.5}Sr_{0.5}CoO_3$ (LSCO) and $LaNiO_3$ (LNO). The reason for this specific choice of systems is that they provide us with a

representative variety vis – a – vis the physical interactions acting within the systems. While the first two (LCMO and LSCO) are ferromagnetic oxides, LNO is a nonmagnetic metallic oxide. The two ferromagnetic systems that we have chosen are also very different from each other. We have already dealt with the magnetic properties of these two systems extensively in Chapter 3. Here, we very briefly) revisit the basic mechanisms via which ferromagnetism arises in them. This is necessary for the study of electrical transport in these systems (their electronic and magnetic states being coupled).

Bulk $La_{0.67}Ca_{0.33}MnO_3$ is a double exchange ferromagnet with a ferromagnetic to paramagnetic phase transition at T_C = 270 K[29]. On the other hand, bulk $La_{0.5}Sr_{0.5}CoO_3$ shows a ferromagnetic to paramagnetic transition at T_C = 250 K[30]. However, unlike LCMO which is a long range ferromagnet below T_C, LSCO lacks such long range ferromagnetic order. Rather, we get a cluster glass like state with ferromagnetic regions embedded in a nonferromagnetic matrix. This cluster glass (or spin glass) state arises from the fact that LSCO contains a mixture of Co^{3+} and Co^{4+} ions. While the superexchange interaction Co^{4+}-O-Co^{3+} is ferromagnetic, the exchange interactions between the ions with the same valency state are antiferromagnetic. The ferromagnetic order is local and the coherence length is not large. The fact that it has a spin state transition, implies that there are regions in the Co^{4+}-O-Co^{3+} network where Co^{3+} is low spin. This breaks the network of ferromagnetically aligned spins. Bulk $LaNiO_3$ is a nonmagnetic metallic oxide[31,32].

In Fig.5.3, we show the resistivity vs temperature curves for the bulk samples of the three oxides. The measurements were done on pelletized samples using standard a.c. four probe technique with lock-in detector in the temperature range 3 K to 300 K in a pulse tube based close cycle refrigerator[33] using a frequency of 173 Hz and a current of 0.1 mA. The data was collected during heating with a heating rate of 1 K/min. It was ensured that the sample was in thermal equilibrium with the base at this rate of heating. The sensitivity achieved in the measurement of the resistance was approximately 1 part in 10^5. As we have emphasized earlier, the three oxides being part of the family of correlated electron systems, their magnetic and electronic states are coupled. Thus, the differences in their magnetic states get reflected in their resistivity behavior also (as seen in Fig.5.3).

In $La_{0.67}Ca_{0.33}MnO_3$, the magnetic phase transition is accompanied by a metal to insulator transition (shown as an arrow in Fig.5.3(a)). Bulk LSCO remains metallic in the ferromagnetic as well as in the paramagnetic regime (Fig.5.3(b)). However, the ferromagnetic T_C at 250 K is reflected in the resistivity curve also as a change in slope at that temperature. This change in slope can be seen more clearly when we plot dρ/dT as a function of temperature (inset of Fig.5.3(b)). Bulk $LaNiO_3$ is a metallic oxide (Fig.5.3(c)). The value of the residual resistivity in our bulk sample (~ 150 μΩ.cm) matches with earlier reports[31,32]. Thus all three bulk samples show the expected behavior, thereby proving that our sample preparation technique is well standardized and gives us good, stoichiometric compounds.
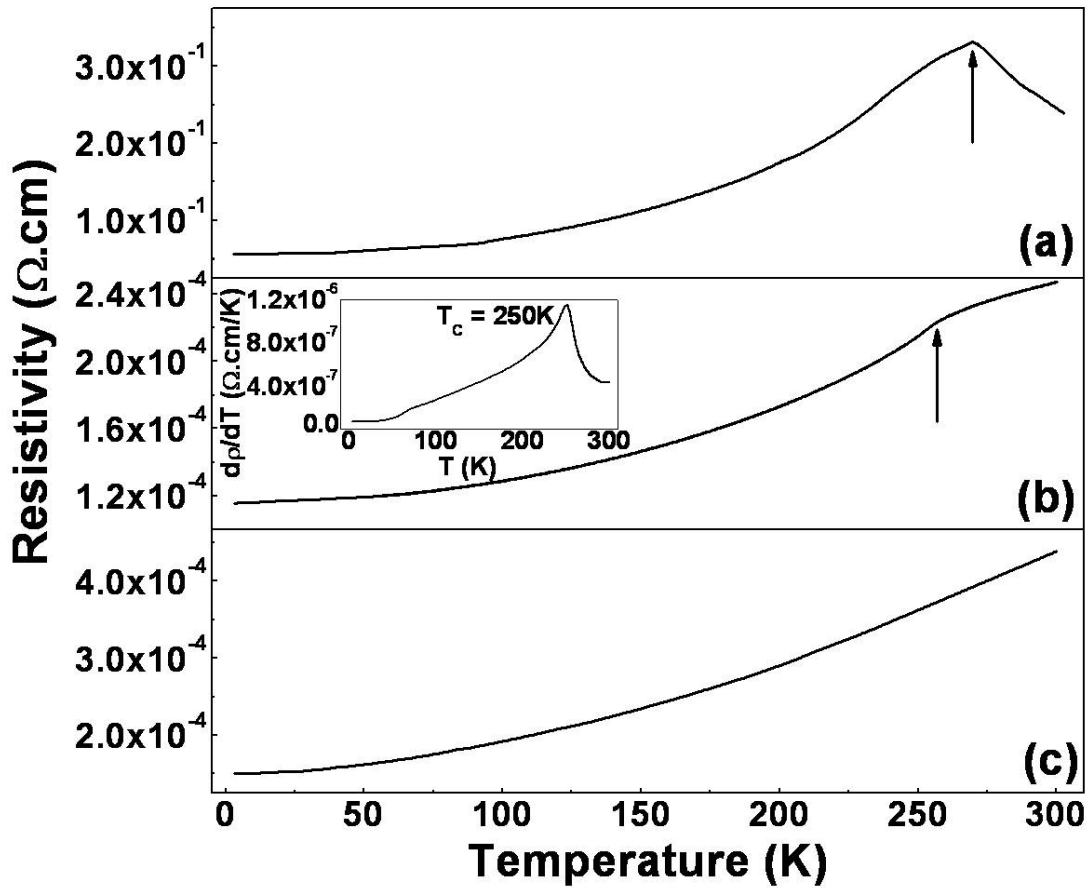
Fig.5.3. Resistivity vs temperature plots for bulk samples of (a) $La_{0.67}Ca_{0.33}MnO_3$, (b) $La_{0.5}Sr_{0.5}CoO_3$ and (c) $LaNiO_3$. The inset in (b) shows $d\rho/dT$ vs temperature plot for bulk $La_{0.5}Sr_{0.5}CoO_3$.

5.4 Electrical transport in nanoparticles of oxides

Our main interest is to probe how these oxides behave when the particle size is reduced to the nanometer level, which we proceed to discuss in this section. Here, we note that all measurements were done on pelletized samples. The pelletization was done at a given pressure, and the samples were annealed post pelletization. *The grain size is the average size in the pelletized condition.* Grain growth to larger sizes was carried out by controlling the annealing temperature.

5.4.1 $La_{0.67}Ca_{0.33}MnO_3$

In Fig.5.4, we show the resistivity vs temperature curves for the nanoparticle samples of LCMO. The resistivity vs temperature curve for bulk LCMO is also shown in the same figure as

an inset. As the particle size is decreased, the absolute value of the resistivity keeps on increasing so that on decreasing the particle size from ~ 3 μm down to ~ 15 nm, the resistivity increases by about four orders of magnitude. The peak in resistivity (it is not an insulator – to – metal transition in the true sense of the word as we had in the bulk samples or single crystals) keeps shifting towards lower temperature with a decrease in particle size and the peak region also becomes broad and shallow. At the lower most particle size of 15 nm, the peak in the resistivity completely vanishes and, as we will show below, this implies a very low volume fraction of the metallic region. In single crystals or in the bulk sample (see the inset of Fig.5.4) where the transport is predominantly single phase, the ferromagnetic T_C coincides with peak in the resistivity which is also the insulator-metal transition. In samples of nanoparticles, the two phase nature of the transport shifts the peak in the resistivity to low temperatures while T_C stays high. T_C for the nanoparticle samples are shown by colored arrows in Fig.5.4; also refer Chapter 3 for the values of T_C in these samples).
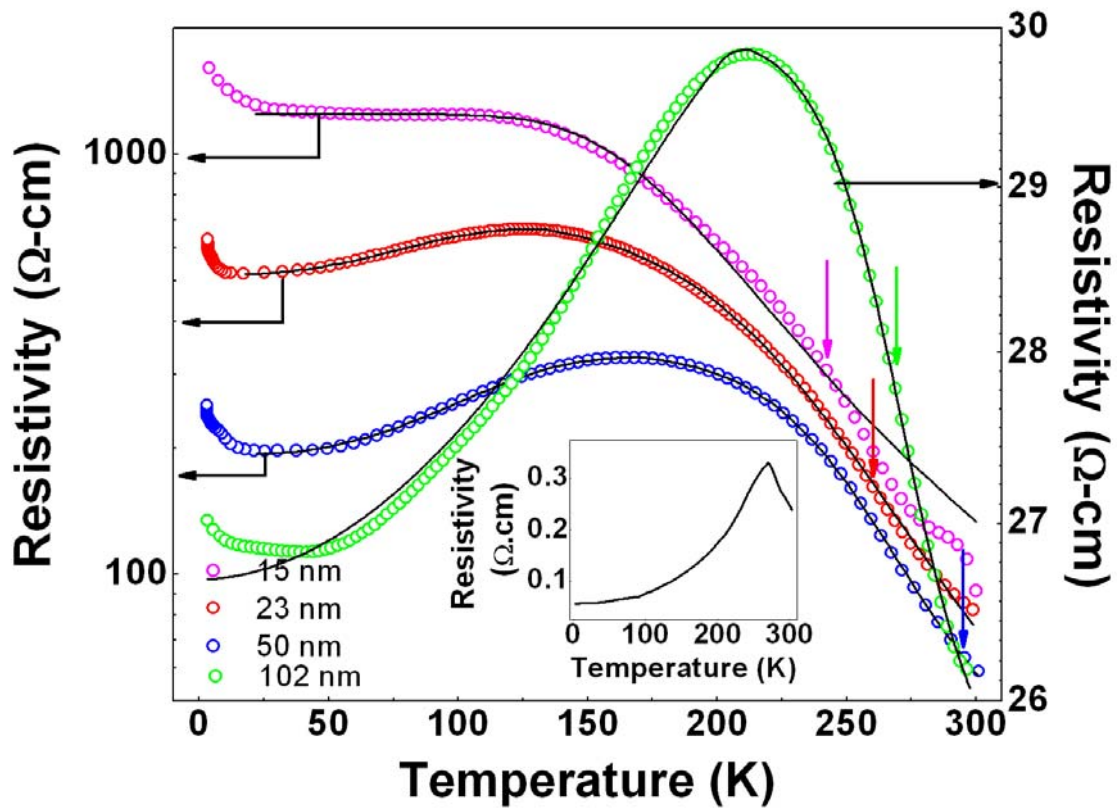
Fig.5.4. Resistivity vs temperature plots for LCMO nanoparticles. The colored arrows show the magnetic T_C in the respective samples. The inset shows the resistivity vs temperature plot for bulk LCMO.

The fact that the peak in resistivity is pushed down to a very low temperature in the nanoparticle samples and it becomes shallow as the resistivity increase on size reduction

indicates the presence of a high resistance phase along with the metallic phase which makes the transition percolative. Thus, these are phase separated samples and we can analyze the data using the two channel transport model of electron conduction via percolation (see Section 5.1 of this chapter). We do this assuming that the insulating channels have a resistivity which follows the Arrhenius model $\left(\rho_i = \rho_{i0} \exp\left(\dfrac{E_a}{k_B T} \right) \right)$ and the metallic channels have the resistivity form $\rho_m = \rho_{m0} + \alpha T^n$, so that the total resistivity of the samples is given by the equation $\dfrac{1}{\rho} = \dfrac{A_i}{\rho_i} + \dfrac{A_m}{\rho_m}$. The fits obtained using this model are also shown in Fig.5.4 as solid lines. The details of the fitting parameters are given in Table 5.1 and also shown in Fig.5.5. Other forms of ρ_i and ρ_m were also tried, but the above expressions yielded the best fit results. We also note that our assumed model fits the experimental data (open symbols) quite well except at very low temperatures (T < 10 K) where the resistivity again starts increasing. This low temperature uprise in resistivity is dealt with separately in later sections. The value of A_m/A_i gives the relative fraction of the metallic and insulating parts in the samples. The ratio A_m/A_i should be an approximate measure of volume (core) contribution and the contribution from the grain boundary which is linked to the surface of the grain. One would thus expect A_m/A_i to have a direct proportionality to the volume to surface ratio, which for spherical particles $\approx d/6$. This is indeed the case as can be seen from the topmost panel of Fig.5.5. ρ_{i0} as well as E_a show monotonous dependence on $1/d$ with both of them increasing as $1/d$ increases. E_a for the nearly "bulk" sample ($d \approx 102$ nm) ≈ 108 meV which is similar to that seen in polycrystalline manganite samples [34]. A few observations need to be noted here. Though the observed data can be fit using the relations given above, there are trends in numbers that point to very high resistivity even for the metallic state. For instance, ρ_{m0} in the metallic phase fraction has a very high value exceeding 1000 Ω.cm. Yet its shows a positive temperature coefficient of resistivity. This value is at least few orders larger than Mott maximum metallic resistivity value. Having a metallic phase fraction of such a high resistivity is a puzzling observation. More intriguing is the observation that while the coefficient α increases sharply on size reduction, the exponent n is nearly constant around 2-2.5.

A gradual enhancement of the activation energy on size reduction would indicate that not only the volume fraction of the insulating phase increases (decreased A_m/A_i), the activation energy of the disordered grain boundary regions also increase. We note that in the parent undoped compound single crystals[34], the value of the activation energy is approximately 400 meV. Thus the highly resistive grain boundary region in the nanoparticles samples, it appears, gradually behaves like a hole depleted region. It is not only without a moment (as the core-shell picture of Chapter 3 would suggest), it is also highly resistive due to absence of holes. The crucial question thus is why should this region be acting like a hole depleted region?

Table 5.1 Parameters of the fits of the high temperature (T > 10 K) resistivity data of LCMO nanoparticles.

Particle size (nm)	ρ_{i0} (Ω.cm)	E_a (meV)	ρ_{m0} (Ω.cm)	α (Ω.cm/K^n)	n
15 ± 2	131 ± 1.3	432 ± 5	1235 ± 1	$(1.4 \pm 0.7) \times 10^{-2}$	2.4 ± 0.1
23 ± 5	90 ± 1	282 ± 3	514.5 ± 0.2	$(6.2 \pm 0.4) \times 10^{-3}$	2.25 ± 0.05
50 ± 15	29.8 ± 0.8	278 ± 1	183.1 ± 0.3	$(5.3 \pm 0.3) \times 10^{-3}$	2.20 ± 0.01
102 ± 20	18.49 ± 0.08	108 ± 1	26.713 ± 0.002	$(2.0 \pm 0.06) \times 10^{-5}$	2.031 ± 0.005

We point out a note of caution about the two phase model that has been used for fitting the data. It assumes that there is a metallic phase (the grain regions) and an insulating phase (the grain boundary regions) through which the transport occurs. Strictly speaking above T_C in the grain regions there are two insulating phases, one the grain boundary region and other the polaronic insulating phase (above T_C) of the grain region. We did not distinguish between the two regions and thus the two phase approximation in its present form is strictly valid below T_C.
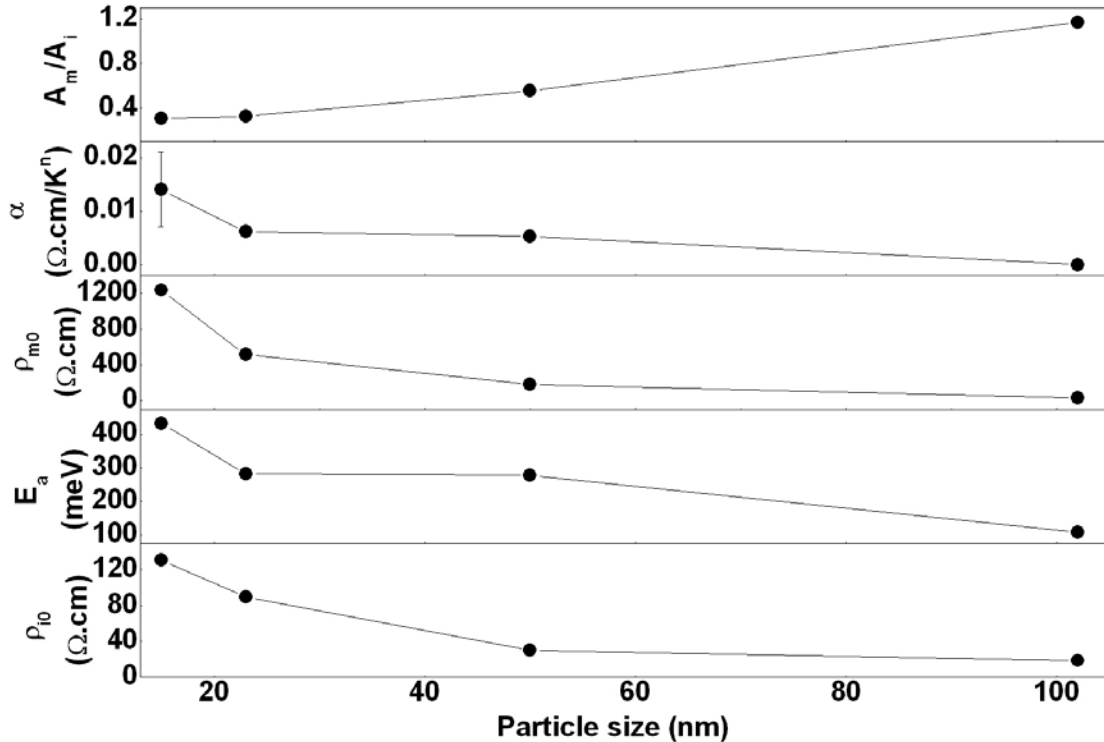
Fig.5.5. Size evolution of the various fitting parameters for the high temperature (T > 10 K) resistivity data of LCMO nanopartices (for details, see text).

To sum up, for T ≥ 25 K, the electronic transport can be described with a rather simple (may be not strictly rigorous) model of two phase transport. Transport through the grain (core) region that is metallic (and ferromagnetic, as seen in Chapter 3) constitutes one phase, and transport through the grain boundary region that is insulating. We also find that even the metallic phase of the grain region can be very resistive with the grain boundary region providing a hole depleted highly resistive region.

5.4.2 La$_{0.5}$Sr$_{0.5}$CoO$_3$

In Fig.5.6, we show the resistivity versus temperature plots for the La$_{0.5}$Sr$_{0.5}$CoO$_3$ nanoparticle samples. While bulk LSCO was metallic throughout the temperature range measured (shown in inset (a) of Fig.5.6), the nanoparticles show presence of an insulating component. We see a gradual transition from a totally metallic sample (bulk) to a totally insulating sample as we reduce the particle size from the μm regime to the nm regime (d ≤ 60 nm). The absolute value of ρ also shows an increase by about five orders of magnitude as a result of the particle size reduction at the lower most measured temperature. The colored arrows in Fig.5.6 mark the magnetic T$_C$ in the respective samples. It is clear that unlike bulk sample that shows a change in slope at T$_C$ the nanosized samples do not show any change in resistivity at T$_C$. It has been shown in Chapter 3 that though T$_C$ is suppressed, the ferromagnetism is retained in these samples. The nanosized cobaltates thus form an interesting class of ferromagnetic insulators.

We analyze the resistivity of the cobaltate nanoparticle samples using similar two phase electron transport model that we used for the manganite samples also, the only difference being in the form of $\rho_i(T)$. Here, the nature of $\rho_i(T)$ was taken to be the Efros – Shklovskii type of hopping with $\rho_i = \rho_{i0} \exp\left[\left(\frac{T_0}{T}\right)^{\frac{1}{2}}\right]$. The constant T_0 gives the energy scale of activation. Earlier reports of electrical transport in bulk samples (grain size > 1 μm) of LSCO with varying composition of Sr [35] provides us with the rationale for this particular choice of the form of $\rho_i(T)$. Mahendiran et. al.[35] have shown that in insulating and paramagnetic LSCO for $x \le 0.17$, the transport in the whole temperature range from 4 K to 300 K follows the Efros – Shlkovskii type relation. Thus, the resistivity of the nanoparticle samples of LSCO have been fit with the equation $\frac{1}{\rho} = \frac{A_i}{\rho_i} + \frac{A_m}{\rho_m}$, with $\rho_m = \rho_{m0} + \alpha T^n$ and $\rho_i = \rho_{i0} \exp\left[\left(\frac{T_0}{T}\right)^{\frac{1}{2}}\right]$. The fits obtained are also shown in Fig.5.5 as solid line curves. (This form of $\rho_i(T)$ also gives a better fit than the form $\rho_i = \rho_{i0} \exp\left[\left(\frac{T_0}{T}\right)^{\frac{1}{4}}\right]$ or a simple activated form as used in the case of LCMO). Details of the fitting parameters are given in Table 5.2 as well as in Fig.5.7. The "36 nm" and "60 nm" diameter samples do not show any metallic region, and we have assumed $A_m = 0$ for these two samples. We also note that similar to the LCMO nanoparticles, the resistivity of the LSCO

nanoparticles also show a low temperature upturn in resistivity for T < 10K. This upturn in resistivity for one of the samples (sample with particle size ~ 126 nm) is shown in the inset of Fig.5.6 as an example. However, we will deal with the low temperature behavior of the resistivity separately in later sections.
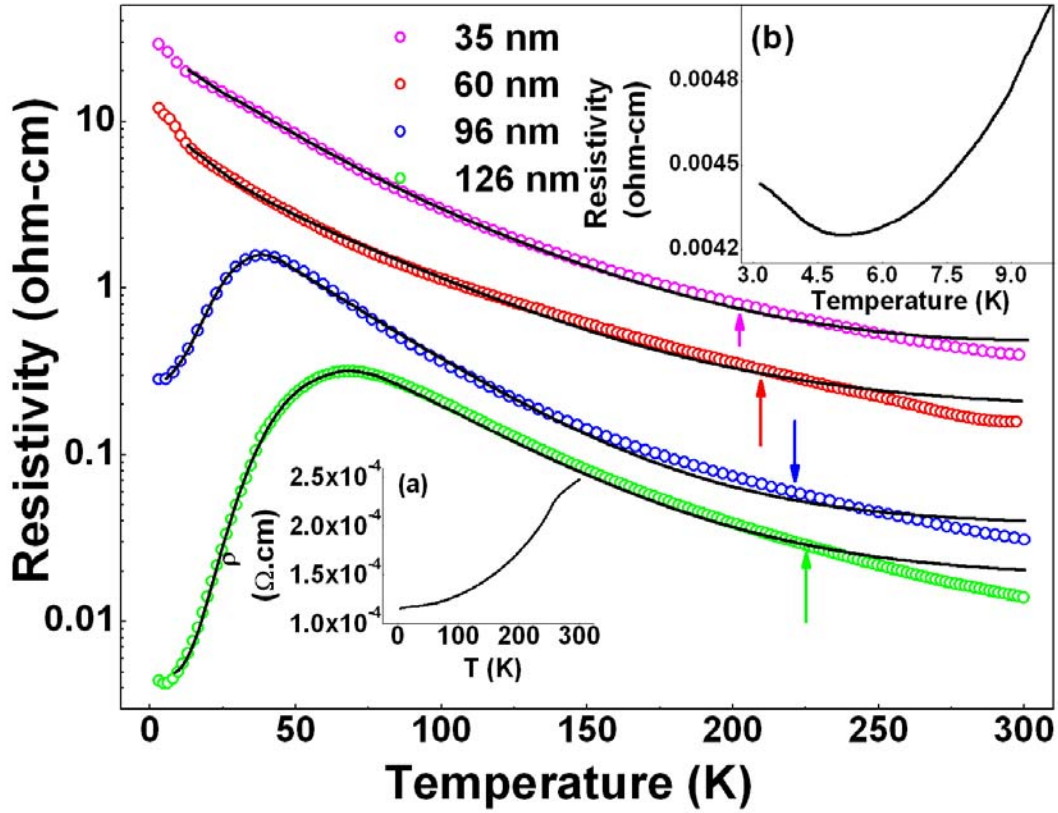
Fig.5.6. Resistivity vs temperature plots for LSCO nanoparticles. Inset (a) shows the resistivity vs temperature plot for bulk LSCO and inset (b) shows the upturn in resistivity below 5 K for the sample with average particle size ~ 126 nm. The colored arrows show the magnetic T_C in the respective samples.

Table 5.2 Parameters of the fits of the high temperature (T > 10 K) resistivity data of LSCO nanoparticles.

| Particle size (nm)	ρ_{i0} (Ω.cm)	T_0 (K)	ρ_{m0} (Ω.cm)	α (Ω.cm/K^n)	n	A_m/A_i
36	0.94 ± 0.02	3329 ± 2	–	–	–	0
60	0.257 ± 0.003	3010 ± 2	–	–	–	0
96	0.0189 ± 0.0002	2036 ± 4	0.243 ± 0.001	(8.6 ± 0.2) x 10^{-4}	2.458 ± 0.006	0.51
126	0.00277 ± 0.00003	1832 ± 7	0.00442 ± 0.00002	(1 ± 0.01) x 10^{-7}	2.123 ± 0.003	0.66
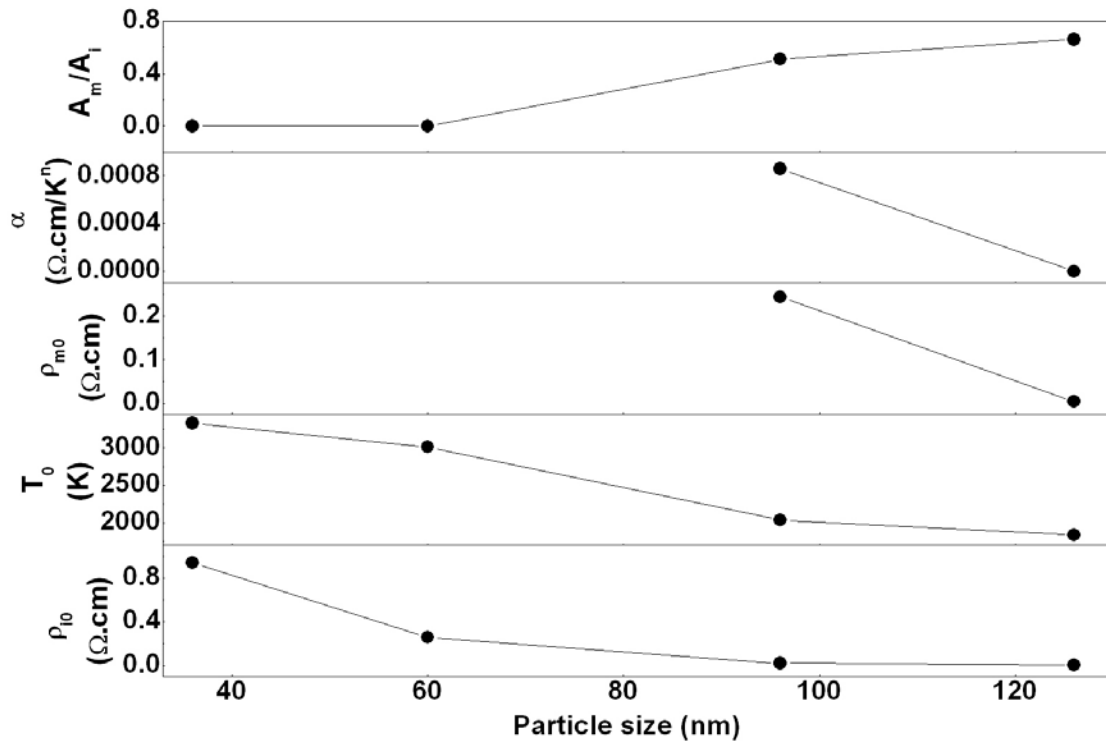
Fig.5.7. Size evolution of the various fitting parameters for the high temperature (T > 10 K) resistivity data of LSCO nanopartices (for details, see text).

The change in the parameter ρ_{i0} as a function of size, is more drastic in the case of LSCO samples where it changes by more than two orders where as in the case of LCMO, the change is less drastic (only a factor of 6) in the same size range. In contrast, the activation parameter of the insulating state as measured by E_a for LCMO is more compared to T_0 as measured in LSCO. In both the nanomaterials the size reduction thus not only increases the insulating phase fraction, it also makes the insulating state more rugged. This particular aspect draws our attention to the nature of the surface and the grain boundary region of these complex oxides which is an unsolved issue. We show below that not all complex oxide nanoparticles have such insulating grain boundary region. The example shown below shows that in some metallic oxides the grain boundary region remains metallic although with somewhat higher resistivity.

5.4.3 LaNiO₃

LaNiO₃ (Fig.5.8) behaves in a very different way from the nanoparticles of the ferromagnetic oxides. The most obvious difference is that the LNO nanoparticle does not show any insulating region (Fig.5.8(b)). It remains metallic down to the lower most measured temperature of 3 K. Since both the bulk as well as the nanoparticle samples of LNO remain metallic, we can fit the resistivity data of both using the equation $\rho = \rho_0 + \alpha T^n$. The fits are also

shown in Fig.5.8 as solid line curves. The insets in the figure show the fitting errors as a function of temperature. The details of the fitting parameters are given in Table 5.3. We find that the only appreciable change that occurs when the particle size is brought down from ~ 3 μm to as low as 23 nm is in the value of the residual resistivity (ρ_0) which increases by only a factor of about 2 for the nanoparticle sample as compared to the bulk sample.

Table 5.3 Parameters of the fits of the resistivity data of LaNiO$_3$.

Particle size	ρ_{m0} (mΩ.cm)	α (10^{-7} Ω.cm/K^n)	n
> 2 μm	0.15 ± 0.00002	1.137 ± 0.002	1.7780 ± 0.0003
23 nm	0.304 ± 0.00002	1.176 ± 0.003	1.7160 ± 0.0003
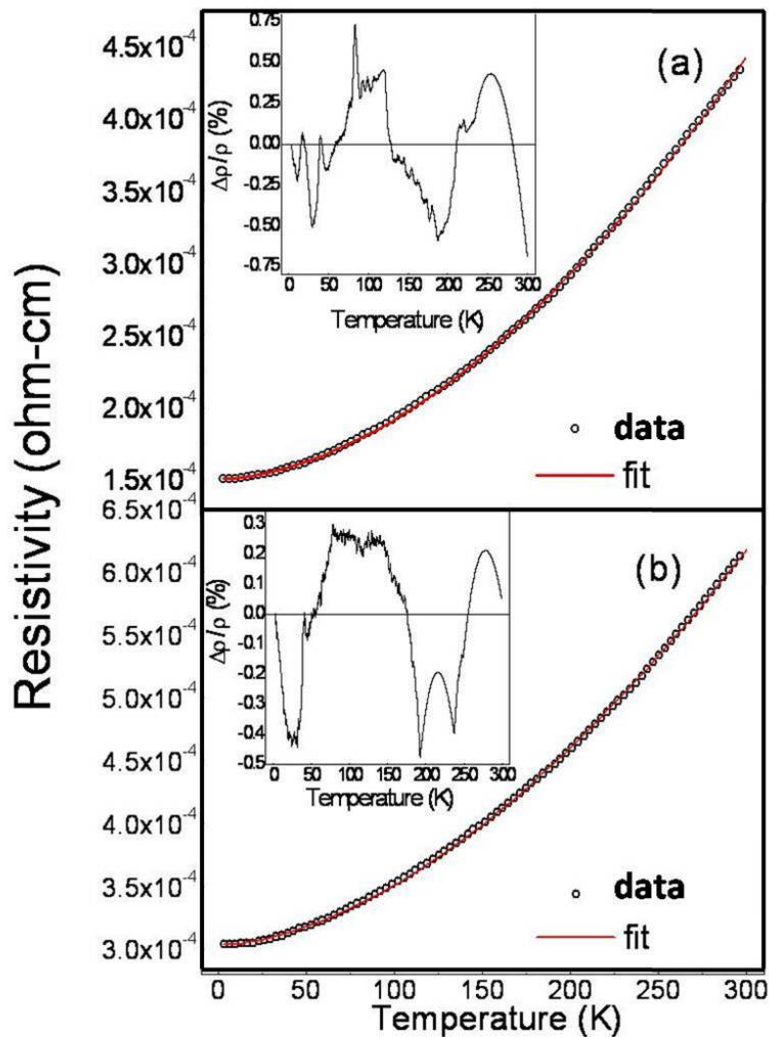
Fig.5.8. Resistivity vs temperature plots for (a) bulk and (b) nanoparticle sample of LaNiO$_3$. The insets show the fitting errors as a function of temperature.

5.5 The nature of grain boundaries

The essential difference between the transport behavior of the nanoparticles of the ferromagnetic and nonmagnetic oxides (presence of insulating component in the former but no insulating component in the latter even for the smallest nanoparticle and down to the lower most measured temperature) arises from a difference in the nature of the grain boundary region in the two classes of oxides. In $LaNiO_3$, in addition to the metallic grains, the grain boundary region is also conducting, although with higher resistivity. As a result, even the nanosized material remains metallic throughout the temperature range measured. In the case of the ferromagnetic oxide nanoparticles, the situation is more involved. The insulating phase here is provided by the grain boundary region itself. Thus, the metallic grains are in contact through an insulating layer which is of the same chemical origin as the metallic nanoparticles. The insulating nature of the grain boundaries arises from an absence of spin order in them. The ferromagnetic oxides, being part of the family of closely correlated electron systems, show a close correlation between the metallic state and the ferromagnetic spin order. The grain boundary in the ferromagnetic oxides constitute a magnetically disordered shell. This spin disorder leads to a loss of metallic behavior. From the analysis of the resistivity data presented in the section above it appears that the grain boundary region is depleted in hole concentration. Since the chemical concentration does not change one would expect that oxygen depletion creates electrons in these systems that compensates for holes and there is carrier depletion at the surface. Test like titration will not be able to detect the oxygen depleted region since it will be too small compared to the bulk region.

Thus, the nature of transport is determined by the nature of the grain boundary (a schematic representation is shown in Fig.5.9) which allows metallic transport in one (nonmagnetic LNO) and activated transport leading to tunneling in the others (ferromagnetic LCMO and LSCO). In case of (a) and (c) the GB region will not have much influence on the transport and the higher resistivity will arise mainly from the nature of grain contact. It is likely that this is the case in $LaNiO_3$. In case of (b) and (d) the nanoparticles have a core-shell structure as we have seen for the LCMO and LSCO particles. In this case the GB region will have a distinct transport property and will thus give rise to two phase conduction. In a way as will show below, as we go to lower temperatures and the difference in the conductivity of the grain region and the grain boundary region starts to differ, the sample consisting of the nanoparticles start to behave as a composite that consist of ferromagnetic nanoparticles in an insulating matrix. In contrast to much studied systems like Ni in SiO_2 matrix or Co in Al_2O_3 matrix (references) the LSCO and LCMO nanoparticles systems have an insulating phase that is not "inert" like SiO_2 or Al_2O_3 , instead it has spins and can behave as insulator whose tunnel barrier can be field tunable. The discussion in the following section address to these issues.
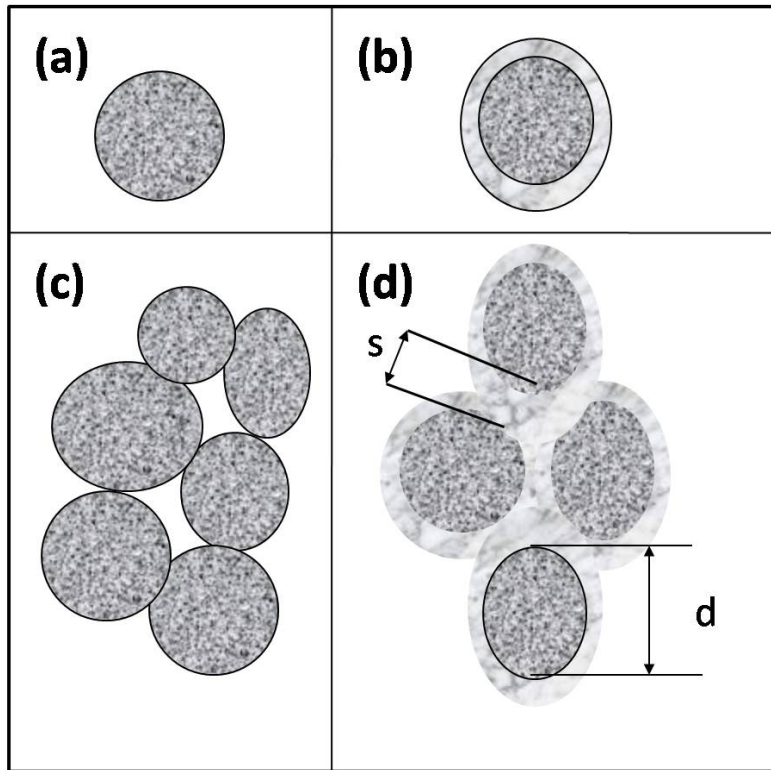
Fig.5.9. Schematic diagram for (a) a single nanoparticle without an insulating grain boundary, (b) a nanoparticle having a surrounding insulating grain boundary (core – shell), (c) LaNiO$_3$ nanoparticles with metallic contact, (d) nanoparticles of LCMO or LSCO in contact via the insulating grain boundaries.

5.6 Electrical transport below 10 K

As has been mentioned earlier, for the nanoparticles of the ferromagnetic oxides, the temperature dependence of ρ shows a steep rise as the temperature is lowered below ~ 10 K. This signals a change in the nature of the charge transport and calls for more detailed investigation. The change becomes more prominent when the average particle diameter is decreased. The transport below 10 K is a likely manifestation of the phenomenon of Coulomb blockade.

Before proceeding further, we give a brief background of transport in granular media (like metal nanoparticle – insulator composite) where one expects to see Coulomb blockade in the electrical transport. The electrical conduction in granular materials like metal particles in oxide matrix (e.g. Co particles in Al$_2$O$_3$ matrix) has been studied both theoretically and experimentally for at least three decades[36]. The transport process here is through the grains that are metallic, and the insulating matrix acts like a tunneling barrier. The observed behavior arises from the interplay between charging effects (Coulomb charging of metallic grains) and intergrain hopping that delocalizes the carriers. Experimentally, it has been found that in such materials the low temperature resistivity follows the relation[37]:

$$\rho = \rho_0 \exp\left(2\sqrt{\frac{\Delta}{k_B T}}\right) \quad \dots\dots\dots\dots\dots\dots\dots\dots\dots(2)$$

Here, ρ_0 is a constant, and the activation energy scale Δ is mostly decided by the tunneling barrier thickness of the oxides that separate the grains, the particle size and the decay length of the tunneling wave function in the barrier. Typically, the value of the activation energy Δ is given by [38] :

$$\Delta = 8\chi e^2 \frac{\left(s/d\right)^2}{\left(1 + 2\left(s/d\right)\right)} \quad \dots\dots\dots\dots\dots\dots\dots\dots\dots..(3)$$

where (s/d) is the ratio of the particle separation (s) to the particle diameter (d), and χ is the inverse of decay length for tunneling. We note here that the activation energy for transport is determined by the parameters χ and the ratio (s/d), and this is distinct from the charging energy of a grain which is E_C (see Section 5.2.1).

The materials that we are investigating are somewhat different from the metallic nanoparticle and insulator composites. In this case, unlike the composites, there is no distinct insulating phase. Here, the insulating phase is provided by the grain boundary region itself (also refer to a detailed discussion on the nature of the grain boundaries in Section 5.5). The insulating grain boundary region, in addition to tunneling, can also show hopping conduction as in disordered materials. Also we will show below that this insulating phase itself can respond to a magnetic field. Thus, the particle separation (s) can be related to the grain boundary thickness (t) as $s \approx 2t$ (also see Fig.5.9(d)). Approximately, the grain boundary thickness t will be close to (but somewhat larger than) δ, the shell thickness of the nanoparticles which we have independently estimated from the magnetization data (in Chapter 3).

For temperatures above 10 K, the resistivity as a function of temperature has been modeled as a two phase conduction where the two phases consist of a metallic phase and an insulating phase. As the temperature is lowered, the distinction between the resistivities of the two phases become more and other low energy scales start to show up. We start getting contributions arising from tunneling between conducting grains through the insulating intervening grain boundary regions. This particular aspect is investigated in the subsequent part of the chapter. In LCMO, it appears that this tunneling process, in addition, also has an effect of spin polarization. A study of the electrical conduction down to low temperatures allows us to look into low lying energy scales that may arise due to the phenomenon of Coulomb blockade. We proceed to do this below.

5.6.1 La$_{0.5}$Sr$_{0.5}$CoO$_3$

Above 10 K, the LSCO nanoparticles follow an ES – type hopping conduction $\rho_i = \rho_{i0} \exp\left[\left(\frac{T_0}{T}\right)^{\frac{1}{2}}\right]$ (see Section 5.4.2 for more details). Below 10 K, the low temperature resistivity follows equation (2) . Although functionally both the equations are similar, yet there is

a change in the temperature dependence at low temperatures. This change becomes apparent from Fig.5.10 where we have plot ln ρ vs $1/T^{1/2}$ for LSCO nanoparticles with average particle size 36 nm and 60 nm for $T < 10$ K. A clear change in the temperature dependence is seen below 5 K. This change in slope actually reflects the crossover from a hopping dominated region to a Coulomb blockade dominated region. This crossover, though not a change in the mathematical form for ρ, makes the physics of transport very different as explained below.
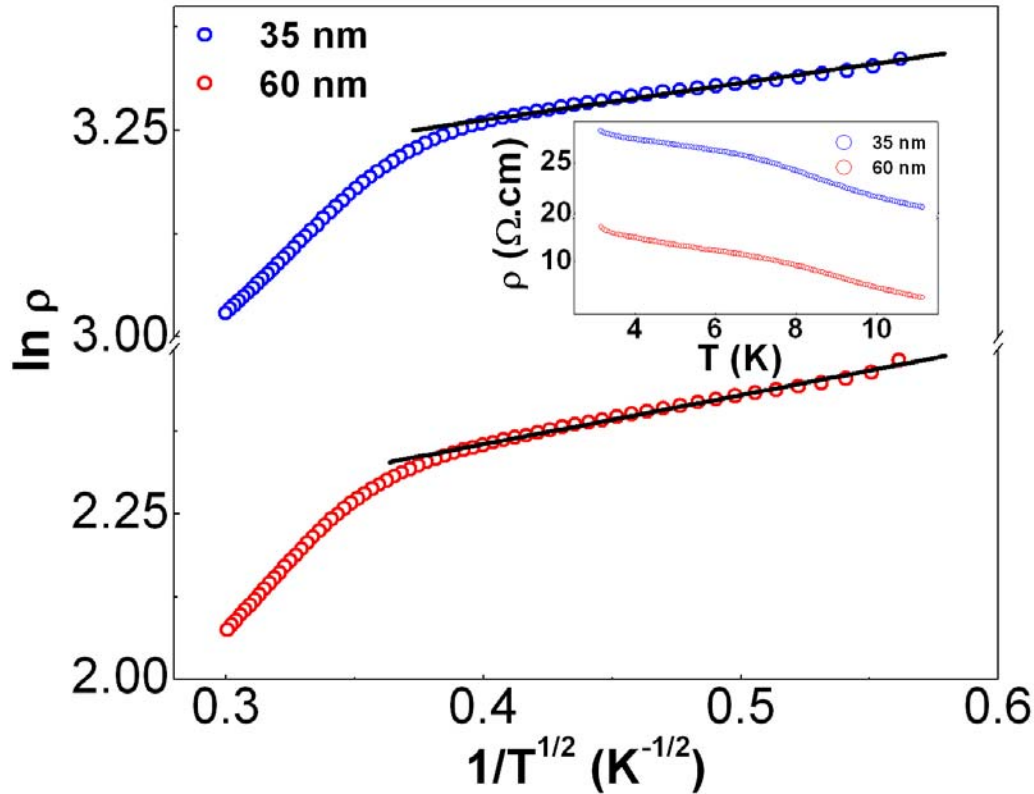
Fig.5.10. ln ρ vs $1/T^{1/2}$ for LSCO nanoparticles with average particle size 36 nm and 60 nm for $T < 10$ K. The solid lines are linear fits in the region 0.4K$< T <$ 5 K. The inset shows ρ vs T for T < 10 K.

In the high temperature region, where the transport is an ES type hopping (activation scale determined by T_0), the transport is dominated by on-site Coulomb interaction, which, in presence of disorder, gives rise to a soft gap in the density of states. The oxide in the grain boundary region is a disordered oxide. In this regime, the metallic nanoparticles do not make much contribution. As the temperature is lowered, this ES type hopping mechanism makes increasingly less contribution to the conduction process and tunneling through the grain boundary region between the metallic nanoparticles becomes the dominant transport mechanism. In this condition, the transport is very similar to that in metal – insulator composites. In this region, the transport follows the equation (2).

The insulating phase as we have seen has a ES type hopping which is functionally similar to the relation above. However the basic physics is different. The cross-over from a ES type hoping to a Coulomb charging dominated region can be seen around 6 K region in the inset and also in the $\ln\rho$ vs $1/T^{1/2}$ plot. The basic physics difference is that in case of ES type hoping there is a soft gap around the E_F that is mainly determined by the onsite Coulomb repulsion of localized charge. That gives a much larger T_0. In this case the gap to transport arises from Coulomb charging of the metallic nanoparticles grains and the energy scale is indeed different.

As can be seen from Fig.5.10, equation (2) fits the transport behavior below 5 K very nicely. The activation energies Δ so obtained are shown in Fig.5.11 where we have plotted Δ as a function of the inverse particle size ($1/d$). The red line in Fig.5.11 shows the result of fitting the experimental points using the relation (3).

Here we have assumed that the average value of "s" does not change much as we change d. (This approximation is valid for smaller size samples ($d \leq 100$ nm), as we have seen in Chapter 3). This allows us to extract the two parameters "s" and χ, the inverse of decay length for tunneling. The fitting parameters we obtain are $s = 9.4 \pm 0.2$ nm and $\chi = 0.074 \pm 0.002$ Å^{-1}. We note that the fitting parameters are within physically reasonable limits. For instance, the interparticle separation $s \approx 2t$, where, $t \approx \delta$, is the thickness of the disordered shell on the nanoparticles. δ is estimated from entirely different experiments (magnetic measurements). The suppression of the saturation magnetization in the nanoparticles (M_S) compared to the bulk saturation magnetization (M_{0S}) gives us the value of δ through the equation $M_S = M_{0S}\left(1 - \frac{6\delta}{d}\right)$ [39]. Substituting the values of $M_S = 0.28$ emu/gm and $M_{0S} = 1$ emu/gm (see

Fig.3.26 of Chapter 3), we get $\delta \approx 4.3$ nm for the smaller particles of LSCO. This gives an independent estimate of $s \approx 2t \approx 2\delta = 8.6$ nm, which is very close to $s = 9.4 \pm 0.2$ nm as obtained from the transport data. The deviation of the data for the largest diameter nanoparticle is a point in question. In this system, the value of observed Δ is much smaller than the temperature range over which it has been evaluated. Also for this sample, the resistance is such that one can have substantial ES type of hopping in the GB region taking place parallely with the tunneling and thus the effective observed gap Δ will be lower. [Note: The Δ found even in smallest particle size sample is ~ 0.03 meV , which is around 0.35 K. This is the lowest temperature till which measurements have been done. So we are in the region where at best $T \sim \Delta/k_B$.]
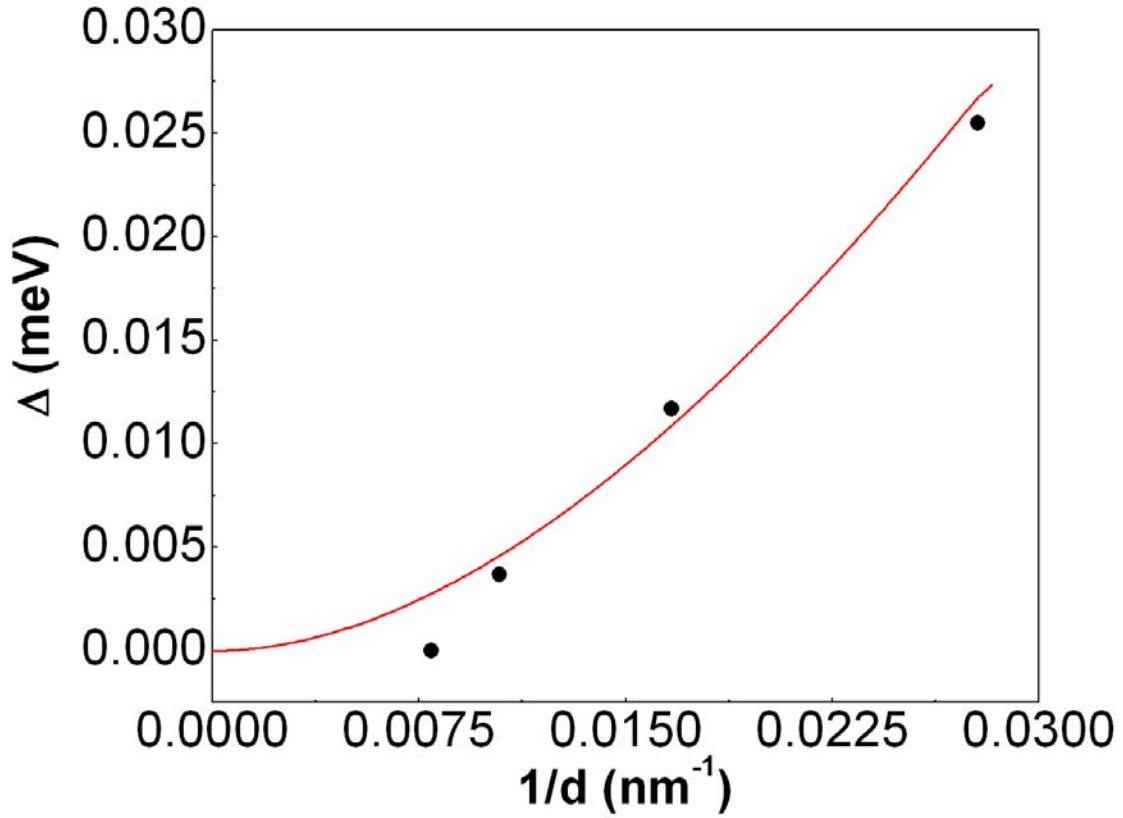
Fig.5.11. Δ vs $1/d$ for LSCO nanoparticles. The solid line is a fit to the equation (3) (for details see text).

Since the transport phenomena that we are trying to probe is intimately linked to the magnetic state of the sample (the low temperature upturn in resistivity is seen only in the ferromagnetic oxide nanoparticles), our next step is to test how the resistivity responds to the application of an external magnetic field. This we do in the region of low temperature i.e. T < 10 K and for the smallest nanoparticle sample ($d \sim 36$ nm). The ρ versus temperature plots taken under different magnetic fields from 0 T to 14 T in the temperature range 0.3 K < T < 10 K are shown in Fig.5.12. In the inset of Fig.5.12, we show the magnetoresistance (MR) as a function of the applied magnetic field at two different temperatures, 0.3 K and 10 K. MR is defined as

$MR(\%) = \left(\dfrac{\rho(0) - \rho(H)}{\rho(0)} \right) \times 100$. The MR shows an almost linear behavior (after an initial sharp

rise for very small $H < 1T$) with the applied field (H). However, the important point here is that even at a field as high as 14 T, we get an MR of only $\sim 25\%$.
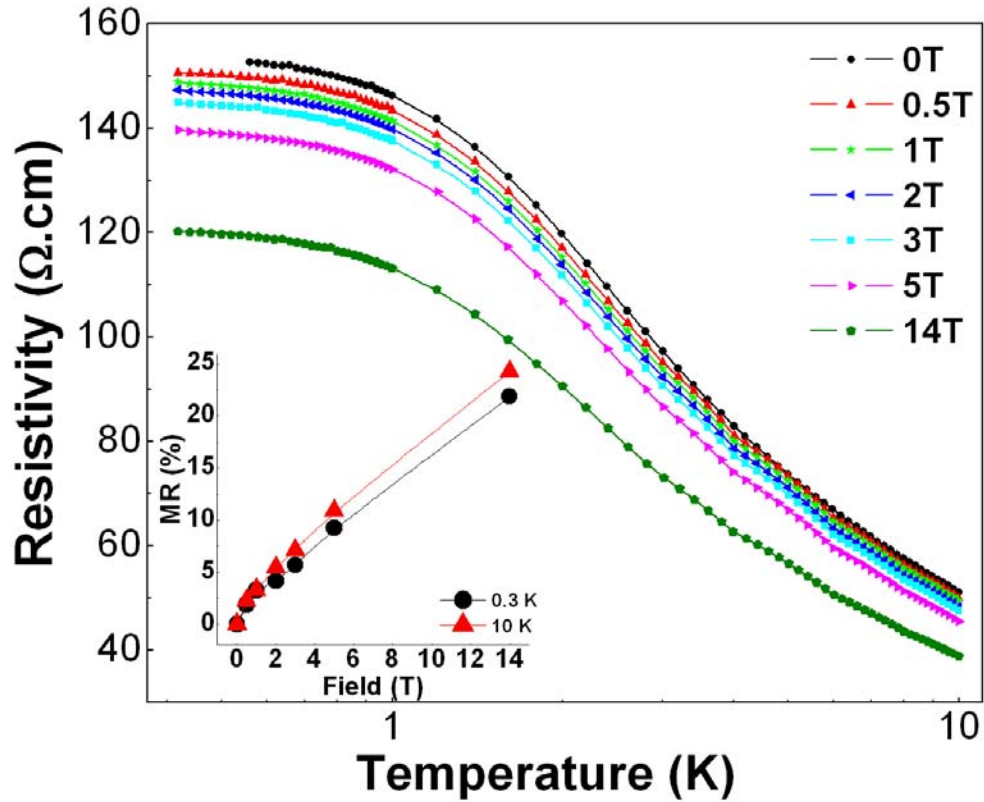
Fig.5.12. Resistivity vs temperature plots for LSCO nanoparticle with average particle size 36 nm taken under different magnetic fields. The inset shows the MR as a function of applied magnetic field at T = 0.3 K and T = 10 K.

Since the resistivity of the system can be described by equation (2), it is interesting to see how the magnetic field affects the parameters of equation (2) and thus give rise to the MR. After the application of the field the resistivity can also be described by eqn (2). An example is shown in Fig.5.13 where we show plots of ln ρ vs. $T^{-1/2}$ at 0 T and 14 T for the sample with average particle size ~ 36nm. Thus MR can arise by a change (reduction) of ρ_0 as well as Δ. To estimate the effect of magnetic field on the barrier height for tunneling, we can estimate Δ and ρ_0 by fitting the curves shown in Fig.5.13, to equation (2). Since (s/d) does not change with magnetic field, the change in the energy Δ can arise from a change in χ, the inverse of decay length for tunneling (see equation (3)).We show the evolution of Δ, χ and ρ_0 with the applied magnetic field in Fig.5.14 (a), (b) and (c) respectively. There is approximately 8% change in the barrier at the highest field. As is seen from the figure, applied magnetic field decreases the barrier height more or less linearly. ρ_0, on the other hand, shows a more sharp decrease for very small values of H ($H \leq 0.5$ T), above which the change in ρ_0 becomes more or less linear. A reason for the decrease in ρ_0 can be an enhancement of the spin alignment in the magnetic field in the neighboring grains between which the tunneling occurs. This will be dominated by the degree of spin polarization of

197

the electrons in the grains. The fact that this does not saturate even at highest field of H=14 T, would mean that there is sufficient spin canting that is not aligned even in a very high field. Another cause can be that in the grain boundary region (that is the insulating part of the tunneling junction) the electrons can have spin-flip scattering that will destroy the spin polarization of the tunneling electron and this would decrease the value of the TMR. The application of the field also aligns the spin (which is truly disordered) in the barrier region, this slowly increases the TMR on application of field.

The decrease in Δ though small has a good effect on the tunnel resistance because it is in the exponential. The cause for its decrease is definitely a decrease in the inverse decay length. Inverse decay length decreases (or decay increases) when the tunneling barrier decrease. So application of the field leads to a lowering of the barrier. Thus there is a spin dependent barrier height. This concept has not been proposed before due to the fact that in most past studies the insulating barrier region did not have spin. We will discuss this again when we discuss results of LCMO nanoparticles.
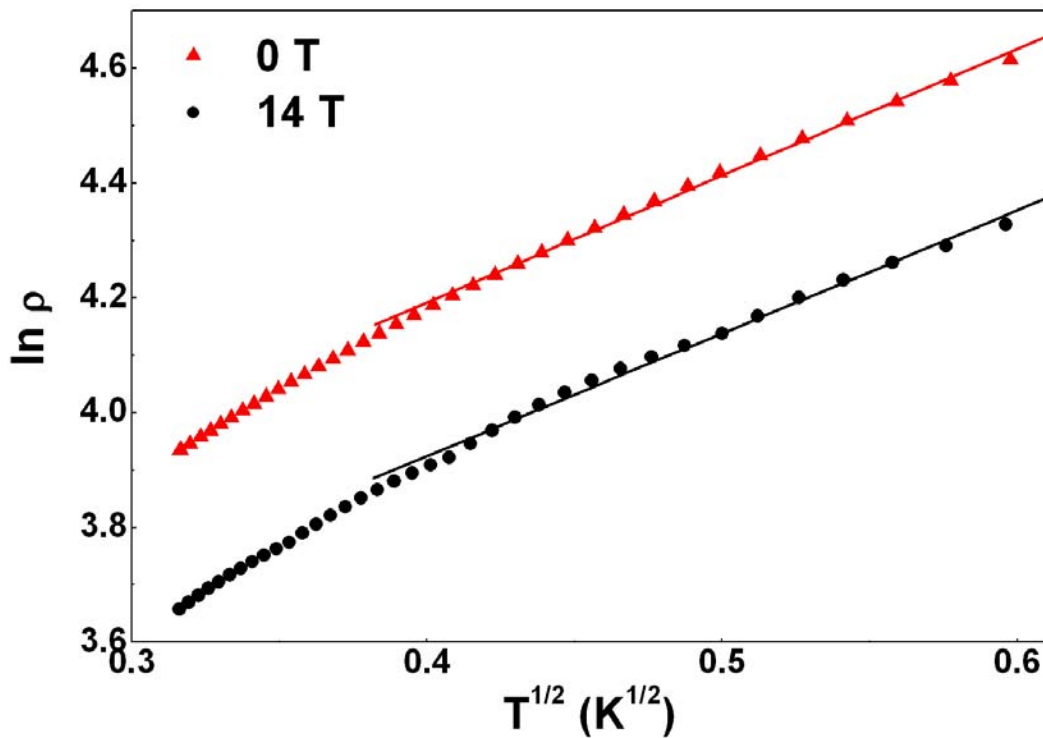
Fig.5.13. ln ρ vs $1/T^{1/2}$ for LSCO nanoparticle (average particle size ~ 36 nm) for T < 10 K at H = 0 T and H = 14 T. The solid lines are linear fits in the region T < 5 K.
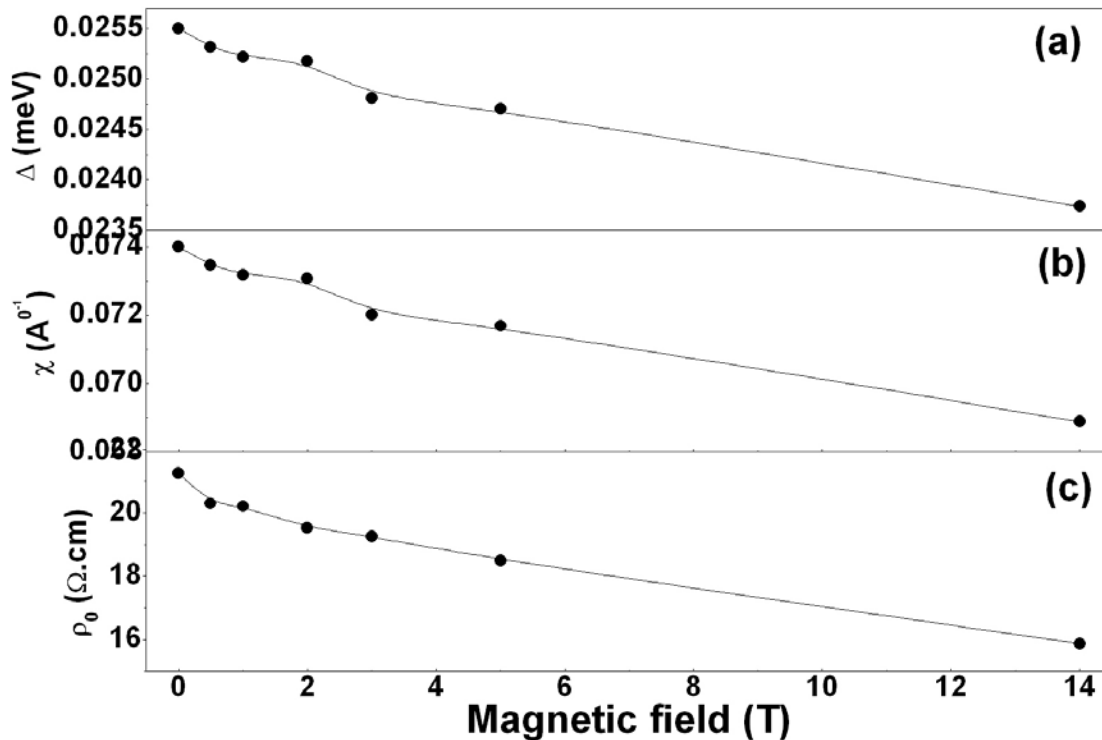
Fig.5.14. Variation of (a) Δ, (b) χ and (c) ρ_0 with applied magnetic field for LSCO nanoparticle $(d \approx 36$ nm).

5.6.2 La$_{0.67}$Ca$_{0.33}$MnO$_3$

Below 10 K in LCMO nanoparticles the resistivity shows deviation from the simple two phase transport as in LSCO. We apply similar explanations here also and see that the resistivity of the LCMO nanoparticles follows the same equation (eqn 2) as the LSCO nanoparticles. This can be seen in Fig.5.15 where we show the plots of $\ln \rho$ vs $1/T^{1/2}$ for two LCMO nanoparticles with the smaller average particle size. (ρ vs T for the samples are shown in the inset of Fig.5.15). From the linear fits to the plots (shown as solid lines in Fig.5.18), the activation energies Δ are obtained. We plot these in Fig.5.16 as a function of the inverse particle size $(1/d)$ and fit the experimental points using the equation 3. As in the LSCO case, the parameters "s" and χ are extracted. We get, $s = 3.6 \pm 0.3$ nm and $\chi = 0.81 \pm 0.06$ Å^{-1}. The thickness of the disordered shell in the smallest size LCMO nanoparticles (as estimated from magnetization measurements) is $\delta \approx$ 1.92 nm. This gives $s \approx 3.84$ nm, which is very close to what we obtain from the fits to the transport data. As we have seen in Chapter 3, in the range of d used for the fit to estimate s ($d \leq$ 100 nm), δ remains more or less constant. [Note: The larger two particle sizes show very small Δ values (~ 0.04 meV)].
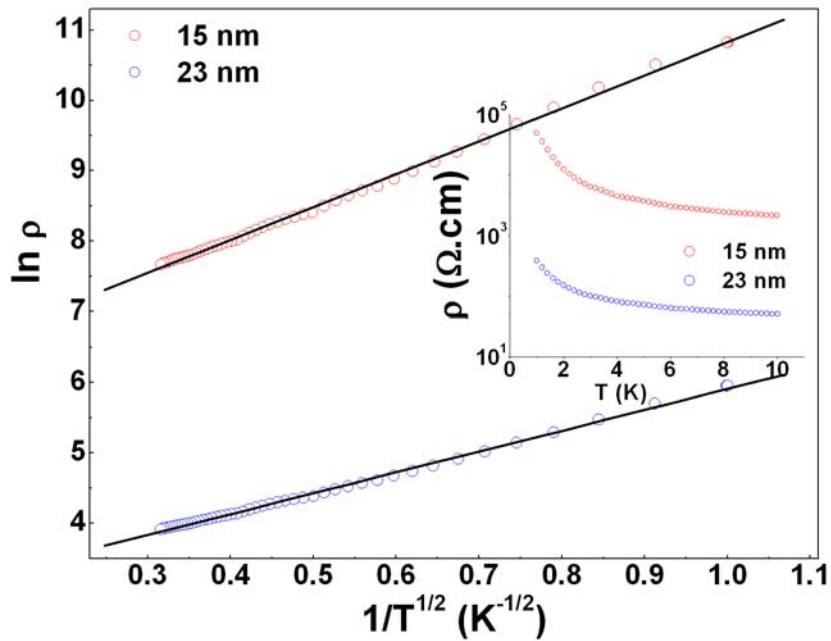
Fig.5.15. ln ρ vs $1/T^{1/2}$ for LCMO nanoparticles with average particle size 15 nm and 23 nm for T < 10 K. The solid lines are the linear fits. The inset shows ρ vs T for the two samples.
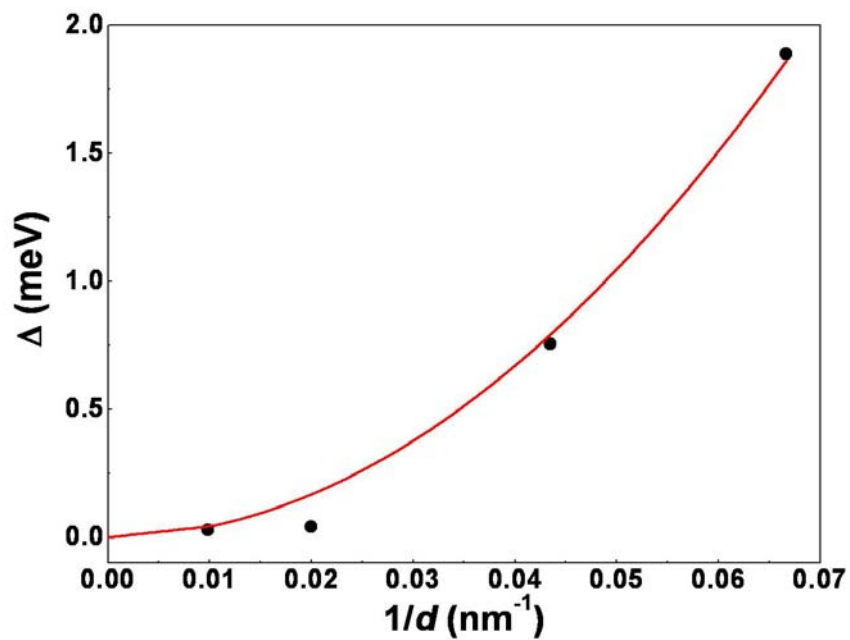
Fig.5.16. Δ vs $1/d$ for LCMO nanoparticles. The solid line is a fit to the equation (3) (for details see text).

The LCMO nanoparticles show a higher response to magnetic field than the LSCO nanoparticles. This is seen from the resistivity versus temperature curves taken in the presence of magnetic field at T < 10 K (Fig.5.17). In the inset of Fig.5.17, we show the variation of the *MR* as a function of the applied magnetic field. It is seen that the *MR* reaches almost 80% at 14 T, while for the LSCO nanoparticles, the maximum *MR* is only ~ 25% (Fig.5.12). The *MR* also shows a sharp rise in the *MR* at low field (till 0.2 T) to ~ 30%. Above 0.2 T, the *MR* increases almost linearly with *H*. This two step behavior of the *MR* is more prominent here in the case of LCMO than that seen in the case of LSCO. This kind of low field mgnetoresistance (LFMR) effects have been observed in polycrystalline samples and have been attributed to the spin dependent transmission of electrons across the grain boundaries.

In this context it is noted that nanostructured films of LCMO have been studied before [40] down to 4.2 K. The average grain size of the films was ~15-25 nm which is very similar to the size of the nanoparticles used by us. The response of these films in a magnetic field is also very similar that it has a rather sharp very low field response followed by a gradual high field response. The MR experiment was carried out in fields upto 6 T. (In this case the response was measured upto 14 T and it showed no sign of saturation.) In the nanostructured film the low field response was related to the grain boundary region and a model was proposed that showed a field variation going as $\dfrac{\Delta R_{GB}(H)}{R_0} = -C_1 erf(C_2 H)$, where C_1 and C_2 are constants. The high-field region was proposed to arise from the bulk of the grain and follow the magnetization and a relation of the type $\dfrac{\Delta R_{Grain}(H)}{R_0} = -C_3 H - C_4 H^3$. While such a model may still be valid at temperature region we are working, we note that the field response is higher in these samples in terms of higher MR for the same field and also we note that at lower temperatures additional contribution comes from the inter-grain tunneling. We will discuss this issue later on.
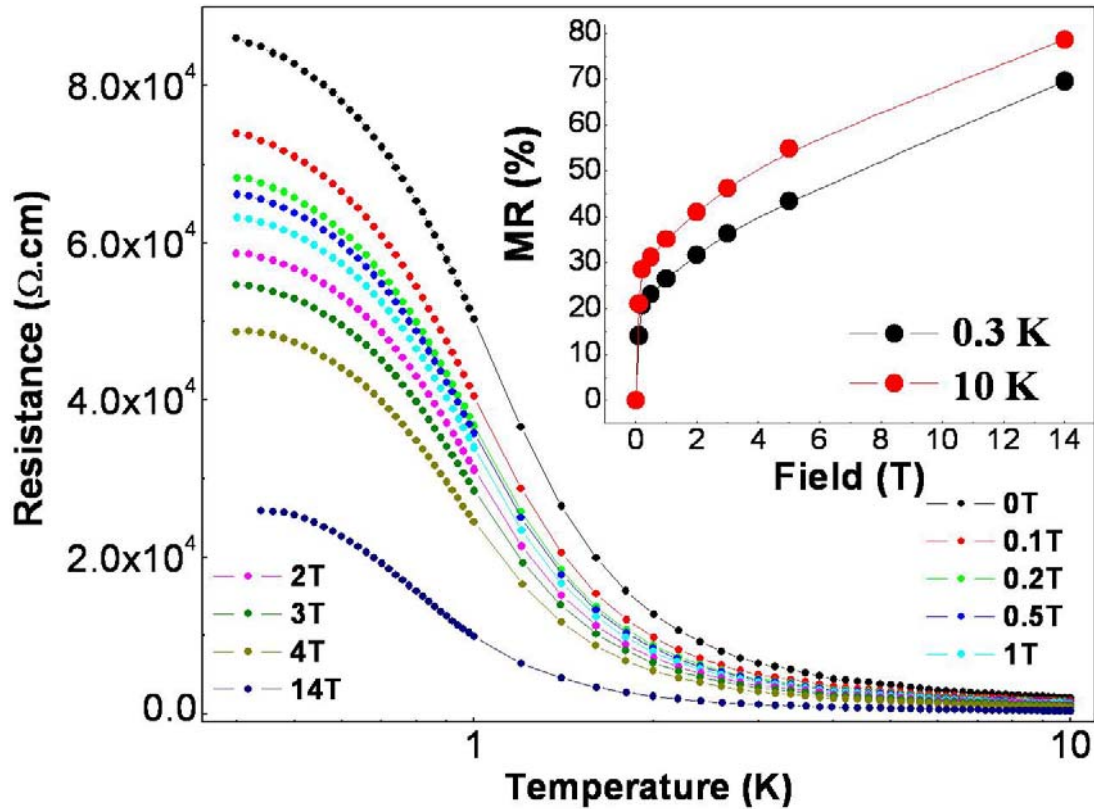
Fig.5.17. Resistivity vs temperature plots for LCMO nanoparticle with average particle size 15 nm taken under different magnetic fields. The inset shows the % MR as a function of applied magnetic field at T = 0.3 K and T = 10 K

As in the case of LSCO, we estimate Δ by fitting the curves shown in Fig.5.17 to the equation 2, and then calculating χ from the equation 3. This enables us to probe the effect of magnetic field on the sample more quantitatively. We have shown the evolution of Δ, χ and ρ_0 with the applied magnetic field in Fig.5.18 (a), (b) and (c) respectively. As is seen from the figure, for small values of *H*, the barrier height does not change appreciably. Change occurs for H > 5T and at *H* = 14 T, we obtain a 25% decrease in the barrier height (this is much larger than the 7% decrease in barrier height that we had obtained for the cobltate nanoparticle sample, and is thus consistent with the fact that LCMO nanoparticles show a much larger *MR* than the LSCO nanoparticles). The increase in MR at higher field thus has a good contribution coming from the lowering of barrier Δ, which in turn arises from a decrease of the barrier height which decreases the inverse the tunneling length χ. However, the insensitivity of the barrier height for small values of *H* is contradictory to the sharp increase in *MR* that we see in this sample at low field (inset of Fig.5.17). This sharp increase of *MR* at low field values can be explained from Fig.5.18 (c) which shows the variation of ρ_0 with field. As can be see, ρ_0 drops sharply at low field values, and thus accounts for the steep rise in *MR* in this field regime. The parameter ρ_0 is linked to the

transmission probability of the electron between two metallic grains and is thus linked to the orientation of the magnetization of the metallic grains. From chapter 3 it can be seen that the M-H curve shows that the M of the samples of this size (~15 nm) reach saturation for H < 0.2T. The sharp drop in ρ_0 occurs within this value of the field. If the dominant transport in this region is indeed inter-grain tunneling that is tuned by the magnetic field then the change at the knee ~35% can be obtained from nearly 50% spin polarization using Julliere relation ($TMR \equiv \dfrac{R_{AP} - R_P}{R_P} = \dfrac{2P_1 P_2}{1 - P_1 P_2}$) for TMR. The low temperature knee in the MR thus can be linked to TMR which we expect if the predominant transport mechanism is inter-grain tunneling. Thus, the results presented so far show that the transport in the sample with nanoparticles below 10K can be described predominantly by inter-grain tunneling. We explore this issue again later on when we discuss the *I-V* curves.
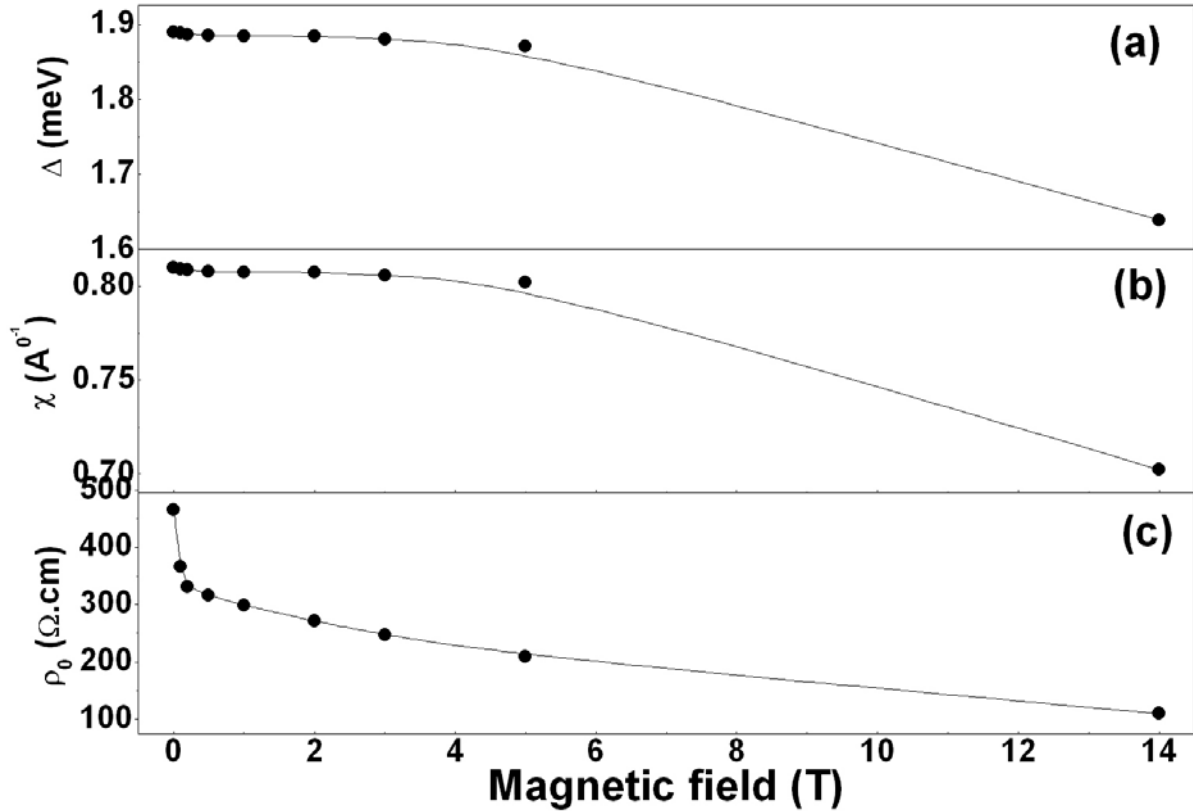
Fig.5.18. Variation of (a) Δ, (b) χ and (c) ρ_0 with applied magnetic field for LCMO nanoparticle ($d \approx 15$ nm).

5.7 I-V characteristics of nanoparticle samples

The important idea that we propose here is that below 10K and for 5K in particular the transport in the nanoparticles systems can be described by tunneling type of transport though the GB region that acts as barrier to tunneling. We have seen that a simple description based on such a scenario can explain the resistivity and MR data below 5K in these materials. We note that past studies in nanostructured manganites that probed these issues did not go to low enough temperatures so that these phenomena can be observed cleanly. We have more than decade in temperature below 5K where we can investigate the phenomena. In this section we carry out a validation of the tunneling idea by direct measurements of the non-linear I-V data. We argue that the transport in this temperature range is through a network of tunnel junctions that consist of the metallic ferromagnetic oxide nanoparticles as electrodes and the intervening oxide regions as tunnel barriers. Thus an investigation of the non-linear *I-V* characteristics in these materials at low temperatures will provide information on the tunneling type transport through these materials. In LCMO, in particular, artificial grain boundary junctions have been studied down to 4K[41] to show that a tunneling type transport takes place through such junctions. The dependence of the I-V characteristics in magnetic field is expected to give information on spin-dependent intergranular tunneling. We note that for LSCO nanoparticles such studies at low temperature have not been done.

5.7.1 LSCO system

First we investigate the LSCO system. In Fig.5.19, we show the *I-V* curves taken at 0.3 K under different magnetic fields varying from 0 T to 5 T (Fig.5.19 (a)), and at different temperatures ranging from 0.3 K to 5 K in the absence of any external magnetic field (Fig.5.19 (b)). All the curves show non-linear behavior, but the features become clearer when we plot the differential conductance (*g*) versus bias voltage curves (Fig.5.20). The differential conductance (*g*) is defined as $g = \dfrac{dI}{dV}$, and is obtained by numerical differentiation of the *I-V* curves. The expected gap Δ is very small even in the sample with smallest grain size ($\Delta \sim 0.03$ meV). This is very small to show up as a clear gap in the I-V data taken at a finite temperature. The data are shown upto ± 5mV .
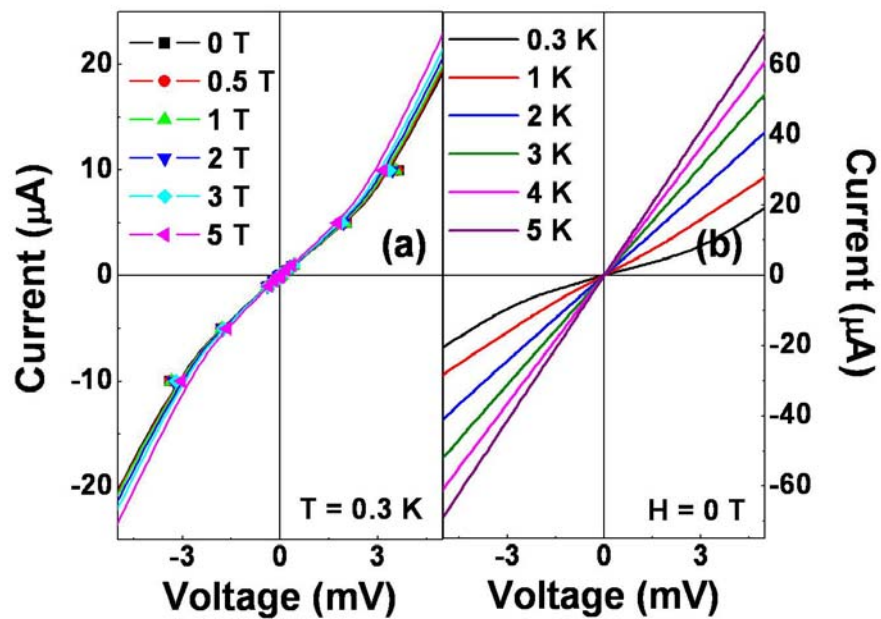
Fig.5.19. *I-V* curves of LSCO nanoparticle with average particle size 36 nm at (a) T = 0.3 K taken under different magnetic fields and (b) H = 0 T taken at different temperatures.
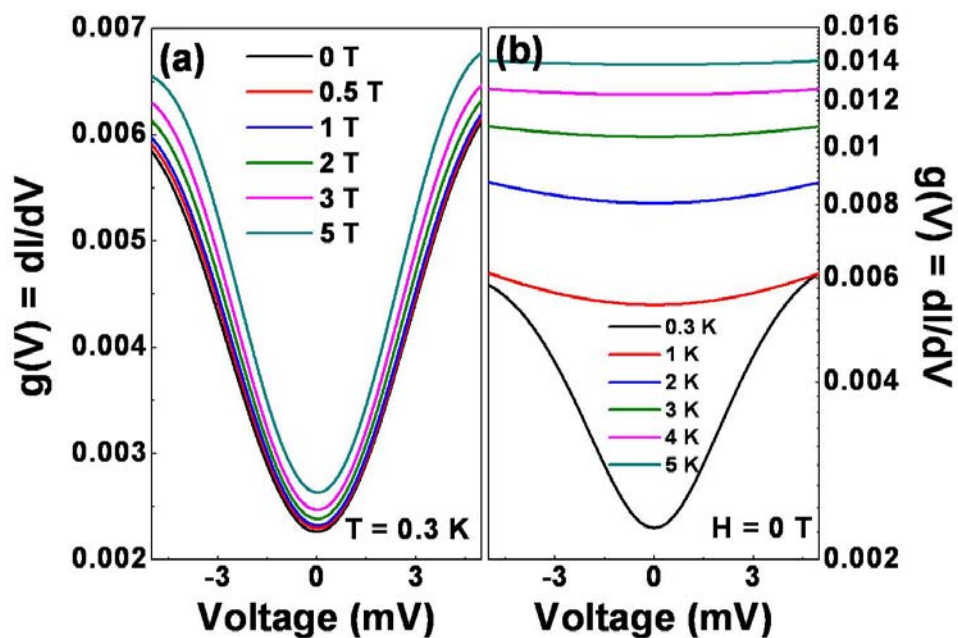
Fig.5.20. The differential conductance vs *V* curves obtained from the curves shown in Fig.5.19.

To explore the nature of non-linearity in the *I-V* characteristics in these samples, the bias dependence of the differential conductance (*g* versus *V* curves) have been fit to the empirical expression:

$$g(V,T) = g_0(T) + \Delta g(V,T) = g_0(T) + g_\alpha(T)|V|^\alpha \ldots\ldots\ldots\ldots\ldots(4)$$

(See section 5.2.1 for a discussion on the terms.) For pure tunneling in a metal-insulator-metal junction, when the electron does not suffer any scattering in the barrier $\alpha = 2$. α decreases as the electron crosses the barrier through the localized states in the barrier. Specifically, as discussed in section 5.2.1, $\alpha = \dfrac{n+2}{n+1}$, where n is the number of localized states in the barrier through which tunneling occurs. For $n \gg 1$, $\alpha \rightarrow 1$.

For fitting eqn. (4) to the data, the bias is limited to below 3 mV (or 5 mV) depending on temperature. This is because beyond that generally the voltage becomes comparable to the barrier height and the sample may also heat up. The typical value of Δ observed by us is less than 0.1 meV for LSCO samples. Thus limiting the fit to below 5 mV is justifiable. Eq. (4) is a two parameter relation that quantifies the non-linearity through the exponent α and g_α, the latter being a measure of the weight of the non-linear transport. g_α, α and g_0 are all functions of T and H. Variation of the parameters g_0, α and g_α as a function of T are shown in figure 5.21.
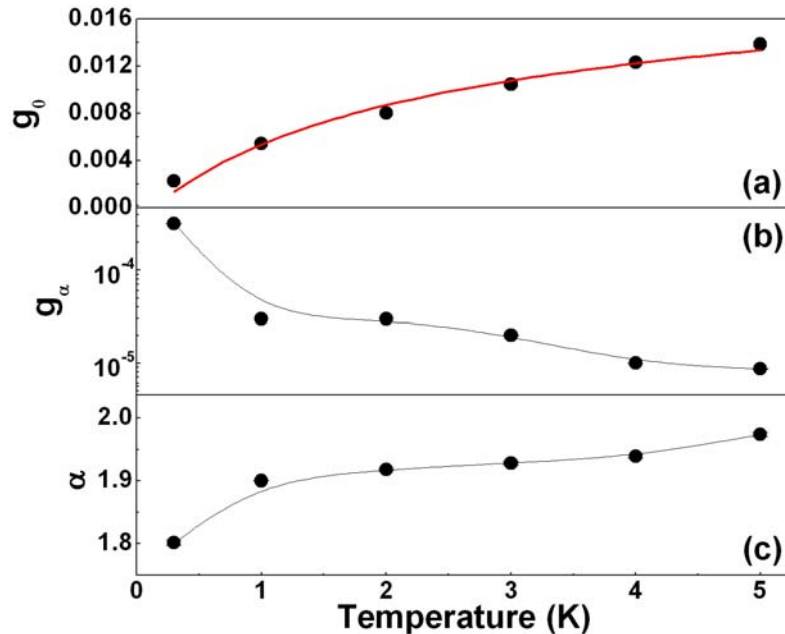
Fig.5.21. Temperature dependence of the fit parameters g_0, g_α and α for LSCO nanoparticle ($d \sim$ 36 nm) in zero field (for details see text). Error bars, where not visible, are smaller than the symbols.

The exponent α, which is a measure of the tunneling type, shows a value close to 2. An exponent $\alpha \approx 2$ is expected in a conventional barrier type tunnel junction[42]. There is a shallow temperature dependence and α showing a small decrease below 1 K. This would mean that there are localized traps in the oxides and the transmission of the electron through the localized state becomes important at low temperatures when the thermal energy is low. The non-linear I-V curve thus clearly establish that below 5 K the transport through these nanomaterials assembly is dominated by barrier- tunneling process. In this case the zero bias conductance g_0 is expected to approximately follow the $1/\rho$ of the sample. The resistivity follows equation (2). To check this g_0 is fitted to the equation, $g_0 = g_0' \exp\left(-2\sqrt{\dfrac{\Delta_{tunnel}}{k_B T}}\right)$, where Δ_{tunnel} is a measure of the activation gap as observed from the zero-bias conductance. The fit is shown as a red line in the upper panel of figure 5.21. The fit is excellent and gives a value for $\Delta_{tunnel} \approx .0357 \pm .0002$ meV. This is very close to $\Delta \approx 0.025$ meV as obtained from the transport data. (The finite difference arises because of the finite voltage used to measure ρ). The voltage dependent term g_α is a clear measure of the non-linearity and it decreases rapidly as T is increased due to the fact at higher temperatures the tunneling is suppressed by parallel transport channels. The non-linear I-V curve taken on the nanoparticles sample of LSCO that validates the basic assumption that transport below 5 K is indeed inter-grain tunneling.

The magnetic field also affects on the I-V curves. This is shown in figure 5.20 (a), where we show the I-V data and the corresponding g-V data as a function of the applied field at the lowest temperature measured (0.3 K). The g-V data obtained from the I-V data in an applied field have been analyzed using equation (4) and the variation of the parameters with field are shown in figure 5.22.
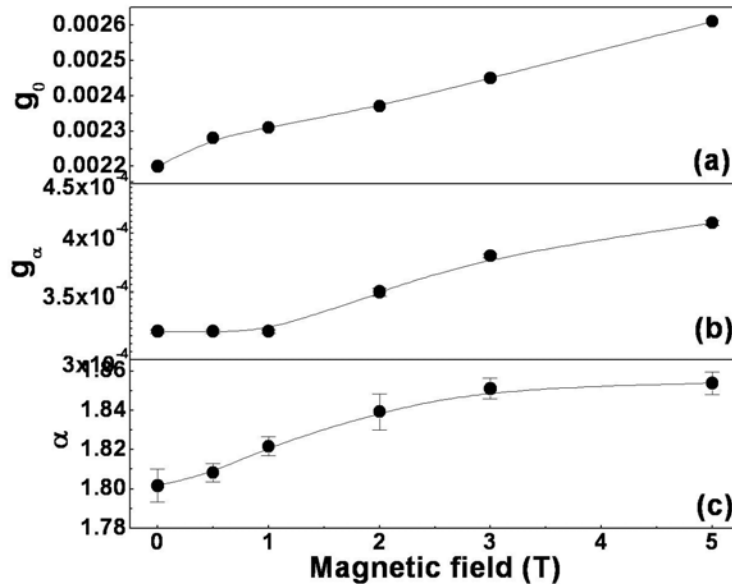

Fig.5.22. Magnetic field dependence of the fit parameters g_0, g_α and α for LSCO nanoparticle ($d \sim 36$ nm) at T = 0.3 K (for details see text). Error bars, where not visible, are smaller than the symbols.

The magnetic field enhances g_0 and the change in g_0 in a field of 5 T is approximately 15%. This is larger than but comparable to the 10% MR (measured from resistivity ρ) observed in the same field at 0.3 K. The enhancement of g_0 can arise from a reduction of the average barrier height and also from an enhancement of spin alignment on application of field. It is difficult to separate out contribution of the effects individually. The non-linear term g_α also gets enhanced in the magnetic field. In a conventional tunnel junction this term arises from the barrier transmission due to finite voltage. Thus enhancement of this term is linked to the lowering of the barrier height. Typically the ratio g_0/g_α for a conventional metal-insulator- metal tunnel junction follows the following relation with the average barrier height φ[42].

$$\frac{G_\alpha}{G_0} \approx F_1 \varphi^{-1} - F_2 \varphi^{-1/.2} \dots\dots\dots\dots\dots\dots\dots\dots\dots\dots\dots\dots\dots\dots\dots\dots\dots(5)$$

where F_1 and F_2 are constants. We do see an enhancement of the ratio on application of field and this will happen if application of the field reduces the average barrier height. This is the conclusion that we reached as an explanation of reduction in the energy Δ on application of the field. Thus we have clear case that the low temperature transport is dominated by the inter-grain tunneling and the effect of magnetic field not only changes the spin polarization as in TMR but it also lowers the average barrier height.

There is an enhancement of the exponent α in magnetic field. This enhancement is small but would signify that tunneling through localized states are suppressed in a magnetic field. These features as we will see are also valid qualitatively for the LCMO nanoparticles which we discuss next.

5.7.2 LCMO system

The LCMO nanoparticles also show non-linearity (non-ohmic behavior) in the *I-V* characteristics at low temperature. The *I-V* curves for the smallest size LCMO sample are shown in Fig.5.23 (*I-V* curves at H = 0 T at different temperatures) and Fig.5.24 (*I-V* curves at T = 0.3 K under different magnetic fields).
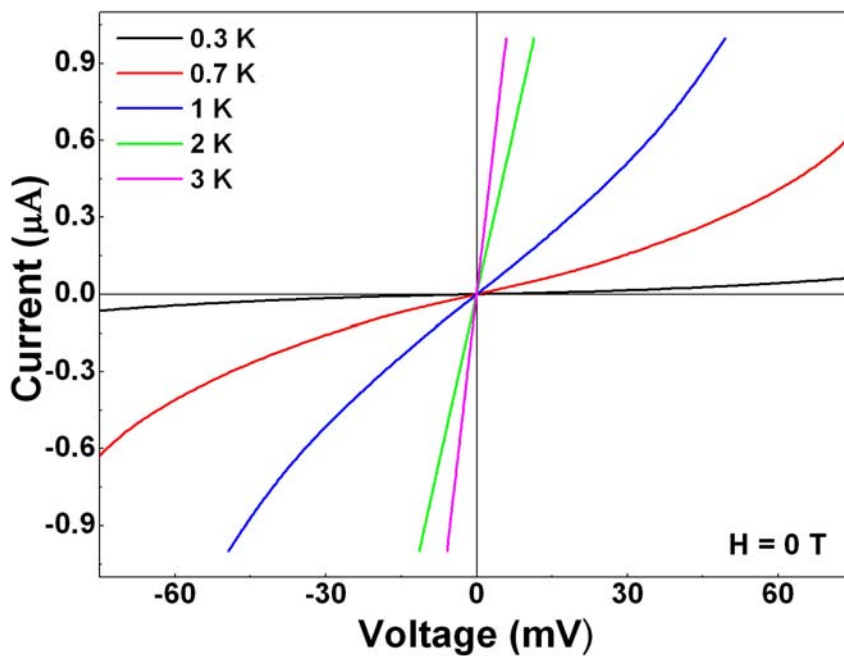
Fig.5.23. *I-V* curves of LCMO nanoparticle with average particle size 15 nm at H = 0 T taken at different temperatures.

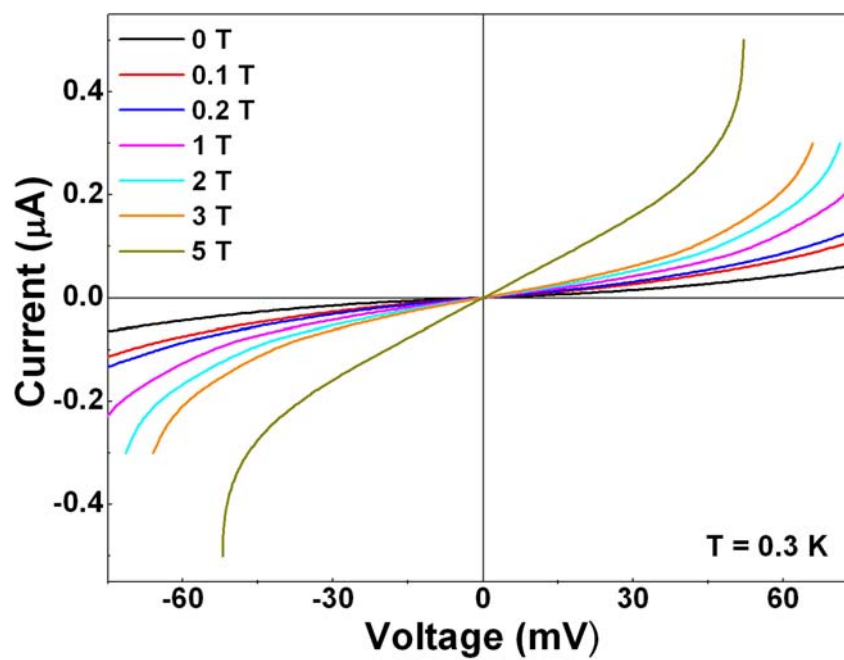Fig.5.24. *I-V* curves of LCMO nanoparticle with average particle size 15 nm at T = 0.3 K taken under different magnetic fields.

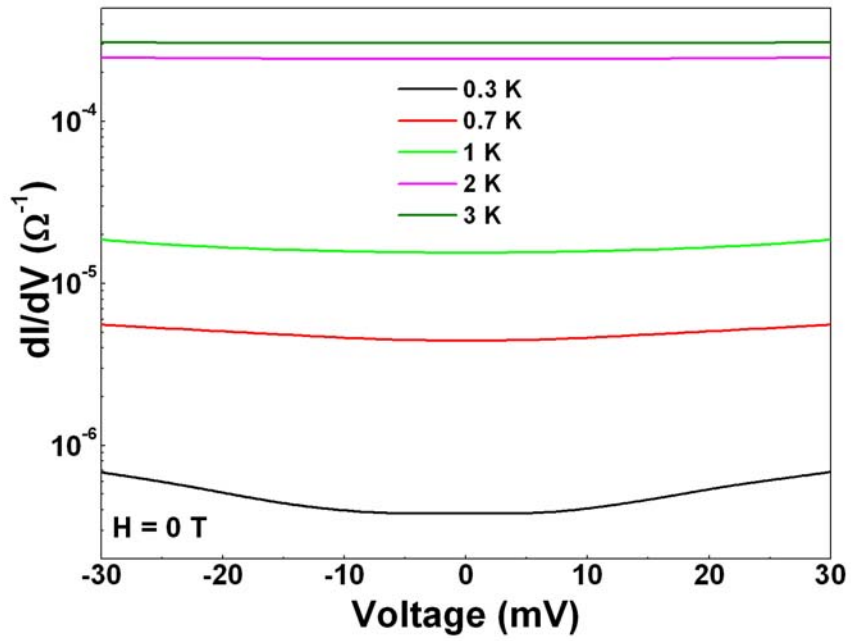The *g-V* curves obtained from the *I-V* curves are shown in figure 5.25 and 5.26.

Fig.5.25. The differential conductance vs *V* curves obtained from the curves shown in Fig.5.23.
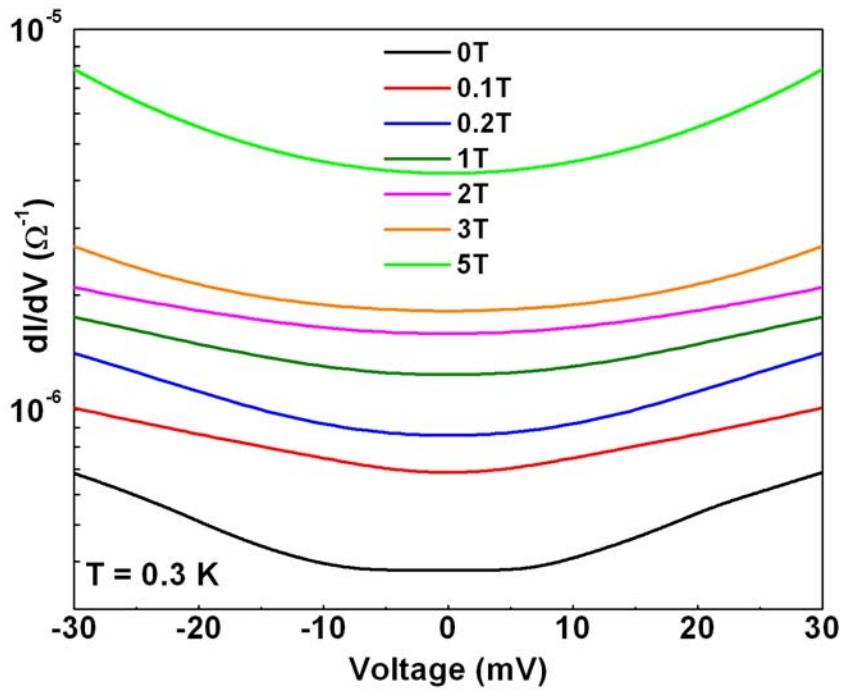
Fig.5.26. The differential conductance vs *V* curves obtained from the curves shown in Fig.5.24.

It can be seen that at lowest temperature (T ~ 0.3 K) and in zero field there is a bias region over which the conductance g(V) is low and flat this occurs for bias $|V| \le$ 5mV. It appears that there is a bias region over which a gap opens up. The size of the gap expected from Coulomb charging for a single junction is E_C which is given by the relation (for a particle of size *d*) is:

$$E_C = \left(\frac{e^2}{2\pi\varepsilon\varepsilon_0 d} \right) \left[\frac{s}{d/2+s} \right] \dots\dots\dots\dots\dots\dots\dots\dots\dots\dots\dots(6)$$

where *d* and *s* has the same meaning as in equation (3). For the manganites using a dielectric constant $\varepsilon \approx 20$ we obtain $E_C \sim 3$ meV . This is similar to but smaller than the size of the gap region observed ~ 5 mV. This difference can be explained in the following way. In a sample like us we don't have a single junction but a collection of junction that are in series and parallel. The observed gap $\Delta_{gap} = N_{eff} E_C$, where N_{eff} is the number of junction in series which in this case is ~2. This value of Δ_{gap} is somewhat larger than but similar to Δ obtained from the temperature dependent resistivity data that was fitted to equation (2). It is thus gratifying that the energy scales that are involved in tunneling process evaluated by different means give values that are within reasonable limits of each other. This is assuring because it revalidates the claim that the observed transport behavior below 5K is indeed inter-grain tunneling that is controlled by Coulomb charging of the metallic manganite grains.

As the temperature is increased, this gap closes very rapidly and one obtains a conventional tunneling curve for a metal-insulator-metal junction. The fit to the tunnel equation (4) thus has been done for $|V| >$ 5mV at lowest temperatures where the gap like feature exists. . The values of the parameters so obtained are shown in figure 5.27.

Fig.5.27. Temperature dependence of the fit parameters g_α and α for LCMO nanoparticle ($d \sim$ 15 nm) in zero field (for details see text). Error bars, where not visible, are smaller than the symbols.

The parameter g_0 in this case is not shown because of the truncation of the data below bias of 5 mV it may lead to error in estimation of g_0. However, a visual observation shows that on heating the sample from 0.3 K to 3 K the zero bias conductance g_0 changes by more than two orders. This change cannot occur just from the alignment of spins and spin polarization effects at the electrodes alone. This arises because the Coulomb gap that leads to depletion of tunneling conductance in the zero bias region gets reduced when T is increased and the depletion rapidly removed. This is compatible with the larger value of Δ observed in resistivity data compared to that in LSCO.

The non-linear term g_α, like that in the case of LSCO rapidly decreases on warming as the tunneling process gives way to other forms of transport above 5K. The coefficient α is very similar to that seen in the case of the LSCO sample and it has a shallow temperature dependence that at higher temperatures approach the expected value of 2.

The magnetic field also affects the nature of non-linearity in the LCMO nanoparticle sample appreciably. This becomes clear when we plot the $g(V)$ versus V curves in at T = 0.3 K under different magnetic fields(Fig.5.26). The depletion in conductance near the zero bias region gets filled up and the gap like feature gradually vanishes in the magnetic field when it is more than 1 T. The $g(V)$-V in the magnetic field is analyzed using (4). The parameters in magnetic field is shown in Fig.5.28.
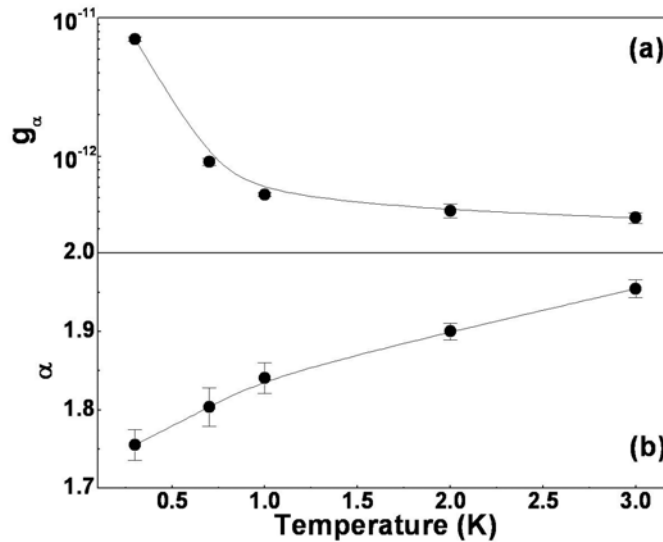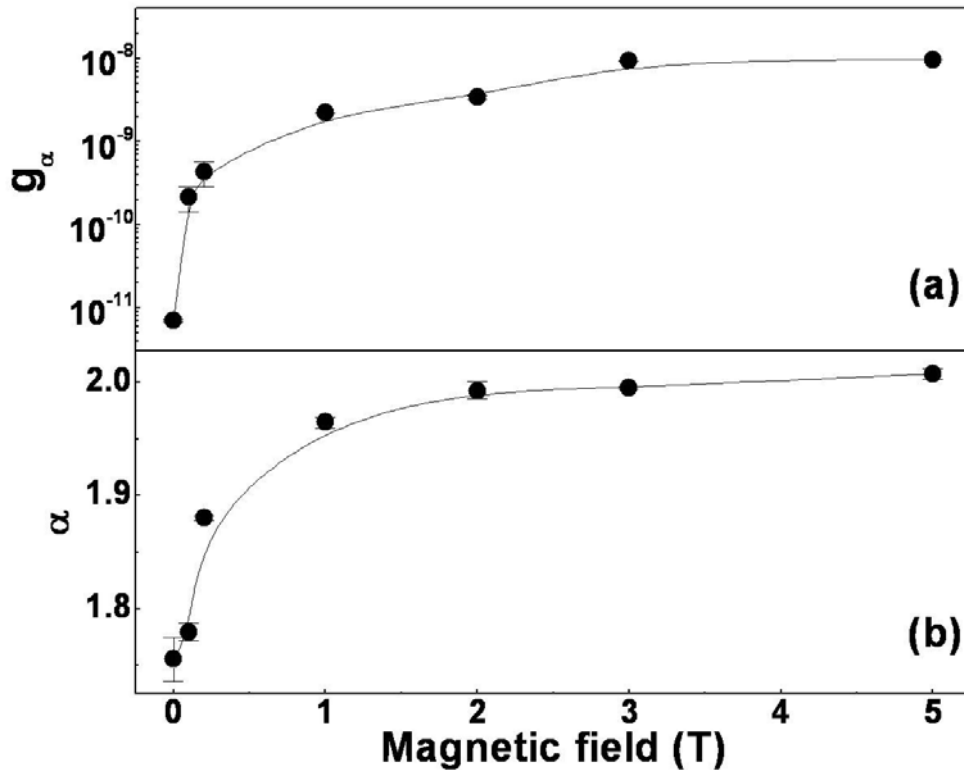

Fig.5.28. Magnetic field dependence of the fit parameters g_α and α for LCMO nanoparticle ($d \sim$ 15 nm) in zero field (for details see text). Error bars, where not visible, are smaller than the symbols.

Due to the reason mentioned before the zero bias conductance is not plotted. However, the data clearly show that there is a large change in the zero bias conductance in magnetic field. An applied field of 5T can change the zero bias conductance by at least one order of magnitude. This is larger than the MR seen in similar field. The large change in g_0 occurs because the magnetic field fills up the gap-like region that arises due to Coulomb charging. This is distinct from the TMR like phenomena that occurs due to alignment of spins parallel and anti-parallel in the electrodes that are spin polarized. The decrease of the gap feature in an applied field is definitely a very major finding of the thesis. Interestingly, the non-linear term g_α also changes by few orders in a magnetic field and the rise is most rapid at low field. We ascribe this change to a lowering of the barrier in a magnetic field as in the case of LSCO but the effect is more drastic in the case of the LCMO. The exponent shows a small but characteristic rise in the magnetic field which we describe as due to suppression of multistep tunneling through localized states in presence of magnetic field.

5.8 Summary of results

We end this chapter by recapitulating the main results that have been obtained so far:

We end this chapter by recapitulating the main results that have been obtained so far:

1. In this chapter, we have made a comprehensive study of the electronic transport properties of nanoparticles of three classes of complex oxides, namely, $La_{0.67}Ca_{0.33}MnO_3$, $La_{0.5}Sr_{0.5}CoO_3$ and $LaNiO_3$. Each of these oxides are distinct in the sense that the ground state of these oxides, in the bulk form, are also very different from each other. While the first two (LCMO and LSCO) are ferromagnetic oxides, LNO is a nonmagnetic metallic oxide. We have shown that the difference in their magnetic properties get reflected in the way the transport properties evolve as the size is reduced. The focus of this chapter is the region below 10 K where we show new results.

2. While nanoparticles of the ferromagnetic oxides become insulating on size reduction, nanoparticles of nonmagnetic LNO retains metallic behavior down to the lowest temperature measured. We believe that this difference arises from a difference in the physical nature of their grain boundaries. While in the nanoparticles of the non magnetic oxide, the nanometric grains touch each other through metallic contacts, in the nanoparticles of the ferromagnetic oxides, the grain boundaries are insulating. The insulating nature of the grain boundaries arises because of the magnetic disorder in them, and due to the fact that in these correlated electron systems, metallic conduction is coupled to the ferromagnetic state.

3. The nanoparticles of the ferromagnetic oxides show very novel properties below 10 K. The temperature dependence of ρ shows a steep rise which is a likely manifestation of the phenomenon of inter-grain tunneling with a contribution arising from Coulomb blockade. The concept of grain boundary inter-grain tunneling in manganites in particular has been proposed before but the effect of Coulomb charging on them is a concept that hes not been discussed in the context of transport in these oxides. An investigation of this low

temperature transport behavior under the application of magnetic field reveals a negative MR. The application of field aligns the spin in the disordered grain boundary (or barrier) region which increases the MR. For the LSCO nanoparticles, the MR does not saturate even at a field of 14 T, which implies that sufficient spin canting still exits, and complete alignment of the spins is not achieved even at this high magnetic field. The LCMO nanoparticles show a much larger MR than the LSCO nanoparticles. Here, the predominant transport mechanism is inter-grain tunneling.

4. The idea that the ferromagnetic nanoparticles, at low temperature, exhibit tunneling type of transport through the disordered grain boundary region (which acts a barrier to tunneling) is further validated by direct measurements of the non linear *I-V* data in this temperature range. Here, the transport mechanism is similar to that occuring through a network of tunnel junctions that consist of the metallic ferromagnetic oxide nanoparticles as electrodes and the intervening oxide regions as tunnel barriers. Through a detailed fitting of the differential conductance curves, we have investigated how the tunneling mechanism responds to temperature as well as magnetic field. The LCMO system, in particular, shows a gap-like region (in the $g(V)$ vs V curves) at zero bias, which gets filled up by the magnetic field. This gap-like region arises due to Coulomb charging and is not a simple manifestation of transport in spin polarized electrodes. The magnitude of the gap matches quite well with the gap calculated for Coulomb charging as given by equation (6) and revalidates our claim that the observed transport behavior below 5K is indeed inter-grain tunneling that is controlled by Coulomb charging of the metallic grains.

References

[1] R.M.Kusters, J.Singleton, D.A.Keen, R.McGreevy and W.Hayes, Physica B, **155**, 362 (1989)

[2] G.Jeffrey Snyder, Ron Hiskes, Steve DiCarolis, M.R.Beasley and T.H.Geballe, Phys. Rev. B, **53**, 14434 (1996)

[3] D.C.Worledge, G.Jeffrey Snyder, M.R.Beasley, T.H.Geballe, Ron Hiskes and Steve DiCarolis, J. Appl. Phys., **80**, 5158 (1996)

[4] G.Jeffrey Snyder, C.H.Booth, F.Bridges, Ron Hiskes, Steve DiCarolis, M.R.Beasley and T.H.Geballe, Phys. Rev. B, **55**, 6453 (1997)

[5] N.F.Mott, *Conduction in non-crystalline materials*, 2nd. Edition, Clarendon Press, Oxford, 1993.

[6] J.M.D.Coey, M.Viret, L.Ranno and K.Ounadjela, Phys. Rev. Lett., **75**, 3910 (1995)

[7] A.L.Efros and B.I.Shklovskii, J. Phys. C: Solid State Physics, **8**, L49, (1975)

[8] Kathrin Dörr, J. Phys. D: Appl. Phys., **39**, R125 (2006)

[9] M.N.Baibich, J.M.Broto, A.Fert, F.Nguyen Van Dau, F.Petroff, P.Etienne, G.Creuzet, A.Friederich and J.Chazelas, Phys. Rev. Lett., **61**, 2472 (1988)

[10] M. Julliere, Physics Letters A, **54**, 225 (1975)

[11] M.Viret, M.Drouet, J.Nassar, J.P.Contour, C.Fermon and A.Fert, Europhys. Lett., **39**, 545 (1997)

[12] Elbio Dagotto, *Nanoscale phase separation and colossal magnetoresistance*, Springer – Verlag, 2002

[13] Matthias Mayr, Adriana Moreo, Jose A. Vergés, Jeanette Arispe, Adrian Feiguin and Elbio Dagotto, Phys. Rev. Lett., **86**, 135 (2001)

[14] R.Mahesh, R.Mahendiran, A.K.Raychaudhuri and C.N.R.Rao, Appl.Phys. Lett., **68**, 2291 (1996)

[15] H.Y.Hwang, S.W.Cheong, N.P.Ong and B.Batlogg, Phys. Rev. Lett., **77**, 2041 (1996)

[16] X.W.Li, Y.Lu, G.Q.Gong, G.Xiao, A.Gupta, P.Lecocur, J.Z.Sun, Y.Y.Wang and V.P.Dravid, J. Appl. Phys., **81**, 5509 (1997)

[17] J.Klein, C.Höfener, S.Uhlenbruck, L.Alff, B.Büchner and R.Gross, Europhys. Lett., **47**, 371 (1999)

[18] S.Lee, H.Y.Hwang, Boris I. Shraiman, W.D.Ratcliff II and S-W.Cheong, Phys. Rev. Lett., **82**, 4508 (1999)

[19] Mandar Paranjape, J.Mitra, A.K.Raychaudhuri, N.K.Todd, N.D.Mathur and M.G.Blamire, Phys. Rev. B, **68**, 144409 (2003)

[20] J.G.Simmons, J. Appl. Phys., **34**, 238 (1962)

[21] J.G.Simmons and G.J.Unterkofler, J. Appl. Phys., **34**, 1828 (1962)

[22] J.G.Simmons, J. Appl. Phys., **34**, 1793 (1963)

[23] L.I.Glazmann and K.A.Matveev, Sov. Phys. JETP, **67**, 1276 (1988)

[24] P.A.Lee and T.V.Ramakrishnan, Rev. Mod. Phys., **57**, 287 (1985)

[25] A.K.Raychaudhuri, K.P.Rajeev, H.Srikanth and N.Gayathri, Phys. Rev. B, **51**, 7421 (1995)

[26] R.E.Cavicchi and R.H.Silsbee, Phys. Rev. Lett., **52**, 1453 (1984)

[27] T.A.Fulton and G.J.Dolan, Phys. Rev. Lett., **59**, 109 (1987)

[28] L.S.Kuzmin, P.Delsing, T.Claeson and K.K.Likharev, Phys. Rev. Lett., **62**, 2539 (1989)

[29] C.N.R.Rao, R. Raveau (Eds.), *Collosal Magnetoresistance, Charge Ordering and Related Properties of Manganese Oxides*, World Scientific, Singapore, 1998

[30] See phase diagram of $La_{1-x}Sr_xCoO_3$ (Fig.3.1(b) of Chapter 3)

[31] K.P.Rajeev, G.V.Shivashankar and A.K.Raychaudhuri, Solid State Comm., **79**, 591 (1991)

[32] N.Gayathri, A.K.Raycahudhuri, X.Q.Xu, J.L.Peng and R.L.Greene, J. Phys. Condens. Matter, **10**, 1323 (1998)

[33] Cryomech, Model PT405 Cryogenic Refrigerator, 113 Falso Drive, Syracuse, New York 13211, USA

[34] Himanshu Jain, A.K.Raychaudhuri, Ya.M.Mukovskii and D.Shulyatev, Solid State Comm., **138**, 318 (2006)

[35] R.Mahendiran and A.K.Raychaudhuri, Phys. Rev. B, **54**, 16044 (1996)

[36] B.Abeles. P.Sheng, M.D.Coutts and Y.Arie, Adv. Phys., **24**, 407 (1975)

[37] O.Chayka, L.Kraus, P.Lobotka, V.Sechovsky, T.Kocourek and M.Jelinek, J. Magn. Magn. Mater., **300**, 293 (2006)

[38] C.J.Yang, M.Zhang and Z.D.Zhang, J. Korean Phys. Soc., **43**, 762 (2003)

[39] In the core – shell model, M_S is proportional to the volume fraction of the core i.e. $M_S = M_{0S}\left(\dfrac{\left(d/2\right)-t}{d/2}\right)^3$. Expanding the cube and ignoring higher powers of t/d, we get the equation $M_S = M_{0S}\left(1-\dfrac{6t}{d}\right)$.

[40] Mandar A Paranjape, K Shantha Shankar and A K Raychaudhuri1, J. Phys. D: Appl. Phys. **38,** 3674 (2005)

[41] Mandar Paranjape, J. Mitra and A. K. Raychaudhuri, Phys. Rev. B, **68**, 144409 (2003)

[42] *Principles of Electron Tunneling Spectroscopy* by E.L. Wolf, Oxford University Press, Oxford U.K 1985

CHAPTER 6. CONCLUSIONS AND SCOPE FOR FUTURE WORK

The focus of this dissertation has been the ground state of complex oxides (manganites and cobaltates), and how it responds to size reduction. The smallest average size of the nanoparticles used were ~ 15 nm. This corresponded to a size reduction of more than 3 orders of magnitude (the bulk samples having an average particle size in the μm regime). The samples (both nanoparticles as well as bulk) were prepared using a chemical route taking care to ensure that the stoichiometry (both cation as well as oxygen) was maintained, and the changes that were observed in the nanoparticle samples (vis – a – vis the bulk properties) arose solely as an effect of size reduction.

6.1 Conclusions

The studies have been done in the context of manganite and cobaltate nanoparticles. The results obtained have been given in Chapters 3, 4 and 5 which have been concluded by summarizing the individual results pertaining to each chapter. In this chapter we list the salient features which emerge for the first time from the work presented in this dissertation.

1. **Role of the structure:** The importance of the crystal structure in determining the nature of the ground state in nanocrystalline complex oxides have been illustrated for the first time in this thesis work. This is the first time that detailed structural work has been done on nanoparticles of complex oxides using high resolution diffraction techniques. These studies have established that the structure plays an important role in determining what the ground state will be and any modification that we see in the physical properties of the nanoparticles (vis – a – vis the bulk physical properties) are not simply manifestations of surface effects as had been believed earlier.

2. **Pressure effect:** We propose for the first time that size reduction acts in a way which is equivalent to applying external hydrostatic pressure. We have shown this quite conclusively for the case of $La_{0.5}Ca_{0.5}MnO_3$ as well as $La_{0.67}Ca_{0.33}MnO_3$. Thus, the charge ordered state seen in bulk $La_{0.5}Ca_{0.5}MnO_3$ gets destabilized when the particle size is reduced to the nanometer regime. The destabilization occurs as a result of increased surface pressure arising from reducing the particle size. This increased surface pressure mimics the effect of externally applied hydrostatic pressure not only qualitatively but also quantitatively (refer Table 4.2 of Chapter 4). Similarly, in nanocrystalline $La_{0.67}Ca_{0.33}MnO_3$ an increased surface pressure results in an increase in the bandwidth vis – a – vis that of the bulk sample (see Fig.3.15 of Chapter 3) thereby leading to an enhancement in the ferromagnetic Curie temperature. Both the effects (i.e. destabilization of the charge ordered state in $La_{0.5}Ca_{0.5}MnO_3$ and strengthening of ferromagnetism in $La_{0.67}Ca_{0.33}MnO_3$) occur as a result of the increased surface pressure in the nanoparticle samples, and are effects which are also seen when the corresponding bulk samples are subjected to external hydrostatic pressure. Although the studies have been done in the context of complex oxide nanoparticles, we believe that the concept that the surface pressure can create an effective hydrostatic pressure and that can act as a change agent may be applicable in other systems also whose properties can change substantially with

moderate hydrostatic pressure. It has already been observed in some cases that high pressure crystal phases that are normally unstable at atmospheric pressure can be obtained in nanocrystalline form and are stable under normal atmospheric conditions. For example, the II-VI semiconductors normally exist in the fourfold coordinate tetrahedral-cubic phase or hexagonal phase. However, at high pressure, a third, six-fold coordinated rocksalt phase is stable. Such rocksalt phase CdS has been identified at normal pressures for 2 nm crystals of CdS synthesized in yeasts[1].

3. **Competing interactions determining the final phase:** This dissertation provides examples of how size reduction can produce completely contrasting effects at the same time. For example, on the one hand, size reduction in $La_{0.67}Ca_{0.33}MnO_3$ modifies the structure in a way which serves to increase the bandwidth thereby enhancing ferromagnetism. On the other hand, it makes the shell disordered which tends to decrease T_C. The two effects act simultaneously and the final state of the particle depends on which effect is stronger. This leads to a non-monotonic variation of T_C with particle size with T_C first increasing with a decrease in the particle size, but for very small particle sizes, T_C again decreasing to a value which is smaller than the bulk T_C. We believe that this can serve to clear up the confusion existing in the community working on nanoparticles of complex oxides where contrasting results have often been reported. This understanding of the mechanism in which the nature of the ground state is determined will also help in bringing in a rational approach while synthesizing samples designed to have a ferromagnetic to paramagnetic Curie temperature at or above room temperature.

4. **Nature of the grain boundary and its importance:** The fact that the surface start having an increasing effect as the particle size is reduced is a known fact. But during this thesis work, we have shown for the first time that even nanoparticles having almost the same particle size can behave in entirely different ways simply due to a difference in the *nature* of their grain boundaries. Thus, nanoparticles of ferromagnetic oxides ($La_{0.67}Ca_{0.33}MnO_3$ and $La_{0.5}Sr_{0.5}CoO_3$) show an activated transport at low temperature whereas nanoparticles of non magnetic $LaNiO_3$ (having the same average particle size) remain metallic down to the lower most measured temperature. The essential difference arises from a difference in the physical nature of their grain boundaries (the details have been given in Chapter 5).

5. **Size reduction leading to strengthening of ferromagnetism:** In most reported oxide systems, size reduction destabilizes the metallic state and reduces ferromagnetic moment. This thesis work brings to light a novel result where ferromagnetism is actually strengthened by size reduction. Thus, $La_{0.5}Ca_{0.5}MnO_3$ which is an antiferromagnetic insulator in the bulk state shows almost full ferromagnetic moment when the particle size is reduced to the nanometer regime.

6.2 Scope for future work

The field of complex oxides has lived up to its name, being extremely complex and fascinating, with the ground state being readily tunable between different electronic and magnetic phases. Nanoparticles of complex oxides, with an added aspect of size reduction, are even more interesting. Although this dissertation deals entirely with the ground state of the nanoparticles of complex oxides, yet in all reality, it explores just the tip of the iceberg. There are still several open issues in this field worth exploring. We end this thesis by listing some of the possible directions in which further investigations could be taken up.

1. The main deficiency of this work is that all the investigations have been done with respect to macroscopic physical quantities. For example, we have established that in $La_{0.5}Ca_{0.5}MnO_3$ nanocrystals, the long range order is lost which leads to the destabilization of the charge order. The structural studies were done using powder diffraction followed by Rietveld analysis. This gave us the average structure of the system on a long range scale. However, nanoparticles are disordered materials, and the average structure might often vary from the structure on a local scale. Even though the long range order is lost, the short range order might well persist. The structure on a short range scale can be investigated using atomic pair distribution function analysis based on neutral total scattering.

2. As has been sufficiently emphasized in this dissertation, in this class of complex oxides, the structural and magnetic properties are strongly correlated. Thus, we can get a local structural understanding of the magnetic characteristics using techniques like x-ray absorption fine structure (XAFS) studies. XAFS measurements can give specific insights into the role of oxygen vacancy, disorder etc. For example, for the manganites, Mn being the magnetic ion in the compound, XAFS measured at the Mn K-edge on the nanoparticles could answer questions pertaining to the presence (if any) of oxygen vacancies around the Mn ion and whether Jahn – Teller distortion exists locally at low temperature.

3. The studies on complex oxide nanoparticles could be extended to nanopatterned structures. Thus, epitaxial films could be grown (using techniques like pulsed laser deposition) which could then be used to create nanopatterned structures (using techniques like e – beam and ion beam lithography) and study how nanopatterning (to a range of size which is similar to the size range covered in this thesis work) affects the ground state of these systems.

References

[1] C.T.Damerson, R.N.Reese, R.K.Mehra, A.R.Kortan, P.J.Carroll, M.Steigerwald, L.E.Brus and D.R.Winge, Nature, **338**, 596 (1989)